UNIVERSITY OF LIVERPOOL

Characterisation of an Electrically Cooled Planar
Germanium Detector for use in the GRI+ Compton
Camera System

Thesis submitted in accordance with the requirements of
the University of Liverpool for the degree of Doctor in Philosophy by

Ellis James Rintoul

November 9, 2020

Abstract

Nuclear decommissioning presents a challenge in the UK in terms of safe and cost-effective clean-up. An aspect of this involves the precise and accurate imaging and quantification of γ-emitting radioisotopes present in a decommissioning environment. In this work, the GRI+ Compton camera system is presented. It is a transportable γ-ray imaging system, comprising of two layers of planar position-sensitive semiconductor detectors; a Lithium-drifted Silicon (Si(Li)) detector and a High Purity Germanium (HPGe) detector, and a tertiary germanium coaxial detector.

The work performed in this thesis focuses on improving the image quality and efficiency achievable by the system through study of the system's HPGe planar detector. This was achieved through development and implementation of Pulse Shape Analysis (PSA) methods, used to improve the position resolution of γ-interactions within the detector, and therefore the imaging quality of the system.

A characterisation process was performed using collimated γ-ray beams to investigate the signal response across the detector surface and through its depth. This was the first such process performed on an electrically cooled HPGe detector manufactured by Mirion Technologies Ltd, that makes use of boron implanted p^+ and amorphous germanium based n^+ strip contacts. The overall performance of the detector was assessed and the charge collection properties investigated. Parametric methods of PSA currently used in the system were optimised using this information.

An alternative method of PSA for use in the planar HPGe detector, signal database comparison, was developed. The signal database was produced through simulation and validated using characterisation scan data. An adaptive grid-search algorithm was then developed to process both single-site and double-site interactions within the HPGe detector. The two methods of PSA were compared when applied to imageable events, consisting of single interactions in the Si(Li) detector and either single interactions or double interactions in the HPGe detector.

The optimal angular resolution of the system was achieved when signal database comparison PSA was applied to the HPGe detector and parametric PSA to the Si(Li) detector. Double-interactions occurring across two strips in the HPGe comprised around 60% of imageable events at 662 keV and so their inclusion yielded a large increase in imaging efficiency. Imaging a 10 cm stand-off ^{137}Cs source produced γ-images with an angular resolution of 8.5° when using single-interactions in the HPGe detector, and of 9.6° when using both single and double-interactions in the HPGe detector.

A user-friendly form of the grid-search algorithm was produced and recommendations made for future use and applications.

Acknowledgements

I would like to take this moment to proffer thanks to those who have given me so many opportunities and offered such tremendous support, and without whom my work would have been a lot less enjoyable to complete, if not impossible.

Firstly, a massive thanks to Andy Boston for not only his supervision and guidance, but also the opportunities given for me to present and attend courses in some fantastic parts of the world. For those days that Andy was unavailable, I must give my gratitude to Laura Harkness-Brennan, for always being there to offer help and encouragement. To other members of the instrumentation group I must say thanks, to Paul Nolan and Helen Boston for the guidance, to Carl Unsworth for the continual coding help and from whom I learnt so much, and finally to Dan Judson, without whom the lab would both figuratively and literally cease to function, I could not have done half the work I did without your input.

To those on the front lines of the Compton camera with me, Adam, Tom and Jaimie, thanks for being fantastic to work with and suffering alongside me every time there was another detector issue. Thanks Tom, for the misadventures in far-flung countries, Jaimie, for always being there to talk Liverpool, and Adam, for the endless feedback, invaluable help, and constant bickering you provided.

To the many members of the nuclear physics group (with special mention to Tom, Lucy and Adam), for the numerous crosswords, too many games of chess, Friday nights, lunch time chats, and everything else, thank you for making the last few years such a pleasure.

And finally but most importantly to those closest to me. Thank you to my family for pushing me to be better and believing in me even during the more tempestuous times. And to Sarah, who's had the honour/misfortune of being by my side for the entire ordeal, you have my eternal gratitude for putting up with me so graciously.

An honourable mention to Augustus John and the Phandalin Five, thanks to each for both the laughs and the suffering.

Sic Itur Ad Astra

Contents

Chapter 1

Introduction

The United Kingdom of Great Britain and Northern Ireland currently generates around 21% of its electricity through nuclear power. This is produced by 15 nuclear reactors operated at seven plants spread across the UK; 14 of which are Advanced Gas-cooled Reactors (AGRs) and one a Pressurised Water Reactor (PWR). All but one of these reactors are scheduled to be decommissioned on a rolling basis from 2023-2030 with the exception being Sizewell B which will remain operational until 2035 [1]. The decommissioning of these reactors falls under the remit of the Nuclear Decommissioning Authority (NDA). The NDA, formed by the Energy Act 2004 as a public body of the Department of Business, Energy and Industrial Strategy, currently oversees and manages the decommissioning and clean-up of the UK's nuclear sites. These currently number 17 such sites across the UK, which includes the sites at which the currently operational nuclear fleet of the UK will be decommissioned. Of these, Sellafield site is the most well-known and hazardous. This is due to its large size and diversity of nuclear facilities currently, or previously, operational on the site. The locations of these sites are displayed in Figure 1.1.

The challenges present in nuclear decommissioning are large and complex, mostly due to a long history of nuclear power generation through varied and non-standard reactor designs in the UK. The technological demands for solutions to problems faced in nuclear decommissioning is therefore high and there is scope to apply technology and techniques developed in nuclear physics to this industry. This thesis presents work performed as part of a collaboration between University of Liverpool Nuclear Physics group, STFC Daresbury Laboratory, the National Nuclear Laboratory, and Mirion Technologies Ltd. (Canberra), to deliver a γ-ray imaging solution for complex nuclear decommissioning environments. Following this section is a more detailed outline of the decommissioning problem faced by the UK, an overview of the technological solution that is investigated in this work, and finally the work contributed within this thesis towards the project.
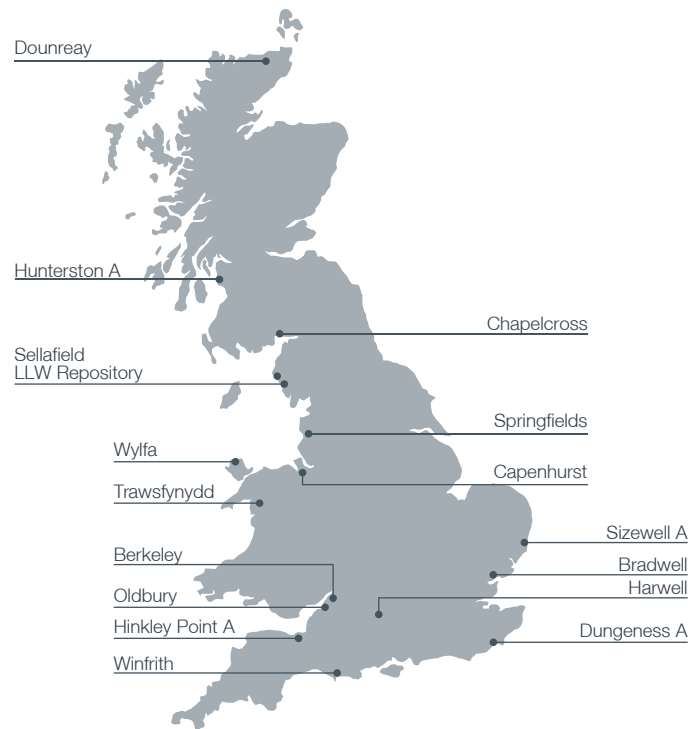
FIGURE 1.1: Map of the decommissioning sites managed by the NDA across the UK, accessed from [2].

1.1 Nuclear Decommissioning

The majority of the NDA's annual decommissioning budget is spent on the management of the Sellafield site, totalling around £2 bn per year [1]. It is expected that total decommissioning and clean-up of the Sellafield site will take 100 years. Sellafield represents the greatest challenge in terms of safe decommissioning, security, and environmental protection. Sellafield is no longer an active site for nuclear power generation since the closure of Calder Hall in 2003, one of the first nuclear power generating stations in the world. Nuclear fuel reprocessing is still performed on site, although this is coming to an end with the closure of the Thermal Oxide Reprocessing Plant (Thorp), in November 2018 and the halting of operations at the Magnox fuel reprocessing plant by 2020 [3]. Cessation of activities at these reprocessing plants as well as the Calder Hall station following its defueling heralds the commencement of decommissioning. In addition to these plants, Sellafield is also home to several waste stores, a mixed-oxide fuel plant, and the Windscale piles and AGR; all of which are in, or soon to enter, the process of decommissioning. These sites, constructed over a long period of time and for a multitude of applications, represent a particularly complex scenario in which decommissioning must be safely carried out.

An increasingly important stage of the decommissioning process is Post Operational Clean-Out (POCO) [3]. The aims of POCO are to reduce both the presence of risks and hazards as well as the costs associated with future care of the plant or facility. This is

fulfilled through the removal of all remaining radiological contaminants present in the environment to be decommissioned. These contaminants pose increased danger to workers required to operate in the affected areas as well as increasing the costs required to care for and safely decommission. Removal of residual activity and thus dose acquired by workers further reduces costs as it would enable increased use of manual labour by bringing safety levels within International Atomic Energy Agency (IAEA) standard guidelines [4] as opposed to requiring remote decommissioning and clean-out. Radiological contaminants that are removed during clean-out are classified as the following waste streams [5] [6]:

Very Low Level Waste (VLLW) - Radioactive content of less than 0.2 GBq/tonne of α, β and γ-activity.

Low Level Waste (LLW) - Radioactive content of less than 4 GBq/tonne of α activity and less than 12 GBq/tonne of β and γ-activity.

Intermediate Level Waste (ILW) - Radioactive content greater than that found in LLW, but not so high as to cause temperature increases.

High Level Waste (HLW) - Radioactive content high enough to cause temperature increases.

Increased level of waste corresponds to increased storage and disposal costs. There is therefore an incentive to classify waste correctly and to ensure that waste is not needlessly classified into a higher category than is necessary. During POCO an emphasis is placed on the characterisation and understanding of the environment which is to be made safe and decommissioned. To perform this, in-situ characterisation measurements must be performed. These environments can often be described as complex scenarios in which the location and activities of radioactive contaminations are unknown. As the contaminant activities are unknown the risks associated are high and consequently human exposure must be minimised during measurement. The environments may comprise inaccessible and hard-to-reach areas which must be characterised from large stand-off distances. For these reasons, when characterisation is performed it requires measurement of the quantity and spectroscopic nature of all radioactive isotopes present with minimum human interaction at a large range of distances. In a nuclear decommissioning environment a large variety of γ-emitting nuclides can be present. These include ^{55}Fe, ^{60}Co, ^{94}Nb, ^{137}Cs, ^{152}Eu, ^{154}Eu, and ^{241}Am [7]. Radionuclides found in these environments that do not emit γ rays, such as ^{90}Sr, will require other means of detection and imaging. The energies of these γ-emitting radioisotopes range from ~0.05 - 1.5 MeV and so the device(s) used to perform the characterisation must be sensitive to a large range of energies. The current process of site characterisation at locations such as Sellafield comprises of three typical steps.

Step 1 - Firstly, γ-ray spectroscopy is performed. This identifies the γ-ray fingerprints of those radioisotopes within the environment. γ-ray spectroscopy information aids

in the understanding of the history of contaminants present at the site as well as informing subsequent clean-out plans.

Step 2 - γ-ray imaging is performed following, or in tandem with, Step 1. This locates the origin of γ rays in the environment through use of position sensitive detector systems. These systems are often formed of collimated scintillator or semiconductor detectors that only allow γ rays incident at certain angles to enter the system, allowing reconstruction of their origin.

Step 3 - Analysis of the spectroscopy and imaging data is performed. From this quantitative, information can be obtained of those present isotopes through modelling and comparison to experimental data. This final step allows dose rate prediction in the characterised area enabling minimisation of worker exposure to the contaminants. It also enables classification of found contaminants into one of the four mentioned waste streams.

These steps are performed either separately, with several detecting systems, or as a combination of steps. A single γ-imaging system capable of Step 1 and 2 must deliver three things. It must be sensitive to γ rays, have a means of recording the direction from which each detected γ ray originates, and be able to produce a "γ-image" that displays the spatial distribution and intensity of the detector γ-radiation. With algorithmic and modelling support the system can potentially provide live dose calculations and quantification of the radiation source activities. Existing systems used in these situations such as the RadScan:800 and RadScan:900 [8], provide position sensitive imaging through mechanical collimation but only achieve low or medium quality spectroscopic information through use of NaI and CeBr$_3$ scintillators, respectively. The mechanical collimator enables the detector to operate as a γ-camera, but reduces the both the system's efficiency and the energy range of γ rays to which it is sensitive. In complex environments in which many radioisotopes of different natures are present a non-distinctive spectrum would be produced, making exact identification of the contaminants present difficult to impossible. The collimator enables γ-ray imaging but with a restricted Field of View (FoV), meaning that multiple angles must be imaged in a large decommissioning environment, such as a contaminated warehouse wall. To image high-energy γ rays of above ~400 keV with a collimated γ-camera, a thick collimator must be mounted and so sensitivity to low energy γ rays is reduced significantly. This reduces their suitability for imaging the full range of isotopes mentioned previously in this section.

An alternative to collimator based γ-ray imaging uses the principle of Compton imaging [9], in which high efficiency γ-ray imaging is possible with a large FoV. Compton imaging is performed by recording two γ-ray interactions and, through use of well-established Compton kinematics, back-projecting the possible γ-ray paths based upon their energy depositions. Through back-projection of many incident γ rays the most likely origin can be determined. The absence of a collimator attenuating incoming γ rays and restricting admission of γ rays to the system allows sensitivity to, and imaging

of, a broad energy range in the region of 100 keV to 2 MeV over a wide FoV and with a high efficiency.

Two transportable Compton camera based solutions currently exist on the market; Germanium Gamma Ray Imager (GeGi) [10], manufactured by PHDs, and Polaris-H [11], manufactured by H3D. These imaging systems make use of a single, position-sensitive, High Purity Germanium (HPGe) and Cadmium Zinc Telluride (CZT) crystal respectively. Single-detector Compton imaging limits the image resolution possible due to the small separation between interactions within the detector. GeGi may also be operated with a pinhole collimator in order to provide high precision images but this lowers the system efficiency drastically. Likewise Polaris-H is hampered by the medium quality energy resolution possible through the CZT crystal and the effect of Doppler broadening [12] and so the image quality is degraded. This is due to the uncertainty introduced to the angles in Compton scattering as a result of uncertainty in the recorded incident γ-ray energy. Both systems provide 4π imaging capabilities for energy ranges of up to 1 MeV for GeGi [10] and <2 MeV for Polaris-H. GeGi reports a spatial resolution of ~6°, though the details of the methodology through which this was achieved are not readily available, while Polaris-H reports an angular resolution of ~20° and an intrinsic imaging efficiency of ~2% [13]. Both systems are capable of producing 2-D images only and so lack a large amount of contextual information about the environment. As 3-D information is not provided, the γ-ray images produced are simply projections onto surfaces and so provide little information in a cluttered and variable depth environment. A more detailed discussion of imaging principles is presented in Chapter 3 in which the achievement of γ-ray imaging through different means is discussed.

A solution is desired that can complete all three site characterisation steps by simultaneously performing 3-D positing sensitive imaging, providing high quality spectroscopy information, and the possibility of dose calculation through activity quantification. Ideally this information would be obtained in real, or close to real, time from a small number of measurements. The complex environments to be characterised necessitate an imaging device that has a wide FoV, sensitivity to a broad energy range, and a high efficiency.

1.2   The GRI+ System

The GRI+ system is a proposed solution for site characterisation required in POCO and nuclear decommissioning. The system is a new iteration of the SmartPET detector system [14] and uses the same principles of planar semiconductor detectors in a Compton camera configuration [9] to provide spectroscopic capabilities, precise γ-ray imaging, and quantitative information about the environment simultaneously. GRI+ is a three-tiered Compton camera, the front two layers of which are position-sensitive. The position-sensitive layers are planar Lithium-drifted Silicon (Si(Li)) and HPGe semiconductor detectors, which provide high-quality spectroscopic information.

The Compton camera nature of this imaging system means that it is capable of delivering a wide FoV, high efficiency and sensitivity to a broad energy range. The use of a combination of Si(Li) and HPGe over competing detecting materials such as sodium iodide scintillator, cadmium telluride semiconductor, and CZT semiconductor detectors provides a better energy resolution which corresponds to an improved ability to characterise sources in complex environments where many isotopes may be present. It also provides more precise Compton imaging due to the high energy resolution achievable. The image resolution possible through a multi-layer Compton camera is also better than that of the only other HPGe-based γ-ray Compton camera available, GeGI, due to the increased separation of the Compton scatter and photoelectric interactions possible with separate crystals. GRI+ has been constructed with the ability to vary the separation between the two planar detectors and can tailor its set-up to situational requirements.

GRI+ is designed to provide 3-D images through combination of γ-ray images with contextual information obtained through other imaging devices attached to the system. This set-up has significantly better energy resolution capabilities than those offered by other detectors as well as a high level of position sensitivity. Overall this will provide more precise imaging and characterisation of the nuclides present in a location. The imaging system will be able to deliver activity quantification through the application of data analysis techniques [15]. Accurate activity quantification can be used to deliver dose rate information about contaminants present in the environment, and so increase the safety and decrease the costs associated with their clean-up. High-precision measurements of the imaged radioisotope activities can reduce the uncertainty when classifying contaminants as VLLW, LLW, ILW, and HLW and so decrease the associated disposal costs. This would be associated with decreased costs in the industry as in-situ measurements would allow for the correct decommission strategies to be employed at each site as opposed to a conservative, and costly, general approach.

1.3   Thesis Outline

The performance of a Compton camera system can be quantified by the imaging quality that is achievable. It is expected that the GRI+ system can deliver a wide FoV, a high efficiency and sensitivity to a broad energy range whilst utilising spectroscopic capabilities to characterise a complex imaging environment. This thesis work has focused on improving the quality of the system's imaging output as well as increasing the imaging efficiency through inclusion and analysis of events that have not been previously used. Improvement of the image quality allows location and characterisation of γ-ray sources in an unknown environment to a higher degree of accuracy as the uncertainty in the source location can be reduced. The work presented in this thesis is the development and investigation of Pulse Shape Analysis (PSA) [16] techniques focused on the planar HPGe detector of the GRI+ system. Application of these techniques improves the position resolution of the detector and therefore the imaging performance of the GRI+

system. This work is split into three distinct sections which are summarised here and explained in more detail below:

Characterisation and Performance Assessment - A Mirion Technologies Ltd. (formerly Canberra) planar HPGe detector was characterised using collimated scans and its performance assessed. This is the novel characterisation of an electrically cooled, Mirion Technologies manufactured, planar HPGe that makes use of amorphous-Ge based n^+ contacts.

Simulation and Validation of a Signal Database - A database of signals was produced through simulation using the AGATA Detector Library (ADL) software package. Average signals produced from known interaction positions in the characterisation process were used to optimise and validate the simulation.

Development and Assessment of a Signal Basis Comparison PSA Algorithm - An adaptive grid-search algorithm was developed to perform database signal comparison PSA. The algorithm can processes single and double-site interaction events and improves the image quality of the GRI+ system. This method of PSA is directly compared to currently used parametric based PSA methods. Their relative advantages and disadvantages are discussed.

The characterisation was performed on the HPGe detector in the system, acquired by the University of Liverpool in late 2015. Characterisation of the detector response function is a necessary process when developing analysis techniques for new detectors. This process is used to understand the detector response to a range of γ-ray energies as well as to allow for the correction of any detrimental effects present in the system. The University of Liverpool has a rich history in characterisation of detector responses through scanning [17] [18] [19]. Methods previously developed and employed at the University of Liverpool were used in this work to scan and characterise the HPGe detector in this work. This detector is the first electrically-cooled planar HPGe that makes use of amorphous germanium based n^+ contacts, manufactured by Mirion Technologies, that has been characterised. Through this process the charge collection properties were investigated and effects such as charge loss, charge sharing and signal response across the surfaces and through the depth investigated. The contribution of cross-talk present in the system was found and corrected for. Development of a signal response function representing the detector volume allowed improvements to be made to already developed PSA algorithm techniques. This was followed by their implementation in the system to improve the position resolution achievable. The signal response characterisation was developed to validate work performed in the second part of this thesis.

The method of PSA studied in the characterisation process is that known as "parametric" PSA, due the simplification of a pulse into several parameters. The characterisation process was used to understand and characterise the parameters that were measured but could not be used to overcome the limitations of this method. The largest

and most important being that of deconvolving and analysing the signals from multi-interaction events. The ability to perform signal analysis on multiple events occurring simultaneously was a problem that was recognised in the development of γ-tracking arrays more than 20 years ago with the proposal of GRETA [20]. The work in this thesis aims to utilise these signal processing and deconvolution techniques in the novel geometry of a planar HPGe detector. This has been implemented through the development of a "signal comparison" database PSA. A database of signals, representing a high granularity of voxelization within the detector, was produced through simulation. This work was performed using a simulation package, ADL [21], developed by the AGATA collaboration [22], which was used to provide a numerical solution of the electric and weighting potentials within the detector through solving of Poisson's equations. A signal database produced through the simulation of charge carrier collection on top of these potentials was calculated and optimised for use in PSA. This optimisation was done through investigation of the space charge present within the detector, a result of the impurity concentrations in the manufacturing process, as well as the temperature dependant charge carrier mobilities and the preamplifier response introduced through the physical electronics. Characterisation data, taken in the first part of this thesis, were used to validate the signal response at select points.

The third and final aspect of the worked performed in this thesis was the development and implementation of a grid-search algorithm. This algorithm was developed to compare experimental signals through a root-mean-square comparison to signals from possible matching positions from the simulated database. This method, known as grid-search comparison, was applied to single-interaction events within the HPGe. The algorithm was expanded to deal with multi-interactions, comprising of two separate γ-ray interactions, through an adaptive grid-search method. This was achieved through convolution of database signals and adaptive searches of the simulated database. Subsequently, positions for each interaction were used to perform Compton image reconstruction through use of an analytical reconstruction code. These positions, representing the closest sub-voxel mm position matches within the crystal, yielded improvements to the image resolution through reduction in the position uncertainty within the detector. An improvement is achieved through implementation of this method for both single-interaction and multi-interaction events. A comparison is made between this method and parametric PSA. The image quality achieved from both is quantified and compared and the relative advantages and disadvantages of each method are discussed. It is hoped that this database PSA method, developed currently for use in the HPGe detector only, will be used continuously in the future to analyse data taken with the GRI+ system. To facilitate this aspiration the database signal PSA method was finalised as a user-friendly and easy to implement stand-alone method.

Chapter 2

Principles of Radiation Detection

A Compton camera relies on two main sets of theory: the functionality and operation of the position-sensitive detectors themselves, and the theory behind γ-ray image reconstruction techniques. In this chapter a theoretical overview of γ-ray detection is given. This covers the interactions of γ rays with matter, the fundamental properties of semiconducting materials, and finally the generation of signals from these materials.

2.1 Gamma-Ray Interactions with Matter

The interactions of γ rays with matter is the principle through which γ-detecting materials are possible. In the energy range of practical γ-ray imaging, ~10 keV through to several MeV, there are three prominent interaction mechanisms. These are photoelectric absorption, Compton scattering, and pair production. Other mechanisms exist, such as Thompson scattering and Rayleigh scattering, but mostly occur at energy ranges that are not relevant to the work performed in this study. A schematic diagram illustrating these three main interaction mechanisms is displayed in Figure 2.1.
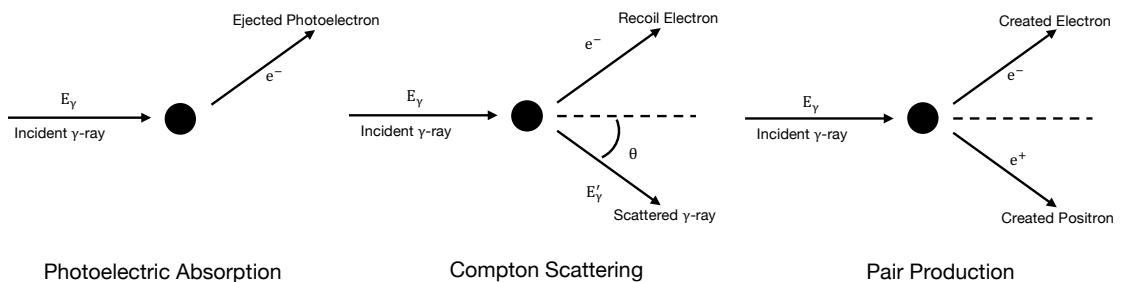
FIGURE 2.1: Schematic diagram of the three main γ-ray interaction mechanisms that occur in the range of ~10 keV through to several MeV.

Each of these mechanisms dominates in a γ-ray energy range dependant on the atomic number, Z, of the material with which it is interacting. In a γ-ray detecting scenario, if the energy range of interest is known then the appropriate detecting material choice can be made based upon the exact ranges over which each type is most

dominant. These ranges are given in Figure 2.2 in which the curved lines represent points where the probability of the competing interaction mechanisms are equal over a range of material atomic numbers and interacting γ-ray energies. The relative cross sections, or probabilities, of photoelectric absorption, Compton scattering and pair production are represented by σ_{PA}, σ_C and σ_{PP} respectively. Shown in red and blue are the atomic numbers of silicon and germanium. These are the two detecting materials used throughout this study. The reasons for these material choices are discussed later but are influenced by the dominant interaction types within each material over the γ-ray energies investigated.
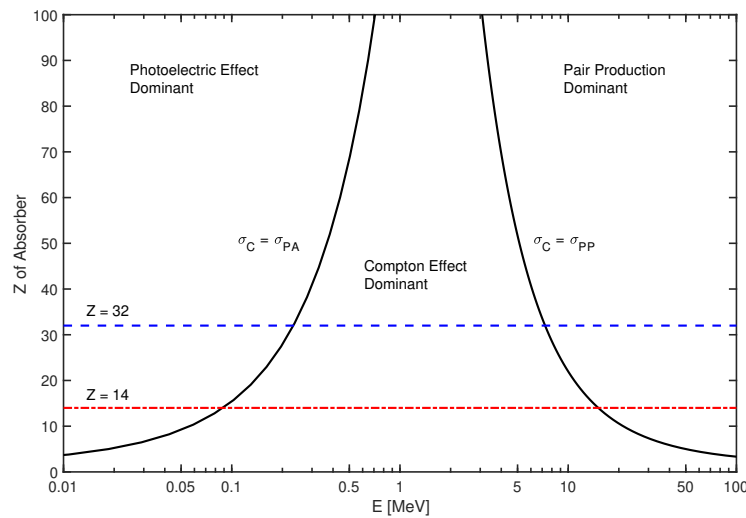
FIGURE 2.2: Dominant interaction mechanisms as a function of Z and interacting γ-ray energy.

The probability of an interaction occurring per unit length within a material is an important factor when considering the volumes of detecting media. It is calculated as the linear attenuation coefficient, μ. This is simply the cross section of each interaction mechanism multiplied by the density of atoms. As such the total linear attenuation coefficient can be expressed as

$$\mu_{Total} = \mu_{PA} + \mu_C + \mu_{PP}, \tag{2.1}$$

where μ_{PA}, μ_C, and μ_{PP} are the linear attenuation coefficients of each of the three mechanisms. From this the fraction of γ rays interacting per unit length can be found for any material. This influences the choice of both the detecting medium and the size of the detector used. In this work it is required that incoming γ rays interact within multiple detectors and so the material must be of a density to promote the needed interaction mechanism and of a thickness either to completely absorb the γ ray or to promote Compton scattering out of the material. The fundamental principles of the three interaction mechanisms are described below.

2.1.1   Photoelectric Absorption

Photoelectric absorption describes the process in which the energy of the γ ray is transferred to the, typically k-shell with 80% likelihood [23], electron of an atomic nucleus. As the full energy is transferred the γ ray is lost in the interaction and as a result the electron is ejected from the target atom's orbit with an energy, $E_{electron}$. This is equal to the initial gamma energy, E_γ, less the binding energy of the electron, $E_{binding}$, as shown in the following equation,

$$E_{electron} = E_\gamma - E_{binding}. \tag{2.2}$$

The liberated, and now free, electron moves through the material and the vacancy left behind is filled by either a higher energy or free electron. If a higher energy electron fills the vacancy a characteristic x-ray is released, in a process known as x-ray fluorescence. This can be immediately reabsorbed, although if it occurs close to the edge of the detecting medium can instead be lost from the system. This results in the γ-ray energy deposition being reduced by a characteristic amount depending on the material. The cross section of photoelectric absorption is highly dependent on the Z of the material with which the γ ray interacts. The probability of it occurring can be approximately expressed as

$$\sigma_{PA} \propto \frac{Z^n}{E^{3.5}}, \tag{2.3}$$

where E is the energy of the incident γ ray and n a value that varies between 4 and 5. As this interaction mechanism is highly dependent on the Z of the target material it is the dominant interaction mechanism in germanium for γ rays of less than 200 keV and in silicon for those less than 60 keV.

2.1.2   Compton Scattering

Compton scattering is the interaction of a γ ray with an atomic electron that results in the partial transfer of the initial full γ-ray energy. Due to the conservation of energy and momentum, the energy transferred in this interaction is related to the angle through which the γ ray is scattered. This relationship allows for the prediction of a γ-ray path based upon the energy deposited in a Compton scatter interaction. This is the fundamental interaction mechanism on which a Compton camera is based. As seen in Figure 2.2, Compton scattering is the dominant interaction over a large range of energies in both silicon and germanium. The relationship between the initial γ-ray energy, E_γ, and the angle θ through which is scatters is related in the following equation,

$$E'_\gamma = \frac{E_\gamma}{1 + \frac{E_\gamma}{mc^2}(1 - \cos\theta)}. \tag{2.4}$$

The energy transferred to the recoil electron, E_{e^-} of rest mass $mc^2 = 511$ keV, is the difference in energy between the initial γ ray, E_γ, and the scattered γ ray, E'_γ. This is the energy recorded in detector following a Compton scatter interaction. The initial γ ray can be scattered by an angle of $\theta = 0°$ through $\theta = 180°$ and produces a characteristic scattering spectrum based upon the initial energy, E_γ. In this equation it is assumed that the recoil electron, E_{e^-}, was initially at rest but in a physical system the momentum of the electron leads to Doppler broadening, a form of uncertainty in the deposited energy that arises due to electron momentum. Doppler broadening is dependent on the interacting medium and is greater for germanium than for silicon [12]. For this reason, silicon is often chosen as a material when the energy deposited in a Compton scatter interaction must be precisely measured.

The probability of Compton scattering occurring is related linearly to the atomic number of the medium. This is due to the number of orbital electrons that act as scattering targets increasing as the Z of the target material increases. The Klein-Nishina formula is used to describe the probability of an incident γ ray of energy E_γ scattering by θ into the solid angle $d\Omega$. This produces an angular distribution of scattered γ rays that is energy dependent. The Klein-Nishina formula is given as

$$\frac{d\sigma}{d\Omega} = Zr_0^2 \left(\frac{1}{1+\alpha(1-\cos\theta)}\right)^2 \left(\frac{1+\cos^2\theta}{2}\right)\left(1 + \frac{\alpha^2(1-\cos\theta)^2}{(1+\cos^2\theta)[1+\alpha(1-\cos^2\theta)]}\right), \tag{2.5}$$

in which $d\sigma/d\Omega$ is the differential scattering cross section, α is equal to E_γ/mc^2, and r_0 is the classical electron radius.

The distribution of the scattering angles is displayed in Figure 2.3 for initial γ-ray energies of 10 keV, 100 keV, 662 keV and 10 MeV. The energies of 10 keV, 100 keV and 10 MeV were chosen to demonstrate the increased preference for forward scattering with increased initial γ-ray energies. At energies greater than 2 MeV, $\theta = 180°$ backscatters are very unlikely [24]. An E_γ of 662 keV is also displayed as it is of particular interest in this study due to its prevalence in many decommissioning environments. This relationship and preference for forward scattering influences the design of Compton cameras and makes the energies of interest relevant to the GRI+ system, 100 keV to 2 MeV, feasible for Compton imaging.

2.1.3 Pair Production

If the energy of the interacting γ ray is more than 1.022 MeV, twice the rest mass of a stationary electron, then pair production becomes a possible mechanism. In this interaction method the γ ray disappears within the Coulomb field of a target nucleus,
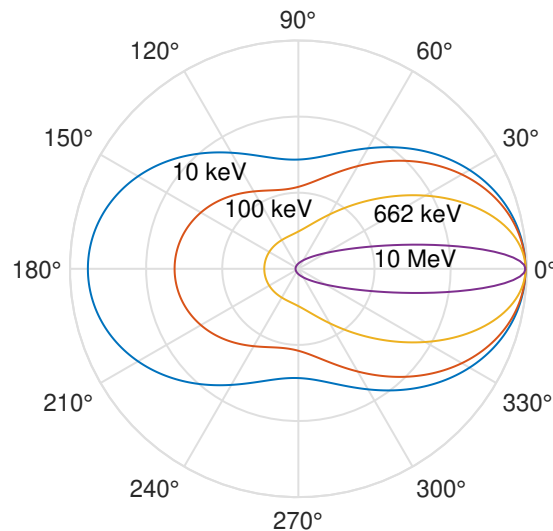
FIGURE 2.3: Scattering distributions described by the Klein-Nishina probability formula for incident γ-ray energies of 10 keV, 100 keV, 662 keV and 10 MeV.

producing an electron-positron pair of mass $mc^2 = 511$ keV each with any additional energy shared between the two particles as kinetic energy. The positron, after thermalising over a short distance, will annihilate with an electron in the medium and produce two back-to-back γ rays of 511 keV each.

The probability of pair production occurring is approximately proportional to the square of the atomic number of the medium in which the interaction is occurring. Due to this is, it is of low probability in germanium below energies of 2 MeV and does not dominate until energies greater than ~8 MeV. As it is unlikely at the energies of interest in this study it is disregarded as an effect.

2.2 Semiconductor Gamma-ray Detectors

The GRI+ system uses three semiconductor detectors to provide spectroscopic information of γ rays. The γ rays interact with the semiconducting material through one of the three interaction mechanisms described previously. Of these three it is most likely that either photoelectric absorption or Compton scattering occurs. Through these, the γ-ray energy is transferred, either partly or entirely, to an electron within the material. The electron travels through the material, losing energy via excitation or ionisation. This process produces charge carriers which are subsequently collected, allowing calculation of the interacting γ-ray energy. This is made possible through the properties of the detecting medium, the movement of charge carriers under the influence of an electric field, and the generation of signals by preamplifiers. The principles of semiconductor γ-ray detectors and the phenomena that make them possible are discussed in the following sections.

2.2.1 Band Structure

A semiconductor is a product of the material's electrical properties, defined by the band structure. The band structure is as a result of their periodic crystalline face-centred cubic lattice structure which dictates the allowed energy states of electrons within said materials. The bands that are of interest for semiconductors are those of the valence band, the conduction band above it, and the forbidden energy region that sits between.

The valence band consists of electrons in the outermost orbital of the atom. The width of the forbidden region is the energy required to promote an electron from the valence band to the higher energy conduction band, which consists of free moving electrons. The width of the forbidden region is the determining factor of the material type. If the valence and conduction bands overlap then electrons can flow freely and so the material is a conductor. When the forbidden region is >5 eV the gap cannot easily be overcome through electron promotion and so the material is an insulator. If the forbidden energy gap is ~1 eV in size then the material can be classed as a semiconductor. This small energy gap makes charge flow possible only in specific circumstances, such as the deposition of energy through one of the γ-ray interaction mechanisms discussed previously. It is this property that makes semiconductor γ-detectors possible. Following the promotion of an electron from the valence to the conduction band a vacancy is left. The vacancy is positively charged and is known as a hole. The electron-hole, $e^- - h^+$, pairs created form the charge carriers found within semiconductor detectors.
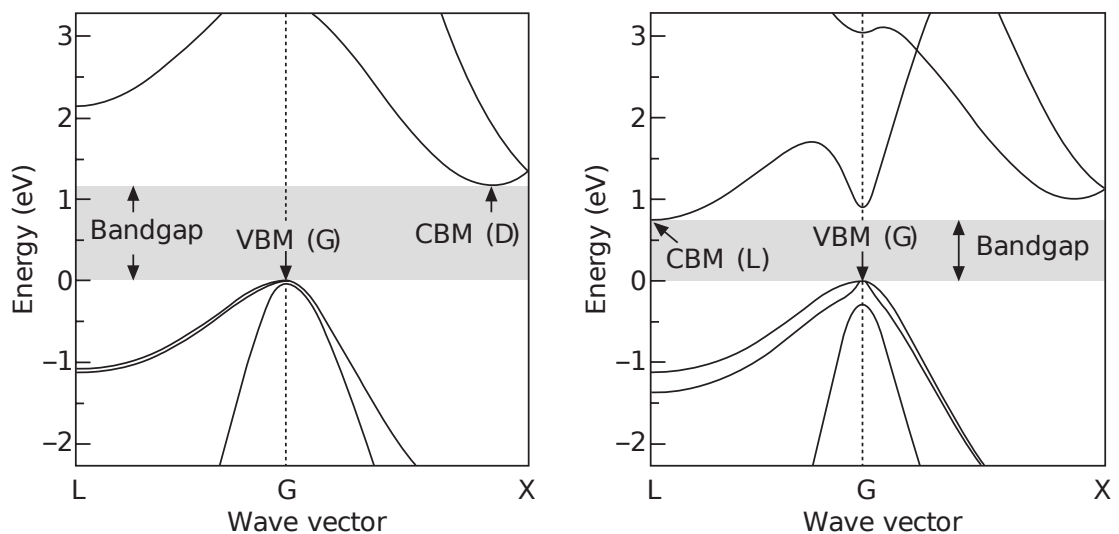
FIGURE 2.4: *E-k* curves representing the band structure of silicon (left) and germanium (right). The VBM and CBM of each material are labelled. Adapted from [25].

Semiconductors can be of a direct or indirect type, depending on the crystal momentum, which is proportional to the electron wavevector, known as the k-vector. In a direct band gap semiconductor the k-vector of the Conduction Band Minima (CBM) energy state and the Valence Band Maximum (VBM) energy state are the same. This matching of k-vectors means spontaneous recombination of an electron with a hole is possible, releasing excess energy as a photon in the process. It also creates a material that is sensitive to light and well suited for use in photovoltaics. If the k-vectors are different then the semiconductor band gap is indirect and spontaneous recombination is not possible as crystal momentum conservation would be violated. Crystalline silicon and germanium are indirect band gap semiconductors and their band structures are displayed in Figure 2.4, adapted from [25]. The energy, E, is plotted against the k-vector, of the lattice, forming an E-k curve. Electrons in indirect band gap materials are less likely to recombine spontaneously and so charge carriers created are longer lived, allowing the material to function as a detector. The size of the band gap, or the difference between the VBM and CBM, is material dependent and is found to be 1.14 eV in silicon and 0.67 eV in germanium at a temperature of 273 K.
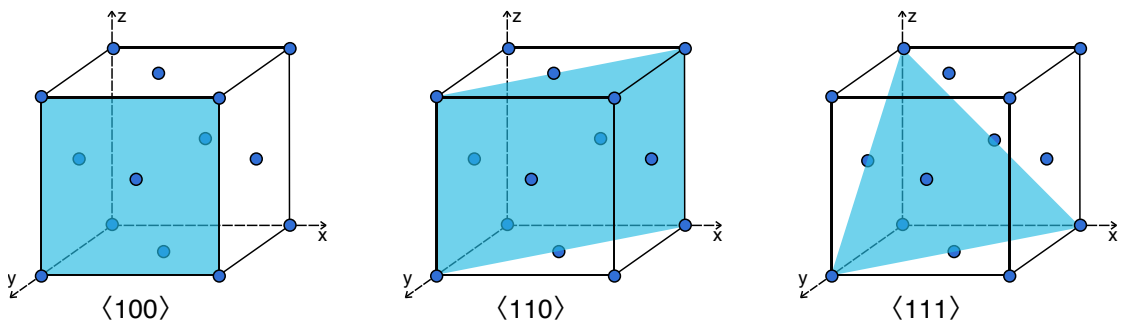
FIGURE 2.5: Planes within a face-centred cubic lattice along with the Miller indices used to define them.

Silicon and germanium each have four valence electrons and so are FCC lattice structures on a two atom basis with an offset of a/4. The spacing of atoms in such a structure varies depending on the lattice plane. These planes can be defined for the crystallographic structure through Miller indices as shown in Figure 2.5. The crystallographic axes produced are <100>, <110> and <111> for a face-centred cube. The k-vector is dependent on the crystallographic axis chosen and varies between $L = <100>$ and $X = <111>$ in this definition. Because of this, the electrical properties of germanium and silicon vary depending on the crystallographic axis orientation along which the charge carriers travel. This has a large effect on the carrier drift velocity, v_d. Crystals are grown along the <001> axis, parallel to the z axis in Figure 2.5, resulting in planar detectors with a depth profile parallel to the <100> axis.

The band structure of a semiconductor can be changed through the removal or addition of electrons to the material. As both germanium and silicon are tetravalent materials, the number of electron and hole charge carriers can be changed through

introduction of ionised trivalent or pentavalent impurities. This decreases or increases the number of electrons relative to the normal tetravalent structure. Germanium and silicon are intrinsic semiconductors, in which the number of electrons and holes are equal. The addition of impurities to an intrinsic semiconducting material turns it into an extrinsic semiconductor. Impurities can be purposefully added or occur during the crystal growing process. The material is changed into either a p-type or an n-type, depending on whether electrons are removed or added. Even in an HPGe crystal small amounts of chemical impurities are present, typically of the order of 10^{10} cm^{-3}, which affect the properties of the material and results in the production of either a p-type or an n-type material.

2.2.2 Charge Carriers

The $e^- - h^+$ pairs produced following a γ-ray interaction are the charge carriers of a semiconductor detector. The number of these pairs formed is proportional to the initial γ-ray energy and depends on the energy required to promote a valence electron to the conduction band, known as the ionisation energy. Holes created in the valance band can be occupied by neighbouring valence electrons. Through this manner holes are able to move through the detecting material while conduction electrons can move freely. The migration of charge carriers through this mechanism is random and charge carriers diffuse away from their site of creation until recombination occurs. If a potential difference is applied to the detector an electric field is created within the medium. This causes the movement of positive and negative charge carriers parallel to the field line directions in opposite directions to each other.

The velocity with which the charge carriers move is dependent on the mobility of electrons, μ_e, and holes, μ_h, as well as the electric field strength, E. In silicon and germanium $\mu_{carrier}$ is dependent on the crystallographic axis relative to the electric field orientation the charge carriers are drifting along. This occurs due to the variation in periodic lattice potential caused by the changing atomic density in the lattice plane. This results in an anisotropic drift velocity within germanium and silicon, particularly at high energies. The orientation of the crystallographic axis is therefore important. The anisotropic drift velocity, v_d, in silicon and germanium can be described as

$$v_d = \mu_{carrier} \frac{E}{\left(1 + \left(\frac{E}{E_0}\right)^{\beta}\right)^{\frac{1}{\beta}}}, \tag{2.6}$$

where E is the strength of the electric field, $\mu_{carrier}$ the experimentally determined mobility for the carriers in question, and E_0 and β experimentally determined constants [26]. A further term to account for the Gunn effect, $-\mu_n$, was added by Mihailescu *et al.* [27]. This introduces a negative contribution to the electron drift velocity at high field strengths, typically above 3 kV/cm, observed by Ottaviani *et al.* [28].

Direction	Carrier	$\mu_0 \ (cm^2/Vs)$	β	$E_0 \ (V/cm)$	$\mu_n \ (cm^2/Vs)$
<1 0 0>	e^-	38609	0.805	511	-171
<1 1 1>	e^-	38536	0.641	538	510
<1 0 0>	h^+	61824	0.942	185	-
<1 1 1>	h^+	61215	0.662	182	-

TABLE 2.1: Table of charge carrier mobility parameters for germanium at 78 K in the <100>, and <111> planes [29].

Parameters of electron and hole mobilities in germanium at 78 K are presented in Table 2.1 for the <100> and <111> directions, calculated by Bruyneel *et al.* [29]. The mobilities of carriers within germanium are presented as it is relevant to the work performed in this study. Other parameterised values describing the electron and hole drift velocity have been previously produced [27] [30] and provide different drift velocities, particularly at high electric field strengths. The values presented in Table 2.1 have been used in the body of this work. From parameterisation in these two axes the drift velocity in any crystallographic orientation can be calculated.
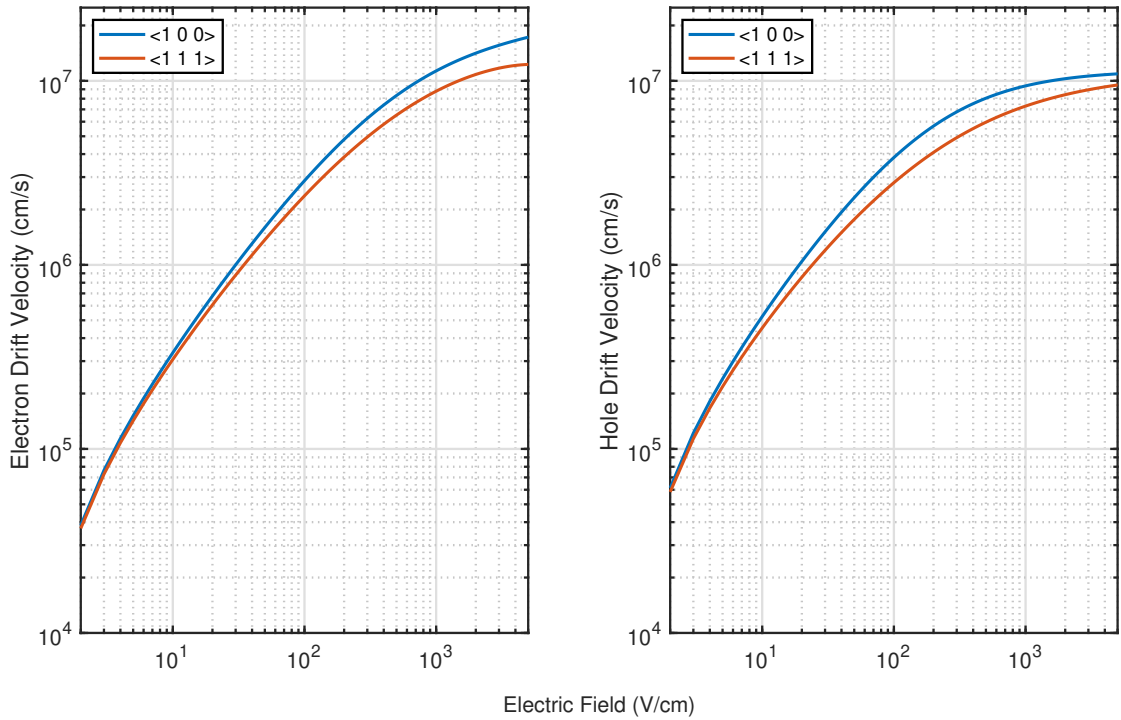
FIGURE 2.6: Electron and hole drift velocities in germanium at 78 K as a function of electric field strength.

The drift velocities in germanium as a function of electric field strength at 78 K have been plotted in Figure 2.6 using Equation 2.6 and the parameters given in Table 2.1. A proportional relationship between electric field strength and drift velocity is observed at low field strengths. The drift velocity for electrons and holes in the two crystallographic axes diverge as field strength increases, although the hole drift velocities in <100> and <111> reconverge at very high electric field strengths of 10^4 V/cm. The field strengths

of relevance in this work are in the region of 10^3 V/cm. At this point an appreciable difference in drift velocity is observed for both electrons and holes between the two lattice orientations in HPGe. In silicon, the mobilities of each carrier are lower relative to in germanium and the disparity between electron and hole mobilities is larger. The hole mobility is described as relatively poor [26] compared to the good hole mobility found in germanium.

2.2.3 The P-N Junction

Operation of a semiconductor detector requires the ability to sweep charge carriers produced in the material by an electric field in order to induce a measurable current. The relies upon the formation of a depletion region within the detector. To create this, p-type and n-type semiconductor materials are combined in thermal equilibrium to form a p-n junction. In this region, the electrons present in the n-type diffuse towards the p-type material whilst the holes within the p-type diffuse towards the n-type. As the electrons within the n-type recombine a net positive space charge is produced on the n-type side. The opposite is true within the p-type material and a net negative space charge is created, thus creating a built-in potential, $V_{internal}$, between the two regions. The associated electric field inhibits further diffusion between the two regions creating a depletion region empty of free charge carriers, resulting in a charge distribution equilibrium. This is illustrated in Figure 2.7 in which an electric field is produced following the creation of positive and negative space charges.
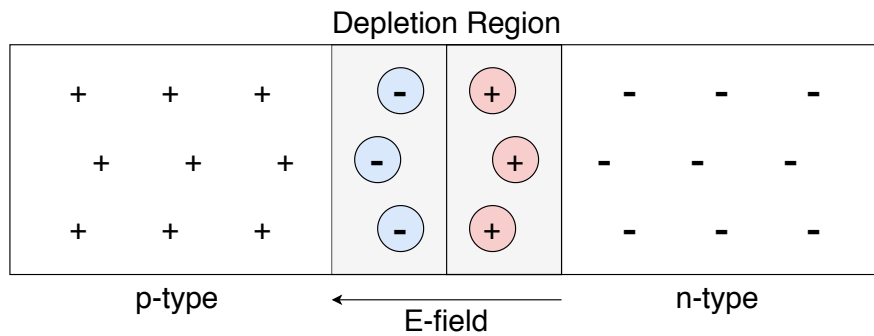
FIGURE 2.7: Semiconductor p-n junction illustrating the creation of a depletion region at the junction of p-type and n-type materials.

The thickness of the depletion region formed is dependent on the magnitude of $V_{internal}$ and is influenced by the impurity concentrations present. Under this internal potential, charge carriers created in the depleted region are swept to the p-type and n-type materials. The strength of this internal potential is small though and may result in charge becoming trapped due to their slow movement as they drift. To increase both the width of the depletion region, and so the volume of the functional semiconductor detector, and the charge carrier drift velocities, an external voltage, V_{bias}, is applied. The bias voltage magnitude is typically chosen to ensure depletion of the entire detector

volume. The width, W, of this depletion region under external bias can be calculated as

$$W \cong \sqrt{\frac{2\epsilon V_{bias}}{qN}}, \tag{2.7}$$

where N is the impurity concentration, ϵ the dielectric constant of the medium, and q the carrier charge. The volume of depleted semiconductor detectors is therefore limited by both the impurity concentration and the bias voltage that can be applied. For this reason, minimising the impurity concentration present in detectors is crucial for depleting and producing large volume semiconductor detectors. This has given rise to materials such as HPGe. The volume is also limited by the external bias voltage that can be applied. At large biases, unwanted current flow can occur in a process known as leakage current; this can inhibit the functionality of the detector. The geometry and impurities of detectors are chosen in such a way that the full detector volume can be depleted without causing large leakage currents. Depleting a planar semiconductor is relatively simple; a bias is applied between one "face" of contacts and the other. These contacts are formed through creation of thin n-type and p-type detector regions, forming n^+ and p^+ contacts, via which a V_{bias} is applied. A Voltage greater than that required for full depletion is often applied as it increases the electric field strength uniformly through the volume and so helps saturate the drift velocity of charge carriers.

2.3   Signal Generation

In a biased and depleted detector a signal can be generated through the movement of the positive and negative charge carriers to their respective collecting contact-electrodes. The movement of both polarity charge carriers through the detecting medium induces a current at the collecting electrodes. A time-dependent signal can be produced at each electrode from this movement of charge according to the Shockley-Ramo theorem [31]. The movement of positive charge carriers, h^+, and of negative carriers, e^-, to their respective electrodes produces a signal comprised of two components. The contribution of these components to the overall signal shape is position dependent and so position of interaction information can be extracted from the signals. Energy information can also be calculated based upon the magnitude of the signals induced at the electrode.

   To understand the formation of these signals at the electrodes and the position dependent nature of them it is necessary to understand the movement of charge carriers through the detector from their point of origin to their termination at the collecting electrodes. The charge carriers follow geometry dependent electric field lines within the detector. This can be calculated from the electric potential found for all points within the detector volume. In addition, the weighting field and potentials are necessary for calculating the current induced at the electrodes as the charge carriers follow their

paths. The following sections describe the steps in calculating the electric and weighting potentials within the detector, from which the fields can be deduced.

2.3.1 Electric Field

The electric field within the detector is calculated from the gradient of the electric potential. Poisson's equation is used to calculate the electric potential for all points within the detector. This is given as

$$\nabla^2 \Phi = \frac{\rho}{\epsilon},$$
(2.8)

where Φ is the electric potential, ρ is the space charge density and ϵ is the dielectric constant of the detecting material. If no trapped charge is present within the detector volume then $\rho = 0$. The Laplacian operator, ∇^2, is used to represent the geometry the potential is being solved over. For a planar detector, as studied in this work, Cartesian co-ordinates are used and thus ∇^2 is given as

$$\frac{d^2}{dx^2} + \frac{d^2}{dy^2} + \frac{d^2}{dz^2} = \nabla^2.$$
(2.9)

When solving Poisson's equation for a physical detector system boundary conditions exist in the form of the geometry and the external applied Voltage. In a planar detector the Voltage is applied between the two faces of contacts and so the value of Φ between the contacts is constrained. In the case of a simple planar detector an analytical solution is usually possible. However, the detectors studied in this work are non-symmetric due to the strip electrode orientations and so a numerical solution would be required to calculate the electric potential at all points within a detector volume. Once the solution has been produced for Φ the electric field at any point within the volume can then be described as

$$E \quad = \quad -\nabla \Phi.$$
(2.10)

With knowledge of the electric field at all points within a detector geometry the movement of charge carriers produced in a γ-ray interaction can be found. This is the electric field path they follow from their point of origin to their termination at the collecting electrodes. Only the charge carrier mobilities in the medium are required to calculate the velocity at which they follow these paths.

2.3.2   Weighting Potential

According to Shockley-Ramo theorem, the charge induced at each electrode is the product of the carrier's charge, q, and difference in weighting potential between the charge carrier's inception and termination at the collecting electrodes, $\Delta\varphi_0$. It is expressed as

$$Q \quad = \quad q\Delta\varphi_0. \tag{2.11}$$

The charge carrier path is found from the previously calculated electric field and so only the weighting potential must be found. The manner through which this is found is the same process as is followed for the calculation of the electric potential. Boundary conditions are implemented in order to solve the Laplacian operator for the detector geometry. For calculation of the weighting potential the Voltage boundary condition is modified and the detector bias is not used. Instead the Voltage is set to one at the electrode for which the weighting potential is being calculated for and is set to zero for all others. This is repeated for each electrode and in this way a weighting potential is calculated for each collecting electrode. Trapped charge within the detector is ignored and so the space charge is assumed to be zero at all points.

Instead of calculating the weighting potential difference between the start and end of the charge carrier path it can be calculated in steps along the path. In this way time-dependent charge signals can be calculated based upon the weighting potential change as the carriers move along their determined path. As such the shape of the weighting potential determines the shape of the charge collection signal. Understanding of the weighting potential through the detector volume is therefore important for understanding detector signal response. To exemplify this, the weighting potential through volume is illustrated in Figure 2.8 (left) in which a multi-strip electrode detector is represented. The detector has three strip electrodes located at $x = 1$ and a large planar contact at $x = 0$. A small gap is present between each separately instrumented strip electrode to which a common Voltage is applied. Due to the small inter-electrode gaps the electric field within follows a linear response through x and is uniform in y and z. The weighting potentials calculated for electrodes A, B, and C as observed by charge carriers travelling along the dotted line and terminating at electrode A are displayed in Figure 2.8 (right).

The weighting potential of electrode A, at which the charge carriers are being collected, is zero at $x = 0$ but rises quickly to one close to the electrode. As this potential is non-zero through the bulk of the detector the electrode is sensitive to the movement of charge carriers at all points along the path. The weighting potential of electrodes B and C do not rise to one but instead are zero at $x = 0$ and $x = 1$. The movement of charge carriers through the detector to electrode A therefore produce no net charge on these contacts. The weighting potential of B and C is non-zero at points through the depth and so while no net charge is collected a transient signal is produced, known as an image charge. The magnitude of these transient image charges is dependent on the magnitude
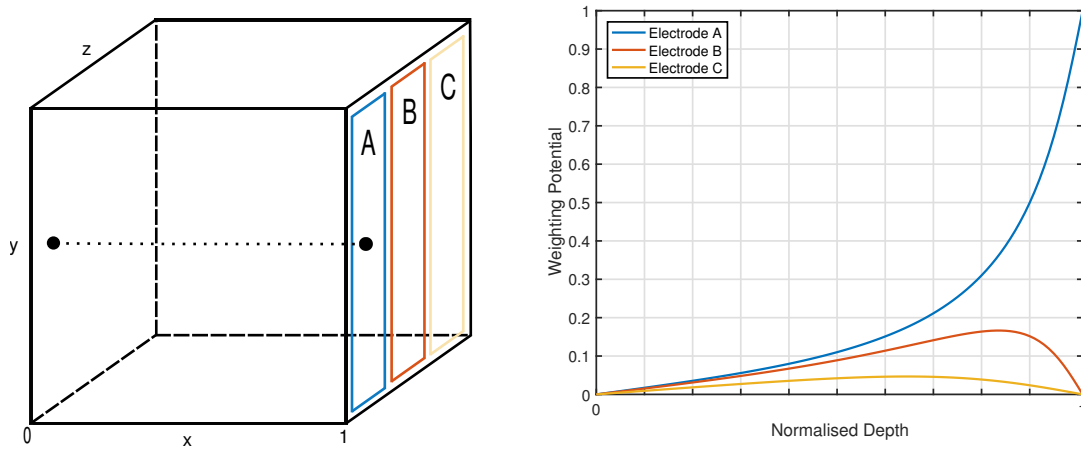
FIGURE 2.8: Left: Illustration of an example detector with three instrumented strip electrodes located at $x = 1$ and a single planar electrode at $x = 0$. An example charge carrier path is represented with a dotted line, terminating at electrode A Right: Weighting potentials as a function of depth in the example detector illustration. Potentials given for A, B and C as seen by charge carriers travelling along the dotted line and terminating at electrode A.

of the weighting potential which is large when close to the charge collecting electrode, at electrode B, and smaller when further away, at electrode C. It is this position-dependent shape of both the produced image charges and charge collection signals that make the application of PSA [16] techniques possible. These techniques are discussed in detail in Section 3.2.

2.3.3 Preamplifiers

During the interaction of γ rays within germanium or silicon, charge carriers are produced and drift along the electric field lines to the collecting contacts. The amount of charge induced at the electrodes is small and hard to measure so preamplifiers are used to process and amplify the charge while keeping noise to a minimum. In this work, charge-sensitive preamplifiers have been used in conjunction with a warm Field Effect Transistor (FET) input stage. The FET input stage produces an amplified current signal and is mounted as close as possible to the detector along with the preamplifiers in order to reduce capacitive loading.

An example of a simplified charge sensitive preamplifier circuit is presented in Figure 2.9. The current is collected by the input capacitor, C_i, integrated by a feedback capacitor, C_f, and then discharged by the feedback resistor, R_f. The product of the feedback capacitor and resistor is equal to the time constant, τ of the feedback circuit, such that $\tau = C_f R_f$. This value is chosen to be large relative to the time required to collected all charge carriers in order to produce an output Voltage signal, V_{out}, that is proportional to the total integrated charge. This produces signals with a magnitude proportional to the energy of the initial γ ray with an exponential decay reflective of the value of τ.
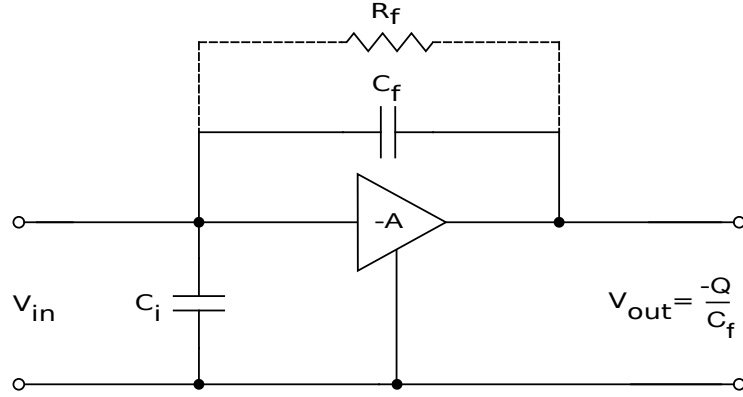
FIGURE 2.9: Simplified diagram of a charge sensitive preamplifier circuit, reproduced from [24].

The preamplifier is designed to process a large bandwidth to allow all components of the signal to pass through to the next stage for further processing.

2.3.4 Energy Resolution

One of the main performance metrics used for radiation detectors is that of energy resolution. This is a quantification of the precision with which the detector can measure the number of charge carriers produced in a γ-ray interaction; equivalent to measuring the γ-ray energy. The energy resolution is expressed as the Full Width at Half Maximum (FWHM) of a Gaussian spectral peak, produced when recording γ rays of a set initial energy. Three main factors contribute towards uncertainty in the measured γ-energy and so the energy resolution is expressed as

$$\Delta E = \sqrt{(\Delta E_S)^2 + (\Delta E_E)^2 + (\Delta E_X)^2}, \tag{2.12}$$

in which ΔE_S is the statistical fluctuation, ΔE_E is noise, and ΔE_X is signal loss. Each of these contributions is explained in more detail below.

- ΔE_S - The number of charge carriers produced following a γ-ray interaction with semiconductor materials is proportional to the energy of the γ ray. The statistical fluctuation in this number is given as

$$(\Delta E_S)^2 = (2.35)^2 F \epsilon_{pair} E_\gamma, \tag{2.13}$$

where F is the Fano factor, ϵ_{pair} the ionisation energy required to produce an e^--h^+ pair in the medium, and E_γ the interacting γ-ray energy. The Fano factor is related to the number of charge carriers produced and is given as the difference between the experimentally observed statistical fluctuation in charge carrier pairs

and the number that is predicted by Poisson statistics. This value is calculated empirically for the detecting medium.

- ΔE_E - The contribution of electronic noise to the system. This is due to electronic components present in the signal processing chain following the detector itself, for example the strip-size dependent capacitance in a planar strip-detector and Johnson noise arising within the preamplifiers [24].

- ΔE_X - A degradation in resolution due to losses within the detector. This can occur due to incomplete charge collection and leakage current. Incomplete charge collection can occur due to loss of charge in regions of weak electric field or as a result of charge carrier recombination. The latter typically only being an issue in large volume detectors. Leakage current is attributed to the movement of current across regions of the detector that are supposed to be insulated and is small in modern germanium and silicon detectors.

The contribution from each effect varies as a function of deposited energy. At low energies the resolution is typically dominated by electronic noise, ΔE_E, while at high energies the contribution from the statistical fluctuation of produced charge carrier pairs, ΔE_S, is much greater. In a fully depleted and biased detector the contribution to resolution from incomplete charge collection should be insignificant and leakage current should be small. The effect of Doppler broadening on the energy resolution, mentioned previously, is typically small when considering single interactions. In a three-tiered system, however, the contribution from this effect on the energy resolution, and subsequent image resolution, is much increased [32].

Chapter 3

Principles of Radiation Imaging

This chapter will outline the commonly used methods of imaging γ-ray sources, including Compton imaging which is the focus of this work. Methods used to enhance the analysis of the data from the GRI+ Compton camera will also be discussed.

3.1 Gamma Ray Imaging

The measurement of γ-emitting isotopes in order to determine their location and nature is known as γ-ray imaging. It has applications in many areas, such as astronomy, medical physics, nuclear security, and nuclear decommissioning. It utilises a device known as a γ-camera to image γ-rays emitted by radioisotopes in the camera's Field of View (FoV). The γ-camera must be able to detect and record incident γ-rays and then form an image of their spatial origins. The detection of γ-rays is done through the mechanisms presented in Section 2.1 within a detecting system, while a mechanism performing the equivalent of a camera lens is used to form an image of their origin. This is done by either restricting the directions that incoming γ-rays can enter the detecting system from, known as collimator imaging, or by reconstructing the path the incident γ-ray took and back-projecting their origin in a method called Compton imaging. The more precisely the γ-origin can be determined the higher the image quality produced by the γ-camera. The principles of these two imaging methods are discussed in detail below.

3.1.1 Collimator Imaging

The angle through which γ-rays can enter and interact with a detection system can be restricted through collimation. In this method a collimator, made of a material through which γ-rays cannot easily pass, is placed in front of a detector. This constrains the angles of γ-rays incident with the detecting medium and so reduces the possible origin points allowing the formation of a γ-image. The collimator must be thick enough to prevent γ-rays passing or scattering through to interact with the detection system. This is typically difficult to achieve above energies of ~400 keV and even at energies below this transmission can occur. Increasing the collimator thickness to prevent this

can compromise the sensitivity of the system. The collimator designs and techniques coupled with detectors have evolved over time and some of the most notable designs are presented below.

Pinhole Camera - A simple pinhole camera [33] utilises a γ-detector within a shielded box, for which a single aperture exists. Only γ rays passing through the aperture can interact with the detector, and so the origins of detected γ rays are constrained. The magnification of the image can be controlled through the aperture size. A small aperture can provide a high-quality image but at the expense of efficiency, as a smaller aperture reduces the number of γ rays that can interact with the detecting medium. To produce high quality images with pinhole cameras the focal point must be matched to the distance of the γ-ray origin point. The focal point can only be adjusted through the aperture size which also effects image quality. For this method the distance between the camera and the γ-ray origin must be known and so is suitable in areas such as medical imaging, where the patient is located at a fixed distance, but is severely hampered in applications such as nuclear decommissioning and security where generally the location of the source is poorly known.

Anger Camera - An Anger camera [34] utilises a parallel-hole collimator to restrict γ rays entering the system and improves upon the simple pinhole camera by utilising a position-sensitive detecting system. This originally comprised a large scintillator detector and multiple photo-multiplier tubes. This detection set-up enables the interaction point of an incident γ rays within the detecting medium to be constrained while the collimator allows γ rays of only certain incident angles to enter the system. This enables imaging at a range of distances but still severely restricts the number of γ rays that can enter the system, resulting in a low imaging-efficiency. The efficiency can be increased by widening the collimator holes but again at the expense of image quality. In a pinhole and parallel-hole collimator, the number of γ rays reaching the detector may only be 0.1-0.01% of those emitted by the source [35].

Coded aperture Imaging - Coded aperture imaging [36] increases the efficiency of the Anger camera by utilising a collimator mask of a patterned design. The pattern allows more γ rays to pass through to the detector by creating more open space in the mask. The pattern of the γ rays interacting with the detecting medium situated behind the mask can then be deconvolved back into an image of the γ-ray origins. The coded aperture results in a higher imaging efficiency detector than a parallel-hole collimator, with typically ~1% of emitted γ rays passing through the collimator to the detector behind [37]. This severely reduces the FoV that can be imaged to typically less than 50° [38]. The range of energies to which a coded aperture system can be sensitive to is also limited. High energy γ rays are difficult to stop [39] and so can penetrate the mask and result in interactions that are not

related to the coded aperture. This reduces the imaging quality and can make imaging high-energy γ rays of above several hundred keV difficult to impossible. Off-axis originating γ rays can also interfere with the image and produce artefacts that must be removed. Generally the mask must also be rotated and more data taken in order to prevent artefacts arising in the images.

The limitations inherent to these collimation techniques, namely a narrow FoV, lack of sensitivity, and restriction in γ-ray energy range to which they are sensitive to can make them unsuitable for certain applications. The nuclear decommissioning challenge presented in Section 1.1 highlights the complexity of the environments that must be characterised. These include cluttered and complex environments with variable stand-off distances and large contaminated areas such as walls. Collimator systems with a narrow FoV that require constant source-to-imaging system distance are therefore unsuited for the task. The γ-emitting isotopes found in a decommissioning environment were shown to be up to 1.5 MeV. To image these high-energy γ rays, thick and heavy collimators would be required which would impact the system sensitivity to low-energy γ rays.

3.1.2 Compton Imaging

Compton cameras, first proposed in 1974 [9], are an alternative method to mechanical collimation for γ-ray imaging. Instead of a mechanical collimator in front of a position sensitive detector another detector is used to exploit the kinematics of Compton scattering and so enable back projection of the γ-ray path. By these means the γ-ray origin can be found. The lack of a mechanical collimator increases the FoV and increases the number of γ rays that can interact with the detecting system. Relying on γ-detectors instead of a collimator also means that a Compton camera is only limited by the energy limits of Compton scattering. For this reason it can be sensitive to a large γ-ray energy range of up to 2 MeV, though it cannot image very low γ rays that do not scatter such as 59.5 keV γ rays emitted by ^{241}Am. Compton cameras are able to provide 3-D information about the γ-ray origin from a single measurement position at small source-to-detector distances due to the parallax effect. At large stand-off distances only 2-D information is possible and the source distance cannot be easily found. Source stand-off can instead be found through combination of multiple measurement positions or through fusion with other scene-data as described in Section 3.1.3.

Principles of Compton Imaging

Compton cameras utilise the interaction mechanism of Compton scattering to perform γ-ray imaging. A diagram of a basic detector set-up that could be used to perform Compton imaging is presented in Figure 3.1.

This example comprises two planar detectors arranged in series. The detectors are pixelated in order to provide position information of γ-ray interactions. An incoming γ ray originating from the right of the diagram along the dotted line is incident on
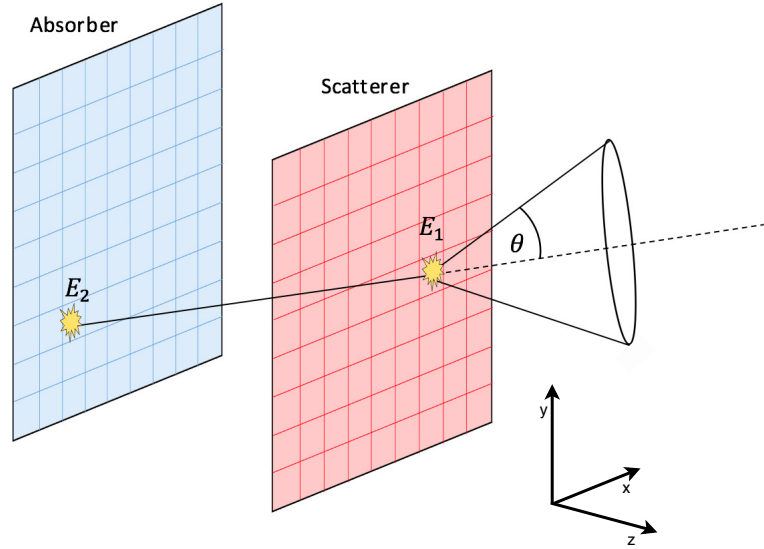
FIGURE 3.1: Diagram of a Compton camera system comprised of two position-sensitive, planar detectors. An incoming γ ray Compton scatters in the front layer depositing energy E_1, and is then photoelectrically absorbed in the second layer, depositing the rest of its energy, E_2.

the front detector, named the scatterer. The γ ray undergoes Compton scattering, depositing some of its energy, E_1, in the first detector before scattering forwards toward the second detector. It is photoelectrically absorbed in this second detector, named the absorber, and so leaves the rest of its energy, E_2. These energies can be related through

$$cos\left(\theta\right) = 1 + mc^2 \left(\frac{1}{E_1 + E_2} - \frac{1}{E_2} \right), \tag{3.1}$$

where mc^2 is the electron rest mass energy and θ the angle through which the γ ray Compton scatters. As the full energy of the γ ray is recorded between the two interactions and the positions of both interactions are known from the position-sensitive detectors the kinematics of Equation 3.1 can be exploited. The angle the γ ray scattered through is known and so a cone can be projected into space. The γ ray is therefore known to have originated on the surface of this cone. Its origin on the cone surface cannot be constrained further without measurement of the recoil electron within the detector. Through the stacking of many of these events the area of highest conic overlap can be determined to be the most likely origin of γ rays. In this manner, γ-ray imaging can be achieved with a two-layer Compton camera. A single detector can be used if the two interactions within it can be deconvolved into separate points. The more precisely the energy of the two interactions can be measured the less uncertainty is present in the angle through which the cone has been back-projected, resulting in higher image quality. For this reason, detectors with good spectroscopic capabilities produce higher quality images when used in Compton imaging than those with poor energy resolution.

The image quality is also dependent on the position resolution to which the γ-ray interactions can be determined and so either highly segmented detectors, signal analysis methods, or a combination of both, are used to determine these positions to the highest precision possible.

Compton Camera Image Reconstruction

Image reconstruction refers to the techniques required for producing γ-ray images from γ-imaging devices. For reconstructing a Compton camera image the cone can be projected onto a spherical surface, losing the depth information in the process, or into 3-D space. In this work cones are back-projected into a 3-D space, producing a map of conic overlaps in (x, y, z). The intensity of overlaps are then shown in the space in front of the camera, usually as x-y slices at each z-distance imaged. The distance of the γ-ray origin can be determined by finding the z-distance slice at which the intensity overlap of cones is highest and the area over which the cones are distributed is smallest. The algorithms used to perform this image reconstruction can be classified as either analytical or iterative and the choice of reconstruction code used is influenced by the imaging scenario. An analytical code is typically faster than an iterative one, but an iterative code may be able to produce higher quality images. The functionality of analytical and iterative reconstruction codes is discussed below.

Analytical Reconstruction - A computationally cheap and efficient analytical reconstruction code, using the back-projected Compton cones, was developed at the University of Liverpool by D. Judson. Each cone is discretised into a number of points per angular degree chosen by the user and projected onto x-y slices that are perpendicular to the z-axis being imaged in. Slices are produced at a chosen distance, or at a multitude of steps in z, and display the number of conic overlaps for each bin. An example of a reconstructed image is given in Figure 3.2, in which a point source has been imaged in x-y at a set z-slice distance from the detector. The number of conic overlaps, in 1 mm bins, is given as an intensity and so the γ-ray origin can be found as the centre of this hot-spot, located at $x = y = 0$ mm. The imaging space chosen centres around the Compton imaging system centre and in this example was $400{\times}400$ mm^2.

Point sources imaged in this manner can be used to quantify the imaging resolution of the system. This is found through fitting of the maximum intensity row and column projections of a point source. A combination of two fits is used; a Gaussian fit is used to account for the background conic overlap and a Lorentzian fit is used to fit the remaining intensity. An example of this is given in Figure 3.3. In Figure 3.3 (left) the data are shown in blue along with the two components of the fit, Lorentzian in red and Gaussian in yellow. In Figure 3.3 (right) the data are again shown in blue and the combined Gaussian and Lorentzian fit is shown in red. It can be seen that a combination of these two fits accurately described the distribution of
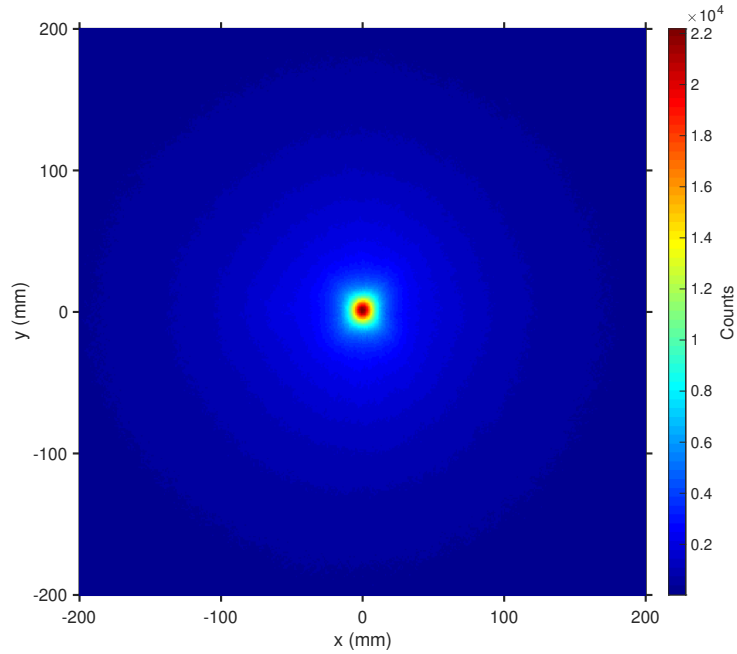
FIGURE 3.2: Imaging slice produced at a set z-distance. The intensity of conic overlaps in x and y are given in mm binning.

conic overlaps. The FWHM of the Lorentzian fit is the quantified image resolution of the system. The resolution in x and y can be averaged and quoted as an angular resolution value in degrees, and so compared to other imaging systems. The image reconstruction performed in this work was done using this analytical reconstruction code in a Graphical User Interface (GUI) package developed by A. Caffrey [40].
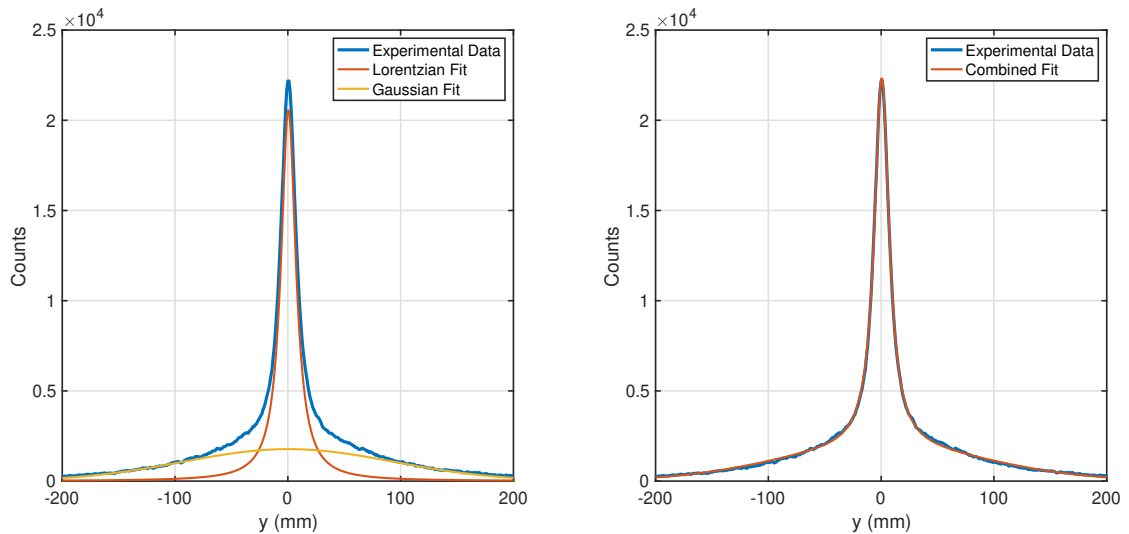
FIGURE 3.3: Projections of the maximum intensity x column from Figure 3.2. Fits are given for the Gaussian background and the Lorentzian intensity separately (left) and combined (right).

Iterative Reconstruction - Iterative reconstruction codes can be used to provide improved position resolution at the expense of increased computational requirements

and reconstruction time. One such form of iterative reconstruction is based upon Maximum Likelihood Expectation Maximisation (MLEM), originally developed for use in single-photon emission computed-tomography image reconstruction [41]. It attempts to reconstruct the most probable source distribution through iteration. A zeroth iteration, akin to an analytical image, is formed through the back-projection of cones. Iterations therein are performed by forward-projecting and inverting the result to form a weighting factor for each cone. By back-projecting the cones again and multiplying by the weighting potential a probability image of the γ-ray origins is produced. This probability map is then multiplied by the back-projected image in order to form the iterated image. The process is repeated with new weighting factors calculated that are dependent on the previous iteration's output. This is computationally intensive and struggles with distributed sources; which may become over-iterated down to a single, or multiple, point sources. A system matrix must typically be calculated also. This describes the relationship between the image space and the projection space and is specific to each imaging system [42]. A correctly calculated system matrix can also prevent iteration of a dispersed source to a point source.

3.1.3 Scene Data Fusion

Scene data fusion is the combining of spectroscopic and γ-imaging data with that of contextual information of the imaged environment scene. The scene-data information can be obtained through any device that is contributing non-γ information. This information is then fused with γ-ray data to provide a complete image of the environment in which the γ-ray sources are located and so can contextualise the γ-image for the observer. Scene-data fusion is a commonly used technique in γ-ray imaging for nuclear security and decommissioning purposes.

Imaging Devices

A commonly used type of scene-data that is fused with γ-images is that obtained from other imaging devices. This type of data-fusion can be found in the Polaris-H [11] and N-Visage systems [43], which both utilise integrated optical cameras in addition to γ-imaging. These two systems also make use of point-cloud generating laser systems, which are commonly found in mapping devices such as Light Detection And Ranging (LiDAR) systems and the Xbox Kinect, the latter of which is employed on the second generation Compact Compton Imager (CCI-2) [44] γ-imaging system. These devices are described in more detail below due to their relevance to γ-imaging in nuclear decommissioning environments. Some of these mapping devices are currently undergoing testing, or have been tested, with the GRI+ system.

Stereoscopic Camera - These devices use two or more individual cameras, each providing a separate image, to provide 3-D images and so obtain distance information

about objects in the environment. In a simple, two-camera system, the 3-D image is produced through matching of pixels between the two separate cameras. This process is complex and can struggle if light levels observed by the two cameras are different or if pixels from one camera are occluded for the other. It can also struggle when matching pixels from large, flat, and bland surfaces, as well as in low lighting areas in general. A stereoscopic camera, the Point Grey manufactured Bumblebee XB3, was previously tested at the University of Liverpool for use in image fusion [45]. Nuclear decommissioning environments may suffer from poor lighting and non-distinctive surfaces, such as walls, that are contaminated and so the stereoscopic camera may struggle in these scenarios.

LiDAR System - LiDAR system use pulsed lasers to measure the distances of objects. The time between the laser pulse leaving the system and returning is used to quantify object's distance. LiDAR systems are not affected by light-levels and can provide very high sample densities, making them suitable for imaging in nuclear decommissioning environments. A Faro X33 LiDAR system [46] has been tested with GRI+ [47].

Xbox Kinect - The Xbox Kinect is a cheap and easily accessible imaging device that is being investigated in conjunction with γ-ray imaging devices to supply scene-data fusion [48]. The Kinect calculates depth using an infrared transmitter in the same time-of-flight method as a LiDAR system. This is joined by an RGB camera to provide more contextual data. The Kinect has a limited camera FoV of ~60° as well as a practical sensor range of 1.2–3.5 m, dictated by the relatively weak infrared transmitter. Nonetheless, it serves as a low-cost, compared to a full LiDAR system, method of producing dense 3-D point-clouds for use in scene data fusion. For this reason the Kinect is currently being investigated for use with the GRI+ system.

The GRI+ camera is designed to be a mobile cart system that, if required, can take multiple images of complex decommissioning environments and combine them together to create a complete map of the scene. Imaging from multiple angles requires complete knowledge of the cart position and orientation at all times. This information can be obtained with the Xbox Kinect as well as through the inclusion of other sensor devices that provide more contextual information, such as GPS trackers and inertia tracking units.

Combination with contextual information is especially important for the GRI+ system as the environments it is designed to image in can require large stand-off imaging of many metres. A Compton camera can achieve full 3-D positional information when imaging at short stand-off distances but at large stand-off distances the accuracy of the distance, or z-axis, information becomes degraded. Scene-data fusion can therefore be used to improve the source stand-off accuracy that is achievable through projection of the γ-ray image onto the environment images, the stand-off of objects within which are

known. This is most typically done through projection of the γ-image directly onto a point-cloud. All three of the above devices can be used to produce a point-cloud representing the entire environment from a fixed position.

3.2   Pulse Shape Analysis Techniques

As shown in Section 3.1.2, the positions of two interactions are used to form the vertices from which cones are back-projected. The interaction positions in a physical system can be determined through segmentation of the detecting volume. This provides sub-volumes with which the point of interaction can be constrained. The planar semiconductor detectors used in this work, detailed in Chapter 4, are segmented into two faces of orthogonal strips. This provides voxel sizes of $5.5{\times}5.5{\times}8$ mm^3 and $5{\times}5{\times}20$ mm^3 for the Si(Li) and HPGe detectors respectively. Interaction positions recorded in a voxel are assumed to be at the centre of the volume. Uncertainty is therefore introduced into the image reconstruction. This uncertainty can be reduced through use of detectors with finer segmentation, and thus smaller voxels, or through the implementation of Pulse Shape Analysis (PSA) techniques. Two commonly used methods of PSA exist that can be implemented in the planar detectors of GRI+. These are a parameterisation based method, known as parametric PSA, and a signal database comparison method, defined as database PSA in this work.

3.2.1   Parametric PSA

The pulse shapes generated within a detector as a function of time can be parameterised through a simple method of parametric PSA. This reduces a full signal to a limited series of parameterised values that describe various aspects of the signal shape. This method has been shown to improve the position resolution of interactions when applied to orthogonal strip planar detectors [49]. For detectors of this geometry, parametric PSA can make effective use of the real charge collection signal recorded by a strip electrode as well as the transient image charges induced on the strip electrodes either side. Through analysis of these signals and their properties the position resolution of the detector can be improved in all three axes. The manner by which this is done is discussed below for the signal types.

Charge Collection Signal - Rise Time Analysis

The largest interaction position uncertainty within the planar detectors considered in this work is in the 20 mm HPGe thickness. Without the application of PSA the point of interaction is set at a z-depth of 10 mm and introduces a large uncertainty when back-projecting cones. The uncertainty in this dimension can be reduced through rise time parameterisation of the charge collection signals produced at each face following an interaction. As the planar detectors used in this work are biased at least several hundred volts above depletion, it is assumed the charge carrier drift velocity is saturated and so

the Shockley-Ramo theorem outlined in Section 2.3 can be applied. From this it is known that the time taken for complete charge collection to occur is a function of the distance through which the carriers have travelled. By parameterising the signal rise times, the time for charge collection, through the detector thickness the depth of an interaction can then be calculated through comparison to characterised values. This application of parametric PSA is known as z-PSA due to its improvement in position resolution in the z-depth of the detector, corresponding to the thickness of a planar detector.
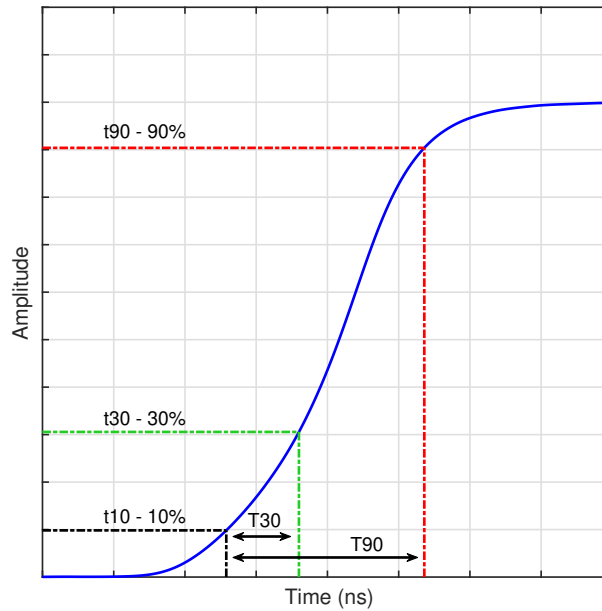
FIGURE 3.4: Typical values used in the parameterisation of a charge collection signal. The time taken for 10%, 30% and 90% of the charge to be collected are recorded as t10, t30 and t90 respectively.

The rise times of a charge collection signal are recorded as the times taken for 10%, 30%, and 90% of the total charge to be collected; these are known as t10, t30 and t90 respectively. An example signal and rise time parameterisation is displayed in Figure 3.4. In a planar strip-detector this is recorded for each face, producing two sets of values. The parameterised rise time values calculated and used in this work are T90 = t90 - t10, T50 = t50 - t10, and T30 = t30 - t10. The initial and final 10% of the signal are not included due to electronic noise, typically present in a charge collection signal, preventing determination of t0 and t100. This excludes the information contained in these parts of the collection signal and so can cause a lack of sensitivity to position in parts of the detector volume. This method requires knowledge of the detector's rise time response as a function of z-depth. This information can be obtained experimentally or through simulation of the electric field within the detector. This method of rise time parameterisation can only be applied to signals produced in single interactions. A multi-interaction event produces convoluted signals which cannot be analysed for rise times.

Transient Image Charges

The parameterisation of signals can be extended to those transient image charges that occur in strip electrodes neighbouring that which is collecting charge. In a planar strip-detector, investigation of these signals can be used to improve the position resolution beyond what can be obtained solely through the width of the strip. As the detectors studied in this work are segmented into faces of orthogonal strips, this method can improve the x-y position resolution. The magnitude of transient image charges areas vary with distance from the interaction position. This is due to the weighting potentials present in a detector, as discussed in Section 2.3.2. Parameterisation of the relative image charge magnitudes induced either side of a charge collecting strip electrode is used to improve the resolution in that axis. This is done through calculation of the image charge asymmetry value,

$$A = \frac{Q_L - Q_R}{Q_L + Q_R},$$
(3.2)

where Q_L and Q_R are the magnitudes of the image charges areas left and right respectively of the charge collecting strip electrode. The change in magnitude of these image charges areas as a function of position is demonstrated in Figure 3.5, which has been produced from average 661.7 keV ^{137}Cs signals produced during the characterisation process presented in Chapter 5. The charge collection signal of a 5 mm wide strip is plotted for a γ-interaction occurring in 1 mm steps across it, along with the image charges induced in neighbouring strip electrodes. The interaction positions are given in mm distance relative to the left strip electrode as the interaction position moves across the centre strip electrode to the right strip electrode. The signal shape of the hit strip electrode does not change as the position of interaction is varied but the magnitude of the image charges either side decrease and increases according to the proximity of that strip to the interaction site.

3.2.2 Database PSA

An alternative to parametric PSA exists based upon signal database comparison. Instead of parameterising charge collection and transient signals into a limited series of values, it compares them to a database of signals. The database contains the unique signals that are produced through the detector volume. The position of an interaction is set to the (x, y, z) mm from which the signals match the most closely. An algorithm is required to compare experimental signals to those in the database. Typically a Figure of Merit (FoM) comparison is made and the closest match set as the (x, y, z) mm position. This is discussed further in Section 7.3.

This method utilises the full signal when performing a comparison and so makes use of the information contained in the initial and final 10% of the signal. Most importantly,
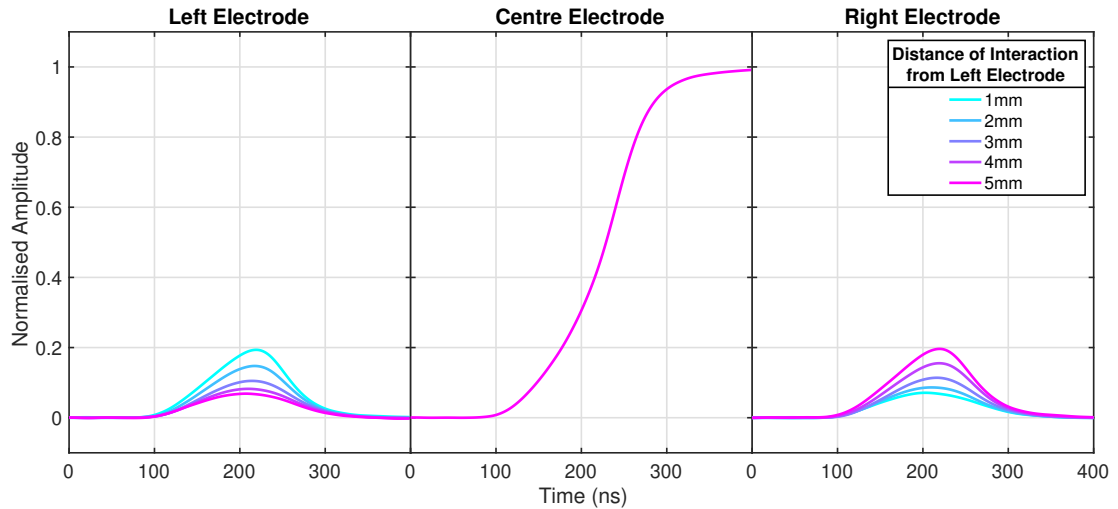
FIGURE 3.5: An example of the changing in the magnitude of image charges relative to position of interaction with a charge collecting strip electrode for nearest neighbour strip electrodes. Produced from average 661.7 keV ^{137}Cs signals.

database signal comparison can be extended to compare multi-interaction events in a detector through convolution of multiple signals from the database.

A database must contain signals through the detector volume. In a planar detector this may represent the signal response on a 1 mm cubic grid. The signal database may be generated experimentally through either coincidence scanning [17] or pulse shape comparison [50] of the detector volume. Alternatively, the signal database can be produced through a validated simulation of the detector fields and charge collection response [21]. This option was selected as the approach in this work and is addressed in more detail in Chapter 6.

Chapter 4

The GRI+ System
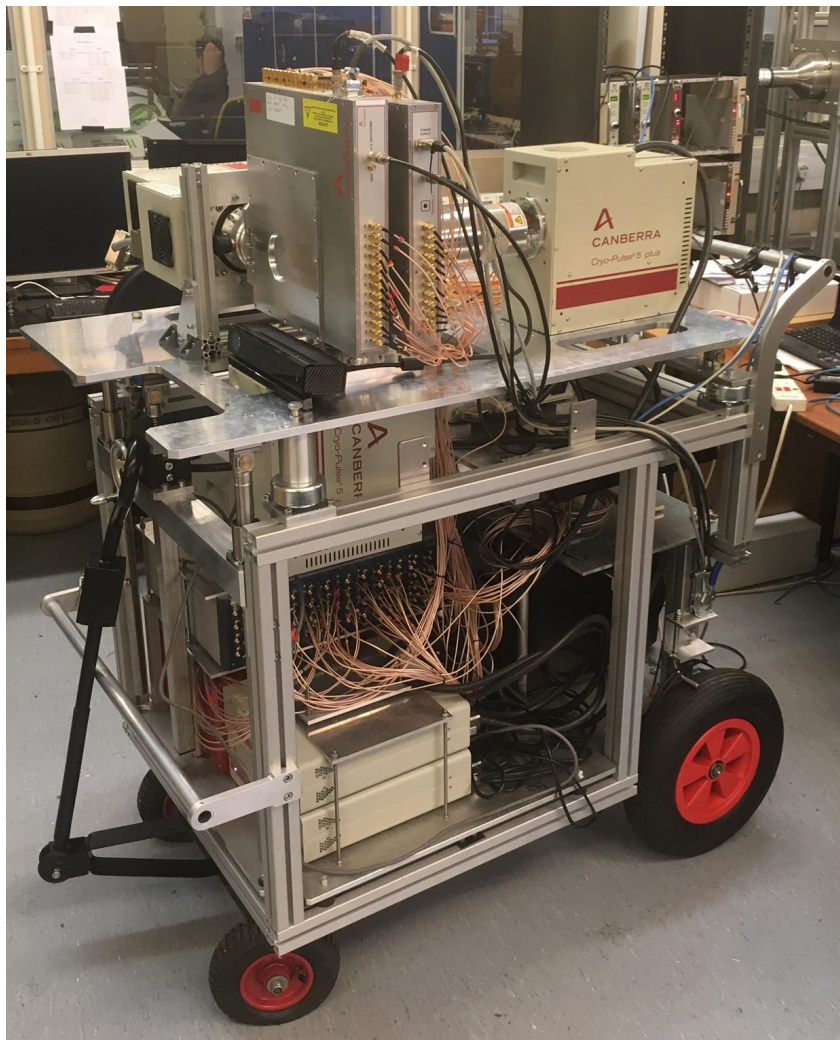
FIGURE 4.1: Image of the GRI+ cart system.

4.1 Detectors

The Gamma-Ray Imager Plus (GRI+) system is a transportable, three-tiered, Compton camera imaging system located at the University of Liverpool. Designed for performing in-situ measurements in nuclear decommissioning environments, it consists of two planar, position-sensitive detectors in addition to a tertiary coaxial layer. The system is mounted on a mobile cart, pictured in Figure 4.1. The cart contains the full computational and electronic support systems required to record analogue signals, digitise and filter recorded data, and save them to disc for analysis. A labelled version of this image is displayed in Figure 4.2.

The three detectors mounted on the cart comprise the Compton camera itself. The front layer is a planar segmented Lithium-drifted Silicon (Si(Li)) detector, designed to Compton scatter incoming γ rays and is known as the scatterer. Situated behind is a segmented planar High Purity Germanium (HPGe) detector that is used to photoelectrically absorb γ rays that have been scattered in the front layer. For this reason, it is known as the absorber. The tertiary layer used is a non-position sensitive Standard Electrode Ge (SeGe) coaxial detector. This third layer is used to improve the imaging efficiency of the system, in particular at high energies. All three detectors are manufactured by Canberra (now Mirion Technologies Ltd.) and are electrically cooled, making them ideal for operation in a transportable system.

4.1.1 Lithium Drifted Silicon Detector

The Si(Li) detector is utilised as the front layer of the Compton camera and fulfils the role of scatterer. A schematic diagram of the crystal housed within the cryostat is shown in Figure 4.3. It is an 8 mm thick cylindrical planar detector with a diameter of 71 mm, segmented into two faces of 13 orthogonal strips. The 13 front-facing AC, p^+, contacts are horizontal while the 13 rear-facing DC, n^+, contacts are vertical. Due to the cylindrical nature of the detector the contacts are of a variable length that is dependent on their position on the detector face. The smallest contacts are therefore located at the edges. The strip contacts have a pitch of 5.5 mm; they are 5 mm wide and are separated by 500 μm gaps. The detector has a resulting position-sensitive voxel size of 5.5×5.5×8 mm^3.

Each strip is coupled with a warm Field Effect Transistor (FET) configuration charge-sensitive PSC823C preamplifier. Each preamplifier has a gain of 400 mV/MeV recorded at 1 MΩ impedance. The DC face contacts are grounded while those on the AC face are biased at +600 V, set well above the depletion voltage of +150 V to ensure saturation of the charge carrier velocities. The crystal is surrounded by a guard ring of 2.5 mm thickness increasing the overall crystal dimension to 76 mm diameter. The guard ring is implemented to prevent edge effects occurring in the detector due to non-uniformity of the electric field across the active detector volume.
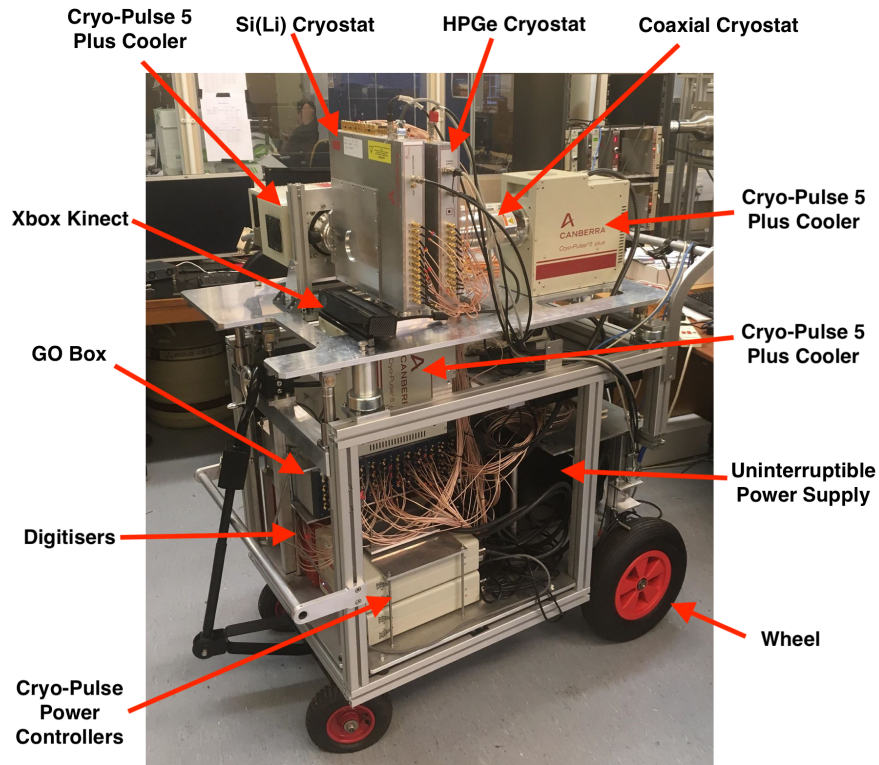
FIGURE 4.2: Labelled image of the GRI+ cart system. The CAEN HV power supply was not present when the image was taken and the LV supply is not visible.
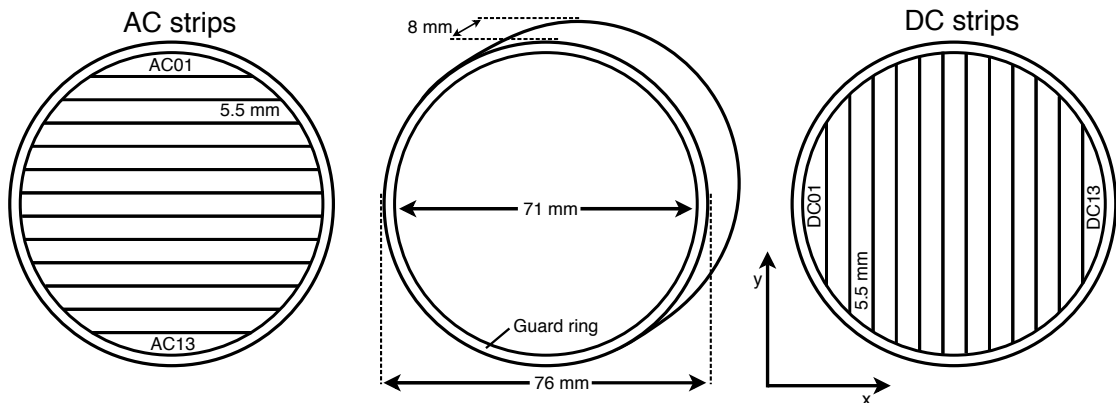
FIGURE 4.3: Schematic diagram of the Si(Li) detector crystal showing the detector crystal and segmented faces.

An initial spectroscopic assessment was performed to demonstrate the energy resolution of the detectors before digitisation of the signals. The results for the Si(Li) detector when recording 59.5 keV γ rays from a ^{241}Am point source are shown in Figure 4.4. The measurements were performed using a Canberra Model 2026 spectroscopy amplifier with a shaping time of 4 μs, connected to an Ortec stand-alone 8k channel EASY-MCA. The average energy resolution, measured as the FWHM of a Gaussian fit, at 59.5 keV for the Si(Li) detector was found to be 1.21 ± 0.04 keV for the AC contacts and 0.95 ± 0.07
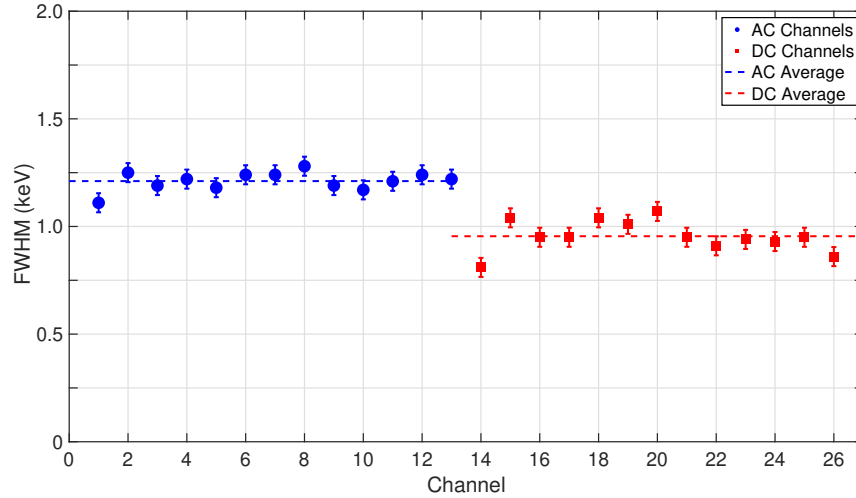
FIGURE 4.4: Analogue energy resolution measurements from the Si(Li) detector for 59.5 keV γ rays from an ^{241}Am source.

keV for the DC contacts. Degraded energy resolution is expected in the AC channel response relative to the DC channel response due to the load resistor present in an AC coupled preamplifier circuit [51]. The excellent energy resolution of the Si(Li) detector at 59.5 keV makes it ideal for measuring low-energy Compton scatter interactions. The response of the Si(Li) detector has previously been completely characterised by Harkness *et al.* [19]. It has reported peak-to-peak noise levels of ~2 keV for the DC channels and 2.5 to 5.4 keV for the AC channels [52].

4.1.2 High Purity Germanium Detector

The HPGe detector is utilised as the second layer of the Compton camera, situated behind the Si(Li), and fulfils the role of absorber. A schematic diagram of the crystal housed within the cryostat is shown in Figure 4.5. The HPGe crystal is oblong and has an active volume of $60{\times}60{\times}20$ mm^3. Each $60{\times}60$ mm^2 face is segmented into 12 strips with front-facing horizontal AC, p^+, contacts and rear-facing vertical DC, n^+, contacts; each with a total pitch of 5 mm. The p^+ contacts are produced through boron implantation while the n^+ are amorphous germanium (a-Ge) based. This produced two faces of thin contacts less than 1 μm thick. The AC contacts are separated by an inter-strip gap of 300 μm while the DC contacts are separated by 250 μm. This results in position-sensitive voxel sizes of ~$5{\times}5{\times}20$ mm^3.

Each strip is coupled with a warm FET configuration charge-sensitive PSC823C preamplifier. Each preamplifier has a gain of 200 mV/MeV recorded at 1 MΩ impedance. The DC contacts are grounded while an operational voltage of -1800 V is applied to the AC face contacts. The depletion voltage was recorded to be -1300 V. The reported impurity concentrations are $0.70{\times}10^{10}$cm^{-3} at the AC face and $0.85{\times}10^{10}$cm^{-3} at the DC face. The crystal is surrounded by a 7.5 mm guard ring. The large guard ring is designed to maintain a uniform electric field and so decrease edge effects as well as to prevent leakage current.
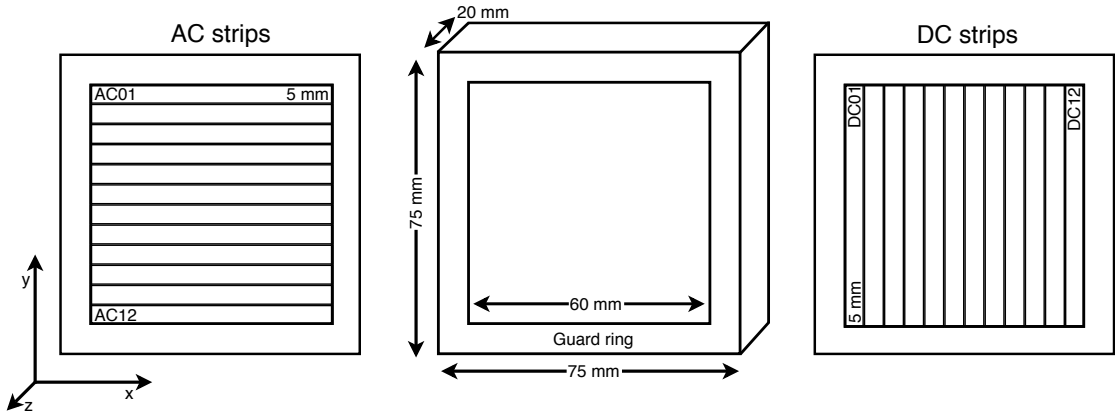
FIGURE 4.5: Schematic diagram of the HPGe detector crystal showing the detector crystal and segmented faces.
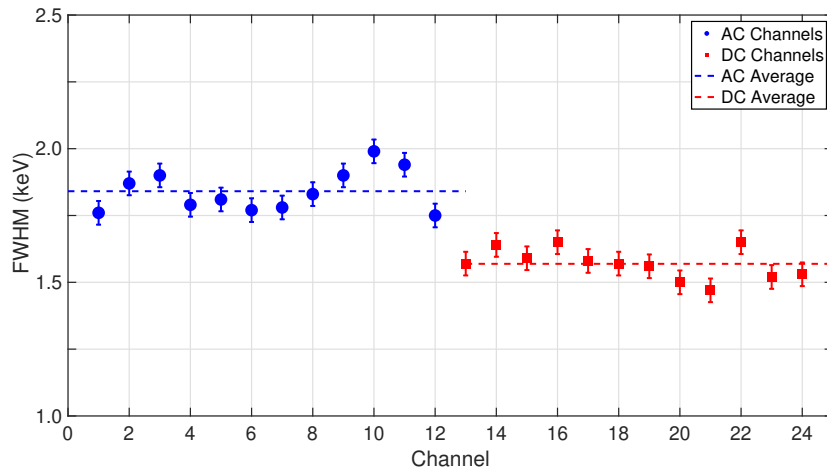
FIGURE 4.6: Analogue energy resolution measurements from the HPGe detector for 122.1 keV γ rays from a ^{57}Co source.

Initial analogue measurements were performed before the full characterisation process discussed in Chapter 5. The FWHM was measured for 122.1 keV γ rays from a ^{57}Co point source using the same analogue set-up as described for the Si(Li) detector. The FWHM results are displayed in Figure 4.6 achieved from Gaussian fits to the photopeaks. The average energy resolution was found to be 1.84 ± 0.08 keV for the AC contacts and 1.58 ± 0.06 keV for the DC contacts. As the system is designed for imaging a large range of γ-ray energies, up to 2 MeV, the HPGe detector must have excellent energy resolution for high energy γ rays. Following the digitisation of the signals using methods described in the following sections, the energy resolution was recorded for a range of energies using a ^{152}Eu source. The resolutions are displayed in Figure 4.10 (left) as the average of all AC and DC channels. The excellent spectroscopic performance capabilities of the detector are clearly demonstrated for a large range of energies.

The electronic noise levels present in the HPGe detector were also quantified. The average peak-to-peak nose was found to be 14.7 keV for the AC face and 14.5 keV for the DC face. This compared well with geometrically similar HPGe detectors that made us of liquid nitrogen cooling as opposed to electrical cooling [53]. An example charge collection

signal and neighbouring image charges, taken from the HPGe DC face, is displayed in Figure 4.7. The charge has been collected from a ^{137}Cs 661.7 keV γ ray interacting once in the HPGe. The noise is small relative to the signal magnitude and does not affect the signal shape, and the subsequent application of PSA methods, for large energy depositions. These measurements compared well to the SmartPET detectors; similar geometry detectors cooled with liquid nitrogen as opposed to electrical cooling [54], and indicated that the electric cooling unit did not have an effect on the HPGe crystal noise levels. It was found in some circumstances that noise could be transmitted from one planar detector to the other via contact between the cryostats. This is discussed more in Section 4.1.4.
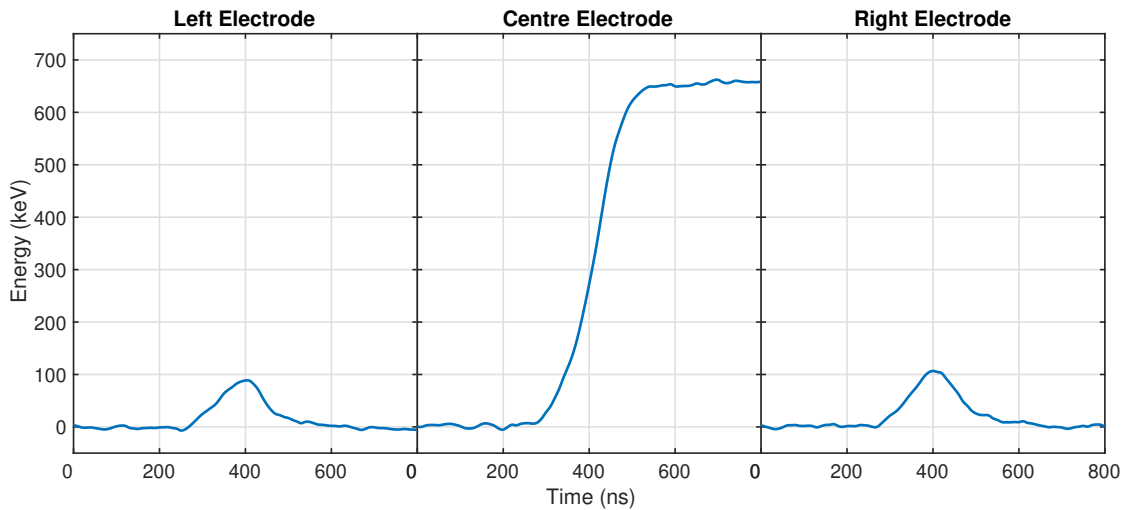
FIGURE 4.7: Digitised signals of a ^{137}Cs 661.7 keV charge collection event and neighbouring image charges, taken from the HPGe detector DC face.

4.1.3 Tertiary Coaxial Detector

A tertiary layer is employed on the cart system in the form a Standard Electrode coaxial Germanium (SEGe) detector. The p-type crystal is not position sensitive and has a diameter of 66.5 mm diameter and a length of 50 mm, making it a large volume detector with high efficiency for γ-ray detection. The p^+ contact is on the axial well while the n^+ contact is on the outer surface of the crystal. It is coupled to a cold FET configuration charge-sensitive 2002CSL preamplifier with a gain of 100 mV/MeV recorded at 1 MΩ impedance. The detector was operated at a bias of +3000 V and the depletion voltage was reported to +2500 V. The resolution of the detector, following the digitisation process described in the following sections, was found to be 1.75 keV for γ rays of 344.3 keV.

The coaxial detector increases the Compton camera system efficiency for high-energy γ rays that would otherwise scatter in both the planar detectors without being photoelectrically absorbed. If it can be absorbed in the coaxial detector subsequent to scattering

in both the planar layers then full deposition of its energy has occurred in the system and the event can be reconstructed.

4.1.4 Electrical Cooling

All three detectors are cooled by Cryo-Pulse 5 Plus electrically refrigerated cryostats that make use of pulse-tube technology. The system includes for each detector a programmable external power controller through which the temperature of the connected cold head assembly can be set. All three detectors are cooled to a set-point of 88.15 K. The pulse-tube coolers utilise hermetically-sealed non-flammable gas and as such no refills are required. This makes this method of cooling well suited for use in long-term in-situ measurements where refills of coolant would otherwise be required. Each cooler is connected to a PC enabling power draw and temperature sensing to be logged and monitored.

The planar detectors within the system were tested for potential noise introduced by the coolers. It was found that microphonic noise was introduced to the HPGe detector only if contact was made between the two planar detector cryostats. The noise induced on the HPGe was found to be periodic with a frequency of ~300 Hz. As this periodicity was long relative to the typical length of a pulse, dictated by the 50 μs preamplifier decay time, it was found not to impact the system. Care was still taken to have a small separation between the Si(Li) and planar HPGe detector cryostats and this issue did not impact the overall performance of the system.

4.1.5 Power Supply

All three detectors share a common High Voltage (HV) and a common Low Voltage (LV) supply when on the cart system. The HV is supplied by a small and compact DT55xxE CAEN power supply. The LV is produced by a custom built unit with 12 V and 24 V rail power supplies for the detectors. The HV supply has a bias shutdown input that is compatible with the TTL logic signal from the detectors. In the event of a loss of cooling or LV, the HV will receive a bias shutdown signal and cease its supply.

4.2 Electronics System

The cart system contains the full electronics suite required to record analogue output signals directly from the detector preamplifiers, digitise and process them, and finally record them to disc. The flow of this process is illustrated in Figure 4.8 with colouring used to differentiate separate aspects of the system. The individual detectors forming the Compton camera itself are shown in blue and their integrated preamplifiers in grey. Following is the Gain-Offset (GO) box, displayed in green, which feeds into a set of CAEN digitiser modules, coloured red. These digitisers, along with the computer operating Multi Instance Data Acquisition System (MIDAS) software, form the Digital Acquisition (DAQ) system used to record the output of the system.
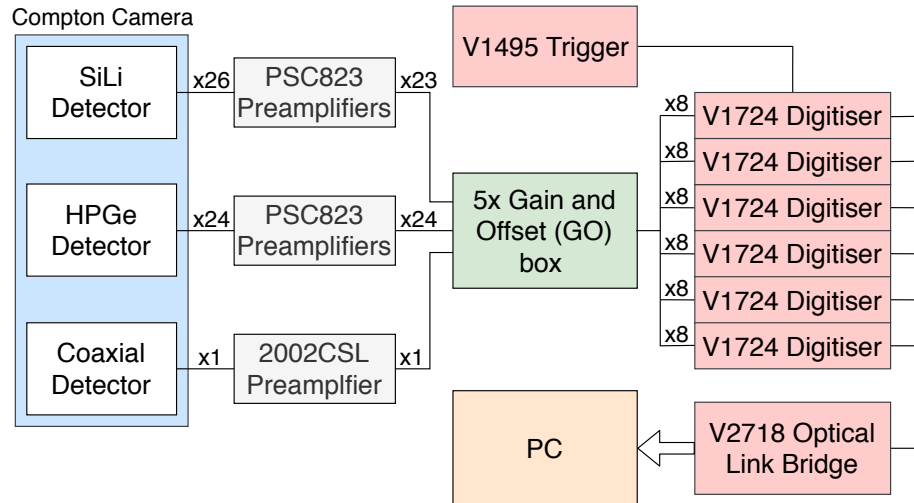
FIGURE 4.8: Schematic diagram of the electronics system used for recording coincidence data from the Compton camera.

4.2.1   Gain-Offset Box

All detector preamplifier outputs are fed into a GO box. The box acts as a high bandwidth amplifier and applies a fixed gain to the signal amplitudes in addition to an offset to the signal voltage. In this work the gain selected was $5\times$ and was applied to all signals. A factor of 5 gain was chosen as it maximised utilisation of the ±1.125 V dynamic range of the digitiser cards used. An offset was chosen for each channel that maximised use of the full digitiser voltage range in both the positive and negative directions. This was required as recorded charge collection signals were positive or negative depending on the detector face input, and image charge signals could have both negative and positive components and were typically a maximum of 30% of the charge collection amplitude.

4.2.2   Digitisers

The digitiser system employed on the Compton cart comprises CAEN digitiser module cards mounted in a powered CAEN 8-slot VME crate. These are used to digitise the analogue signals output from the detector preamplifiers as well as to create coincidence triggering logic, necessary for operation of a multi-tiered Compton camera. The digitisation of the detector signals is performed by 6 CAEN V1724 digitiser cards, each with 8 14-bit channel inputs. These cards function as Flash Analogue to Digital Convertors (FADC) with 100 MHz sample rate, and so produced digitised signals with 10 ns samples. For each signal 126 samples were chosen for saving to disc, totalling signal lengths of 1260 ns. The dynamic range of each card is 2.25 V (±1.125 V). As 6 cards are used, each with 8 inputs, in total only 48 channels can be digitised. In the GRI+ system all 24 planar HPGe channels are digitised along with the singular coaxial output and 23 of the 26 Si(Li) channels. The three channels not included are the edge strips with the smallest area. A universal clock is set by the first digitiser card and chained through the other five. Each digitiser card makes use of CAEN's Digital Pulse Processing for

Pulse Height Analysis (DPP-PHA) firmware. Two other CAEN module cards are used with the system. A CAEN V1495 general purpose VME board is used to set universal trigger logic as well as to reset and synchronise the clock signal. Trigger logic determines which triggers will cause the output and recording of all signals. Finally, a CAEN V2718 VME to PCI bridge card is used to provide an optical link between the digitisers and a PCIe x8 CAEN Controller card mounted in a PC. The optical link electrically isolates the PC from the VME crate and digitiser cards as well as providing a high rate of data throughput.

Triggering

A Trigger and Timing Filter (TFF) is contained within the DPP-PHA firmware and provides trigger signals as well as trigger time stamps. The TFF performs a RC-CR^2 filter which acts as a digital Constant Fraction Discriminator (CFD), providing a high pass filter in the process. Through this process of integration and double-differentiation, a bipolar RC-CR^2 signal is produced which has a zero crossing point, independent of the input pulse height. When a trigger threshold is passed by the signal the trigger logic of the system is armed and a time stamp, corresponding to the zero crossing, is recorded.

Moving Window Deconvolution

The CAEN DPP-PHA firmware contains a trapezoidal energy filter which acts as a digital shaping amplifier. It forms a trapezoidal signal, the amplitude of which is proportional to the input pulse height. This is similar in functionality to a Moving Window Deconvolution (MWD) algorithm [55] [56] and will be defined as the MWD in this work. The average of the trapezoid height, calculated in FADC units, is recorded as the signal energy. The basic steps of an MWD algorithm are illustrated in Figure 4.9. In this example a preamplifier pulse has been amplified by a GO box and then digitised, shown in Step 1. The effect of the preamplifier on the signal shape is then removed by correcting for the finite decay time of the pulse. This is done through deconvolution of the decay from the pulse and results in the step function shown in Step 2. A moving average window, the width of which determines the subsequent rise time, is moved across acting as a high-frequency noise filter and smoothing the step function. This produces a trapezoidal shape as shown in Step 3. The height of the created trapezoid is proportional to the charge deposited in the detector. An average value of the trapezoid flat top is taken in the range of the Peak Average Window (PAW) to produce an energy of the measured signal. The parameters used to produce this trapezoid, such as the trapezoid flat top, trapezoid rise time, and pulse averaging window, are selected by the user and typically chosen to provide the best energy resolution possible. The digital shaping parameters used in the majority of this work were selected to be a trapezoid flat top of 2.5 μs and a trapezoid rise time of 7.5 μs for all three detectors. The PAW was selected to be 640 ns and was placed centrally on the trapezoid flat top. these settings provided a good energy resolution while also allowing a high data throughput.
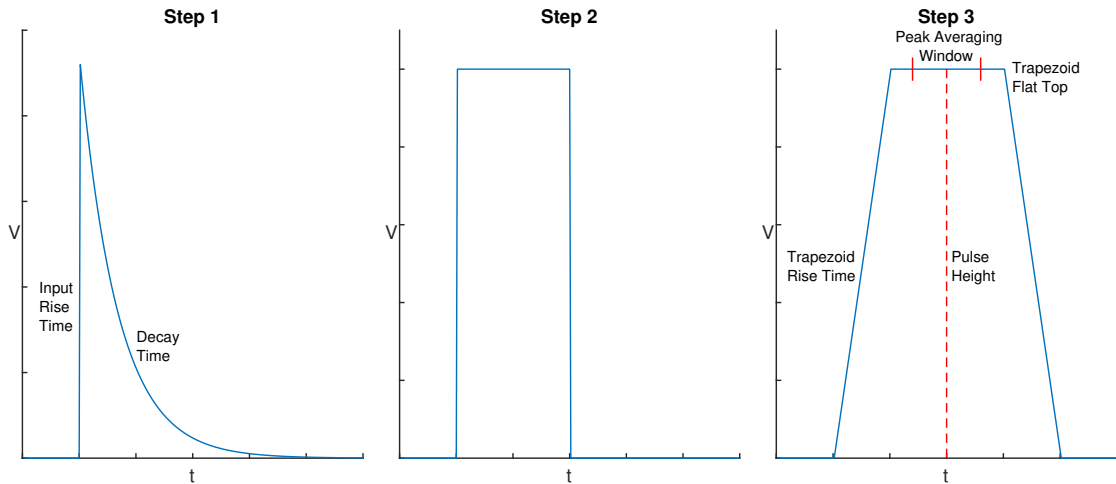
FIGURE 4.9: Example signals produced during three stages of the MWD algorithm. Step 1 shows a typical preamplifier pulse with a short rise time and long decay. The step function produced following correction for the finite decay time is shown in Step 2. Step 3 shows the trapezoid produced after the application of a moving average window across the signal in Step 2.

4.3 Data Collection

The output of the digitising system is collected as data, the type of which can be determined through choice of triggering logic and output mode. One of two trigger modes can be selected. These are "coincidence" mode and "singles" mode. Coincidence mode enables operation of the GRI+ system as a Compton camera. In this mode an event comprises an interaction in both the scatter detector and the absorber detector within a time frame defined by a coincidence window. A trigger signal from both detectors is required within the coincidence window for readout to occur, this is known as a two-tier event. If an interaction also occurs in the coaxial detector during the coincidence window then it is known as a three-tier event if three trigger signals are received within the coincidence window. The AC faces of each of the planar detectors are used for triggering due to their good timing response as a result of strong electric fields, and both are required to register charge collection higher than the set trigger threshold. The other trigger mode, singles, reads out signals if any channel in the GRI+ system registers an energy greater than the trigger threshold. An event in singles mode so comprises at least one interaction in any detector and is typically only used when operating a single detector. Data collected in the manner are used to perform energy calibration gain-matching by collecting singles event data for each individual detector.

For a selected trigger mode the output mode must be selected. There are three output modes that can be selected from. The modes decide the number of channels that are read out following a successful trigger. These are output of only the individual channels that passed the trigger threshold, output of triggered channels and nearest neighbouring channels, and output of every channel active in the system. The final of the three output modes was used in almost all situations as the signals from channels neighbouring a

charge collecting strip electrode was required for PSA methods. Following a trigger in the selected mode of coincidence or singles the channel number, signal samples, time stamp, and MWD energy are output from the digitisers for those channels decided by the output mode. The output data can be both live sorted and saved to disc for future analysis.

4.3.1 Data Sorting and Classification

Charge is determined to be real or noise during the data sorting process. Data are sorted within MTsort [57] and a BaseLine Difference (BLD) method is used to distinguish between real charge and noise. In this method the standard deviation, σ, of a signal's baseline noise is calculated over the first 30 samples and compared to the average amplitude of the last 30 samples. A signal is judged to be real if the difference is found to be greater than 3σ.

Events are classified within the system based upon the number channels that have registered charge collection and are judged to be real by the BLD method. The number of channels on a detector face registering real charge is known as the fold. A coincidence event can be represented by $F[\sharp, \sharp, \sharp, \sharp, \sharp]$, where each value is the fold for the channels of a given detector face. The channels are grouped into faces for the planar detectors and so the first four numbers represent the scatterer AC, the scatterer DC, the absorber AC, and finally the absorber DC channels respectively. The final number is the singular coaxial channel and is a 1 in a three-tier event. In the example of a two-tier event in which each detector registers real charge in a single strip on each face the description would be F[1,1,1,1,0]. In the case of only a single detector being used to collect data, the event can be described with just two numbers, detailing the fold on each face. For example a measurement taken in singles mode with just the HPGe detector that registered two charge collecting strips on the AC face and just one on the DC would be described as F[2,1].
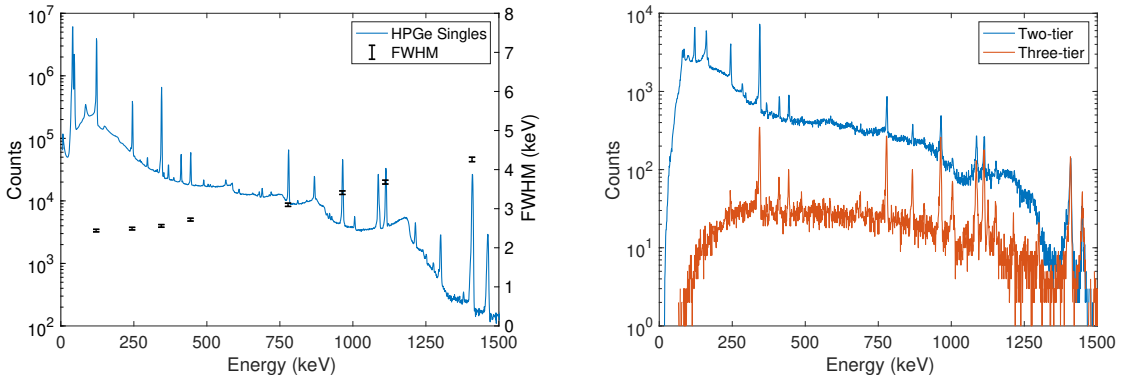
FIGURE 4.10: Singles ^{152}Eu F[1,1] recorded in the HPGe detector (left) with associated FWHM energy resolution for prominent peaks and coincidence two-tier F[1,1,1,1,0] and three-tier F[1,1,1,1,1] ^{152}Eu spectra (right).

An example spectrum taken with the HPGe detector operated in singles mode is displayed in Figure 4.10 (left) for a ^{152}Eu source depositing energy in F[1,1] events.

The resolution as a function of photopeak is also plotted. An energy resolution of less than 4.5 keV is recorded for energy depositions of 1408.0 keV. An example spectrum of summed coincidence data taken by the camera is shown in Figure 4.10 (right) for a ^{152}Eu source depositing energy in F[1,1,1,1,0] and F[1,1,1,1,1] events.

The summed energy of the system is calculated from the DC energies of each planar detector due to its superior energy resolution. Two-tier events make up the majority of events at low energies while three-tier events are only likely to occur above ~200 keV. This is due to the low likelihood of a low-energy γ ray Compton scattering twice before photoelectric absorptions in the tertiary layer. When the photopeaks are fitted with a Gaussian distribution and the background is excluded, the number of two-tier and three-tier events are equal at ~1.5 MeV. Beyond this energy a higher fraction of incident γ rays interact in all three layers of the camera. Inclusion of the third-tier therefore more than doubles the number of imageable events above this energy. A feature of note is the presence of low energy x-rays in the two-tier energy sum spectrum but not in the three-tier sum spectrum. These occurred due to true coincident events between x-rays interacting in the front scatterer layer and γ rays interacting in the second absorber layer.

In addition to being summed through the system, the energy can be summed across a detector face. This is known as "addback" and is the adding back of all energies deposited across a detector face in a multi-channel event. Addback allows the energy recovery of a γ ray that scatters multiple times within a single detector and can be used to increase the system's efficiency.

4.3.2 Cross-talk

Operation of the detector in addback mode increases the efficiency of the system but also produces unwanted effects within the addback spectra. These are due to electronic coupling between adjacent channels within the detector; in the HPGe and Si(Li) detectors this is observed as proportional cross-talk [58]. Proportional cross-talk causes a proportional shift in the baselines of channels neighbouring a charge collecting channel. Thus when the energies are calculated by the MWD algorithm for charge collection in two neighbouring channels a different energy is calculated to what was actually deposited during the γ-ray interactions. Depending on the magnitude of energy deposited this results in peak broadening or peak splitting.

This proportional cross-talk and subsequent peak splitting can be corrected after the fact by applying a linear correction factor to the recorded energy. Ideally, a correction would be applied to the baseline itself so as to avoid this effect when analysing the traces but a correction in the MWD energy is simple and computationally inexpensive. A linear correction factor can be found by plotting the keV shift present in an addback photopeak energy against the γ-ray energy. An example of this process is presented in Figure 4.11 in which a correction factor was found for fold 2 events on the HPGe AC face, a fold 2 being an event that is F[1,2] or F[2,1]. In Figure 4.11 (left), known γ-ray
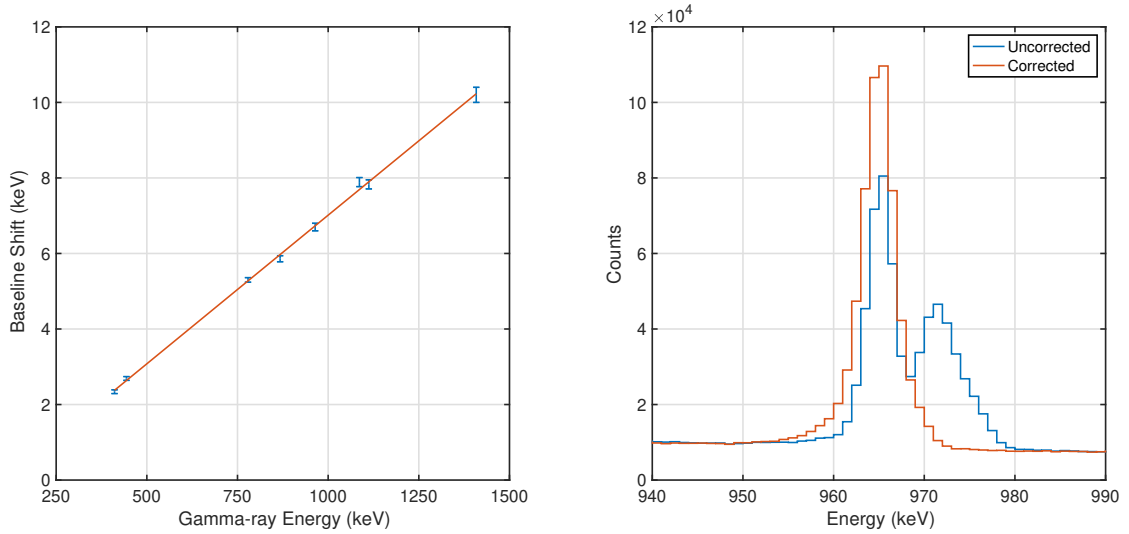
FIGURE 4.11: Plot of ^{152}Eu γ-ray photopeak energies against a baseline shift following a fold 2 neighbouring event (left). Uncorrected and corrected energy spectra of fold 1 and fold 2 events (right).

energies were recorded from a ^{152}Eu source. An addback spectrum was then produced for fold 2 events that occurred in neighbouring channels. The difference in energy between the recorded addback photopeak position and the correct position was plotted as the baseline shift. A linear fit was then applied and used as a subsequent correction factor. Figure 4.11 (right) shows an uncorrected energy spectrum in blue, focused on the 964.1 keV photopeak, produced from fold 1 and fold 2 events. The fold 2 nearest neighbour events produce a photopeak shifted to the right away from its proper position. The same photopeak is shown in red subsequent to application of the correction factor. Fold 1 and fold 2 events are now both located at the correct photopeak position. The energy resolution of this new cross-talk corrected addback peak is degraded relative to that of the fold 1 peak due to the increased number of uncertainties present when adding back energy.

A correction factor was found for fold 2 events in the Si(Li), and for fold 2 and fold 3 events in the HPGe. In each case a factor was found for the AC channels and the DC channels separately. The cross-talk shifts as a percentage of the deposited energy were found to be 0.68% and 0.80% between fold 2 events on the Si(Li) AC and DC faces respectively. For fold 2 events in the HPGe it was found to be 0.67% on the AC face and 0.31% on the DC. The highest correction was require for fold 3 events in the HPGe in which contiguous neighbouring strips are hit. In this case it was found to be 0.81% for the AC face and 0.61% for the DC face.

A small contribution of differential cross-talk was found to be present in the system. While proportional cross-talk affects the baseline of a signal, differential cross-talk occurs during the rise time of a signal and can mimic image charges within the system [59]. The effect of differential cross-talk is noticeable when comparing experimental to simulated signals and is discussed in Section 7.2.2.

Chapter 5

Detector Characterisation

Precision scans were performed of the HPGe detector using collimated γ-ray sources affixed to motorised scan systems in order to characterise the detector response as a function of interaction position. Characterisation of planar detectors has been carried out previously at the University of Liverpool on the Si(Li) detector in the GRI+ system [19] and the Ortec manufactured HPGe detectors that constituted the previous iteration of the Liverpool Compton camera system, SmartPET [18]. Two types of collimated γ-ray scans were performed. Low-energy surface scans were performed in order to investigate the nature and uniformity of the detector response to interactions close to the AC and DC contacts as a function of x-y position; revealing information about the charge collection performance and relative sensitivities of detector regions. A high-energy side scan was carried out to characterise the signal response through the z-depth of the detector. The side scan process enables the parameterisation of charge collection pulses as a function of γ-ray interaction position for use in PSA development and optimisation. The set-up and experimental processes of each scan are described separately below with associated results.

5.1   Am-241 Surface Scan

The HPGe crystal was scanned using a 1 mm diameter collimated ^{241}Am source. Two surface scans were performed; one with the collimated γ rays incident on the AC face of the detector, and one with them incident on the DC face. Surface response data were produced for interaction positions close in z-depth to the AC strip contacts, the AC surface scan, and for positions close in z-depth to the DC strip contacts, the DC surface scan. ^{241}Am was chosen for the face scan as it predominantly produces a single γ ray of 59.5 keV which, due to its low penetration range in germanium of ~1 mm, reveals the response of the detector close to the charge collecting strip electrodes. For γ rays of 59.5 keV incident in germanium, the cross section of Compton scattering is 6.7% that of photoelectric absorption [60]. This ensures that photoelectric absorption dominates the data recorded. Due to the low-energy, the range of a γ ray that does Compton scatter is small and so is likely to be photoelectrically absorbed very close to the point of scatter.

In addition to revealing information about the structure of the strip contacts and the charge collection properties of the HPGe detector, the scan data were also used to produce transient image charges from known x-y γ-ray interaction positions. As the x-y position was known and the image charges originated in the first mm of the detector they were constrained in (x, y, z). For this reason they could be used to validate the image charges of a simulated pulse database from corresponding (x, y, z) positions in Chapter 6.

5.1.1 Scanning Set-up

The digitiser and GO box set-up described in Chapter 4 was used to output all 24 channels if a trigger threshold of 8 keV was passed by an AC or a DC channel. HV and LV power were supplied by nuclear instrumentation modules as opposed to the cart system, which was not complete at the time of these measurements. A collimated ^{241}Am source was placed on a platform and attached to a Velmex motorised scanning system that gave full position control in x and y. This enabled scanning of the collimated γ-ray beam across the detector crystal faces. A picture of this set-up is shown in Figure 5.1. The arm was moved in 1 mm steps with a precision of 100 μm across the faces of the detector and a dwell time of 10 s at each position. An incident count rate in the HPGe of ~450 59.5 keV γ rays per second was recorded.
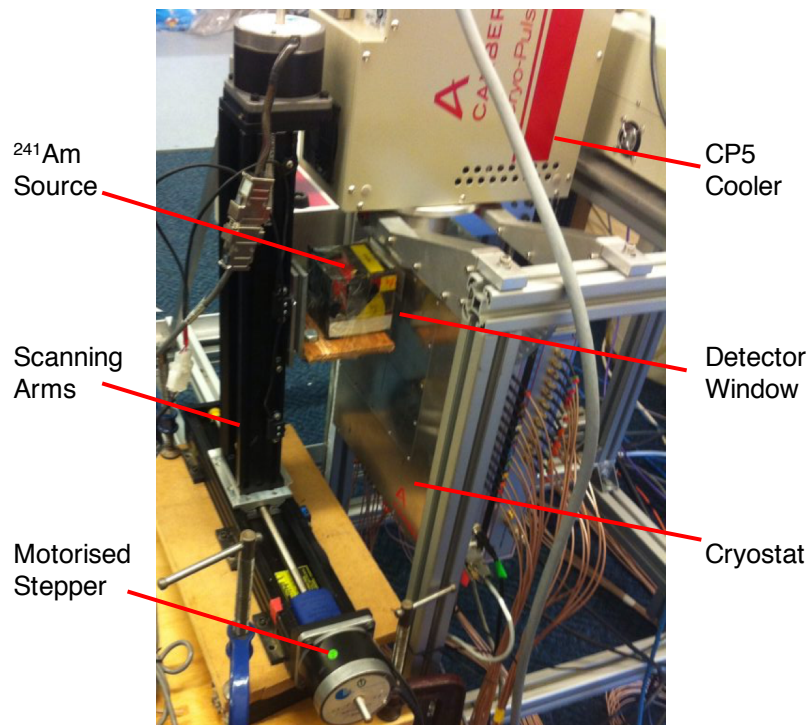
FIGURE 5.1: Photograph of ^{241}Am scan experimental set-up.

The collimator was a 1 mm internal diameter tungsten insert placed in a lead block containing a 1.64 GBq ^{241}Am source. The 40 mm collimator length in addition to an 18 mm distance between the collimator and the crystal resulted in a maximum beam

divergent spot size of 1.9 mm incident on the front of the HPGe crystal. This was calculated from

$$d = A\left(1 + \frac{2D}{L}\right),\tag{5.1}$$

where d is the maximum diameter of the beam spot size, A the internal diameter of the collimator, L the internal collimator length, and D the distance between the collimator end and the detector crystal. The use of a lead block and tungsten collimator minimised the number of γ-rays incident on the detector that were not part of the collimated beam.

Sorting and classification of the surface scan data follow the methods described in Section 4.3.1 with one notable exception; the BLD method was not used to distinguish between real charge and noise. This was due to the small size of the signals in a multi-fold event relative to the electronic noise in the signal. The BLD most importantly failed to identify correctly charge-shared events (discussed in the following sections), in which the charge shared was extremely unequal, as real charge. Instead, a 5 keV low-energy threshold was set when sorting the data. A signal was classed as having real charge if an MWD energy of greater than 5 keV was recorded. Any signal registering above this noise threshold was summed in the detector addback for a given face and the fold incremented. As such, an F[1,1] event is defined as a single strip on each of the AC and the DC faces registering an MWD energy of above 5 keV, and a F[2,1] event one in which 2 AC strips and 1 DC strip registered above the 5 keV threshold. This method was validated through manual investigation of real event classification and was found to report the correct event fold reliably when measuring 59.5 keV energy depositions.

5.1.2 Intensity Maps

Intensity plots are often used to display the uniformity of detector response. They can reveal areas of the detector in which the charge collection response is poor. Intensity plots were produced as a function of collimator x-y position for those events with an addback energy that passed a 6 keV wide energy gate placed on the 59.5 keV photopeak collected over the 10 s dwell time. Any event where both the AC and the DC addback energies fell within this gate contributed towards the intensity map in Figure in 5.2. The intensity maps are displayed for the surface scan in which the γ rays were incident on the AC face (left) and on the DC face (right). In these plots the AC strips are horizontal and are numbered 1-12 from top to bottom. The DC strips are numbered 1-12 from left to right and are vertical. The response was observed to be mostly uniform with a decrease in intensity occurring at x-y positions corresponding to the collimator being located on the inter-strip gaps in-between the strip contacts.

The intensity drop present on the inter-strip gaps was explored by investigating the energy spectra recorded in each strip. The spectrum obtained from strip AC06 is displayed in Figure 5.3 (left). The y-axis has been chosen to magnify the low-energy
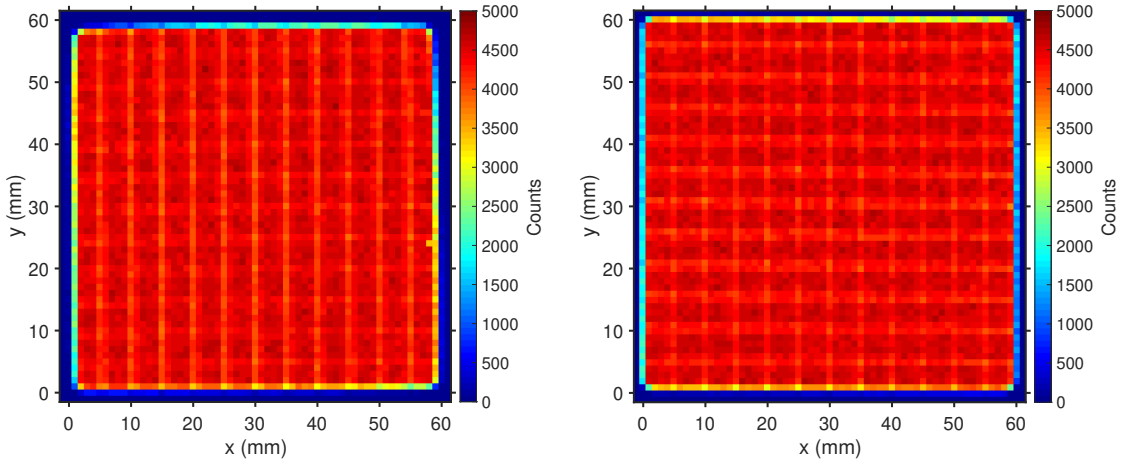
FIGURE 5.2: Intensity map from the AC surface scan (left) and the DC surface scan (right) for those events that pass a 6 keV wide addback gate set on the 59.5 keV photopeak. The AC strips are horizontal and the DC are vertical.

tailing that was found to be present in the 59.5 keV photopeak, which is indicative of charge-loss in the detector. This was found to be typical for all AC and DC strips. The lower bound placed on the 59.5 keV photopeak gate was reduced by 5 keV and so a widened photopeak gate of 52-63 keV applied, shown in red. The intensity maps where then reproduced with this new gate and the plot from the AC surface scan is shown in Figure 5.3 (right). A fully uniform response is obtained with the inclusion of the low-energy tailing present in the photopeak. This indicates that charge is being lost at the inter-strip gaps of the detector.
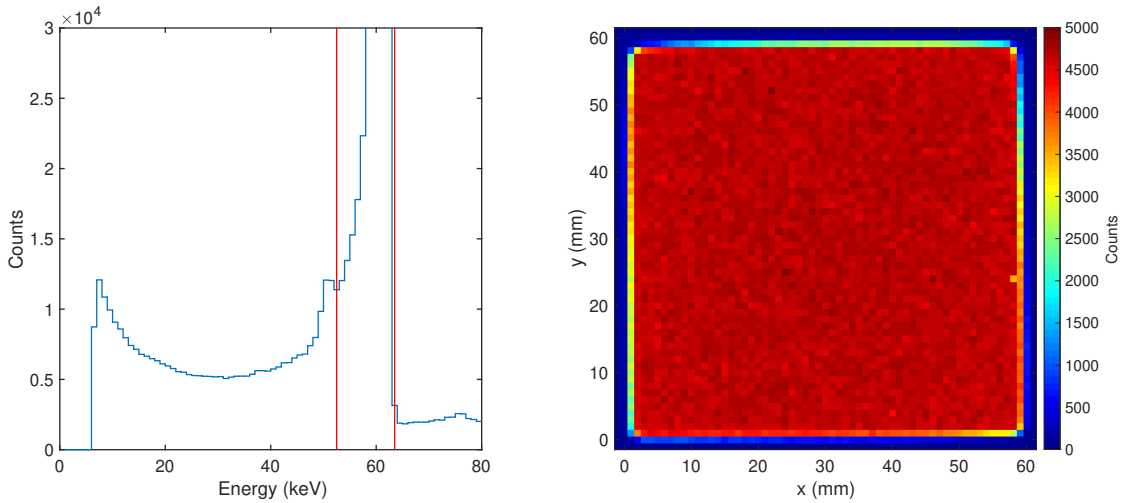
FIGURE 5.3: Energy spectrum for strip AC06 (left) and intensity map from the AC surface scan for those events that pass a widened addback gate of 52-63 keV placed on the 59.5 keV photopeak (right).

This effect was attributed to either the loss of some of the charge carriers to the inter-strip gap or to charge sharing. Charge sharing could occur at the inter-strip gaps due to the charge carrier cloud produced following an interaction being collected by two neighbouring strip electrodes. This effect has been observed previously in germanium

strip detectors [61] and more recently in the Ortec manufactured HPGe strip detector of the previous iteration of the Liverpool Compton camera system [58]. A charge-share event of this nature may share charge unequally between two strips and while the majority of charge would therefore be collected by one strip the other may fall below the 5 keV energy noise threshold. This would result in a decrease in intensity on the inter-strip gaps. This charge sharing is attributed to the occurrence of regions of electric field splitting between strip electrodes and, as such, charge carrier clouds occurring in this region are collected and shared by both electrodes. Weak electric fields could also result in the incomplete collection of charge carriers in these regions and so results in some carriers being collected on the surface between the strip electrodes.
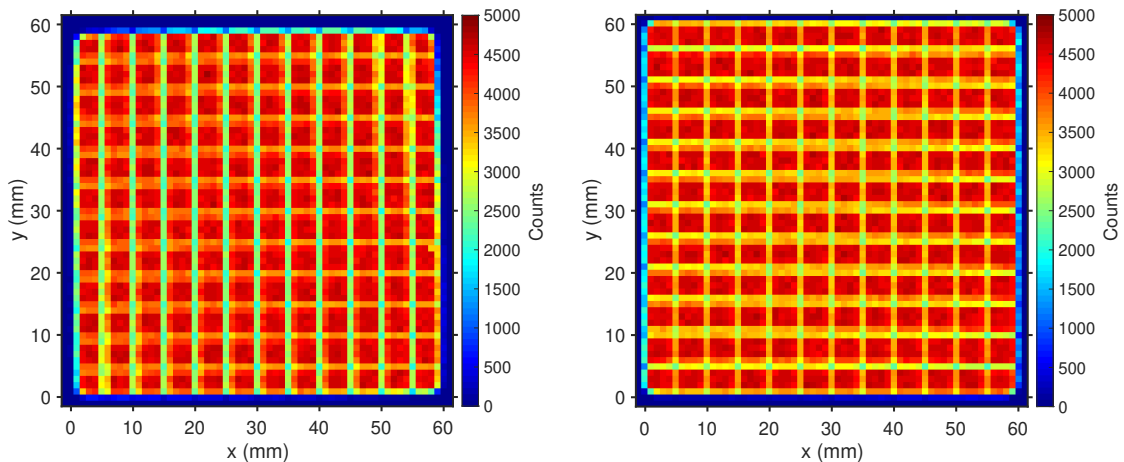
FIGURE 5.4: Intensity map from the AC surface scan (left) and the DC surface scan (right) for those events that pass a 6 keV wide addback gate and an F[1,1,] gate set on the 59.5 keV photopeak. The AC strips are horizontal and the DC are vertical.

To investigate this charge-loss further, the intensity maps were reproduced with the added requirement that the event be single-pixel. This was achieved through application of a fold gate. An event was only included if each face registered a fold 1 event in which the deposited energy passed the 6 keV wide photopeak gate, resulting in F[1,1] events. The produced intensity maps are displayed in Figure 5.4 and show a large decrease in counts at positions corresponding to the AC and DC inter-strip gaps. At these positions a higher fold is recorded on the AC face, the DC face, or both. The decrease in intensity at the inter-strip gaps is too large to be attributed to Compton scattered and subsequently absorbed γ rays due to their low probability of occurrence. Instead this decrease is attributed to the previously described charge sharing mechanism. The AC surface scan displayed in Figure 5.4 (left) shows a larger decrease in counts between the vertical DC strips relative to the horizontal AC strips. The vertical strips are on the far side of the detector relative to the incident γ rays while the horizontal are on the near side. The DC surface scan (right) appears to be less clear as to whether the decrease in counts is larger between the AC or the DC strips. To clarify this, slices were taken from the DC surface scans in Figure 5.2 and Figure 5.4 to show more clearly the changes in intensity. They were taken along the centre of DC06 to show the AC strips

and their inter-strip gaps and along the centre of AC06 to show the DC strips and their inter-strip gaps. These projections are shown in Figure 5.5.
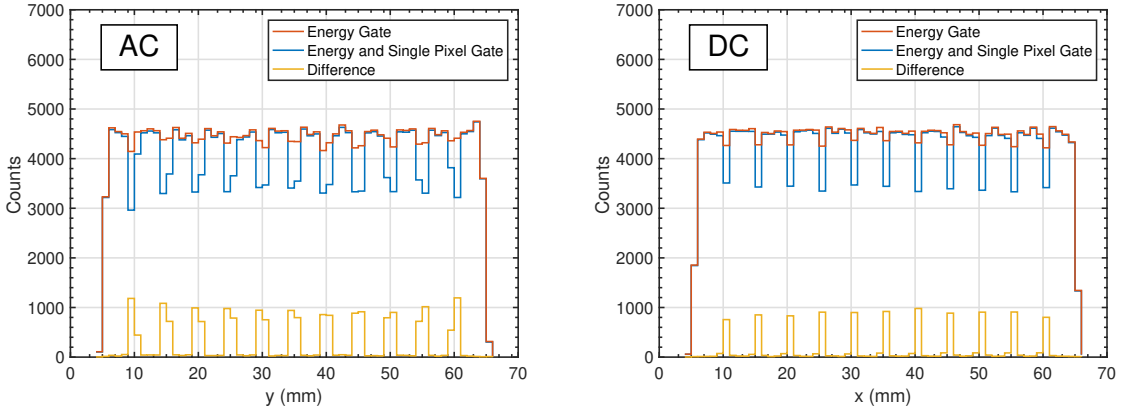
FIGURE 5.5: Slice taken from the DC surface scans across the AC strips and inter-strip gaps (left) and the DC strips and inter-strip gaps (right).

When a slice is taken across the AC strips (left) and the DC strips (right) it can be seen that the fewer counts are found at the AC inter-strip gaps than at the DC inter-strip gaps when a single-pixel gate is applied. This again corresponds to the electrodes on the far side of the detector relative to the incident γ rays. The decrease in single-pixel events for the AC inter-strip gaps is observed to predominantly occur over a range of 2 mm as opposed to 1 mm as seen between the DC strips. This trend is also observed for the AC surface scan if a similar intensity slice is taken and, as such, differences in beam divergence is discounted as a cause. A possible reason for this occurrence could be the slightly wider inter-strip gaps present between the AC strips, 300 μm as opposed to the 250 μm separating the DC strips. Full-photopeak events that did not pass the single-pixel gate were attributed to charge sharing. The percentage of charge-shared events from the DC surface scan was found from Figure 5.5 for the AC and DC collection. Equivalent slices were taken from the AC surface scans from Figures 5.2 and 5.4 to find the percentage of AC and DC charge-shared events. The percentage of the total photopeak events that fell into this category for the AC and DC surface scan slices is displayed in Table 5.1. In each case it is found that the larger percentage of charge-shared events correlates with the far side electrodes relative to the incident γ rays. It is thought that the charge sharing occurs predominantly for each scan on the electrodes on the far side of the detector due to diffusion of the charge carrier cloud as it travels the full 20 mm z-depth of the detector.

Face	AC Surface scan	DC Surface Scan
AC Face	4.7%	7.6%
DC Face	7.7%	4.2%

TABLE 5.1: % of full-photopeak energy charge-shared events occurring between the AC and the DC electrodes for each of the surface scans.

5.1.3 Inter-strip Gap Effects

An intensity map was produced of charge-shared events in order to investigate their total effect on the detector response. This was done by taking the difference between the energy gated intensity maps in Figure 5.2, and the energy and F[1,1] gated intensities in Figure 5.4. The intensity maps produced are displayed in Figure 5.6 for the AC surface scan (left) and the DC scan (right); they represent the total number of events that fail the F[1,1] gate and as such are multi-pixel events. High count intensities are found at positions corresponding to inter-strip gaps with hot spots at the intersections of the AC and DC inter-strip gaps. This is as expected, as multi-pixel charge-shared events are more likely to occur between strips and most likely at the intersections of four strips. These events were quantified to be 11.5% of 59.5 keV γ-rays incident on the AC face, and 10.3% of those incident on the DC face. These events cannot be entirely attributed to charge sharing as there is a possibility that a small number may be due to Compton scattering.
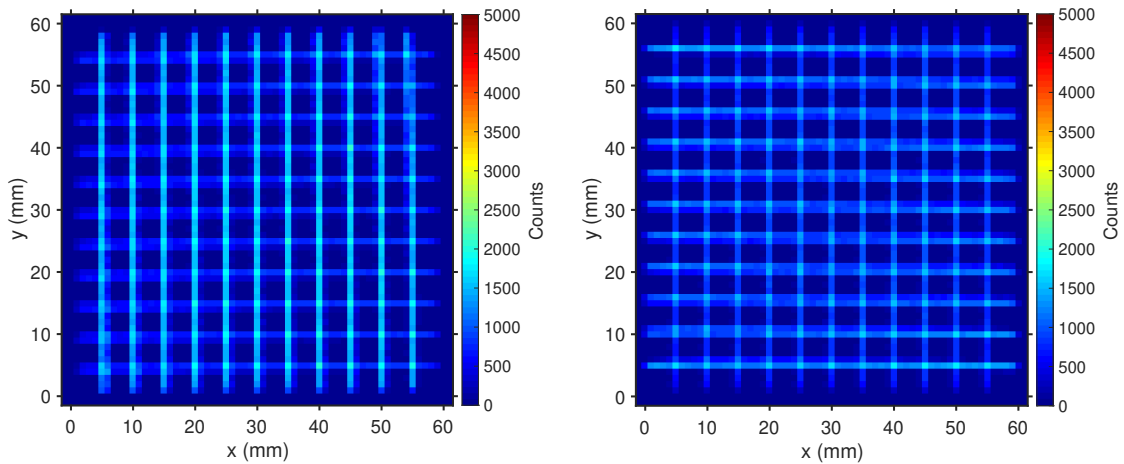
FIGURE 5.6: Intensity map from the AC surface scan (left) and the DC surface scan (right) for those events that deposit the full photopeak energy but are not F[1,1]. The AC strips are horizontal and the DC are vertical.

No attempt was made to identify and correct these charge sharing events, though in future work it should be investigated. An ability to distinguish a fold 2 event due to charge sharing as opposed to a fold 2 event due to scattering would yield an improvement in the system's imaging efficiency as well as allowing the utilisation of events with precisely known positions. It has been proposed that analysis of the leading edge of the pulses that form a charge-share event could yield this information [62] but due to the low-energy events produced from these surface scans it would be difficult to distinguish features within a pulse that are small relative to the noise present in signal.

It was proposed by Cooper *et al.* [58] that as charge sharing was the consequence of weak lateral electric field between the adjacent strip electrodes then the strength of the field would vary as a function of position. As such, the magnitude of the charge collected would vary as a function of interaction position. It follows that an interaction occurring precisely at the midpoint between two strip electrodes would share equal charge and

interactions closer to a particular electrode would therefore share more charge to that strip and less to the more distant neighbouring strip. This was tested by producing energy spectra of those adjacent multi-strip events that comprise Figure 5.6 for the AC and DC surface scans. The charge collected by each of two neighbouring strips in a F[2,1] and a F[1,2] event are plotted in Figure 5.7 for the AC surface scan (left) and the DC surface scan (right). The low-energy threshold gate of 5 keV caused a sharp cut-off and as such the spectrum begins at 6 keV. The 6 keV wide photopeak energy gate was kept although lowering it may include charge-share events where some charge falls below the noise threshold it may also lead to the inclusion of events where the charge is lost in-between the electrodes. As these spectra consist of those events in which the full γ-ray energy is split between two adjacent strips the possible energy depositions due to Compton scattering and subsequent absorption are constrained. A scattered 59.5 keV γ ray can impart 0-11.3 keV to the electron within the detector, scattering out with an energy range of 48.3–59.5 keV for angles of scatter between 0 and 180°. For a fold 2 event passing the photopeak energy gate it would therefore be expected that anything outside of the range of these two energies, marked by black lines in Figure 5.7, could be confidently attributed to charge sharing while energies within these regions could partly comprise of scattered γ rays. The contribution from these types of events is likely to be small due to low probability of Compton scattering within germanium at 59.5 keV relative to the probability of photoelectric absorption. The region between these limits is then indicative of the type of charge sharing that has occurred between the strip electrodes and would reveal information in relation to the position sensitive nature of charge sharing.
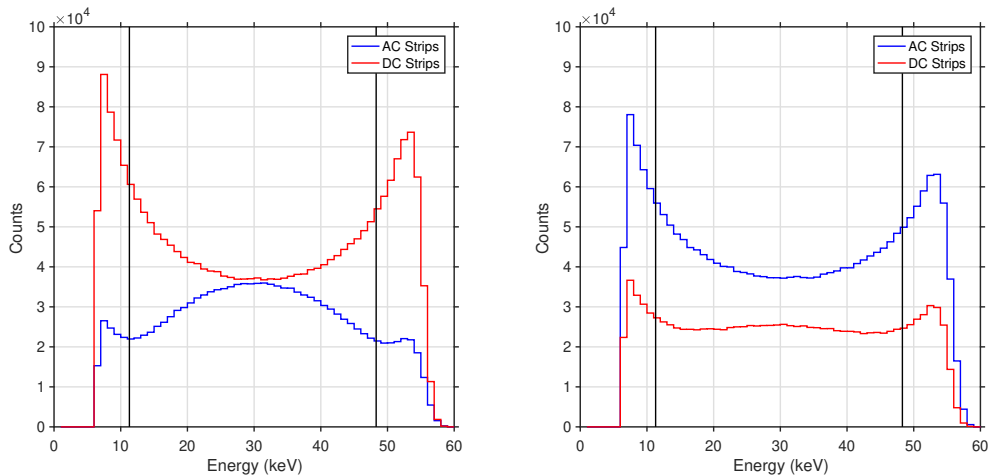
FIGURE 5.7: Energy spectra of those events involved in a neighbouring fold 2 event between the AC or between the DC electrodes for the AC surface scan (left) and DC surface scan (right). Vertical lines show the energy limits of a Compton scattered then photoelectrically absorbed 59.5 keV $\gamma - ray$.

For the AC surface scan in Figure 5.7 (left) charge sharing is seen to occur predominantly on the far side electrodes as expected due to charge carrier cloud diffusion during the drift time. There is not a strong splitting on the near-side electrodes and

instead equal sharing of charge between the two adjacent strips is observed with a local maximum appearing at 30 keV. Figure 5.7 (right) shows the same spectrum from the DC surface scan with the charge sharing again predominantly occurring on the far side electrodes relative to the collimator but with less of a preference for equal charge sharing on the near side compared to the AC surface scan. These results are contrary to those observed by Cooper *et al.* [58] in the geometrically similar SmartPET HPGe detector in which strong splitting was observed on the near-side electrodes and weak splitting on the far-side. No large preference for equal charge sharing was found. The reason for this occurrence in the Mirion manufactured HPGe may be due to the difference in inter-strip gap width between the two faces or to the newer a-Ge contact technology that is used.
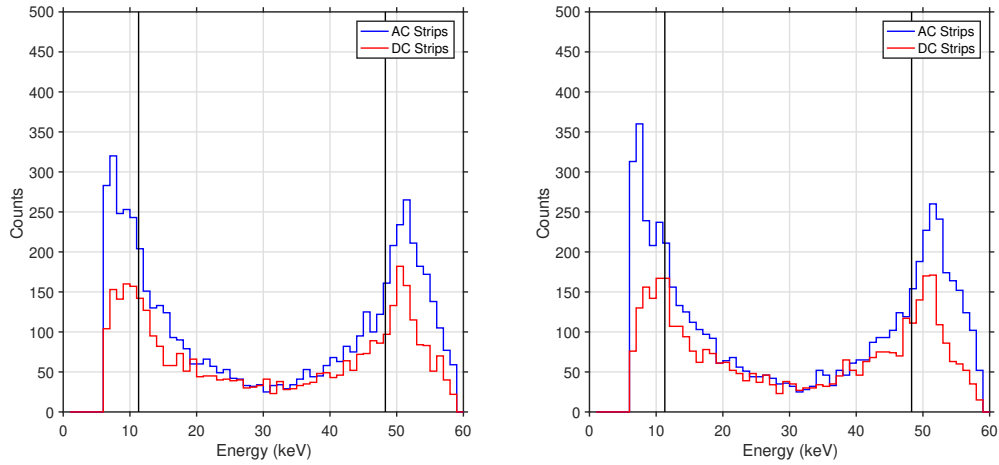
FIGURE 5.8: Energy spectra of those events involved in a non-neighbouring fold 2 event between for the AC and DC electrodes for the AC surface scan (left) and DC surface scan (right). Vertical lines show the energy limits of a Compton scattered then photoelectrically absorbed 59.5 keV $\gamma - ray$.

A similar spectrum produced for non-adjacent events as opposed to neighbouring events is displayed in Figure 5.8. Few events are present when one or more strips separates the charge collecting strip electrodes. This is as expected due to the low probability of a 59.5 keV γ ray scattering and not being immediately absorbed by the neighbouring strip but by the next one over. Charge sharing would not be expected to be present for these non-neighbouring strips and this is observed in the low level of events outside of the range of possible Compton scattering. These events were also not constrained to any particular regions of the detector. Those events outside of the Compton scattering limits can be disregarded as there are very few and do not result from any significant effect within the detector.

5.1.4 Rise Time Maps

Average T30 and T90 rise time maps of the detector surfaces were produced from the AC and DC surface scans as a function of collimator position. These maps were produced as a means of investigating the potential effects of electric field splitting on the inter-strip gaps as well as the overall field uniformity across the surface of the detector. The t10,

t30, and t90 of each experimentally recorded F[1,1] event that passed the 6 keV wide photopeak was calculated. From these, an average T30 and T90 value was produced at each 1 mm position if at least 1,500 events were included in their calculation, in order to minimise statistical uncertainty. The T90 parameterised maps are displayed in Figure 5.9 and the T30 maps in Figure 5.10. The AC rise time maps are given for the AC surface scan (a) and the DC surface scan (c) while the DC rise time maps are given for the AC surface scan (b) and the DC surface scan (d). Figure 5.9 shows that the AC T90 rise time is around 130 ns when the γ rays are incident on the AC contacts and around 170 ns when they are incident on the DC contacts. The DC T90 rise times show a similar collection time of around 180 ns for both surface scans. In Figure 2.6 it was shown that the drift velocities of electrons and holes in germanium are around 10^7 cm/s. As the HPGe crystal is 2 cm thick, charge collection times of around 200 ns would be expected. The values observed in Figure 5.9 are reasonably close to this, though the AC rise time response is significantly faster. This discrepancy is addressed later in this chapter.
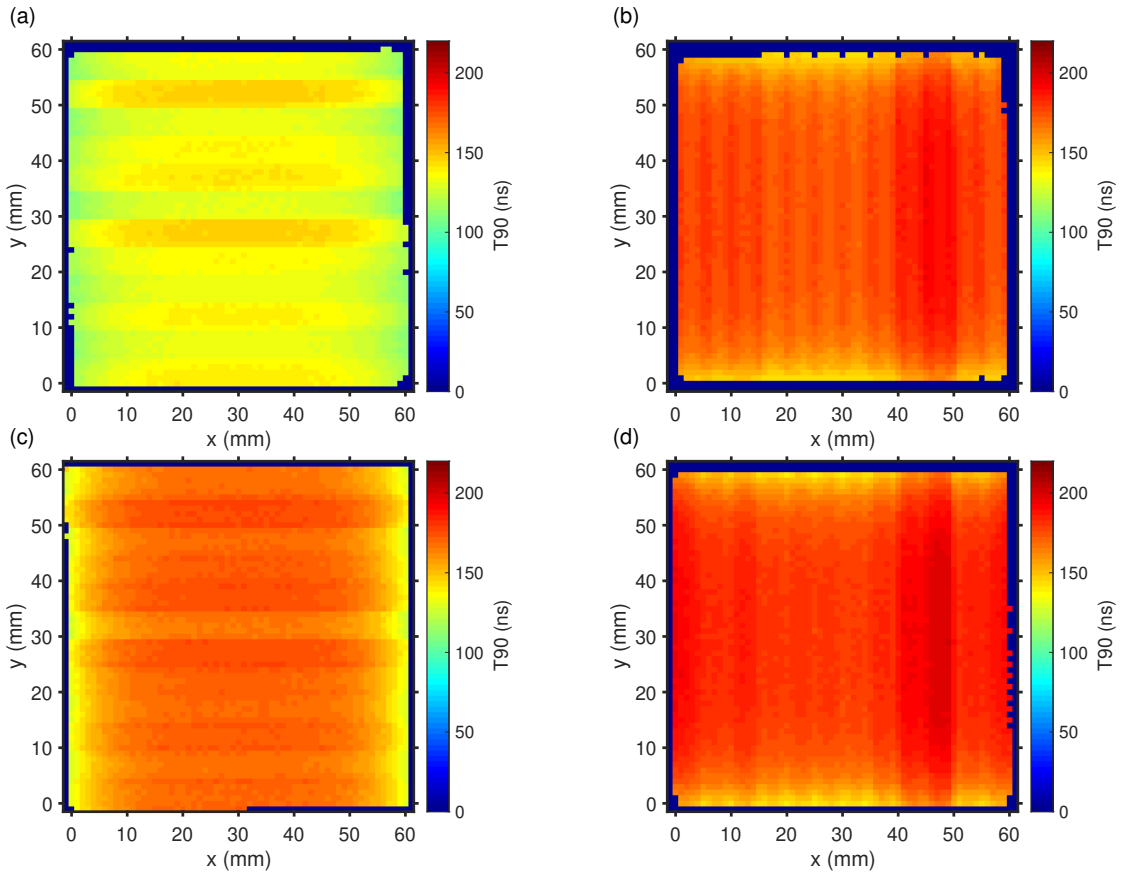
FIGURE 5.9: Average T90 rise times values produced as a function of collimator position for the AC surface scan AC rise times (a) and DC rise times (b) and the DC surface scan AC rise times (c) and DC rise times (d). All averages comprise of at least 1,500 F[1,1] full photopeak energy events.

The T90 rise time maps reveal a lack of uniformity between strips belonging to both the AC face (a and c) and the DC face (b and d). The average T90 value would be

expected to be uniform across each face of the detector as the strip contacts are of constant length and have identical capacitance. This difference between strips on each face is attributed to the calibration of the preamplifiers themselves that was performed prior to the delivery of the detector. The T90 rise time varies by as much as 20 ns between strips on a given face. This variation must be accounted for if utilising the T90 parameter in PSA. There is also an observed variation in rise time values along the length of each individual strip; T90 values are seen to be up to 40 ns faster at the strip ends close to the detector guard ring than in the centre. The T90 rise time response is observed to be 20% and 15% faster at the ends of the AC and DC strips respectively compared to the rise times present more centrally on the strips. The 7.5 mm guard ring surrounding the HPGe detector is implemented to maintain uniformity of the electric field across the entire active volume and to decrease edge effects that may occur due to electric field variation. It would be expected to prevent this non-uniform response. Scans take during characterisation of the Si(Li) detector presented longer rise times at the strip edges [19] and was attributed to a weaker electric present at the detector edges, despite the 5 mm guard ring present.
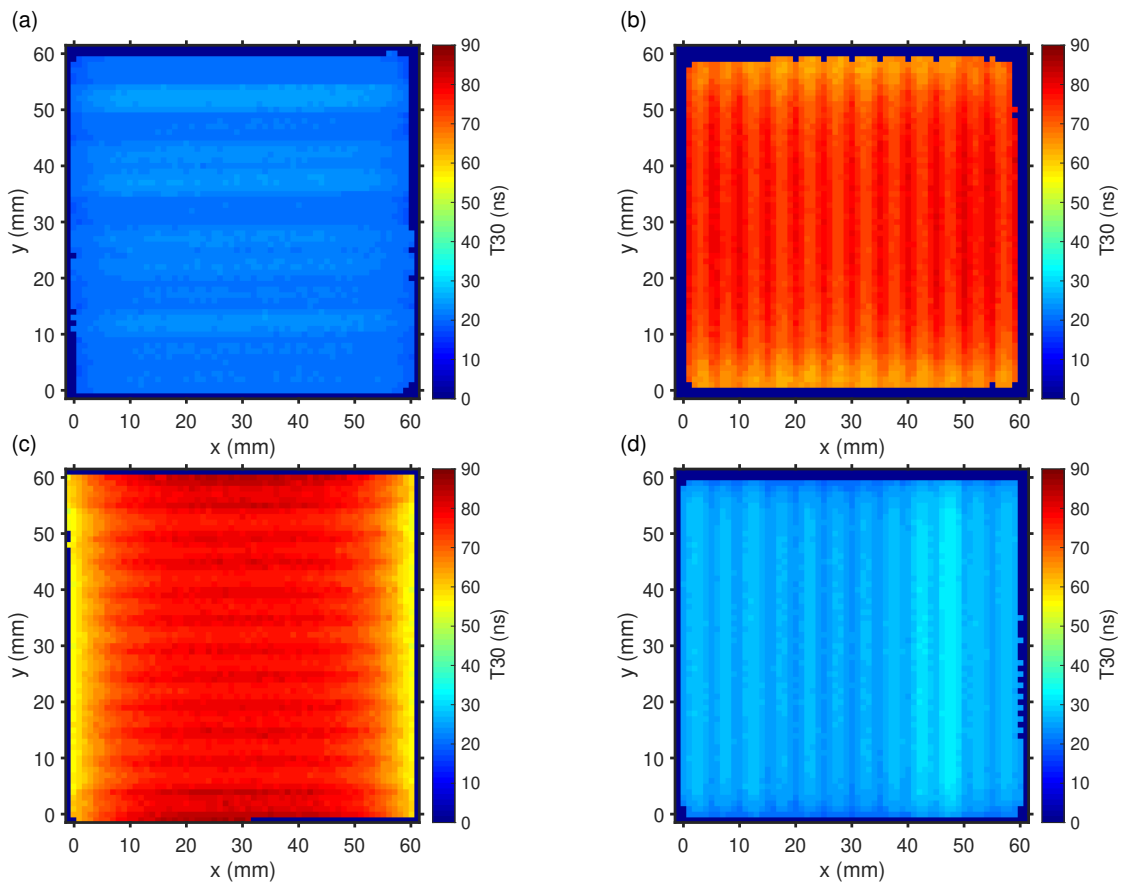
FIGURE 5.10: Average T30 rise times values produced as a function of collimator position for the AC surface scan AC rise times (a) and DC rise times (b) and the DC surface scan AC rise times (c) and DC rise times (d). All averages comprise of at least 1,500 F[1,1] full photopeak energy events.

The T30 map, displayed in Figure 5.10, was produced as it is a parameter often employed in PSA for z-depth analysis and is dependent on the collection of the primary charge carriers. For this reason it is highly position sensitive and may be revealing as to the contact structure and field strength when compared with T90 parameterisation. As T30 is sensitive to the z-depth of interaction it is thus fast or slow depending on the face the collimated γ rays are incident on relative to the primary charge carrier collecting electrodes. In Figure 5.10 non-uniformity is again observed between strips on a given face with up to 20% variation for the DC surface scan DC collection (d). Variation in rise time is again observed along the length of the strips on each face, with a decrease in T30 of up to 30% between the strip centres and ends present for DC surface scan AC charge collection (b).
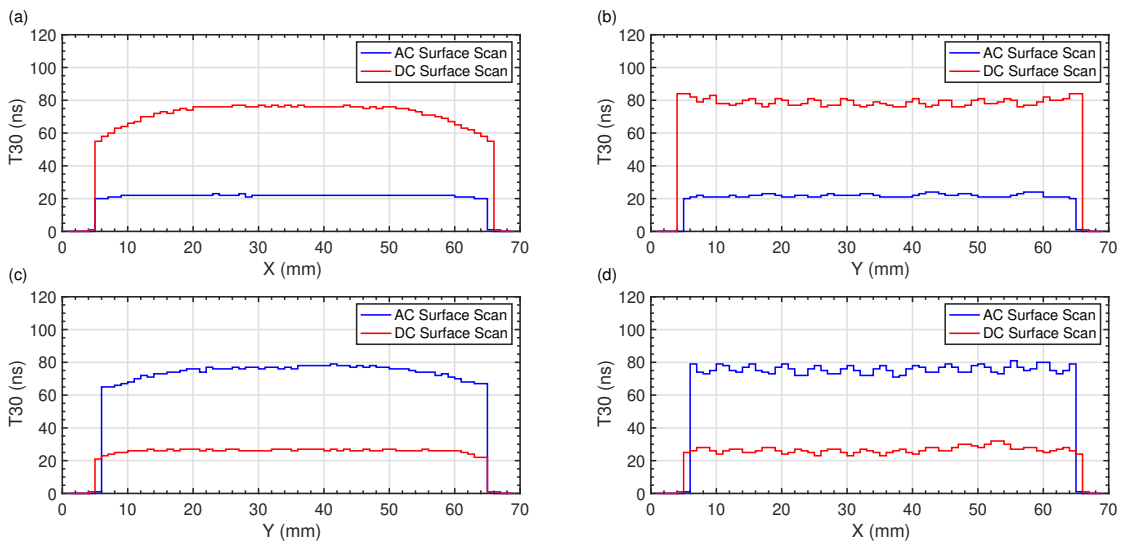
FIGURE 5.11: The AC and DC rise times are shown in each plot as a slice taken along strip AC06 (a), across the AC strips (b), along strip DC06 (c) and across the DC strips (d).

To observe the variation in T30 rise times present in these scans more clearly, slices were taken through the centre of AC06 and DC06 for each surface scan and the rise time slice for each face plotted in Figure 5.11. This resulted in rise times for each face displaying both the variation along a single strip and across every strip for that face. AC and DC surface scan rise times slices are taken along strip AC06 (a) and across the AC strips (b), and along strip DC06 (c) and across the DC strips (d). The slices taken along AC06 (a) and DC06 (c) show a mostly uniform response when the collimated γ rays are incident on the charge collecting face but a decrease in rise time is clear when the charge carriers are incident on the far face relative to the electrodes and must travel the full 20 mm depth of the detector. In this case they are subjected to a potential non-uniformity in the electric field for a longer period of time, causing a large variation in T30 along the strip length. When the slice is taken across the AC strips (b) the response is again mostly uniform when the γ ray is incident on the AC face and does not present much difference between the strips and the inter-strip gaps. The charge collection of γ rays

incident on the far face shows local minima and maxima present for the inter-strip gaps and the strips respectively, with the T30 rise time in the inter-strip gap being up to 5 ns slower. The equivalent slice across the DC strips (d) shows the same response for charge collected from the far face relative to the DC electrodes with local minima and maxima in rise time occurring on the strips and inter-strip gaps and differences of up to 8 ns present. However, for γ rays incident on the DC face and collected by the DC strips the maxima correspond to strips and the minima to the inter-strip gap, implying a faster charge collection for γ rays interacting in the inter-strip gap. This is contrary to observations other characterisation work [19]. The lack of minima and maxima in the AC rise times for interactions occurring on AC strips and inter-strip gaps is proposed to be due to a stronger lateral electric field splitting, despite the slightly larger inter-strip gap width relative to the DC gaps.
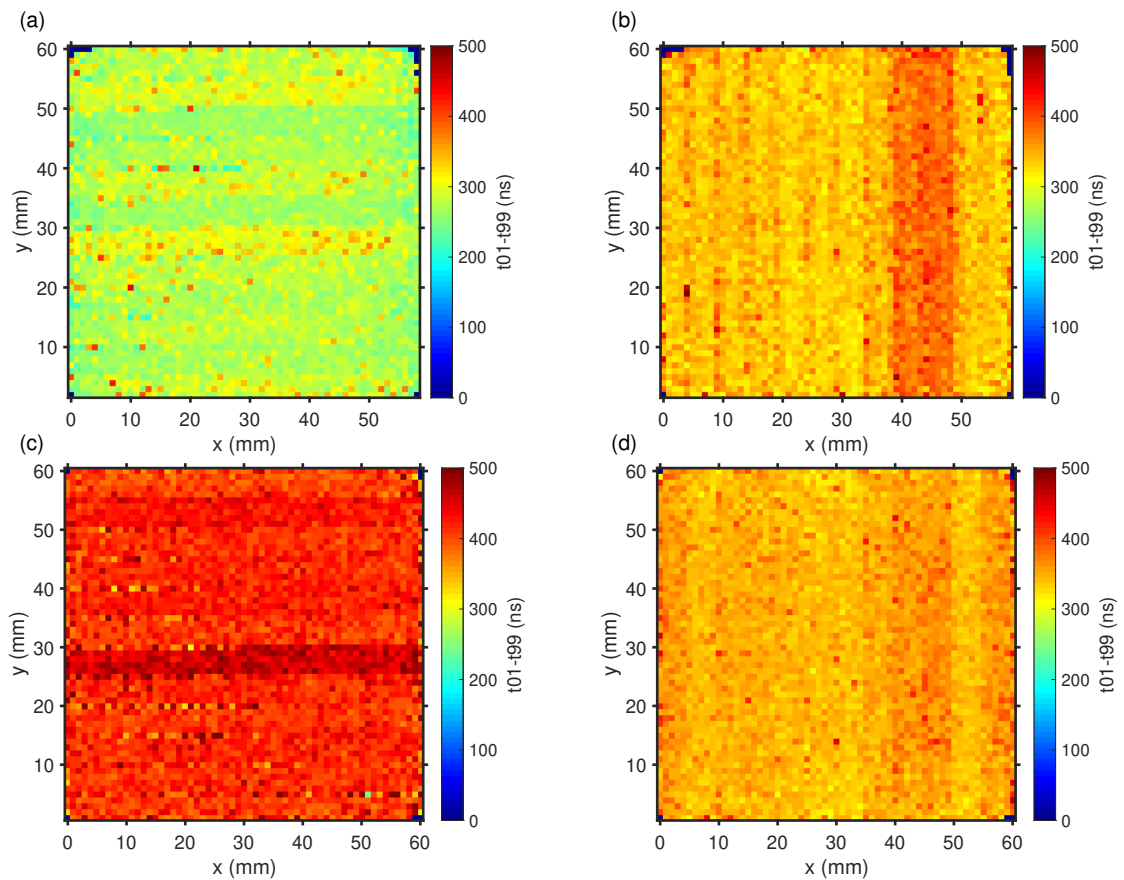
FIGURE 5.12: Average signal rise times between 1% and 99% of total charge collection. Maps displayed for the AC surface scan AC rise times (a) and DC rise times (b) in addition to the DC surface scan AC rise times (c) and DC rise times (d).

The effect of parameterising charge collecting signals between 10% and 90% of their amplitude has been investigated through production of average signals as a function of position. By producing an average signal at each position from multiple events the effects of electronic noise in the signal can be lessened. With the removal of noise the full pulse length can be explored and parameterised. The inclusion of the first and final 10% of the signals may more accurately represent the charge collection properties across the

detector surface. Average signals were formed at each *x-y* position from F[1,1] events that passed the photopeak energy gate. Only 200 signals were used for each average due to data processing limitations. Examples of the average signals are displayed in Figure 5.24 in a later section. T30 and T90 rise time maps were produced from the average signals, as opposed to the previous method of finding an average T30 and T90 from multiple signal measurements. Agreement was found between these maps and the maps produced with the previous method and the same rise time features were present. As agreement was found, rise time maps of the time between 1% and 99% of the total charge collection were produced, known as t01-t99. This more accurately represents the time for complete charge collection within the detector. The rise time maps are displayed in Figure 5.12 for the AC rise times from the AC surface scan (a) and the DC surface scan (c), as well as the DC rise times from the AC surface scan (b) and the DC surface scan (d). Statistical noise is present across the maps and represents the uncertainty in the location of t01 and t99. In these maps no variation is seen in the charge collection along the length of the strips; in each case the response is uniform. Little variation is also seen between the strips and inter-strip gaps compared to the T90 rise time response. The DC t01-t99 rise times are of similar values for both surface scans, while the AC total collection time is much faster for the AC surface scan relative to the DC surface scan, which produces the slowest charge collection times. This is a result of the slower h^+ drift velocities in HPGe. It can be concluded that the shape of the charge collection signals do change along and across the charge collection strips, but the time for complete charge collection remains the same. Parameterisation of the signals into values such as T30 and T90 that do not include the first and last 10% of the pulse accentuates the difference in pulse shapes and produces large variations in rise times. This is discussed more in Section 5.3.2.

5.1.5 Charge Loss and Collection

The characterisation process included an analysis of the charge collection properties of the detector. This was partially explored through investigation of the inter-strip gap effects, but not assessed across the entire detector surface. It is expected that the charge collected by the AC face the DC face be linear as a function of γ-ray energy as the number of electrons produced in a γ-ray interaction is equal to the number of holes. As such, the charge calculated during the collection on each face should be identical if the associated uncertainties with charge collection are ignored. This was tested by producing a matrix of the AC charge collection versus the DC charge collection. Charge loss during the drift from interaction site to charge collecting strip electrodes would manifest as a deviation from the linear relationship between the two charge collecting faces. Figure 5.13 (left) displays the matrix of the MWD calculated AC energy against the DC energy for all F[1,1] events that pass the 5 keV low-energy noise threshold. This yields information about the possible loss of charge occurring during the drift time but not necessarily on the inter-strip gaps. The vast majority of events displayed fell into

the range of 57-63 keV but ~1% of the events that record between 57-63 keV on the AC face are affected by the occurrence of incomplete charge collection on the DC face, highlighted by the red box in Figure 5.13 (left). These highlighted events are shown as a function of collimator position in Figure 5.13 (right) and occur on the boundary between the DC strip electrodes and the guard ring. These are the same type of events classified as charge sharing in Section 5.13 but manifest as a fold 1 event as opposed to a fold 2 as the rest of the charge is shared with the guard ring as opposed to an adjacent strip. This effect is observed between the guard ring and strips on the DC face but not on the AC face. This is potentially due to regions of weaker electric field at the edges of the DC strips.
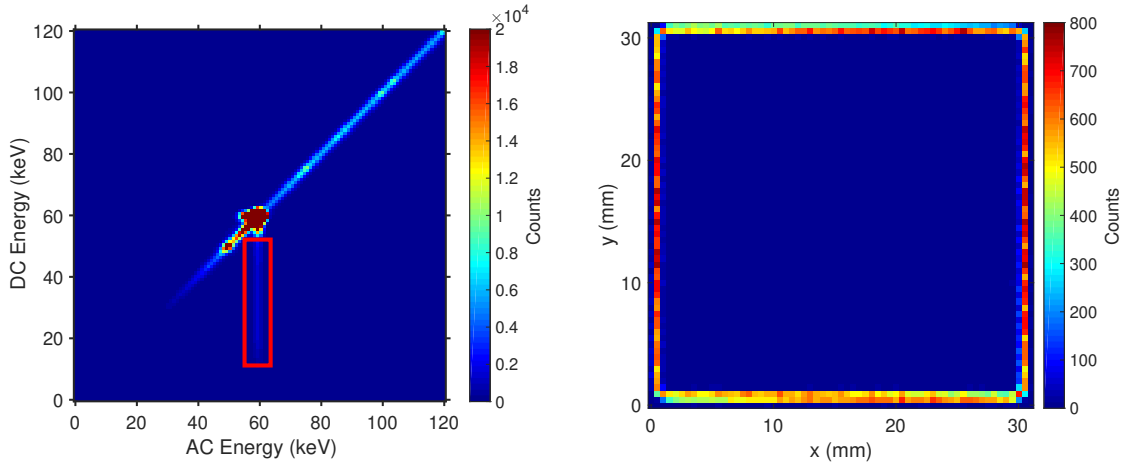
FIGURE 5.13: Plot of the AC recorded energy vs the DC recorded energy for F[1,1] events (left) with events corresponding to apparent DC charge loss boxed in red along with the positions at which these events occur within the detector (right).

The other notable feature in Figure 5.13 (left) is the number of counts present at 50 keV which, if gated on, occur evenly distributed across the face of the detector and do not appear if fold 2 events selected for. They can be attributed to the escape of the K-shell x-rays K_α and K_β which have respective energies of 9.88 keV and 10.98 keV. A K-shell electron is ejected from the germanium followed by the escape of the K_α or K_β, resulting in a recorded energy of the full photopeak minus 9.88 keV or 10.98 keV. This effect is seen prominently in these data due to the low penetrative range of the 59.5 keV ^{241}Am γ rays of ~1 mm and the large surface area of the HPGe crystal that was scanned.

A small amount of low-energy tailing was present in the AC and DC charge collection, occupying the region between the main photopeak energy and the escape peak. Incomplete charge collection would not likely manifest as both sets of charge carriers losing equal amounts of carriers and so the tailing at this point is due to charge being lost to the detector system entirely due to the escape of the K_α and K_β, or charge sharing occurring on both faces in which some falls below the low-energy noise threshold for each. The latter was found to be partly the case with these events occurring in positions

corresponding to intersections of inter-strip gaps on both faces of the detector as well as evenly spread the detector face and so attributed to the K_α and K_β escape.
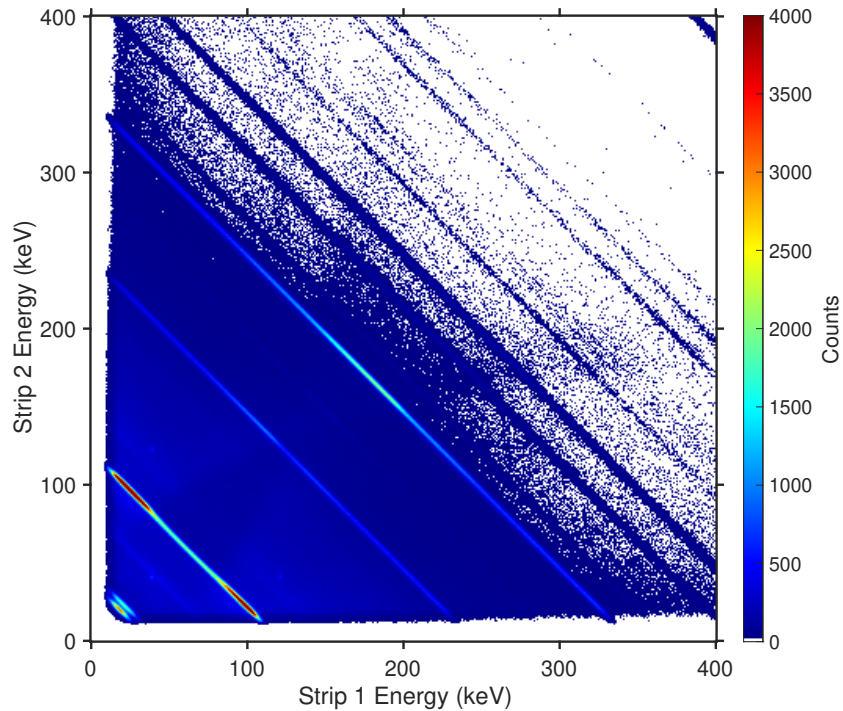
FIGURE 5.14: Energies of a F[2,1] event in the HPGe in which the events occur in adjacent strips of the AC face produced from a ^{152}Eu flood source measurement.

To investigate the charge collection properties within the bulk of a detector without the effects of escape peaks, a larger range of energies, up to 1408.0 keV, was used to repeat the F[1,1] matrix of AC energy versus DC energy. If charge sharing were to occur at larger energies it would be less affected by the threshold due to the magnitude of the energies shared. This was achieved with a flood ^{152}Eu source which produces energies ranging from 121.8 keV to 1408.0 keV. It was observed that low-energy tailing occurred at all energies but preferentially on the DC face. Due to the non-position sensitive nature of the flood source measurement the location of these events could not be determined and cannot be wholly attributed to either threshold effected charge sharing or charge loss. It was noted however that if fold 2 events were looked at then this effect disappeared at higher energies suggesting that there is no evidence of charge loss, only charge sharing in which some charge falls below the low-energy threshold.

The possibility of charge loss on the inter-strip gaps was discussed previously. This can occur due to regions of weak electric field between two strips [64]. It was difficult to investigate this effect with the low-energy surface scan data so the ^{152}Eu flood data were used to produce fold 2 events between neighbouring strips to investigate this particular mechanism. The energies of the two events occurring in adjacent AC strips of a F[2,1] event have been plotted against each other in Figure 5.14, where a straight diagonal between the axis represents complete charge collection of the full γ-ray photopeak energy. A plot of the energies in a F[1,2] event between adjacent DC strips shows an identical
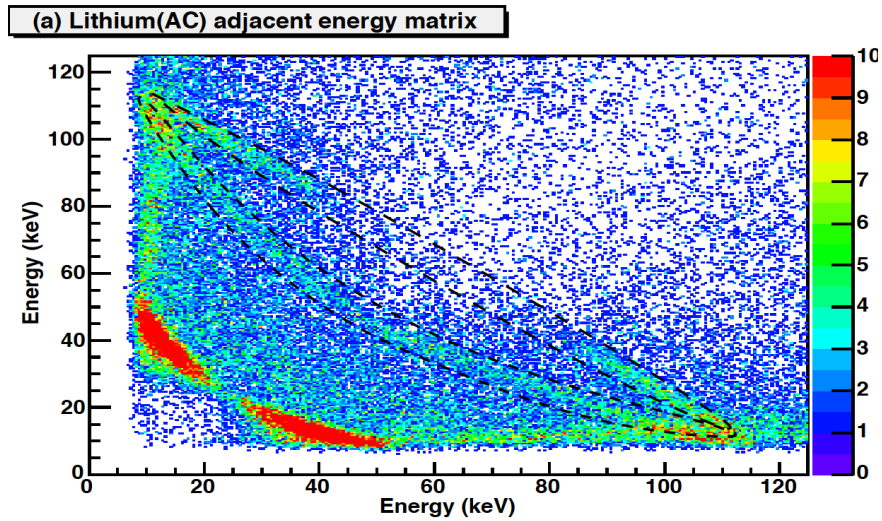
FIGURE 5.15: Energies of a fold 2 event from the GREAT planar detector for 59.5 keV and 122.1 keV incident gammas. The curved intensities present below the diagonal lines are a result of charge loss occurring in the fold 2 events [63].

response. Charge loss occurring for these neighbouring events would manifest as curved arcs beneath the straight lines. This was observed in the GREAT planar detector pictured in Figure 5.15. The lack of such features present within the HPGe studied here indicate that no, or negligible, charge is lost on the inter-strip gap and that potential charge loss observed previously in the ^{241}Am surface scan can be more confidently attributed to charge sharing events in which some measure of the charge falls below the low-energy threshold.
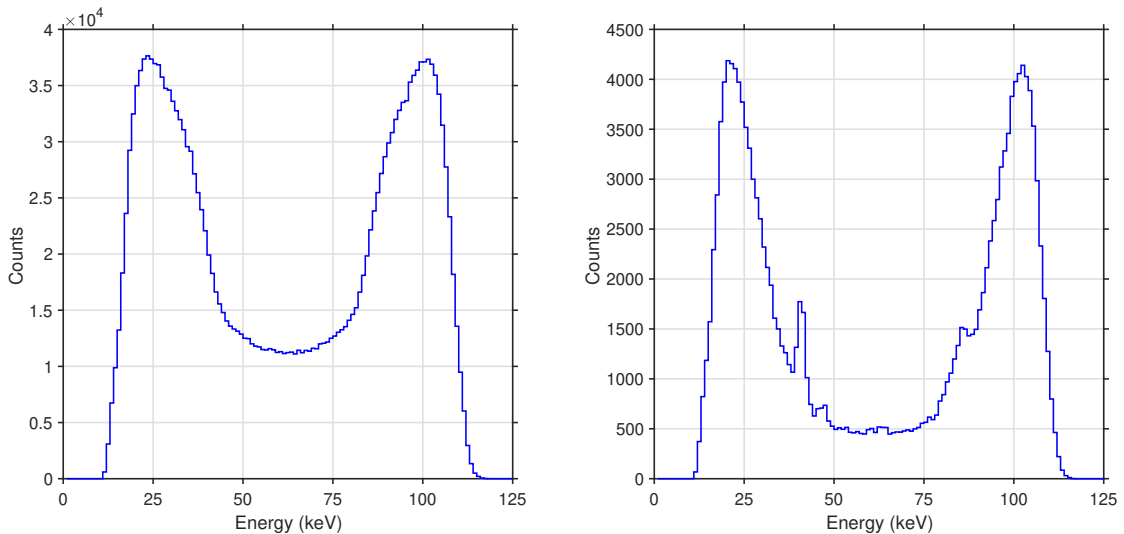
FIGURE 5.16: AC collected energies of a fold 2, 121.8 keV, event for neighbouring strips (left) and non-neighbouring (right) from a ^{152}Eu flood source measurement.

Fold 2 AC energies that pass an addback gate placed on the 121.8 keV photopeak were projected on to a single axis. This was done for the above case in which the charge collecting strip electrodes are adjacent as well as for a similar case in which

the charge collecting strip electrodes are separated by one or more strips. These are shown in Figure 5.16 left and right respectively. The 121.8 keV spectrum for adjacent strips (left) appears to follow the same observed effects as seen for the ^{241}Am surface scan in that local maxima are present that correspond to the energy depositions of a Compton scattered and subsequently absorbed 121.8 keV γ ray. For 121.8 keV the possible deposited energies for a scatter and an absorption fall between 0-39.3 keV and 82.5-121.8 keV. Those energies that are separated by a whole strip or more (right) show a decreased ratio of counts appearing in the forbidden region between the distribution present in the allowed energy deposition ranges. This is potentially indicative of the angle through which the γ ray has scattered as there are now geometric constraints on the possible angles due to the scatter and following absorption in a strip located at least 5 mm away. A notable feature is the peak at 40 keV and a corresponding smaller one at 82 keV, these are the result of a 40 keV x-ray from the ^{152}Eu source which was placed close to the detector face.

5.2   Cs-137 Side Scan

A side scan was performed in order to investigate the position sensitive nature of the pulses formed through the depth of the detector and thus characterise the rise time response through z-depth. A characterised rise time response can be used in parametric z-PSA methods to improve the position resolution through the 20 mm z-depth of the HPGe and therefore improve the image quality of the Compton camera system. These side scan data were also used to validate a simulated signal database, discussed in Chapter 6.

5.2.1   Scanning Set-up

A 1 GBq ^{137}Cs source was collimated through the use of a tungsten collimator to produce a beam of high-energy γ rays with which the side of the detector was scanned. The two-part tungsten collimator consisted of an initial 100 mm long insert with a 5 mm internal diameter followed by an 80 mm long, 1 mm internal diameter collimator with a 25 mm diameter and 5 mm thick flange. This ensured collimation of the isotropic source into a pencil beam and resulted in a maximum beam spot size due to beam divergence of 1.84 mm incident on the base of the HPGe active crystal volume at $y = 0$ mm and of 2.5 mm at $y = 60$ mm. The collimator was inserted into a lead block housing and the assembly mounted atop a precision Parker scanning table [65] which enabled movement x and y with an accuracy of 100 μm.

The detector cooler was mounted on a steel frame supported platform, suspending the detector cryostat and housed crystal above the collimated γ-ray beam as shown in Figure 5.17. This enabled a range of movement in x-z that encompassed the full 60×20 mm^2 base of the detector. The collimated source produced ~450 661.7 keV γ rays per second and was moved in 1 mm steps with a dwell time of 300 s at each position. The
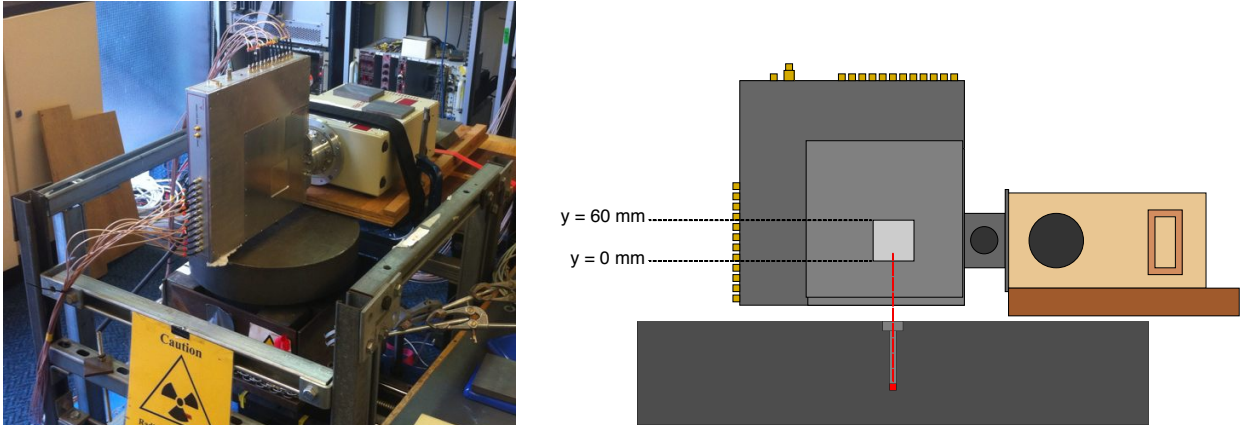
FIGURE 5.17: Photograph of the side scan set up with detector cryostat held above lead block containing the source and tungsten collimator (left) and a corresponding schematic diagram depicted from the side facing the detector window illustrating the collimated beam penetrating the bottom of the cryostat (right).

digital acquisition system used to record and save data was the same as that used for the surface scans and the GRI+ system and the BLD method was used for distinguishing real charge signals from noise.

5.2.2 Intensity Maps

Side scan intensity maps displaying the number of full-photopeak events as a function of collimator position were produced. The strip orientation is shown in Figure 5.18 (left). The DC strips are normal to the page numbered from left to right in ascending order and are located $z = 0$ mm while the AC strips, located at $z = 20$ mm, are parallel relative to the page and numbered 1-12 in increasing distance from the collimated source.

The intensity maps are displayed in Figure 5.18 for addback photopeak-gated (top right) and for photopeak-gated single-pixel F[1,1] (bottom right). The photopeak ad-dback gate was 8 keV wide and placed on the 661.7 keV ^{137}Cs photopeak. The full photopeak energy gated intensity map in Figure 5.18 (top right) shows a higher intensity of 661.7 keV events in the centre of the detector relative to the edges. This is due to the increase in scattering probabilities for 661.7 keV γ rays as opposed to the 59.5 keV from the surface scan and as such, γ rays that scatter near the edges are more likely to escape the detector. At 661.7 keV the cross section of photoelectric absorption is 2.6% that of Compton scattering [60] and so the domination of absorption interactions observed with [241]Am does not occur. Because of the high scatter probability the use of a fold gate does not preclude scatter events that occurred within a single pixel, though these were observed to constitute a small minority of the pulses as discussed in in Section 5.2.3. There is also a slight decrease in intensity in positions corresponding to the inter-strip gaps that becomes much more distinguished in Figure 5.18 (bottom right) when the F[1,1] gate is applied and all events occur within single pixels. The reduction present in F[1,1] gated events is due to multi-interaction events that scatter and are absorbed

within a single pixel and as such are more likely to occur centrally in a pixel than not. It is also possible that the charge sharing mechanism discussed previously contributes to this effect and causes a further reduction in F[1,1] events on the inter-strip gaps.

The reduction in counts when no F[1,1] gate is applied (top right) is due to the same low-energy tailing present in the ^{241}Am surface scan. This is shown in Figure 5.19, where the side scan intensity maps have been produced for all events in which energies above 10 keV are registered by both the AC and the DC strips (top) and for 661.7 keV addback in which the lower bound of the photopeak energy gate has been reduced to 650 keV. Uniformity of response is observed for all energy events bar two hot spots, located at $x = 13$ mm and $x = 27$ mm. These were produced due to a scanning system error in which the collimated γ-source dwelt for longer than the set time at these positions. When the photopeak gate was widened to include the low-energy tailing present in the system the effects of the interstrip gaps are no longer observed and the expected intensity distribution is produced.
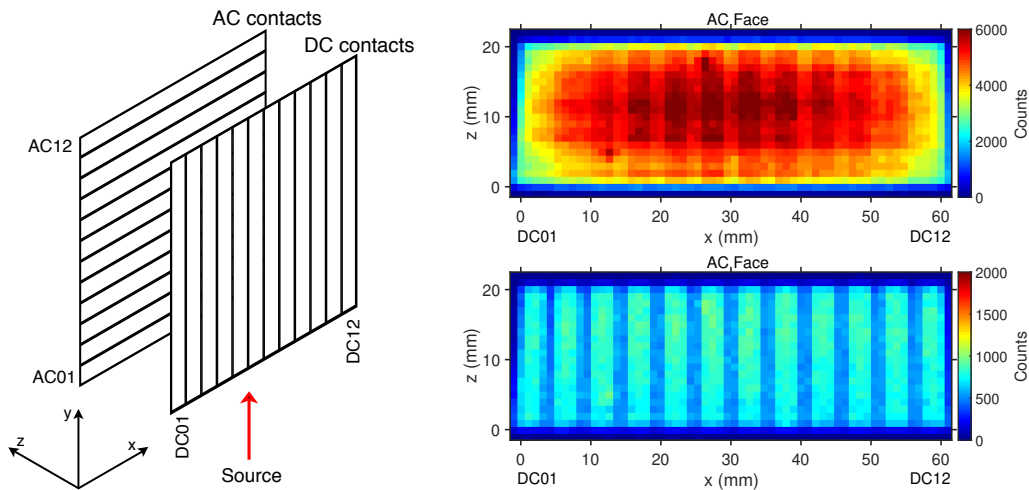
FIGURE 5.18: Schematic diagram of strip orientation and source location (left). Intensities of the side scan for 661.7 keV addback gated (top right) and 661.7 keV addback and F[1,1] gated (bottom right).

5.2.3 Rise Time Response

As described in Section 3.2.1, the time taken for charge collection to occur is a function of the distance through which the carriers have travelled. If the charge carrier rise time response through the detector 20 mm z-depth is understood then the depth of interaction for recorded events can be determined. To understand the rise time response through depth, the average rise times as a function of collimator position have been produced for T30 and T90. T30 has been investigated as it is representative of the charge collection time of the primary charge carriers for a given face and so highly position sensitive, while T90 is characteristic of the total charge collection time for all carriers in the system. These rise time maps are displayed in Figure 5.20. The T90 maps are displayed for the
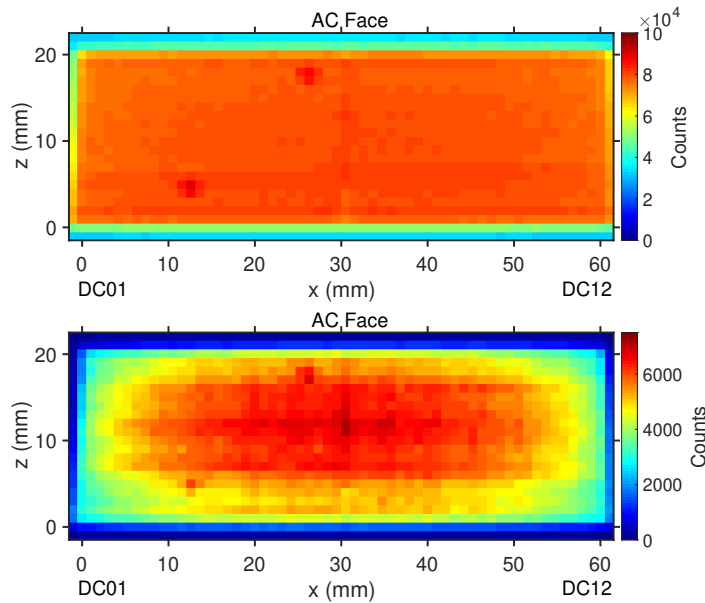
FIGURE 5.19: Intensity map from the side scan for those events that register above 10 keV on the AC and DC strips (top) and for those that pass a widened addback photopeak gate of 650-665 keV (bottom).

AC charge collection (a) and the DC charge collection (b) along with T30 maps for the AC charge collection (c) and the DC charge collection (d). Positions at which at least 100 F[1,1] events passed the addback energy gate were included in the maps.
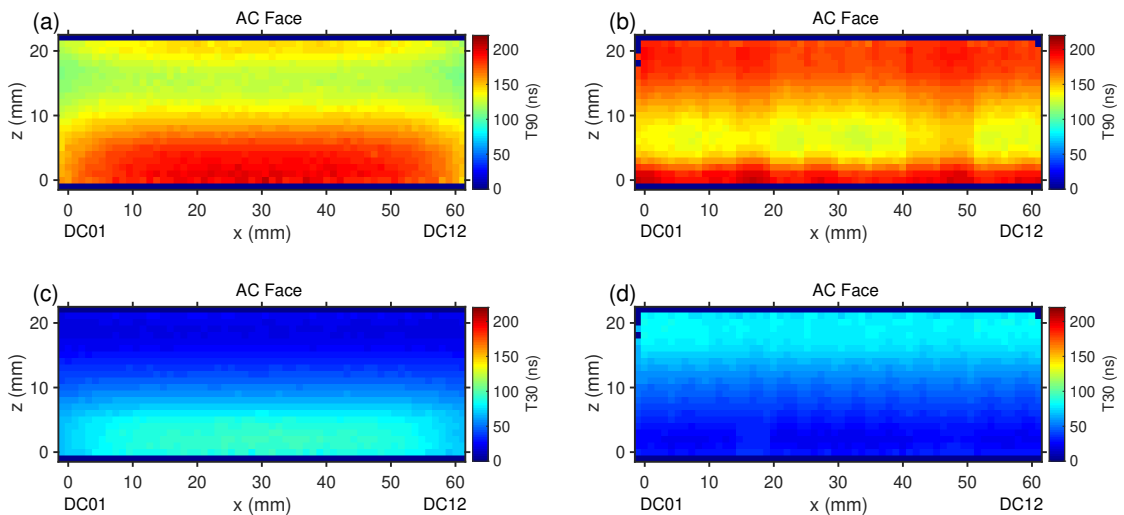
FIGURE 5.20: Rise time maps produced from a ^{137}Cs side scan for the AC T90 charge collection (a), the DC T90 charge collection (b), the AC T30 charge collection (c), and the DC T30 charge collection (d).

The T90 times in Figure 5.20 (a and b) show charge collection times that are fastest at distances of ∼5 mm from the collecting strips. This is representative of the weighting fields within the detector. Due to the 20 mm thickness and 5 mm wide contacts, the charge collecting strip electrodes are sensitive to the movement of carriers throughout the entire *z*-depth. The fastest charge collection times therefore occur at points where

the collection time for both sets of carriers is minimised. It would be expected that this point be slightly offset towards the h^+ collecting AC face due to their slower mobility relative to e^- [27]. This is difficult to observe in these maps and instead is discussed more in Section 5.3.2. The T30 rise times in Figure 5.20 (c and d) show the position sensitive nature of this parameterisation. Fast rise times are observed close to the charge collecting face for the primary carriers while slow collection times are observed when the carriers must travel the 20 mm z-depth. In both the T30 and T90 rise time maps the variation in collection time between a strip centre and a strip end is seen for the AC charge collection. It is only observed in the AC map due to the strip orientation relative to the incident γ-beam. Likewise, due to strip orientation, the variation in T90 rise times between strips for a given face is observed in the DC charge collection times.

In order to use these interactions for the characterisation of rise times through z-depth there must be confidence that multi-interaction events that occur within a single pixel do not contribute. These types of events cannot be simply parameterised as they are a convolution of two charge collection signals. To achieve this for the charge collection pulses, an average signal was formed for each strip at each x-z collimator position. Signals were time aligned to t10 and included in the formation of the average if they passed the photopeak energy gate. To exclude those that were formed of multiple interactions within a single pixel, a Root-Mean-Square Deviation (RMSD) from the mean was calculated. This was done by comparing the average signal at each x-z position with each individual constituent event. Creation of a cut-off threshold for events could therefore be used to exclude those that deviated from the average by too much. The RMSD histograms of AC06 and DC06 are shown in Figure 5.21. A 0.02 threshold was chosen for this work and is displayed in red.
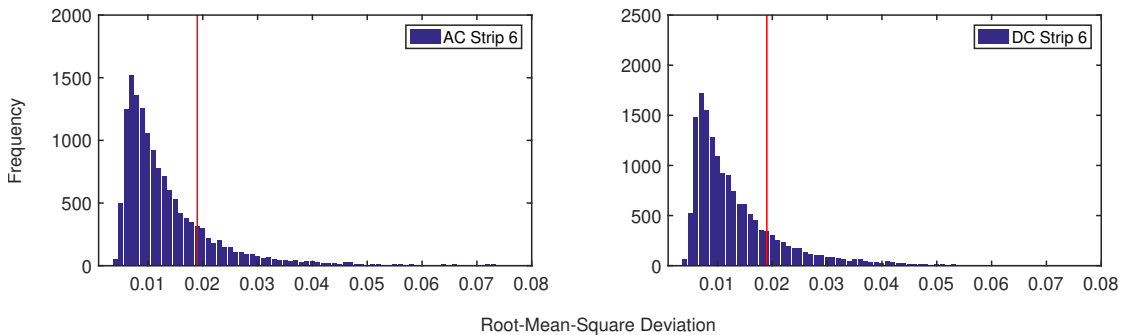
FIGURE 5.21: RMSD for AC06 and DC06 between average signal for each x-z position and each interaction constituent event. The vertical red line represents the cut-off point with all events to the right not included in further analysis.

To demonstrate the effectiveness of this method, the average signals at a selected x-z mm position are shown in figure 5.22 for strips AC06 (left) and DC06 (right) along with pulses that were accepted by the RMSD cut in blue and those rejected in red. The average signal is shown in green. It is observed that only a small amount of those signals rejected appear to be constructed of scatter and subsequent absorption events. Few are produced due to the confinement already implemented through the use of single-pixel
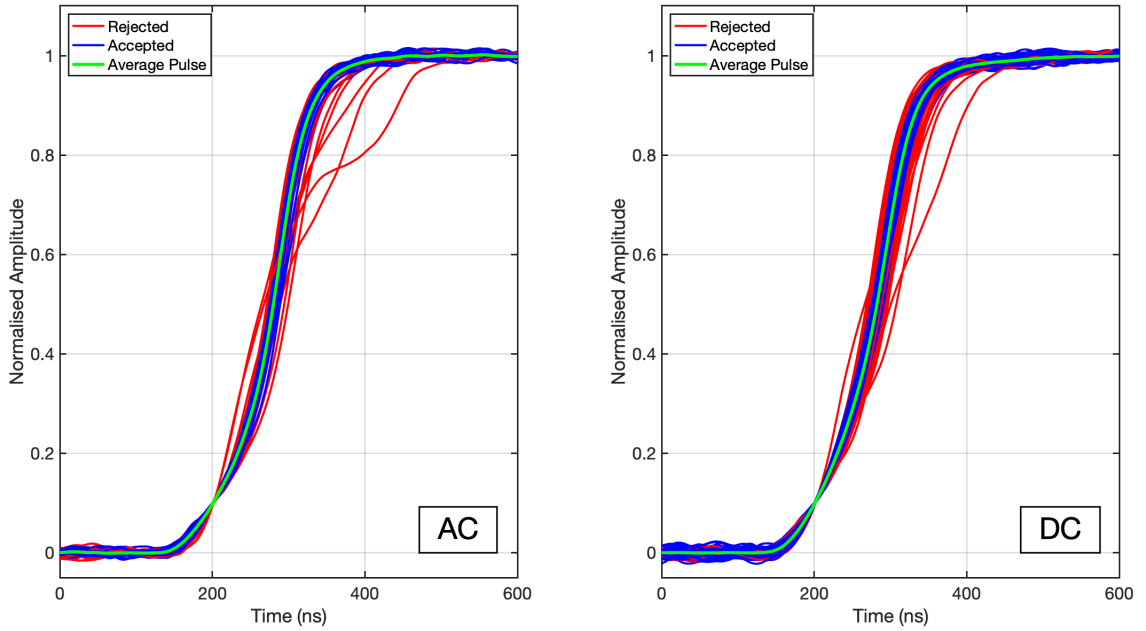
FIGURE 5.22: 661.7 keV charge collection signals that pass (blue) or fail (red) the RMSD cut when compared against the average signal (green).

events. The scattering angle of 661.7 keV γ rays is predominantly forward focused and so a forward scattered γ ray would, at maximum, have only the 5 mm pixel width to travel before entering another pixel and registering as a fold 2 interaction. The majority of rejected signals are those of full charge collection in a single interaction but are rejected due to deviation from the average signal for each face. This large deviation from the mean occurs due to the change in signal shape along the length of a strip as observed in the surface scan. The larger deviation from the mean is observed in the DC signals due to the strip orientation relative to the collimated beam. γ rays may occur along the full DC strip length for a fixed x-z position but only across the width of an AC strip and so a larger deviation is seen. Average charge collection signals at each z-position were formed following the RMSD cut for each x-z position. These are displayed in Figure 5.23 for strips AC06 (left) and DC06 (right). The signals have been interpolated to 1 ns and aligned to t10, 10% of the normalised pulse amplitude, to better display the variation in pulse shapes.

The t10 alignment was chosen for presentation as it is the point from which T30 and T90 are measured and illustrates the difference in signal shapes between the two charge collecting faces. The blue pulses represent collimator positions close to the DC strips, located at $z = 0$ mm, while the purple pulses represent positions close to the AC contacts, at $z = 20$ mm. The overall range of shapes is similar between the two sets of signals, though differences can be observed. These are in the first 10% of the signal shape and in the final part of the DC signal leading edges which occur at positions 5 mm or less from the associated charge collecting strip electrodes. The prominent curvature
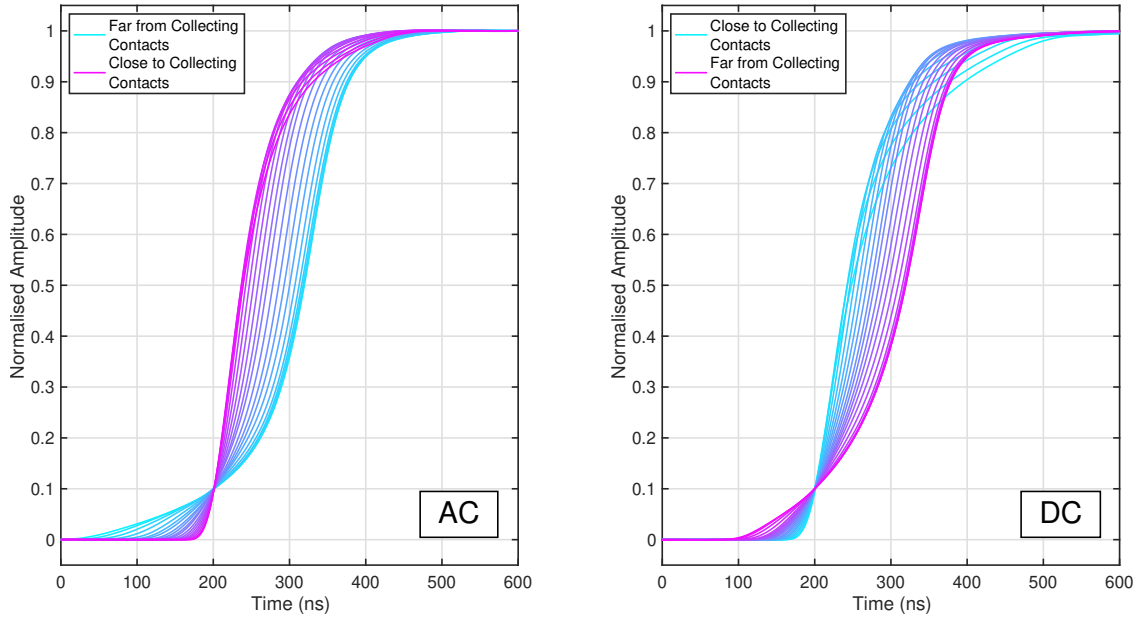
FIGURE 5.23: Average charge collection signals that pass an RMSD cut aligned at t10 through depth from AC06 (left) and DC06 (right).

in final half of the DC charge collection at these positions is shaped by the collection of the h^+ at the AC face. This corresponds to the slower h^+ drift velocity causing increased times for full charge collection at these positions. The effect is not seen in the final part of the AC signals at positions close to the AC contacts and far from the DC contacts due to the faster e^- drift velocities.

5.3 Parametric PSA Optimisation

The scan data taken have been used to understand and characterise the signal response at the detector surfaces as a function of x-y position, and also through depth as a function of x-z position. This has allowed the formation of average signals at constrained positions within the detector. These average signals have been investigated in order to understand how well the parametrisation of a pulse into a simple set of values represents the charge collection properties of the detector. It also reveals the level of sensitivity to change that can be achieved with parametric PSA methods. Once understood, parametric PSA methods can be confidently applied to experimental data to improve the image quality of the GRI+ system.

5.3.1 Image Charge Response

The image charge asymmetry parameterisation described in Section 3.2.1 is a well understood process that has been previously applied to geometrically similar HPGe strip detectors [49]. The ^{241}Am surface scan data have been used to verify that the image charge response as a function of position allows the same methods to be applied. Average charge collection signals and neighbouring average image charges, produced in

Section 5.1.4, are displayed in Figure 5.24 for strips AC06 and DC06 at a range of AC surface scan collimator positions. The positions have been selected to highlight the image charge magnitude change across strip widths, and so cover 1 mm steps through y at $x = 30$ mm to highlight the AC response and 1 mm steps through x at $y = 30$ mm to highlight the DC response. Small variation is seen in the charge collection pulse while the image charges vary in magnitude between 8% and 16% of the normalised height for the near-side AC strips and between 14% and 26% for the far-side DC strips. The smallest sensitivity to changing collimator position observed in the image charge magnitudes occurs when the interaction is happening furthest from the image charge sensing strip and the image charges are at their smallest. These trends are also observed when considering the equivalent plots produced from the DC surface scan data. As the image charge magnitudes and signal shapes are found to be sensitive to γ-ray interaction position they can be employed in x-y PSA methods.
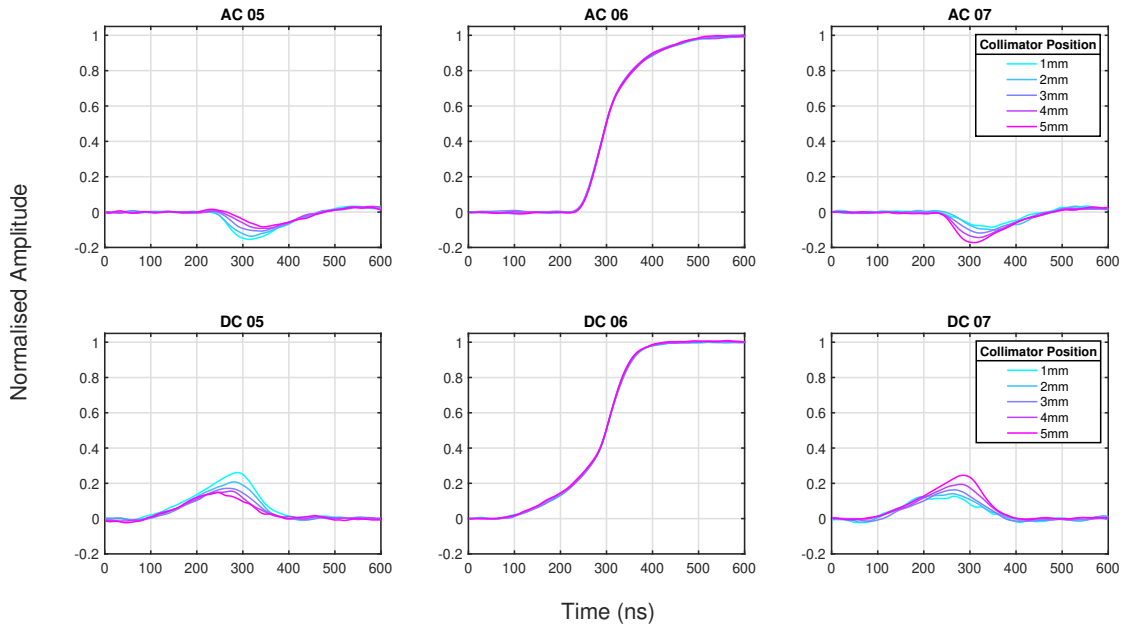
FIGURE 5.24: The average charge collection signal and neighbouring transient image charges for 5 collimator positions across the width of AC06 (top) and DC06 (bottom).

The surface scan revealed that the parameterised rise times varied along the lengths of strips; with maxima occurring at the centres and minima at the ends. As parameterisation of the signal between 1% and 99% of its amplitude yielded constant rise times in x-y, it was attributed to changing charge collection signal shapes. To investigate whether the transient image charge shapes and amplitudes were affected by this, average charge collection signals and neighbouring image charges were produced for a range of positions along a strip centre. The average signals from AC06, aligned at t50, are displayed in Figure 5.25 for collimator positions along the length of the strip. The γ rays were incident on the DC contacts and so the h^+ carriers travelled the full 20 mm z-depth before collection at the AC strip electrodes. The range of positions was chosen to highlight the changing signal shape at positions close to the end of the strip. Signal

shapes at the strip centre were consistent with those observed 16 mm from the strip end. Alignment of the charge collection signal was chosen to be 50% of the amplitude as it displays the variation in the first ~30% of pulse. The start and end points of the signal, t01 and t99, are at the same points resulting in constant total charge collection times. The primary h^+ charge carriers, collected in the first 30% of the pulse, are found to be responsible for the rise time variation found when parameterising the signals. At positions corresponding to the strip ends they are collected more slowly than in the strip centres, this results in parameterisation reporting faster rise times. The corresponding image charges produced are found to be smaller at the strip ends than at the centre. It can be concluded that the pulse shape variation along the length of the strip does not affect the parameterisation of neighbouring image charges. As the image charges on each neighbouring strip change in magnitude equally at each point along the strip, the asymmetry parameterisation used and discussed in Section 3.2 is not affected.
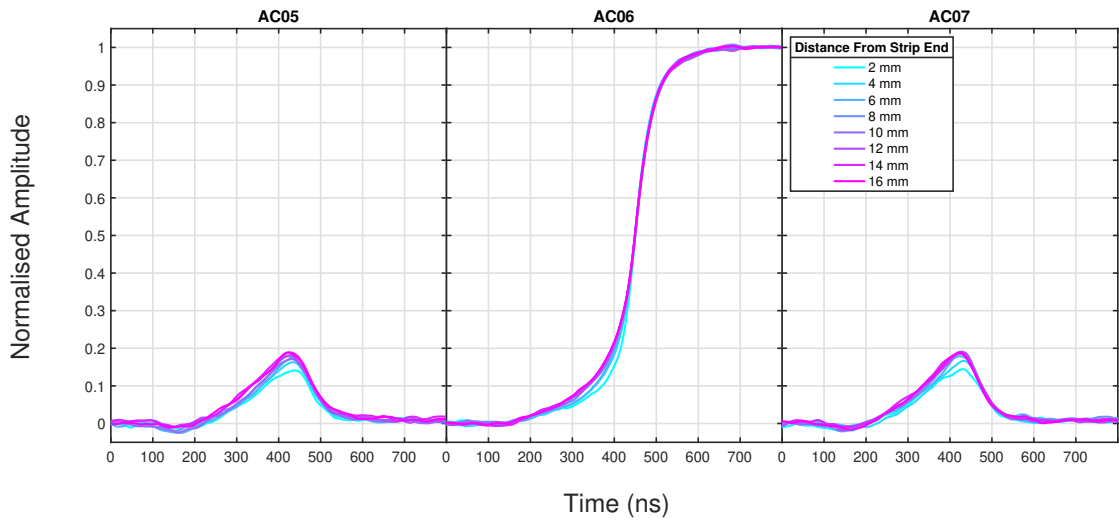
FIGURE 5.25: Average pulses and neighbouring transient image charges produced in AC06 for a range of collimator positions along the central length of the strip.

5.3.2 Pulses through Depth Response

To develop and apply z-PSA methods, the rise time response through the 20 mm depth of the detector must be characterised. The average signals from all strips at each z-depth mm position, produced following the method in Section 5.2.3, have been parameterised into T30, T50, and T90 values. The T30 and T90 profiles are displayed in Figure 5.26 for AC06 and DC06. Error bars represent the standard deviation of rise time values for that strip at each depth position. The collimator position is relative to the DC contacts, at which the T30 values are correspondingly small at around 10 ns for DC06 and relatively large at around 20 ns for AC06. The variation in rise times for T30 collection is largest at those points where the charge carriers must travel the bulk of the detector and smallest close to the respective charge collecting strip electrodes. This is most clearly seen in the AC h^+ collection, which has a large standard deviation of

20 ns at positions close to the DC contacts. The largest T90 variation of around 30 ns corresponds to positions close to the DC contacts and the smallest closer to the AC contacts for both sets of charge carriers, the reason for this is unknown. There is also a lack of position sensitivity present in T30 values close to the charge collecting contacts for both the AC and DC collection. This affects its suitability as a parameter for determining position of interaction in z-depth at these positions.

If the linear portions of the T30 collection times are quantified they can offer a basic form of z-PSA in which the detector is divided into sections. The gradient of this linear component gives an indication of the sensitivity to position that these methods offer. For the AC T30 collection it is found to be 6 ns per mm and for the DC collection it is 4 ns per mm. This sensitivity is fairly low given the variation in rise times that occur. A feature of note is the point at which both sets of charge carriers are near-fully collected in the same amount of time, corresponding to the AC and DC T90 crossing point. It would be expected that, due to the difference in charge carrier saturated drift velocities discussed in Section 2.2.2, the point of equal collection times would occur offset from the centre towards the face collecting the slower h^+ charge carriers. This was observed by Boston *et al.* [18] for the geometrically-similar planar SmartPET detector. For the HPGe studied in this work it is believed to be indicative of the information lost during parameterisation between t10 and t90 only. This is discussed in more detail later in this section. The T90 charge collection times are overall slightly slower for the total DC collection than for the AC collection, with the slowest rise time occurring at positions close to the DC contacts. It would be expected that the slowest charge collection time occur close to the DC contacts, as this is the point at which the h^+ carriers must drift through the entire 20 mm z-depth before collection. Again, this is representative of the t10 to t90 parameterisation.
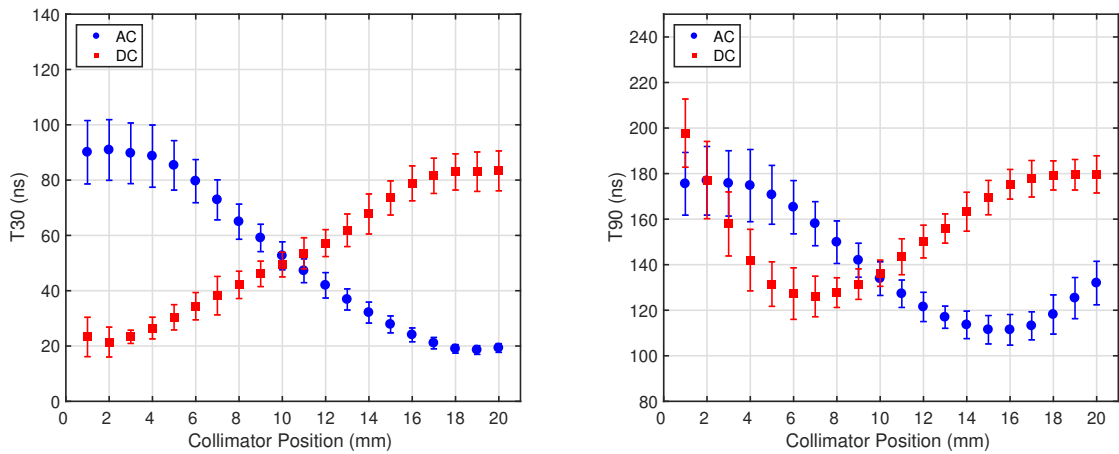
FIGURE 5.26: T30 and T90 parameterisation of AC06 and DC06 through depth. The collimator position is relative to the DC contacts such that the AC contacts are located at 20 mm.

A method of depth-of-interaction determination, previously employed in the Smart-PET germanium detectors [54], utilises a matrix of T30 versus T90. Gating upon areas

of the intensity matrix can be used to divide the detector z-depth into subsections. For the detector studied in this work a matrix of T30 versus T90 is displayed in Figure 5.27 for AC06 (left) and DC06 (right). It comprises all F[1,1], full photopeak events recorded during the side scan. For both the AC and the DC matrices a tick shape is formed from T30 against T90. The tick produced from AC06 shows a high intensity of counts for fast T30 rise times and between 100 and 150 ns T90 rise times. The DC tick shows a larger intensity of counts at slower T30 times, between 40 and 100 ns, with corresponding T90 times of between 125 and 190 ns. The tick was investigated as an initial z-PSA method to improve the position resolution through z-depth. Due to the large variation of T30 and T90 values found at each depth, as evidenced in Figure 5.26, it was found that the best improvement that could be achieved through this method was to take 4 subsections of the tick. Gating upon these subsections provided a depth of interaction position resolution of 5 mm, an improvement on the 20 mm physical voxel size. As the number of subsections that could be gated on could not be increased further, other methods of z-PSA were pursued and are discussed later in this section.
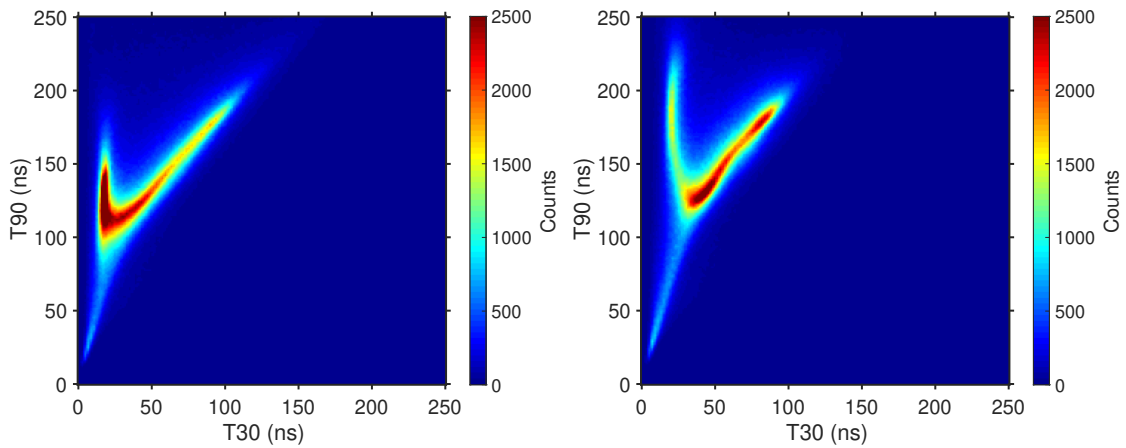
FIGURE 5.27: T30 versus T90 for AC06 (left) and DC06 (right) for all side scan events.

Before z-PSA methods were explored further, the effect of parameterisation between t10 and t90 through z-depth was investigated. It was observed in the surface scan data in Section 5.1.4 that such a parameterisation could result in misrepresentation of the pulse rise times due to a loss of information. A parameterisation was performed on the average pulses through depth between t01 and t99; the time taken between 1% to 99% of the total pulse amplitude to be reached. It was possible to interrogate these values due to the averaging of many pulses and would not typically be visible due to the presence of noise in the signals. The t01-t99 rise times as a function of collimator z-position are shown for AC06 and DC06 in Figure 5.28. This more accurately represents the time for total charge collection in the detector. In this figure the longest charge collection times are now observed to occur for the AC h^+ collection and positions close to the DC contacts, located at 1 mm. The point of equal rise time is shifted 1 mm closer to the AC h^+ collecting strips when compared to the T90 parameterisation in Figure 5.26.

Large sensitivity is also seen in the first and last few mm of the detectors for both charge carrier collection times.

A unique and linear t01-t99 rise time value can be found for all 20 mm z-positions if a combination of AC and DC charge collection times are used. The gradient of this linear component is quite large, 16 ns per mm for the AC collection and 9 ns per mm for the DC collection. If it were possible to parameterise between 1% and 99% of a typical experimental pulse then this method would be an excellent technique for providing depth-of-interaction information. A further plot, parameterising the collection time between 1% and 30%, was created and is shown in Figure 5.29. A linear gradient is again observed through the entire detector z-depth if a combination of AC and DC charge collection is used. A sensitivity, represented by the gradient, is found to be 14 ns per mm for the AC collection and 7 ns per mm for the DC collection. Following this, a recommendation can be made that future work attempt to utilise these parts of the signals that offer high rise time sensitivity at all points through the detector.
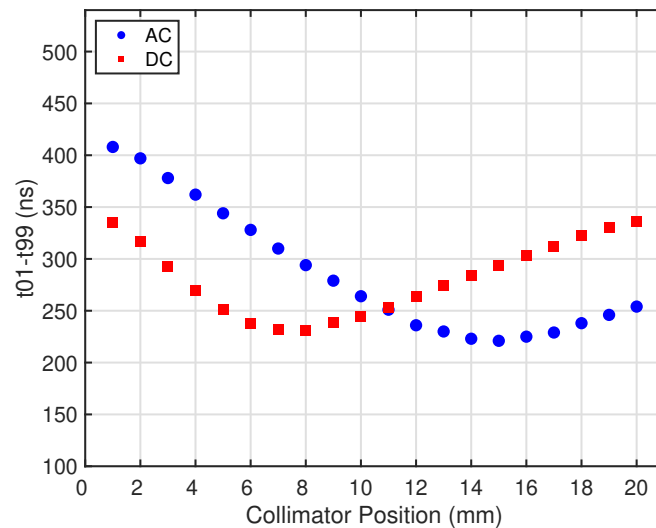
FIGURE 5.28: Parameterisation of pulses through depth between 1% and 99% of the total charge collection. The collimator position is relative to the DC charge collecting strip electrodes such that the AC strips are located at 20 mm.

In the surface scan rise time maps a large variation was observed in T90 between strips on a given face. A smaller variation was also observed in T30. This was also looked at prior to z-PSA optimisation. The T30 and T90 rise times as a function of collimator z-position were produced for each of the 24 strips and are displayed in Figure 5.30. The difference in rise times present for a given face is small when considering the T30 parameterisation, though it is largest close to the DC contacts. The T90 rise times vary by up to 20 ns for strips on a given face though the largest variation is close to the AC contacts.

This variation between rise times for strips on a given face, as well as the lack of rise time uniformity along a strip's length, has led to an implementation of z-PSA in which the rise times are characterised for each pixel through depth. In this manner,
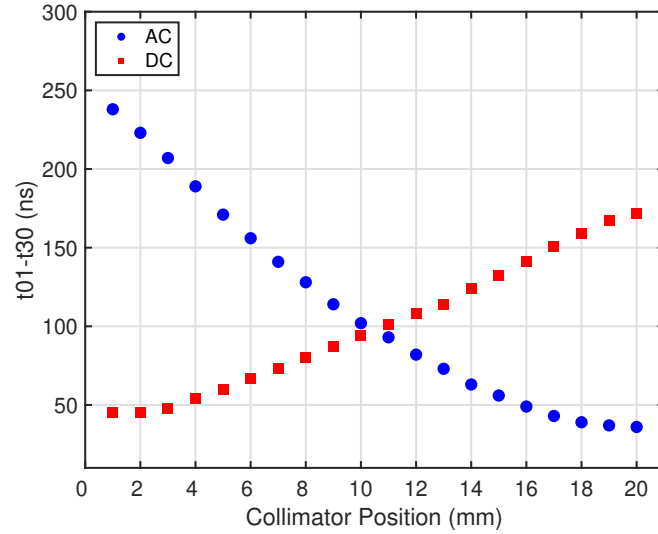
FIGURE 5.29: Parameterisation of pulses through depth between 1% and 30% of the total charge collection. The collimator position is relative to the DC charge collecting strip electrodes such that the AC strips are located at 20 mm.
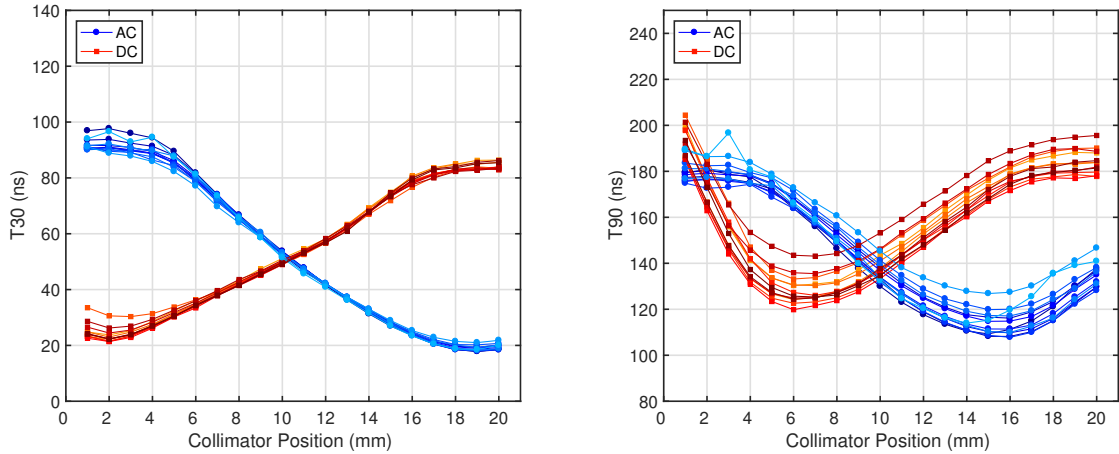
FIGURE 5.30: T30 and T90 rise times for all 24 strips through z-depth. The collimator position is relative to the DC contacts such that the AC contacts are located at 20 mm.

instead of a strip being represented by a single T30 or T90 value, it is represented by 12 values, corresponding to the pixels formed with the 12 orthogonal strips on the far face. This creates, for each rise time parameterisation used, $12{\times}12{\times}20$ values and so sub-divides the detector into $5{\times}5{\times}1$ mm^3 rise time voxels. The z-PSA applied in this work is a χ^2-minimisation based method that makes use of T30, T50 and T90. These parameterisations were chosen as they provide sensitivity through the full 20 mm z-depth. T30 and T50 are of similar profiles with a linear component through most of the detector bulk but a lack of sensitivity near the contacts. T90 provides good sensitivity close to the contacts but cannot be used by itself due to non-unique values present through z-depth. A χ^2-minimisation is made between an experimental signal rise times and the parameterised rise times for each collecting face. The values compared were dependent on the pixel in which the interaction occurred and the best match in

z-depth was found. The effectiveness of this method was verified through an observed improvement in the resolution of reconstructed images, which can be found in Chapter 9, and through comparison to the collimated side scan data which is demonstrated here. Individual experimental signals from known collimator z-positions were analysed with the z-PSA method and the difference between the found position and the collimator position histogrammed. The experimental signals compared were those that passed the RMSD check in Section 5.2.3 and were so confirmed to be single interactions. The results of this are displayed in Figure 5.31 (top) for all collimator positions and in Figure 5.31 (bottom) from 4 mm subsections of the detector z-depth.

When considering the entire 20 mm z-depth, the performance of z-PSA is found to be good. In total, 48.3% of the events analysed are placed at the same z-position as the collimator and another 40.3% at ± 1 mm from the collimator z-position. In total, 95.5% of analysed events are placed ≤ 2 mm from the collimator z-position. Divergence of the collimated beam could account for some events occurring 1-2 mm away from the collimator. When subsections of the 20 mm z-depth are considered it can be seen that z-PSA is effective at all depths. For every 4 mm subsection, ~40-50% are placed at the same z-position as the collimator. This represents a high accuracy for the employed z-PSA method through the entire 20 mm z-depth of the detector when compared to side scan data. Some of the effectiveness of this method can be attributed to over-fitting of the data for this comparison. The comparison has been performed on the same data that were used to produce the characterised z-PSA rise times at all positions. It is expected that the actual application of this method would not be as effective as displayed here, but nonetheless it can be stated that a high accuracy is achievable with z-PSA through the entire 20 mm z-depth of the HPGe detector.
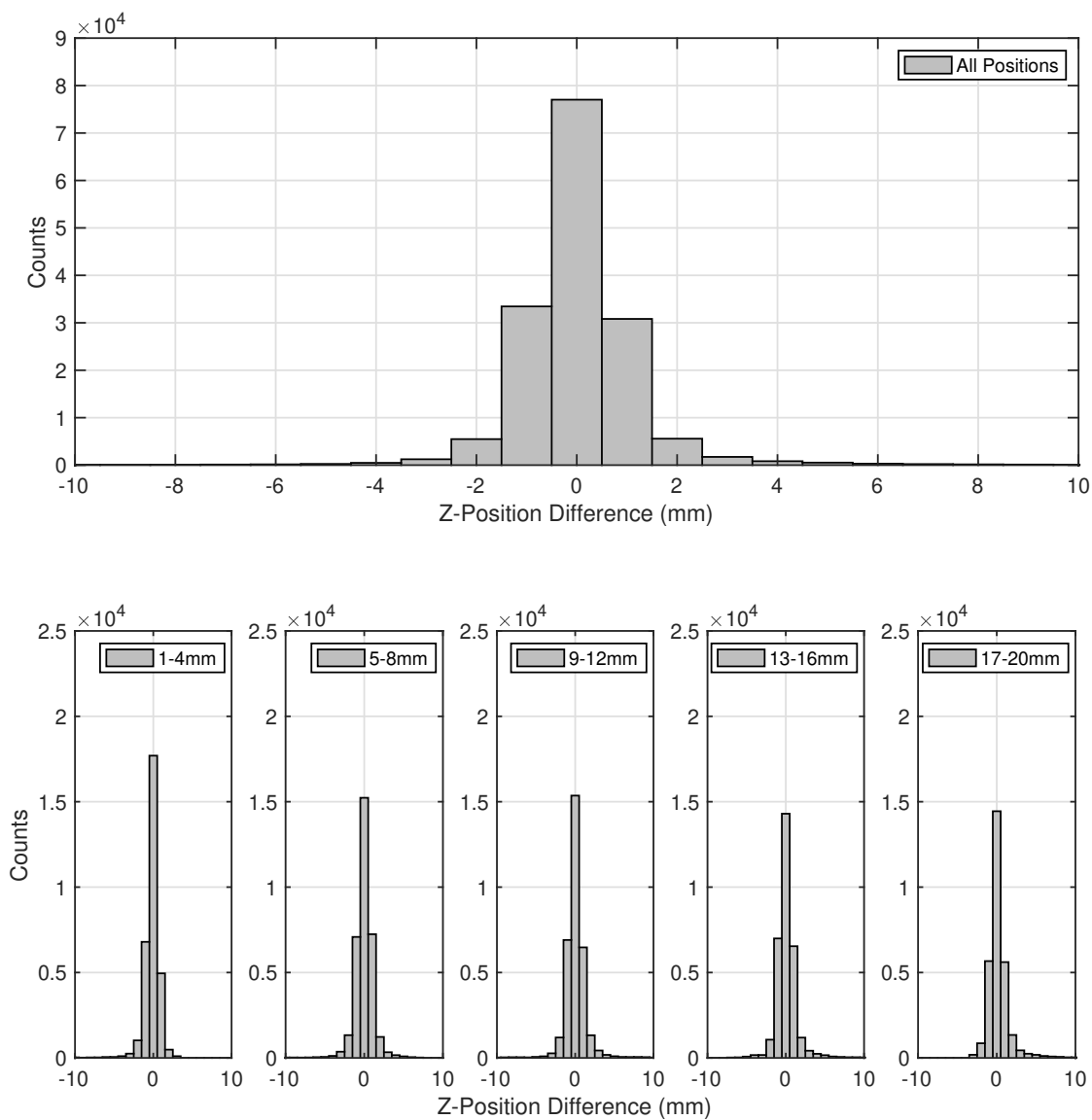
FIGURE 5.31: Histogram of the difference in mm between the known collimator position and the position found through the χ^2-minimisation z-PSA method from all positions (top) and for subsections of the z-depth (bottom).

Chapter 6

Detector Simulation

The image resolution of a Compton camera is dependent on several factors, such as the energy resolution, Doppler broadening, and the position resolution of interactions within it. The intrinsic position resolution is a result of the size of the voxels formed by the orthogonal segmentation of the detector faces and as such for the HPGe is $5{\times}5{\times}20$ mm^3. This was improved in the previous chapter through the implementation and optimisation of parametric PSA, which improved the position resolution in both the widths of the strips and the 20 mm depth of the detector. Parametric PSA is a computationally inexpensive and "online" method of PSA in that it can be performed and applied as the data are taken with very few computational resources. The work following the characterisation of the HPGe detector has focused on a more computationally intensive "near-live" method of PSA that overcomes some of the limitations of parameterisation PSA and is known as signal database comparison PSA. This method of PSA can be performed as the data are recorded, but to do so requires PSA farms of computational resources.

The database of pulses used for this method of PSA can be produced experimentally using an (x, y, z) position sensitive coincidence scan set-up to record average pulses for a range of positions covering the active detector volume. To do such a measurement is a long process with every position within a volume on the chosen granularity requiring many events to form a reliable average. The set-up costs to create such a coincidence scanning system can also be prohibitive. Progress has been made in performing these measurements using a faster pulse shape comparison method [50], but the process is complex. A desired database of signals on a 1 mm cubic grid for the HPGe detector studied in this work would consist of 72,000 positions and producing experimental signals at each of these is not feasible. Instead, the work performed herein has relied on the simulation of a pulse signal database and subsequent validation at selected points. Often this method is employed with coincidence scanning in which only select points are validated. Simulation of the signal database required the solving of the electric and weighting potentials specific to the detector geometry followed by the simulation of interactions and subsequent charge carrier trajectories that induced the signals at the electrodes for each generated position within the detector volume.

6.1 The AGATA Detector Library

For the HPGe detector the simulation process was carried out using the AGATA Detector Library (ADL) [21], a C based simulation package developed at the Institut fur Kernphysik der Universität zu Köln by Bart Bruyneel and Benedikt Birkenbach. Other simulation packages exist in the MATLAB based Multi Geometry Simulation code (MGS) [66] and the Java AGATA Signal Simulation toolkit (JASS) [67]. ADL was chosen for this work as it comes with pre-defined geometries including a simple planar detector that was adapted to that of a multi-strip planar detector in previous work by Jon Wright [68] and was improved upon to represent the HPGe detector studied in this work better.
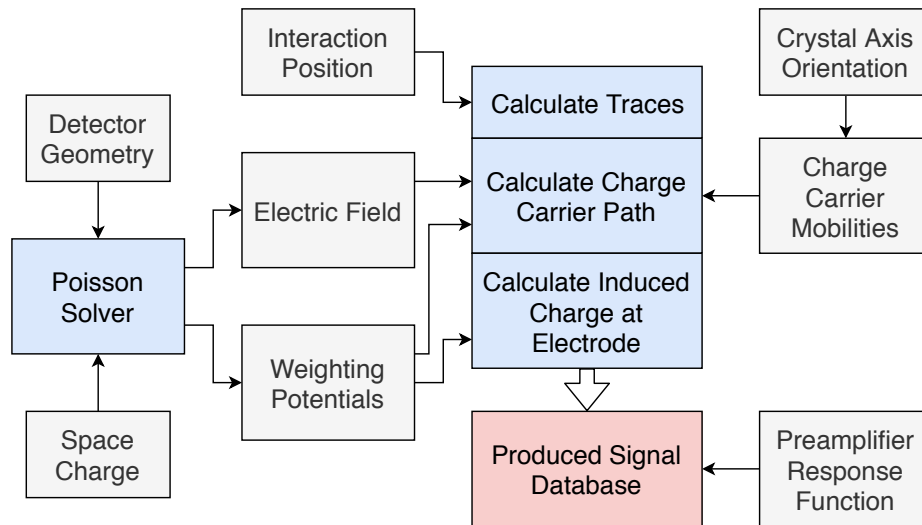
FIGURE 6.1: Block diagram representation of the ADL simulation process. User input parameters at each stage shown in grey and the inbuilt ADL processes in blue.

The workflow of ADL is shown as a block diagram in Figure 6.1. The ADL in-built routines are displayed in blue while the grey boxes represent input parameters for the different steps and are chosen by the user. The first step utilises a Poisson solver to solve the electric and weighting potentials analytically or numerically within the detector on a mesh defined by the user. The input for this step is the detector geometry and the space charge present in the detector. The weighting potentials are output and used to calculate the signal traces in a 3-part routine that starts with an initial interaction site chosen by the user. From this it calculates the charge carrier trajectory using the electric field, weighting potentials and the crystallographic axis determined charge carrier mobilities. As space charge is not used for calculating the induced signal, the weighting potentials and the charge charrier paths are used to calculate and record the signals for each of the defined electrodes which are then output into the simulated pulse database for that position. ADL has inbuilt routines to account for the front end electronic effects present in a physical system but they were not employed in this work and instead the electronics were accounted for separately and the raw signals were output from ADL.

6.2 Electric Field Simulation

As described in Section 2.3.1 the electric potential within a detector, and therefore the electric field, are calculated through the solving of Poisson's equation. The segmented strip detector used in this work is close to a symmetric planar detector but the nature of the orthogonal strip electrodes on each face meant that a more complex solution was required than solving the potential for a 2-D plane within ADL and then extrapolating to 3-D. As such, an analytical solution could not be applied and the equations were solved numerically through a finite differencing technique. The solution to this on a defined cubic grid is found through Successive Over Relaxation (SOR) [69] in which each grid point representing active material on the defined mesh is taken as the average of its 6 nearest neighbours plus a contribution from the SOR method. This is repeated until the change in value between iterations reaches a small enough value that is user defined and in this work was chosen to be compatible with the computing power utilised.

Variable	Value
AC Strip Width	4.75 mm
AC Inter-Strip Width	250 μm
DC Strip Width	4.7 mm
DC Inter-Strip Width	300 μm
Guard Ring Width	7.5 mm
Detector Depth	20 mm
AC Impurity Concentration	0.70 $\times 10^{10}$ cm^{-3}
DC Impurity Concentration	0.85 $\times 10^{10}$ cm^{-3}
Contact Thickness	1 μm

TABLE 6.1: Variables used to define detector geometry within ADL.

The mesh chosen to perform the calculations on was a 0.2 mm cubic grid and this was also used to define all aspects of the detector geometry. ADL was run within a virtual machine with only 8 GB of available memory and so this was the best granularity possible. In future work a simulation on a 0.1 mm grid would better represent the contact thicknesses and differences in inter-strip widths and would be feasible with more computational memory. Input parameters used to define the geometry were those described in Section 4.1.2 and are summarised in Table 6.1. The impurity concentrations provided by the manufacturer were the values recorded at the charge collecting electrodes and so a linear impurity gradient was then modelled through the detector. This impurity gradient informed the simulation of the space charge present at each point within the detector volume and as such, the equations presented in Section 2.3 are no longer valid as Equation 2.8 could not be equated to zero. Instead the space charge density was taken into account for all points within the detector and the electric potential was calculated as

$$\frac{d^2\Phi}{dx^2} + \frac{d^2\Phi}{dy^2} + \frac{d^2\Phi}{dz^2} = \frac{-\rho(x,y,z)}{\epsilon_r}, \tag{6.1}$$

where $\rho(x, y, z)$ is the position dependent space charge density, Φ the 3-D electric potential and ϵ the relative dielectric constant of germanium. The operational bias of the detector was implemented as a boundary condition for the solution of the electric potential and so -1800 V was applied to one set of electrodes and 0 V to the far face of orthogonal electrodes. The electric potential was solved using the SOR method on the chosen mesh and results are displayed in Figure 6.2 for an *x-y* slice through z (left) and a *x-z* slice through y (right) in volts. The *x-y* slice is taken in z at 2 mm distance from the DC electrodes and the colour scale selected in such a way as to demonstrate the slight variation in electric potential due to the strip electrodes present while the *x-z* slice shows the full variation of the electric potential field through depth from the -1800 V biased AC electrodes at $z = 0$ mm to the grounded DC electrodes at $z = 20$ mm. The uniformity of the potential in x is shown and there are no evident field variations towards the detector edges due to the modelling of the guard ring in the detector geometry, which has been excluded from these plots.
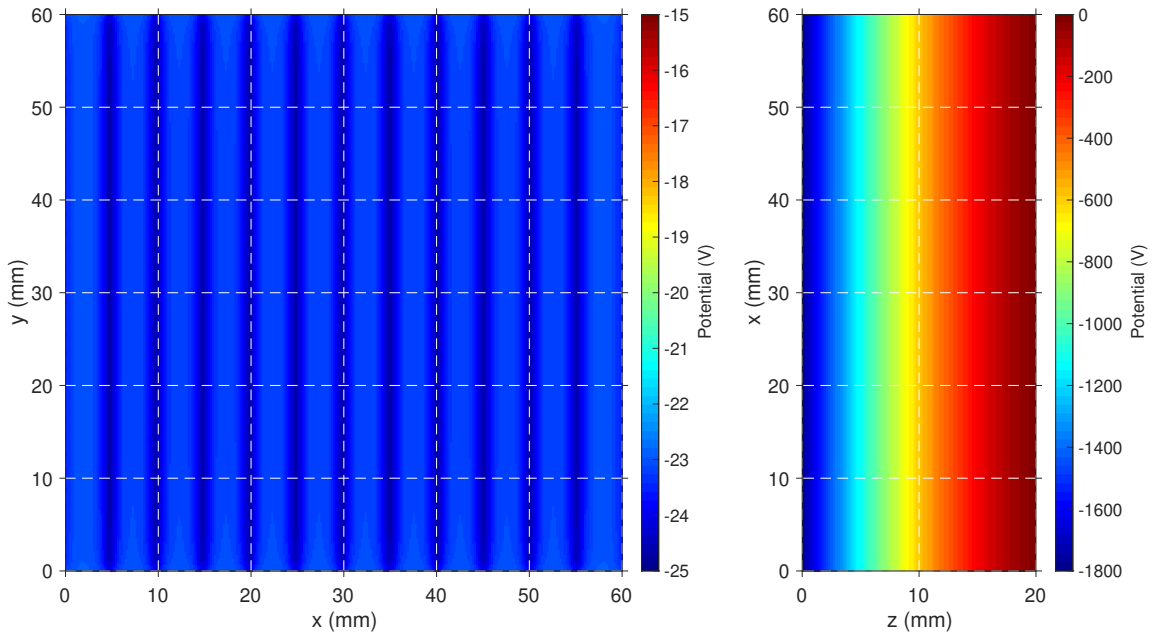
FIGURE 6.2: Electric potential of the active bulk volume of the detector, guard ring excluded, taken as a slice in *z*-depth at $z = 2$ mm from the DC electrodes (left) which reveals the contact structure, and a slice through $y = 30$ mm (right) showing the field change through depth.

The electric field at any point within the detector volume can now be represented in 3-D coordinates by the inverse gradient of the electric potential field using,

$$E(x, y, z) = -\nabla\Phi(x, y, z). \tag{6.2}$$

6.2.1 Weighting potential

The weighting potential and field are required for the calculation of the induced signal at each contact for each step on the charge carrier path. They can be calculated through the same process as the electric potential but with a modification to the applied voltage boundary condition and the removal of the space charge contribution. Instead of the operational bias used in the electric field calculation the contact of interest is set to 1 V and all others to 0 V. As such, 24 individual weighting potentials are generated for the 24 strip electrodes. The weighting potential of strip DC03 is displayed in Figure 6.2 taken at the same slices used to display the electric potential.
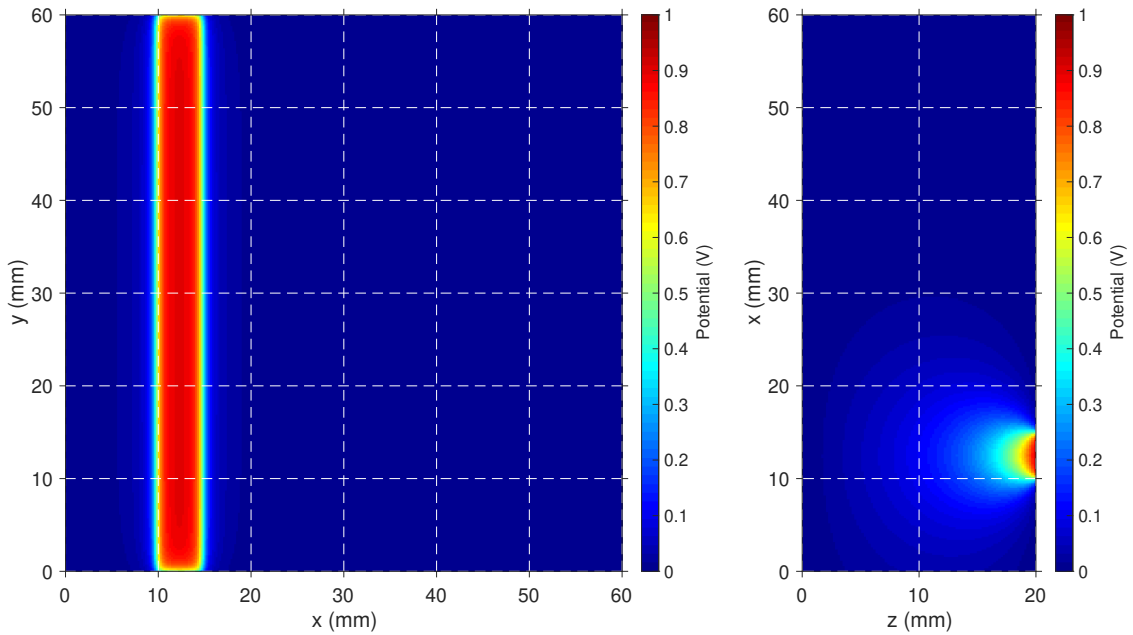
FIGURE 6.3: Weighting potential of a strip DC03 taken as a slice through the z-depth (left) and through y (right). The guard ring has been excluded from the plot and only the active detector volume is displayed.

Close to the DC contacts for the x-y slice (left) the weighting potential is observed to be close to 1 for the entire strip with a small decrease present at the strip ends and a rapid decrease in x as the distance from the contact increases. When a slice is taken through the detector depth (right) the weighting potential has a small value through much of the detector volume and rises quickly near the $z = 20$ mm contact. The profile of this potential through depth is shown in Figure 2.8. In x-positions neighbouring the studied contact the ballooning of the potential outwards can be discerned.

6.3 Pulse Shape Formation

ADL generates the pulses induced at all electrodes using an iterative process. A position of interaction is chosen by the user as the charge carrier origin. For this position ADL calculates the electric field strength and thus the direction of travel of the charge carriers and moves each set of charge carriers to a new position. The new field strength is

calculated and the charges moved again and so on until the charge is terminated at the collecting electrodes. The number of steps and the time between each step are user set parameters and defined such that complete charge collection can occur at the electrodes. The mobility of the charge carriers is defined in the planar germanium detector by the orientation of the crystallographic axis. The HPGe crystallographic axis was aligned such that the depth through z was parallel to the <001> axis and the mobility parameters taken from Bruyneel *et al*. [29]. These parameters are displayed in Table 6.2 for the <100> and <111> axes. At each step along this path this path the signals are instantaneously induced at each of the 24 collecting electrodes based upon their individual weighting fields at that point. The signal length was chosen to be 750 ns with a 1 ns time step with only single interaction events considered.

Direction	Carrier	$\mu_0(cm^2/Vs)$	β	$E_0(V/cm)$	$\mu_n(cm^2/Vs)$
<1 0 0>	e^-	38609	0.805	511	-171
<1 1 1>	e^-	38536	0.641	538	510
<1 0 0>	h^+	61824	0.942	185	-
<1 1 1>	h^+	61215	0.662	182	-

TABLE 6.2: Table of electron and hole mobility parameters in the <100> and <111> axes taken from Bruyneel *et al*. [29].

Although the electric and weighting potentials were solved on a 0.2 mm cubic grid, a 1 mm cubic grid was chosen as the simulated pulse database granularity. As such, 72,000 simulated events were produced on a 1 ns sampling, representing the $60\times60\times20$ mm^2 active volume of the detector. The 1 mm cubic grid was chosen due to computational limitations. A limit exists on the position resolution achievable, based upon the initial size of the charge carrier cloud produced and its diffusion whilst drifting. This limit is potentially 1 mm in some detectors such as those used in GRETA [70] but may be less in planar HPGe detectors due to the thin nature of the detectors resulting in little diffusion [71].

6.3.1 Charge Carrier Trajectory

The positions of the charge carriers as a function of time can be output from ADL, thus allowing investigation of the formation of the signals and the movement through the electric field. Any irregularities in the signals produced could be investigated by first looking at the charge carrier paths through the electric fields to the contacts. The charge carrier trajectories are output from ADL on the same 1 ns sampling as the signals produced from their movement.

The initial verification of the detector response was performed by outputting the raw simulated signals from a range of positions through the detector depth along with the corresponding charge carrier trajectories. As such, the induced signal at each electrode could be observed as a function of the charge carrier position. An example of this is shown in Figure 6.4 for 4 positions through the detector depth labelled as A, B, C and

D. In each case the charge collection pulse is shown for the AC electrode involved in the charge collection as well as one if its nearest neighbours. The AC contacts are situated at $z = 0$ mm and the DC at $z = 20$ mm.
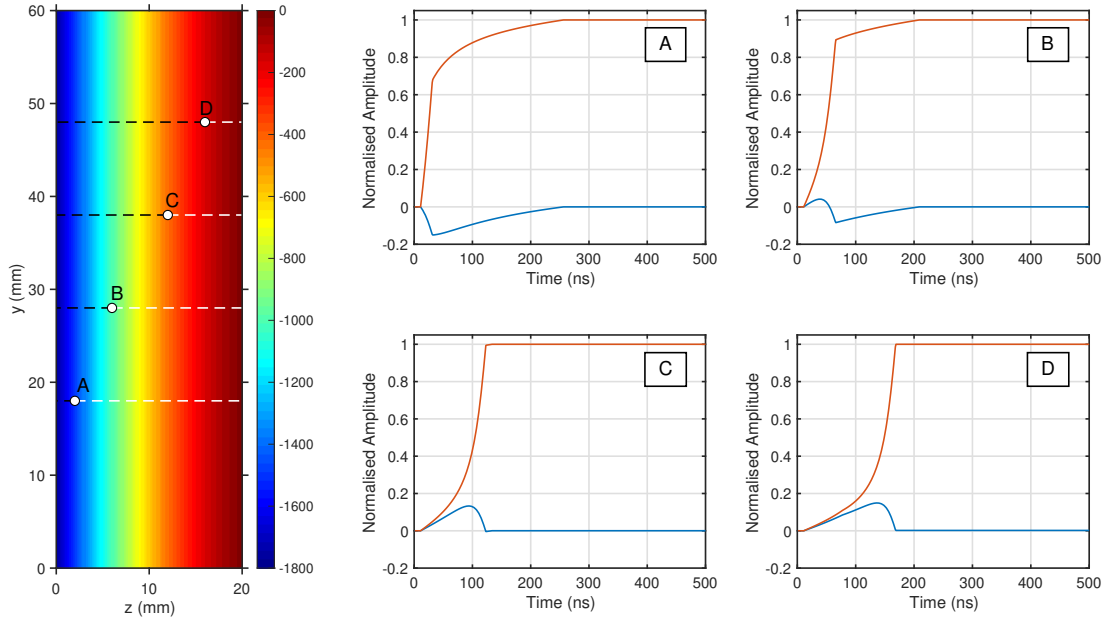
FIGURE 6.4: Electric potential through z-depth of the detector taken as a slice through x. The charge collection signals and nearest neighbour transient signals are shown for 4 positions and the corresponding charge carrier path displayed in black for the electrons and white for the holes. The signals are of the hole collecting AC strips located at $z = 0$ mm.

The pulse shape is seen to change through the detector depth as the position of interaction ranges from close to the hole collecting AC electrodes, A, through to positions close to the electron collecting contacts at $z = 20$ mm. At position A the initial fast rise time of the pulse is created through the almost immediate collection of the holes at the nearby electrodes while the slower top part of the pulse is due to the movement of the electrons through the bulk of the detector to the far side. At B, bipolar transient image signals are now induced in the electrode neighbouring the collecting strip due to the gradient change of the weighting field the charge carriers are travelling through. Finally, at point C and D, fully positive image charges are observed due to the shallow weighting field gradient and the charge collection pulse shape is dominated by the collection of the holes at the $z = 0$ mm AC electrodes. The charge collection pulses and neighbouring image charges change appropriately in shape and magnitude through the range of positions studied.

It is proposed that this ability to track charge carrier movement through the detector could be used to investigate further those events in which charge carrier collection occurs on the inter-strip gap as discussed in Chapter 5. To do so would require a fully validated pulse database that represented the pulse shapes in the detector accurately.

6.3.2   Preamplifier Convolution

As described in Section 4.1.2 the HPGe is instrumented with charge-sensitive PSC823C preamplifiers. These preamplifiers have an effect on the leading edge of generated pulses within the detector. A limited rise time is present in the charge collection due to the finite bandwidth of the system introduced by the delay of the charge collection loop responding to the input charges. An exponential decay also occurs due to the subsequent discharge from the capacitor. Canberra have reported an input rise time of 50 ns and a decay constant of 50 μs for the preamplifier models used [72].

In order to account for these effects introduced by the physical electronics within the detector, they are modelled and replicated such that they can be introduced to the simulated signals. This was performed using a preamplifier response function developed [73] to replicate the effect of the front end electronics within the detector using

$$V\left(t\right) = \int_0^t I\left(t - t'\right) R\left(t'\right) dt',\tag{6.3}$$

where the simulated input current, $I(t)$, and the preamplifier response function, $R(t)$, are used to reproduce the observed signal, $V(t)$. $R(t)$ is given by

$$R\left(t\right) = \frac{g}{1-c}\left(\frac{1}{1 + \frac{1-c}{c}e^{(-bt)}} - c\right)e^{\left(\frac{-t}{t_d}\right)},\tag{6.4}$$

where g is the signal gain and b and c are parameters that determine the shape of the signal through its rise time and curvature. The c and b parameters used during the initial inception of the response were calculated from experimental testing by inputting a step-function into the preamplifiers and recording the output. The method was replicated for this work and a square wave was input into a detector containing PSC823C preamplifiers using a pulser and the resultant output taken as the preamplifier response. The square wave was convoluted with Equation 6.4 and the parameters b and c chosen such that a good match was obtained.

The results from the square wave pulser test are displayed in Figure 6.5. The pulser input is shown in yellow as the square wave step function. This was input to the preamplifier test input and the output from the preamplifier recorded in blue. The square wave still has a rise time present but it is small compared to the effect of the preamplifier and so is assumed to be instantaneous. Convoluting the square wave with Equation 6.4 using the best found parameters of $b = 0.08$ and $c = 0.05$ yielded the red pulse, in which the preamplifier has been accounted for. The optimum values of b and c were found through a χ-squared minimisation process. The response function with the chosen parameters was then convoluted with the signal database and so replicated the physical effect of the detector preamplifiers.
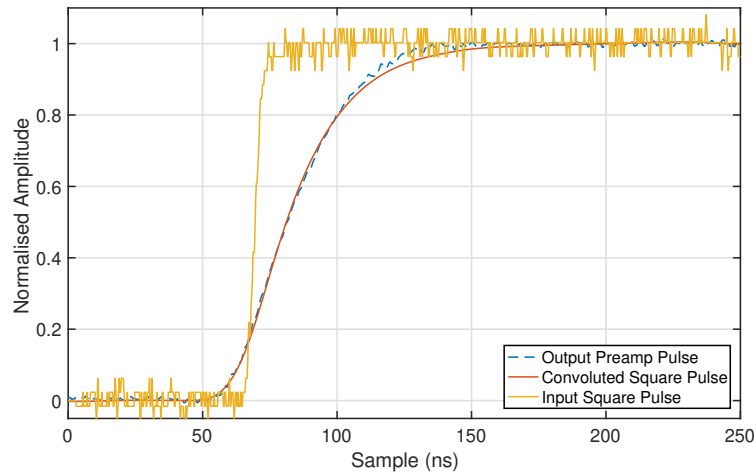
FIGURE 6.5: Square wave input into preamplifier test input (yellow) and resultant preamplifier output (blue). These are compared to the convolution of the square wave with the preamplifier response function for the chosen parameters (blue).

6.4 Simulation Results

Some typical results from the simulated database signals are shown in Figure 6.6 for strip DC06 after the preamplifier response function had been convoluted through the database. A complete analysis of the pulse database and optimisation of the simulation to match experimental data is presented in Chapter 8 as a validation process. The initial database output using simulation parameters supplied by the manufacturer are shown here. The pulses originate from interaction positions corresponding to a fixed x-y position and a range of z-positions through the detector depth (top) and for a fixed y-z position and a range of y-positions across the 5 mm width of a contact (bottom). Shown are the two nearest neighbours to the charge collecting contact which show the image charge response through the detector depth and across the strip contact width.

The initial response that can be observed is of one that appears to model appropriately the charge collection signal response that is currently understood to occur through detector depth and across a strip from the analysed characterisation data in Chapter 5. Through the detector depth (top) the charge collection pulses show a spread that seems to correspond well with observed depth characterisation as well as displaying the overturning of the final part of the pulse leading edge that occurs in positions close to the collecting electrodes. Through depth the neighbouring transient charges change from negative polarity to bipolar close to the collecting electrodes and then finally positive when far from the electrodes.

Across the 5 mm width of the strip (bottom) the image charges range from 7% of the charge collection magnitude to 22% as a function of distance from interaction position, values that match those observed in the detector characterisation. The charge collection signal shows some variation in shape across the 5 mm width but that has been observed in the characterisation data also. The signals with the steepest rise time corresponds to positions across the centre 3 mm of the strip while the signals with the
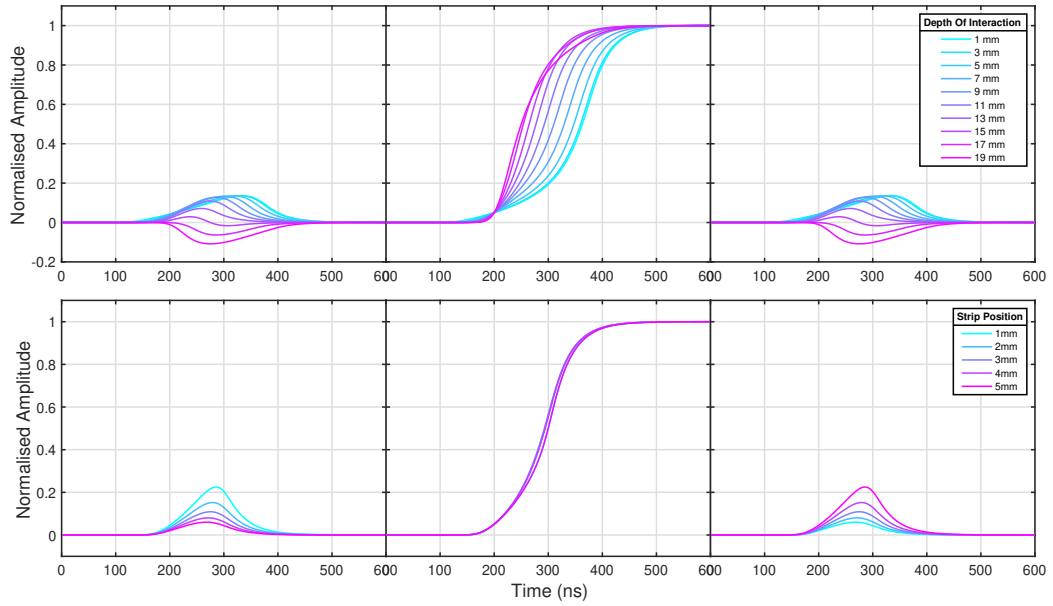
FIGURE 6.6: Charge collection signal of DC06 and transient image charges from nearest neighbour electrodes for a range of positions through depth (top) and across the 5 mm width of the strip (bottom).

slower rise times are present at 1 mm and 5 mm across the width. AC06 was also investigated to interrogate the simulation response across the same range of z-positions and across a strip with constant x-z-position for the hole collection and similar results were observed. As appropriate signal response was observed from the simulated pulse database, validation of the pulse shapes could be performed.

Chapter 7

Simulation Validation and Algorithm Development

Following the generation of the signal database, comparison could be made between the simulated and the experimental signals. Firstly, an optimisation process was carried out in which parameters used to produce the database were refined in order to better match the physical system. This was done through comparison of the simulated database to average experimental signals recorded during the side scan characterisation process at known positions. The signal response of the database was then validated through comparison to experimental signals produced in both the face scan and the side scan characterisation. Finally, a database PSA algorithm was developed to compare experimental and database signals and produce sub-voxel interaction positions.

7.1 Simulated Optimisation

In the previous chapter the electric and weighting potentials were solved using the manufacturer provided geometry and impurity concentrations at the AC and DC faces. The impurity values were quoted with a large uncertainty meaning the exact space charge present through the detector depth was unknown. The database of simulated signals was generated using charge carrier mobility parameters determined by Bruyneel $et\ al.$ [29] at 78 K. The mobility parameters are known to be temperature dependent in germanium and follow a $T^{-2.3}$ relationship for electrons and $T^{-1.6}$ for holes [74] [75]. The CP5 coolers used had a temperature set point of 88.15 K but the actual crystal temperature was unknown and could not be determined without direct mounting of a temperature diode on the crystal. It would be expected that the crystal temperature would be the same temperature or warmer than the set-point temperature. Due to uncertainties in the detector space charge as well as the crystal temperature an optimisation process was performed. Select points of the simulated database were compared to the average signal formed at known positions during the characterisation process.

7.1.1 Singles Scan Data Comparison

The simulation parameters used, namely those defining the impurities and mobility parameters, were tested through comparison to the ^{137}Cs side scan characterisation data. This comparison was used to optimise the simulated pulse shape response through the 20 mm depth of the detector. The signals used were those formed in Section 5.2.3 and represent the average signal response of each of the 24 strips at each of the 20 mm points through the detector z-depth. These signals were normalised and interpolated to a 1 ns basis. An approximate simulated equivalent was generated through the generation of the average simulated charge collection signal of each strip at each mm z-depth. This average at each z-depth was formed of the signals of the 60×5 mm positions of each strip. This was done in order to be consistent with the average experimental signals formed.

An RMSD comparison of the average simulated and experimental signals for strips AC06 and DC06 at several z-depths was then performed. First an RMSD method was employed to time align the simulated and experimental pulses. In this method the simulated signal was aligned to a set sample and the RMSD between it and the experimental equivalent found. The experimental signal was then shifted in 1 ns steps from -200 ns relative to the simulated signal to $+200$ ns. The smallest RMSD found was taken as the closest alignment between the two. Shifting of signals was performed due to the difficulty of finding and aligning to t0. For the comparison three z-depths were considered. These were 1 mm, 10 mm and 19 mm. These positions were selected as they represented positions close to the DC contacts, the mid-point, and near to the AC contacts respectively. This was done to ensure the parameters the simulation was optimised for were not skewed towards a fit at a single point in the detector. An RMSD comparison was performed between the experimental and simulated charge collection signals at these three depths. The simulation parameters were then adjusted until the smallest total difference was achieved for the AC and DC compared positions. As the impurity values and the mobility parameters both have an effect on the signal shape they were investigated in conjunction with each other. The results from the impurity concentration optimisation are displayed first followed by the mobility parameter optimisation.

The space charge was calculated within ADL based initially upon the manufacturer provided impurity concentrations of 0.70×10^{10} cm^{-3} at the AC contacts and 0.85×10^{10} cm^{-3} at the DC contacts. A linear gradient was plotted between the values at each face and used to calculate the impurity through depth. A linear gradient was used as the detector is relatively thin and the change through crystal thickness has been shown to be approximately linear in germanium crystals [76]. A range of values was tested and at each combination the RMSD for AC06 and DC06 calculated at each of the three z-depths. Average simulated signals from a selection of the tested values are displayed in Figure 7.1 for DC06 at 10 mm depth. Signals were produced with mobility parameters corresponding to 88 K and have been aligned to 5% of the normalised height for display purposes. The average experimental signal for DC06 is plotted in black.
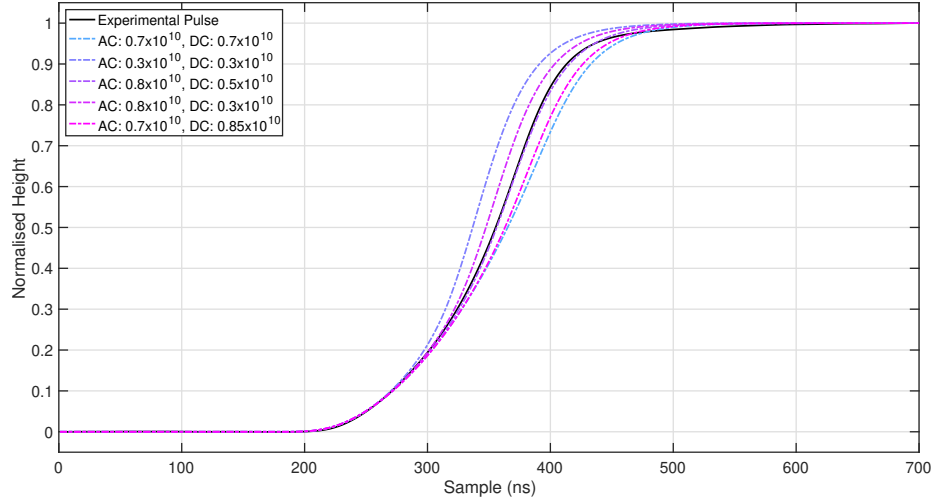
FIGURE 7.1: Comparison between the average simulated and experimental charge collection signals of strip DC06 at a z-depth of 10 mm. The impurities are quoted in impurities per cm^3. The simulated pulses are produced with mobilities parameters corresponding to 88 K

The fastest charge collection occurs when the impurities are set as 0.30×10^{10} cm^{-3} at the both the AC and the DC faces while the slowest corresponds to higher impurity values of 0.70×10^{10} cm^{-3} at each face. This change in the simulated signal shape and rise time is from the electric field shape being influenced by the space charge, introduced through impurities present. The smallest RMSD between the experimental and simulated signals was found for an impurity concentration of 0.80×10^{10} cm^{-3} at the AC contacts and 0.50×10^{10} cm^{-3} at the DC contacts. These values produced the best match for AC06 and DC06 at the three compared z-depths. These values are a reversal of the relative concentrations at each face provided by the manufacturer. They do not differ much in absolute magnitude from the quoted values and so were deemed acceptable as simulation parameters in this work.

The effect of temperature on the signal shapes was investigated through changing the mobility parameters. The initial values used corresponded to a temperature of 78 K. The cooler set temperature of 88.15 K could not be verified to be the actual operating temperature of the crystal and so simulated pulses were produced for a range of temperatures. The mobility values were calculated at each temperature following the $T^{-2.3}$ and $T^{-1.6}$ relationship for electrons and holes. A selection of the tested temperatures are displayed in Table 7.1 along with the corresponding electron and hole mobility as a percentage of the mobilities at 78 K.

Carrier	78 K	83 K	88 K	93 K	98 K
Electrons	100%	90.54%	82.45%	75.47%	69.40%
Holes	100%	86.68%	75.77%	66.73%	59.16%

TABLE 7.1: Table of charge carrier mobility parameters in germanium as a percentage of the quoted values given at 78 K for a range of temperatures.

While the mobilities were varied, the impurity concentrations were fixed at 0.80×10^{10} cm^{-3} at the AC contacts and 0.50×10^{10} cm^{-3} at the DC contacts. A comparison between the average experimental and simulated charge collection signals is shown in Figure 7.2. The fastest charge collection is seen to correspond to lower temperatures while the charge collection is slower when the temperature is warmer. This is expected due to the relationship between temperature and mobility outlined above. The smallest RMSD for AC06 and DC06 at the three z-depths was found at a temperature of 88 K. This correlates with the cooler set temperature and was chosen as the final value for this work.
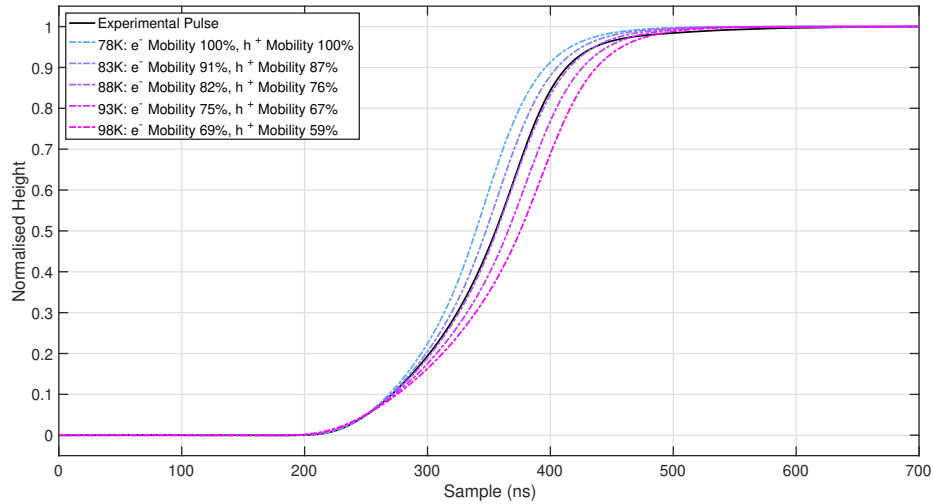
FIGURE 7.2: Comparison between the average simulated and experimental charge collection signals of strip DC06 at a z-depth of 10 mm. The mobility parameters at each temperature are given as a percentage of the mobility at 78 K. The simulated pulses are produced with impurity concentrations of 0.8×10^{10} cm^{-3} at the AC contacts and 0.5×10^{10} cm^{-3} at the DC contacts.

The final aspect of the simulation optimisation was the preamplifier convolution applied to all simulated signals. The initial parameters of the convolution were based upon the measurement of the preamplifier response. This was taken from a single PSC823C preamplifier in a different detector and applied to the database. It was observed in Chapter 5 that the average rise time response of the charge collection signals was not constant for all strips on each face. This was attributed to the initial preamplifier calibration performed by the manufacturer. This variation between strip responses was accounted for in the simulation by optimising the preamplifier response function parameter, b, and the decay time t_d. The parameter c was kept constant. The average experimental signal was produced for each strip and compared to the average simulated at the three z-depths. The parameters b and t_d were varied until the smallest RMSD was achieved. The value of b was found to be between 0.05 and 0.1 while the optimal t_d values found were significantly different to those originally used and were between 27 and 33 μs. The preamplifier convolution was then applied to a simulated database created with the optimal charge collection mobilities and impurity concentrations. This was then set as the final simulated signal database used for this work.

7.2 Simulation Validation

Validation of the simulated database signal response was performed subsequent to parameter optimisation. Side and surface scan characterisation data were used to confirm the signal response at known points within the detector volume. Ideally this process is performed with coincidence scan data [77] as events are then constrained in (x, y, z). The data taken in the characterisation process for this thesis were singles data in which events are constrained in only x-z for the side scan and x-y for the surface scan. Methods discussed below have been employed to compare these singles data with the simulated database for positions within the crystal.

7.2.1 Side Scan

To validate the signal response of the detector through the 20 mm z-depth of the HPGe detector the ^{137}Cs side scan characterisation data were again used. In the simulation optimisation process an average experimental signal was compared to an average simulated signal at several z-depths. Following this it would be expected that the signals match at all positions through the 20 mm z-depth. As the singles side scan data can only be constrained in y and z, exact positions in the detector cannot be compared. Instead a different approach was used to validate the charge collection signal through depth. The signals of F[1,1] full-photopeak ^{137}Cs events from the HPGe side scan were output from MTsort. The produced signals represented over 1.74×10^4 interactions occurring at all z-depths within the detector. The collimator position for each interaction was recorded and so the depth of interaction in z for each of these events is known. Determining the closest match between each of these experimental charge collection signals and a position with the database can be used to validate the signal response through depth. If the closest match is found to be at the same z-depth, or close to, as the collimator was located then the signal response can be confirmed as appropriate.

The AC and DC charge collection signals for each interaction were individually normalised and aligned by t30 to a chosen sample. The simulated database was aligned by t30 to the same sample. The AC and DC charge collection signals for each experimental event were then compared through an RMSD method to simulated signals from all possible positions. This totalled 500 positions from the $5 \times 5 \times 20$ mm^3 voxel that each interaction is constrained to. The smallest RMSD match between the experimental and the 500 possible positions from the database was taken as the found position of interaction. From this method the found z-depth of each interaction was produced with a z value found for the AC face and the DC face. The magnitude of the RMSD was also recorded.

The differences in mm between the collimator position in z, relative to the DC contacts, and the found database z-depth were histogrammed for all events compared. An RMSD threshold was applied to these events. Only events with an AC and a DC RMSD of 0.01 or less were accepted. Events that did not pass this threshold were observed
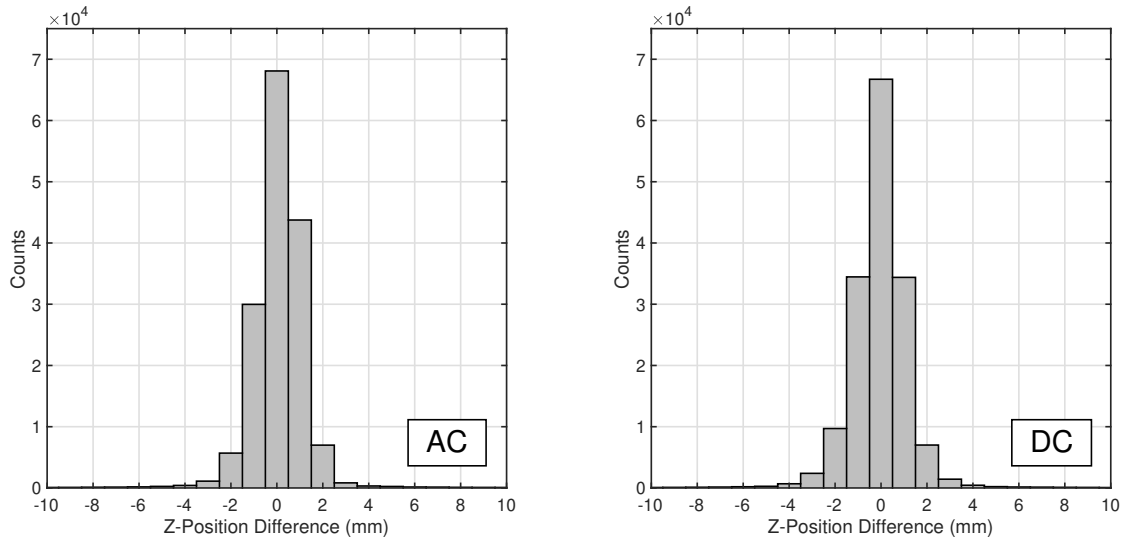
FIGURE 7.3: Difference in *z*-position found between collimator position of experimental F[1,1] ^{137}Cs 661.7 keV signals and the closest database position match. AC and DC differences are shown separately for all events.

to consist of multiple interactions within a single voxel and so consisted of convoluted charge collection signals. This reduced the number of events to 1.59×10^4, a reduction of 8.28%. A histogram of the *z*-position difference for these events is displayed in Figure 7.3 for the AC difference (left) and the DC difference (right). The largest number of events for each face are in the 0 mm bin and the majority of the remaining events at ±1 mm. This indicates that when considering events from the full 20 mm *z*-depth of the detector the best found match from the database corresponds to positions within 2 mm of the collimator position. Due to beam divergence events not all interactions occur at the same *z*-depth as the collimator is located and some deviation from the 0 mm difference is attributed to this effect. The consistent agreement found between experimental and simulated signals through *z*-depth can be used as evidence of appropriate signal response through depth for all strips.

The *z*-difference histograms produced through database comparison were compared to the same events analysed with the parametric *z*-PSA method discussed in Chapter 5. Showing that the histogrammed *z*-difference distribution is similar to or better than the parametric *z*-PSA equivalent will support the validation of the *z*-depth signal response. Those events that passed the RMSD threshold and were compared to the simulated signal database were analysed with parametric *z*-PSA. The histogrammed *z*-difference results are displayed in Figure 7.4. The *z*-difference distribution is observed to be similar to that in Figure 7.3 with the majority of events binned at 0 mm and ±1 mm. To quantify the results better the *z*-differences as a percentage of total events were calculated and are given in Table 7.2 for the AC, DC and parametric histograms. The percentage of total events that fall into the 0 mm, the 1 mm and the 2 mm bins are given as well as the sum of these. The database determined difference was found to be comparable for the AC and DC distributions. Each found more than 95% of events to be within 3 mm
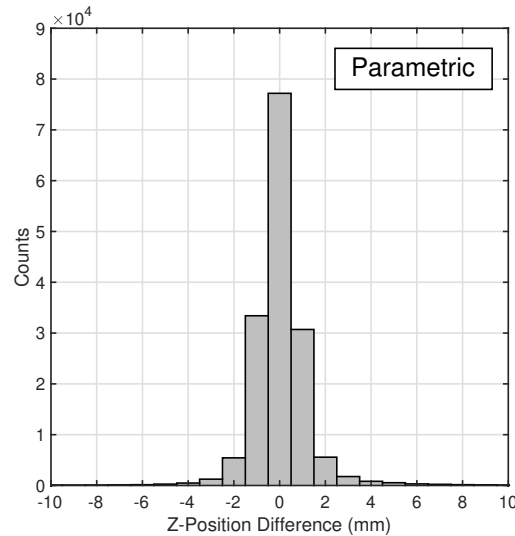
FIGURE 7.4: Difference in z-position found between collimator position of experimental F[1,1] ^{137}Cs 661.7 keV signals and the z-position determined by parametric z-PSA.

of the collimator location. The parametric z-PSA method performed the best, with a total of 48.3% of events being located at 0 mm difference. It was discussed in Chapter 5 that some amount of this can be attributed to over-fitting. The parametric z-PSA method works well on the data that were used to produce the rise time arrays on which is it based. It can be said that this is true for the validated simulation, in that it was also compared to the data used to optimise it. The true ability of the PSA methods can only be compared through the imaging of experimental data.

PSA	0 mm	1 mm	2 mm	$\leq$ 2 mm
Database AC	42.7%	46.2%	8.0%	96.9%
Database DC	41.8%	43.2%	10.5%	95.5%
Smallest-RMSD Match	43.2%	44.5%	8.6%	96.3%
Parametric z-PSA	48.3%	40.3%	6.9%	95.5%

TABLE 7.2: Number of events as a % of the total events analysed through database and z-parametric PSA found at 0, 1, 2 and $\leq$ 2 mm difference between collimator and found position.

A final check was performed by choosing the z-difference of each event from the AC or DC based on the match with the smallest RMSD. If doing so yielded a larger portion of events being found at a smaller z-differences it would imply that when a good signal match is found for one face the other is failing to find a close match. This could occur at positions at which the charge signal shape is reliant on charge carriers travelling a large distance before collection. These positions would be most influenced by incorrect mobility parameters within the simulation and so would produce poor quality matches or large z-differences. This is also displayed in Table 7.2 as the "smallest-RMSD". The smallest-RMSD match shows no clear improvement over taking z-differences from each face independently and provides a distribution of events that fall between the number of recorded events at all z-differences for the AC and the DC. As no improvement is

obtained from the smallest RMSD match it can be inferred that good agreements are found for the signals from both faces for all events. Because of this it was decided that when obtaining the depth of interactions from two sets of signals that the average found z position would be taken.

The Smallest-RMSD match showed that for each event both the AC and the DC signal comparisons find a good match with the database. It did not give information as to whether the interactions were found to be in the correct location or whether areas of the detector produced low quality matches for both signals. This was checked through production of an average difference map. The average difference between the best experimental signal and simulated match is expected to show whether certain areas of the detector show large over or under-estimations of the depth of interaction. This would confirm whether the mobility parameters and the pulse shapes are being correctly simulated. At each point of the scanned $20{\times}60$ mm^2 detector base the average z-difference was calculated for all events at that position. The map is displayed in Figure 7.5 for the average AC difference (top) and the DC difference (bottom). The AC contacts are situated at $z = 20$ mm and are horizontal. The DC are normal to the page and located at $z = 0$ mm.
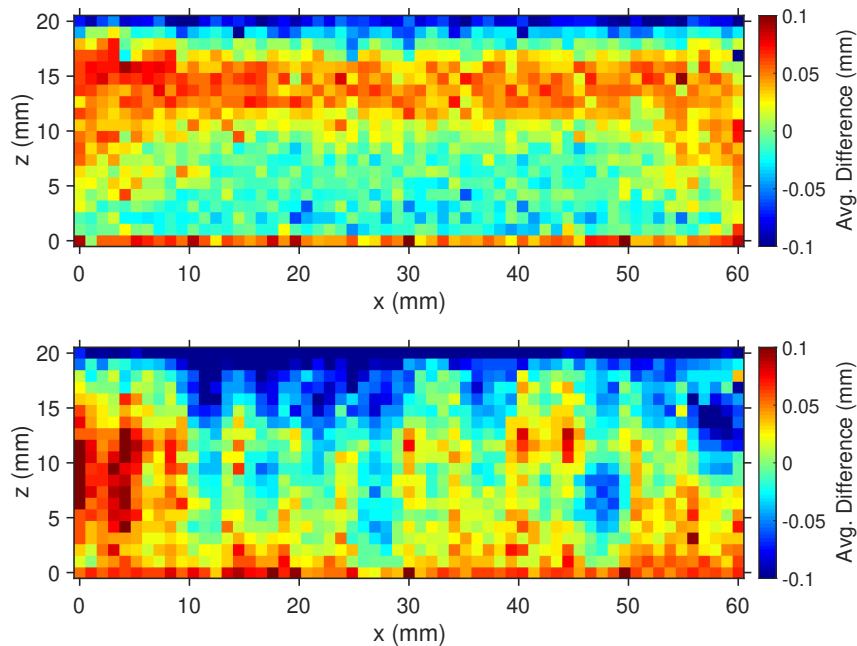
FIGURE 7.5: Average z-difference as a function of collimator position found between the AC signals (top) and the DC signals (bottom). The average difference is given is given in mm.

The average z-difference map produced when comparing AC signals shows a difference of 0 in the range of $z = 1$ mm to $z = 10$ mm. At these positions the events are located at the same z-depth as the collimator or in equal amounts either side. In the range of $z = 10$ mm to $z = 15$ mm the average difference is an over-estimation of ~0.05 mm. These positions are thought to be the areas from which the disproportionate number of $z = +1$ mm events are found relative to $z = -1$ mm events in Figure 7.3 for

the histogrammed AC z-difference. The over-estimation of 0.05 mm is more pronounced at the detector edges located at $x = 0$ mm and $x = 60$ mm. This is attributed to the changing pulse shape observed along strip lengths with different shapes present at the strip centre compared to the strip ends. It is possible that this change is not replicated accurately in the simulated signal database. This consistent difference in average z is not observed in the DC map. This is expected due to the histogrammed z-difference for the DC comparison in Figure 7.3 in which an equal number of events are found at +1 mm and -1 mm. The variation in average difference observed in the DC map is between individual strips. This is attributed to the separate preamplifier convolution applied to each strip and shows that the parameters used produced a better fit for some strips than for others. For example DC06, located between $x = 30$ mm and $x = 35$ mm, shows a very small average difference while others consistently over-estimate or under-estimate the z-position. For each average difference map an over-estimation of ~0.05 mm is present at $z = 0$ mm while a 0.05 mm under-estimation occurs at $z =20$ mm. This is due to these positions corresponding to the detector edges. Events at these locations can only be incorrectly positioned in one direction and so the average difference is biased towards it. The band of 0.05 mm over-estimation present in the AC map corresponds to the fastest charge collection for the AC contacts, as observed in Figure 5.28. Due to this, the difference is attributed to the mobility parameters selected as they would have the greatest effect at this point. The differences found between collimator and found positions from the side scan validation are adequate and display a similar response to the parametric method when selecting depth of interaction. In future it would be ideal to reinvestigate both the preamplifier convolution for each strip as well as mobility parameters and impurity concentrations.

7.2.2 Surface Scan

The image charge signal response across the detector strip widths was validated through comparison to the surface scan. This was done to confirm the image charges were of appropriate amplitude across the width of a strip. The side scan could not be used for this due to the orthogonal segmentation of the two faces. Interactions produced by the ^{241}Am surface scan occur in the front 1 mm of the detector due to the short penetration range of the 59.5 keV γ rays. The interactions can therefore be constrained by the collimator in x and y in addition to a short range in z. This restriction has allowed use of the surface scan characterisation data to validate the changing image charge amplitude across the 5 mm strip widths. Average single-pixel full-photopeak signals were formed at x-y positions across the detector face using the same method described in Chapter 5. The average charge collection signal and neighbouring image charges produced covered the full 60×60 mm^2 face of the detector for both the AC and DC surface scans.

The signals produced across the 5 mm width of a strip were investigated. The charge collection signal was disregarded since it does not change across this range, as was observed in Figure 5.24 previously. Only the image charges produced in the two

neighbouring strips were considered for each position. The test performed was a simple confirmation of the image charge amplitudes at each of these points. It was expected that a good match would be found as the charge collection signals have already been validated. The average experimental image charge signals were compared to simulated image charges from positions corresponding to the collimator location. The simulated signals were an average of the signals produced at 0 mm z-depth and 1 mm z-depth. It was assumed that this was a good approximation to the average signal formed from the 59.5 keV γ rays.
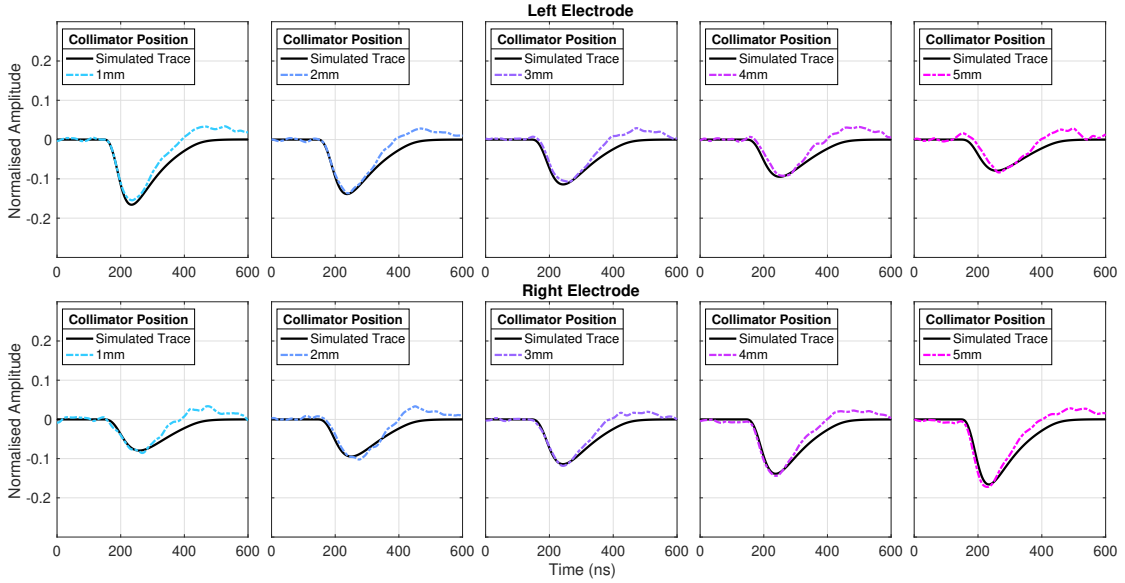
FIGURE 7.6: Average AC image charges from 5 collimator positions covering the width of strip AC06 for the strips to the left (top) and right (bottom) of a charge collecting strip-electrode. The collimated γ-beam was incident on the AC contacts.

The image charge comparison was performed for both AC surface scan data and DC surface scan. Examples are presented here from the AC surface scan. A range of 5 positions was taken across the middle AC06 and the image charges produced in the strips neighbouring either side are displayed in Figure 7.6. These image charges were produced when the γ-beam was incident on the charge collecting strip-electrodes. They were compared to the average simulated trace of $z = 0$ mm and $z = 1$ mm taken from the same x-y position. The AC image charges are observed to be of the correct amplitude in each of the 5 positions and of the correct shape along the leading edge. Both simulated and experimental signals vary from a normalised amplitude of -1.8 when the interaction was close to the image charge observing strip to -0.08 when the interaction was located 5 mm away. A notable difference between the experimental and the simulated image charge shapes is the consistent overshoot of the experimental pulse as it returns to base line. This is tentatively attributed to differential cross-talk occurring during the charge collection rise time.

The image charges induced on the DC contacts located on the far side of the detector relative to the incident γ rays are shown in Figure 7.7. Data from 5 collimator positions

were taken across the width of DC06 and image charges produced in the neighbouring strips either side are shown in comparison to the simulated equivalent. The image charges are again observed to change amplitude across the strip width with slight differences in height present at 2 mm and 4 mm. At both these positions the average experimental image charge is slightly larger than the simulated signal. This difference is minor and would not affect the ability to find the correct position when performing an RMSD comparison as the difference is small relative to the difference in amplitude between image charges.
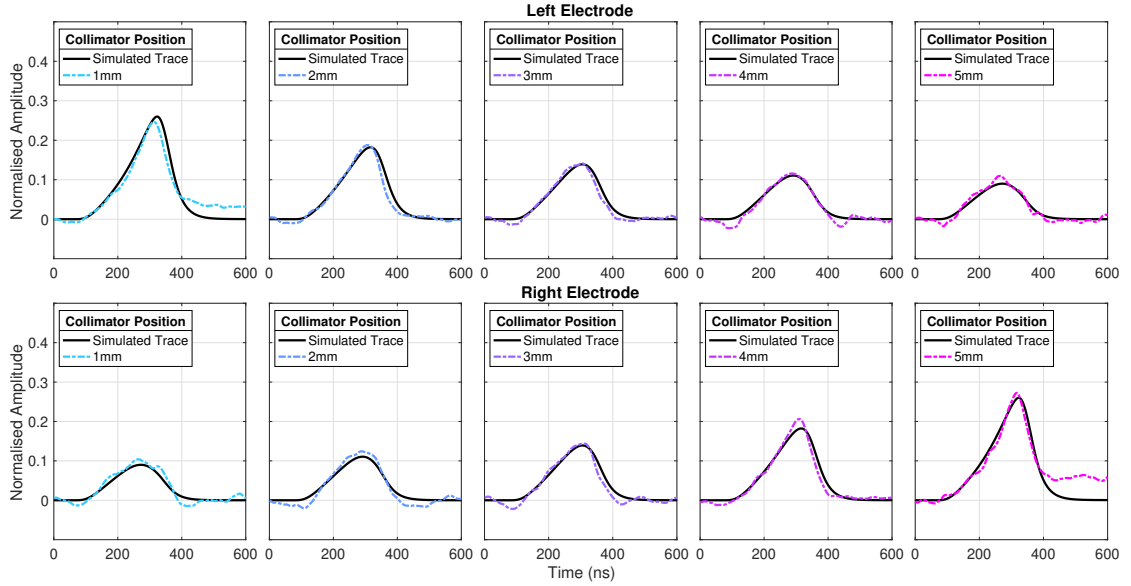
FIGURE 7.7: Average DC image charges from 5 collimator positions covering the width of strip DC06 for the strips to the left (top) and right (bottom) of a charge collecting strip-electrode. The collimated γ-beam was incident on the AC contacts. Charge sharing is visible at collimator positions of 1 mm and 5 mm.

A relatively large difference present in the DC image charge shapes is seen at 1 mm and 5 mm collimator positions when the interactions are close to the image charge observing strip. The undershoots observed in these signals returning to baseline correspond to unequal charge share events occurring between the charge collection strip and the neighbouring strip. The charge shared is below the 5 keV energy threshold for individual events but is clearly seen when an average of many hundreds of events is formed. It is prominent in the DC image charges but not observed in the AC image charges as the events compared here are from the AC surface scan. As discussed in Chapter 5, charge sharing occurs predominantly on the far side relative to the incident γ rays.

In each case it was decided that the differences present between the experimental and the simulated signals shown were due to physical effects in the system, which are not accounted for in the simulation. In future work effort should be made to correct for these experimental effects either by removing them from the recorded signals or by introducing them to the simulation in much the same way the preamplifier convolution was. This is the method employed in the AGATA detector simulations [78]. For the

focus of this work it was not necessary and it was decided that the differences would not affect the functionality of a grid-search algorithm. Similar results to these were observed when comparing image charges produced in the DC surface scan. The image charge amplitudes matched the experimental signals across the 5 mm strip width, while charge sharing was observed on the contacts on the detector far side relative to the incident γ-ray beam.

From these comparisons the simulated image charges can be said to follow their experimental counterparts closely in amplitude. This proves an accurate modelling of the weighting potentials for contacts neighbouring charge collection. Incorrect or mis-modelled weighting potentials would greatly affect the image charge shapes and amplitudes and this is not observed to be the case. This serves as sufficient validation of the surface response and in particular the transient image charge response.

7.3 Database PSA Algorithm

To improve the position resolution of the HPGe detector using the simulated signal database a grid-search algorithm was developed. The algorithm performs PSA analysis through comparison of simulated and experimental signals. Finding the closest match between the two sets of signals gives sub-voxel interaction position. The algorithm was initially developed to process only F[1,1] events within the HPGe. These events were simple and quick to compare and so a "brute force" grid-search was employed. The algorithm was subsequently expanded to deal with multi-interaction events within the HPGe, these being F[1,2] & F[2,1] as well as F[2,2]. Processing these higher-fold events required the use of an adaptive grid-search as opposed to a simple grid-search [79]. This reduced the necessary computational power required to process each event. Both grid-searches were developed within MATLAB and used the same input data format. Both algorithms output the (x, y, z) positions and the associated interaction energies in the format used by the image reconstruction algorithm.

The signals required by the database algorithm to perform PSA are exported from MTsort when histogramming experimental data. The charge collection neighbouring image charge signals were output along with strip numbers and MWD calculated energies for each processed event. Each signal was interpolated within MTsort prior to exportation and so was 1.2 μs long comprising 620 samples on a 2 ns basis. Signals were output to text files, 1,000 per file, depending on their fold. As a different algorithm was used for processing different events, the folds were classified as F[1,1], F[1,2] & F[2,1], and F[2,2]. As F[1,1] and F2 (F[1,2] & F[2,1], and F[2,2]) events were processed differently the algorithms for each are described step by step below. Example matches found between experimental and simulated signals were produced from 661.7 keV γ-ray depositions within the system.

7.3.1 Single Interactions

F[1,1] events were investigated first. These events are processed as single-interaction events although the only constraint is that they are single-pixel events. As each interaction is constrained to a voxel only 500 possible positions exist, which are the $5{\times}5{\times}20$ mm positions within the voxel. An RMSD comparison is used to compare the experimental signals to each of these 500 possible positions and the best match, or RMSD, is taken as the (x, y, z) position. This is done for the signals from the AC and the DC faces. The steps taken by the grid-search algorithm are outlined below. Prior to carrying out these steps the database of signals representing all 72,000 positions within the detector is loaded into memory within MATLAB. The database contains 24 signals on 1 ns basis at each position. At each position the signals of each face are aligned to a common sample based upon t30 of the charge collection signal at that point.

- **Step 1** - Normalisation and Alignment: A file containing 1,000 F[1,1] events is loaded into memory. For each event the signals from the AC and the DC faces are separately normalised and aligned by t30 relative to the charge collection signal. All signals are interpolated to a 1 ns basis to match the simulated signals.

- **Step 2** - Supertrace Formation: AC and a DC 'supertraces' are created for each event. These are concatenations of the charge collection signal and the neighbouring image charges. From each signal 600 samples are taken, producing 1800 ns long supertraces for charge collection signals with two image charges. Simulated supertraces are produced for the 500 possible positions.

- **Step 3** - RMSD Comparison: The experimental supertraces for the AC and DC contacts are each compared to the 500 simulated supertraces. An RMSD value is produced for each comparison. The smallest difference for each face is then chosen as the most likely position.

- **Step 4** - Position Determination: The final interaction position is determined from the two (x, y, z) positions found. The z-depth of interaction is taken as the average of the AC and DC found positions. The x position is taken from the AC found position and the y is taken from the found DC.

- **Step 5** - Event Readout: The HPGe (x, y, z) positions are written out to a text file along with the MWD calculated energy. Positions for the Si(Li) interaction are included so that the data can be imaged. The Si(Li) position can be output with or without parametric PSA applied.

The average of the AC and DC found z-depths is taken due to the reasons outlined in Section 7.2.1. The x and y positions are taken from either the AC or the DC based on strip orientations as each face accurately finds either the x or y based on the image charge magnitudes. The time alignment by t30 to a common sample assumes that time
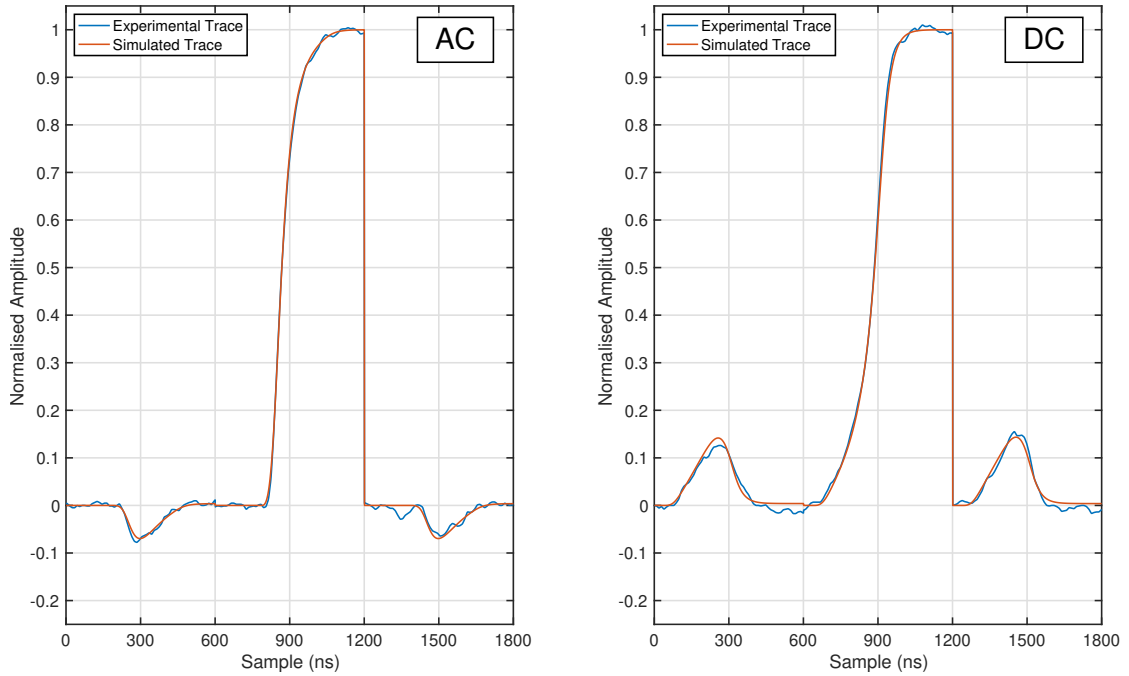
FIGURE 7.8: Example matches between experimental and simulated supertrace found by database PSA of an F[1,1] event. The AC supertrace is shown left and the DC right.

jitter introduced when reading out from multiple digitiser cards is either non-existent or small and can be ignored. This was observed to be the case when viewing supertraces.

An example of the best match supertraces for an F[1,1] event are presented in Figure 7.8. In this case the AC found match was located at $(x, y, z) = (27, 7, 14)$ mm and the DC at $(x, y, z) = (25, 6, 15)$ mm. For each a small RMSD was found for the supertrace comparisons. Similar z-depths were found by each face and an average was taken as $z = 14.5$ mm. The final interaction position was output as $(x, y, z) = (27, 6, 14.5)$ mm.

7.3.2 Multiple Interactions

Following the implementation of an F[1,1] grid-search, the algorithm was then expanded to deal with F2 events. When considering multi-interaction events two voxels must be considered. In each voxel 500 possible positions exist for the interaction. The total possible position pairs are therefore $500 \times 500 = 250,000$. Due to this, the RMSD method employed in a simple grid-search could not be feasibly used. The difficulty in developing a multi-interaction grid-search is not due only to the number of positions that much be compared, but to the convolution of multiple signals. An example of this convolution for two low-energy interactions within a single voxel given in Figure 7.9. In this case two charge collection signals are convoluted together, as are the image charges either side. If the charge is collected in separate but neighbouring strips the convolution is then present between charge collection signals and transient image charges. The signals at this point must be deconvolved into their separate components in order for a fit to be found between it and the simulated signals. As deconvolution of an experimental signal into its constituent signals is not feasible, the simulated signals are instead summed

together and compared. The uncertainty still remains in the time alignment of the signals. It is not known when in time each pulse began and what the time difference is between each interaction. Because of this, not only must 250,000 pairs of positions be compared, signals must be tested at all time alignments for a good match to be found.
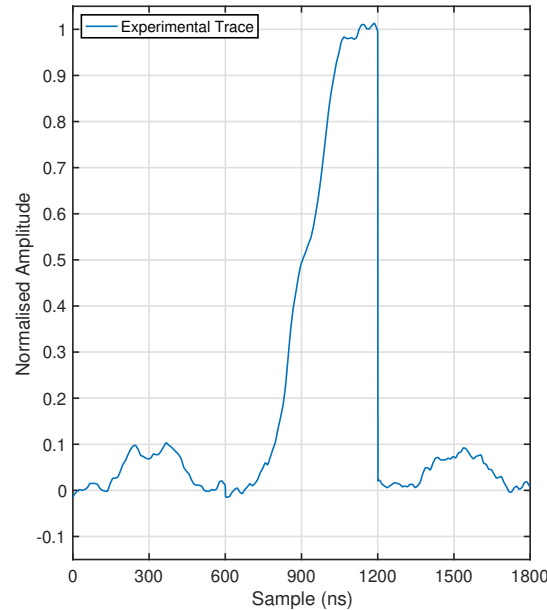
FIGURE 7.9: An experimental charge collection pulse from a single-pixel multi-interaction event. The two components of the pulse are clearly distinguishable as are the two components present in the neighbouring image charges.

Due to these reasons a multi-step adaptive grid-search algorithm was developed. This method means not all position pair possibilities must be compared. Instead an initial guess of the events is made which are then time aligned. A rough grid-search is then performed, followed by a fine grid-search. The steps carried about by this algorithm are outlined below as well as illustrated as a flowchart diagram in Figure 7.10.

- **Step 1** - Normalisation and Alignment: A file containing 1,000 F[1,2], F[2,1] or F[2,2] events is loaded into memory. The fold 1 face, if present, is normalised and aligned to t30 of the charge collection signal. The charge collection signals on the fold 2 observing face are designated Pulse 1 and Pulse 2. Pulse 1 is the first charge collection signal observed when considering strips 1 through 12. All signals on the fold 2 face are normalised relative to Pulse 1. The face is then aligned to t30 of Pulse 1, regardless of whether this signal is convoluted with an image charge or not. All signals for the event are interpolated to a 1 ns basis.

- **Step 2** - Supertrace Formation: Supertraces are formed of the charge collection signals and neighbouring image charges. For the fold 1 observing face this is an 1800 ns supertrace formed of a charge collection signal and two neighbouring image charges (if not an edge strip), each being 600 ns long. For the fold 2 face there are two sets of 500 possible positions from the two hit voxels. This results in the
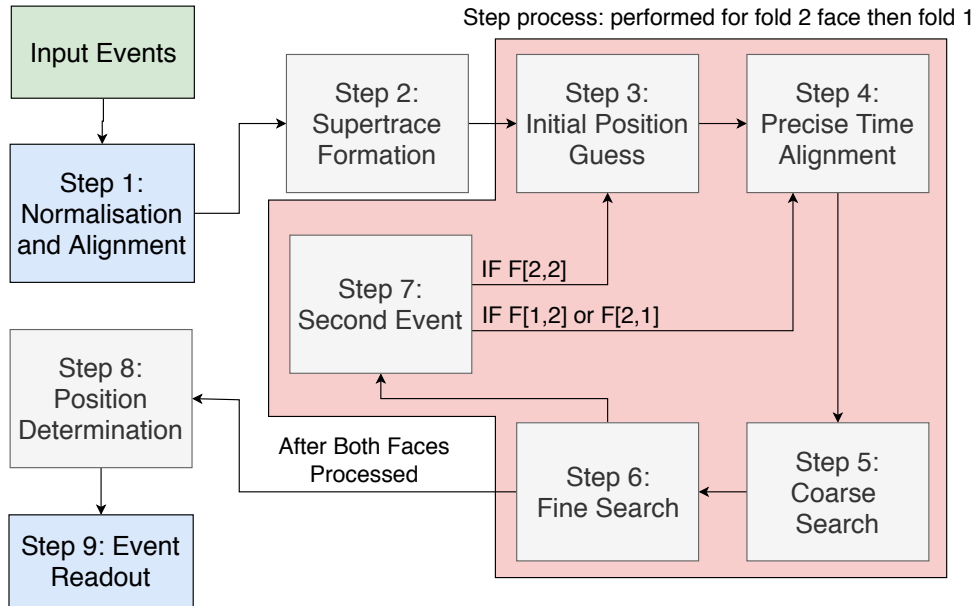
FIGURE 7.10: Flowchart diagram of the adaptive grid-search step process. Steps 3 through 7 are performed for each detector face starting with the fold 2 observing face. If the second face is a fold 1 event then Step 3 is skipped.

creation of 500 supertraces for each of Pulse 1 and Pulse 2. The supertraces are of a length that encompasses the hit strips of Pulse 1 through Pulse 2 as well as the external image charges. As such they are of variable length. The supertraces are scaled to match the energy deposited in the two interactions. An example of a Pulse 1 and Pulse 2 supertrace when two strips separate the charge collection events is given in Figure 7.11.
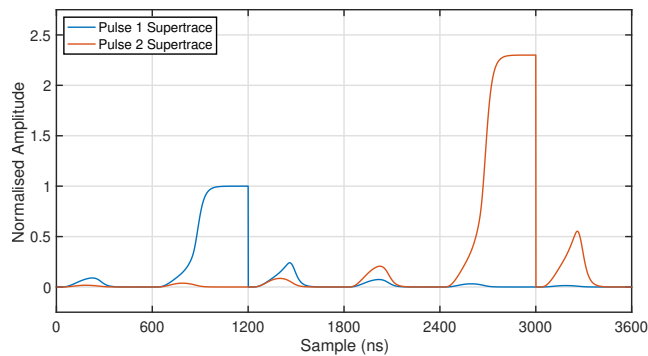
FIGURE 7.11: Supertrace examples from positions within each of the two hit voxels. Two strips separate the charge collection strips and supertraces of Pulse 1 and Pulse 2 are formed from all significant charge contributing strips.

- **Step 3** - Initial Position Guess: The fold 2 event is considered first. As the database is aligned at t30 it is assumed that the alignment of Pulse 1 is correct. An initial guess of Pulse 1 and Pulse 2 is performed for which a rough time alignment of Pulse 2 is needed. Only 20 positions of Pulse 2 are considered representing the hit voxel centre through z-depth. From each position the charge collection signal of

Pulse 2 is time aligned though RMSD minimisation with the experimental signal from the voxel. The time alignment is performed by shifting Pulse 2 from -200 ns to $+200$ ns in steps of 20 ns relative to its initial alignment and selecting the alignment based upon the smallest RMSD. An example of the alignment is given in Figure 7.12 (left). The alignment found in this example does not account for the image charge present in the experimental signal and differences in alignment are due to the large step size in the time alignment process. This has also resulted in exclusion of the signal baseline due to poor time alignment and/or matching of the signals. The rough alignment and initial guess is the reason for the signal leading edge not occurring within the compared sample length. Each of the 20 aligned Pulse 2 signals are summed with all 500 possible Pulse 1 signals. An RMSD comparison is performed for each of these 500 combination for each Pulse 2 depth. The supertrace with the smallest RMSD is selected as the best initial guess. An example of this best initial guess fit is given in Figure 7.12 (right).
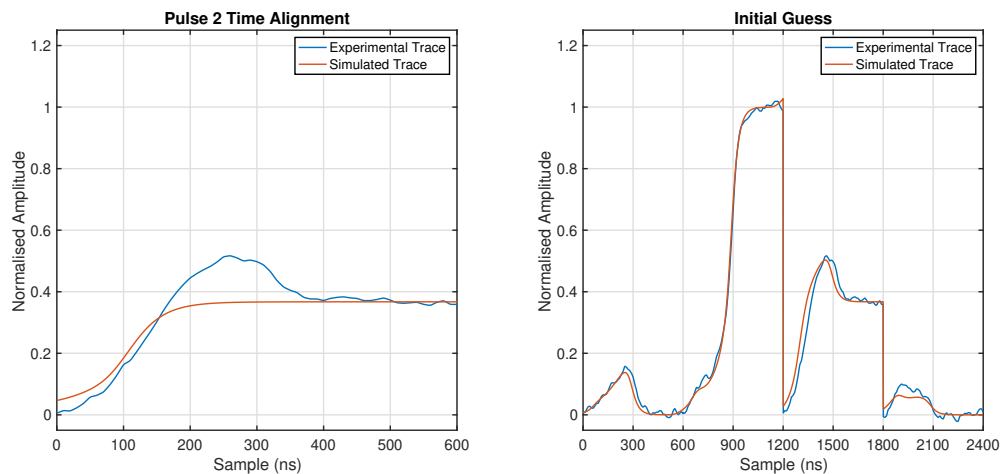
FIGURE 7.12: Examples of the initial guess performed by the algorithm. Time alignment of Pulse 2 charge collection during the initial guess (left) and subsequent best supertrace guess for Pulse 1 and Pulse 2 (right). The poor alignment is due to the large time steps used in the alignment process.

- **Step 4** - Precise Time Alignment: The guess of the charge collection signal shapes for Pulse 1 and Pulse 2 allows an accurate time alignment to be performed for each interaction. This would be too computationally intensive if many signals were to be tested. The supertraces of Pulse 1 and Pulse 2 used to form the initial guess supertrace in Step 3 are both time aligned. The same time alignment RMSD minimisation method is used. The supertraces of both Pulse 1 and Pulse 2 are each scanned in 5 ns steps. Pulse 1 is scanned from -200 ns to $+200$ ns while Pulse 2 is scanned from -100 ns to $+100$ ns around the alignment value found in Step 3. All possible time alignment combinations of the two supertrace are therefore tested. From this a precise value of the time alignment for Pulse 1 and Pulse 2 is found and is applied to both sets of 500 supertraces.

- **Step 5** - Coarse search: Following an improved time alignment of the supertraces a new coarse search is performed. Pairs of positions corresponding to the centres of each hit voxel are tested. This coarse search does not test x-y positions at each depth so reduces the number of position-pairs to consider from 250,000 to $20 \times 20 = 400$. The summed supertrace of Pulse 1 and Pulse 2 is compared to the experimental supertrace at each possible position-pair. The depths of interactions for the two events are fixed based upon the smallest determined RMSD. An example of the best fit achieved at this stage is given in Figure 7.13 (left) in which the pulses have been correctly time aligned and the charge collection signals accurately matched.
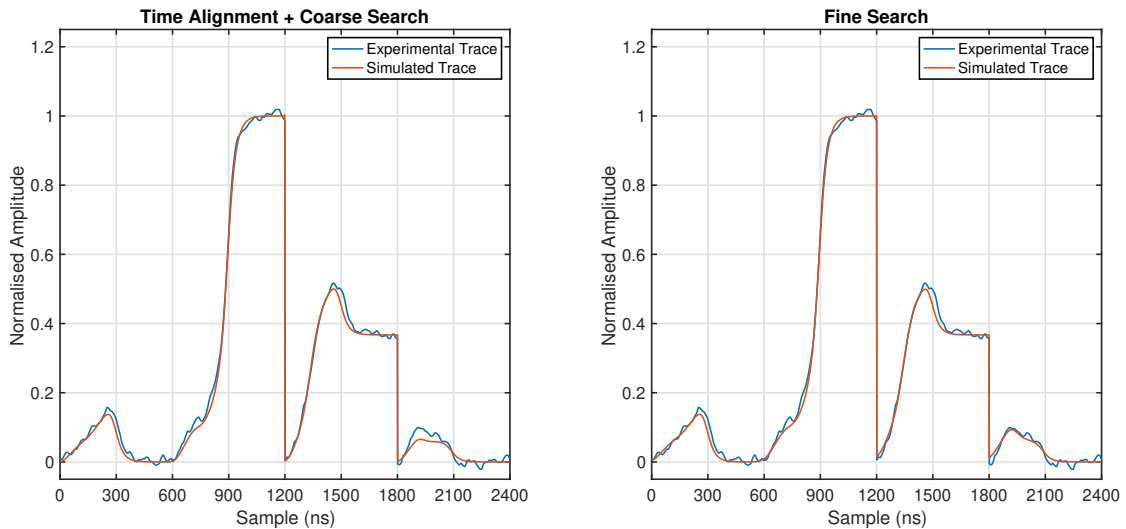
FIGURE 7.13: Matches between experimental and simulated supertraces during the fold 2 grid-search process. The match following precise time alignment and subsequent coarse search through z is shown left. The final match achieved after a fine x-y search is given right.

- **Step 6** - Fine search: Position-pairs from fixed z-depths are then compared for all x-y combinations. This totals $25 \times 25 = 625$ possible position-pairs. The summed supertrace of Pulse 1 and Pulse 2 for each position-pair is compared to the experimental supertrace. The x-y positions of the two events are fixed based upon the smallest RMSD. An example of the best fit achieved at this stage is given in Figure 7.13 (right). The image charges have now been fitted and the match is complete.

- **Step 7** - Second Event: Following the processing of the fold 2 observing face the second face is analysed. If the second face is also fold 2 the above steps are repeated from Step 3 onwards. If the second face is a fold 1 then the initial guess is not performed. Instead the final found events from Step 5 and Step 6 are input as the initial guess and the Step 4 precise time alignment is performed from there.

- **Step 8** - Position determination: The final interaction positions are selected from the four determined (x, y, z) positions. The first event is selected for based on a

threshold method discussed in Section 7.4.1. This event is chosen to be the scatter event or the first event to occur in a multi-interaction event. As with the F[1,1] process the x and y positions are taken from the AC and DC positions respectively and the z-depth as an average of two.

- **Step 9** - Event Readout: The HPGe (x, y, z) positions and MWD calculated energies are written to a text file. Positions for the Si(Li) interaction are included so that the data can be imaged with the reconstruction algorithm. The Si(Li) position can be output with or without parametric PSA applied in MTsort.

The algorithm functions in an almost iterative process in that a time alignment is found, followed by a position guess, then another time alignment and finally a final position determination. The time alignment of Pulse 2 performed during the initial guess ignores image charges and so in some cases does not correctly align the signals. This is especially true in the case of an image charge sitting within the signal leading edge. The image charges cannot be included, however, as the position of Pulse 1 is not known and so the polarity and magnitude of the image charges are unknown. For this reason the initial guess attempts to produce a close enough signal to the convoluted real signal that a precise time alignment can then be performed.

The precise time alignment in Step 4 includes these image charges with the charge collection signal. This allows a good time alignment to be achieved even if the exact charge collection signal and image charge magnitudes have not been found. The coarse search and fine search are then performed with the applied time alignment values. This improves upon the match of first the charge collection signal and then the image charges either side. The two matches given in Figure 7.13 display this process. Following the initial guess in Figure 7.12 the precise alignment step is carried out and a better match produced through the coarse search. The coarse search was not displayed separately in this example as the z-depth of interaction was not improved upon from the initial guess. Finally, a better match in x-y is found through the fine search and the image charge matches are improved upon as shown in Figure 7.13. The following subsections show examples of best found matches between multi-interaction experimental and simulated signals. The separations of charge collection signals in a multi-interaction event are treated separately due to varying contributions to imaging resolution and efficiency as discussed later in Section 8.1.1.

Non-adjacent Interactions

In a fold 2 event non-adjacent interactions are those in which at least one strip separates the two charge collection signals. These are classified as those with one strip separation and those with greater than one. When there is more than one strip separating two interactions the primary image charges of each are not convolved. This type of interaction does not have significant convolution of charge collection and image charge signals. For

this reason they produce the best matches between experimental and simulated signals on the fold 2 observing face.
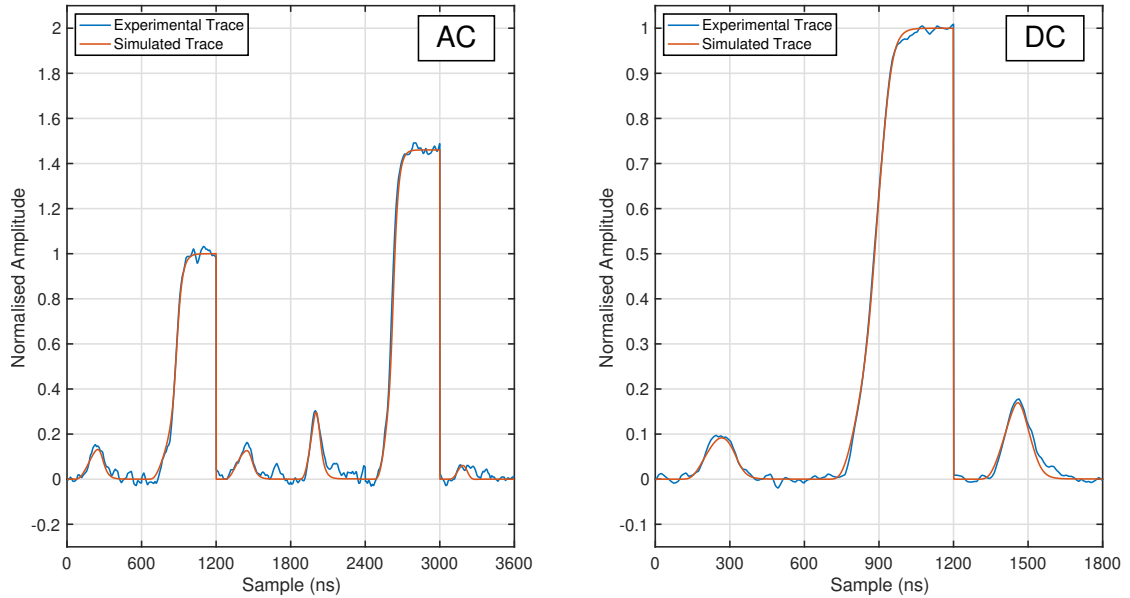
FIGURE 7.14: An example of the match found between the experimental and simulated supertrace for a non-adjacent F[2,1] event in which more than one strip separates the two charge collection pulses.

An example of this event type is shown in Figure 7.14. The fold 2 observing AC face is displayed left while the opposite face, observing convoluted charge collection signals, is shown right. In this example, the fold 2 positions were found to be $(x, y, z) = (33, 12, 6)$ mm and $(x, y, z) = (34, 30, 11)$ mm with energies of 225 keV and 335 keV respectively. These values were then input into the convoluted fold 1 face as the initial guess and positions of $(x, y, z) = (34, 12, 9)$ mm and $(x, y, z) = (32, 32, 12)$ mm determined with the same respective energies. The interactions corresponding to each energy give reasonable agreement in found z-depth and result in average positions of $(x, y, z) = (33, 12, 7.5)$ mm and $(x, y, z) = (34, 32, 11.5)$ mm being found for the 225 keV and 335 keV interactions. The fluctuation observed in the AC experimental supertrace (left) is noise present in the system.

In the case of the events being non-adjacent with a single strip separating the charge collection events the image charges from each are convoluted. Although the two charge collection signals are completely distinct the convolution of two image charges leads to a greater uncertainty when finding a match, as there are a larger number of possible combinations that could produce an image charge at the observed magnitude. The algorithm still finds good database matches for this event type as the z-depth of the interactions can be accurately found.

Adjacent Interactions

Adjacent interactions are those in which the charge collection signals occur in neighbouring strips. This results in a charge collection signal convoluted with the image charge of

the neighbouring interaction. This convolution can introduce uncertainty to the pulse alignment to t30 as it can sit within the leading edge of the signal. An example of a fold 2 adjacent event is given in Figure 7.15. In this example, the image charge sits atop the left charge collection signal, Pulse 1, for the AC face. In this case the signal is correctly aligned to t30 in the initial steps. The image charge of the left pulse is convoluted with the charge collection signal of Pulse 2 and sits somewhere within the leading edge. This introduces a larger uncertainty when determining time alignment and so produces lower quality matches with large RMSD values. The image charges not convoluted with charge collection signals are of the correct magnitude while the image charge atop the charge collection signal is of a smaller magnitude. It is hard to judge the quality of the match of the image charge sat within the charge collection signal leading edge as it is not clearly defined.

In this example, the fold 2 AC interactions were found to be at $(x, y, z) = (29, 40, 15)$ mm and $(x, y, z) = (31, 43, 18)$ mm for 102 keV and 377 keV interactions respectively. The fold 1 face found $(x, y, z) = (26, 44, 13)$ mm for the 102 keV interaction and $(x, y, z) = (31, 42, 18)$ mm for the 377 keV. Again, good agreement is found for the z-depth from each face. The final position was taken as $(x, y, z) = (29, 44, 14)$ mm for the 102 keV interaction and $(x, y, z) = (31, 42, 18)$ for the 377 keV interaction. It was observed that in many cases when the image charge sat atop a charge collection signal that the best fit achieved underestimated the image charge magnitude while the image charges external to the two interactions the events were correctly matched.
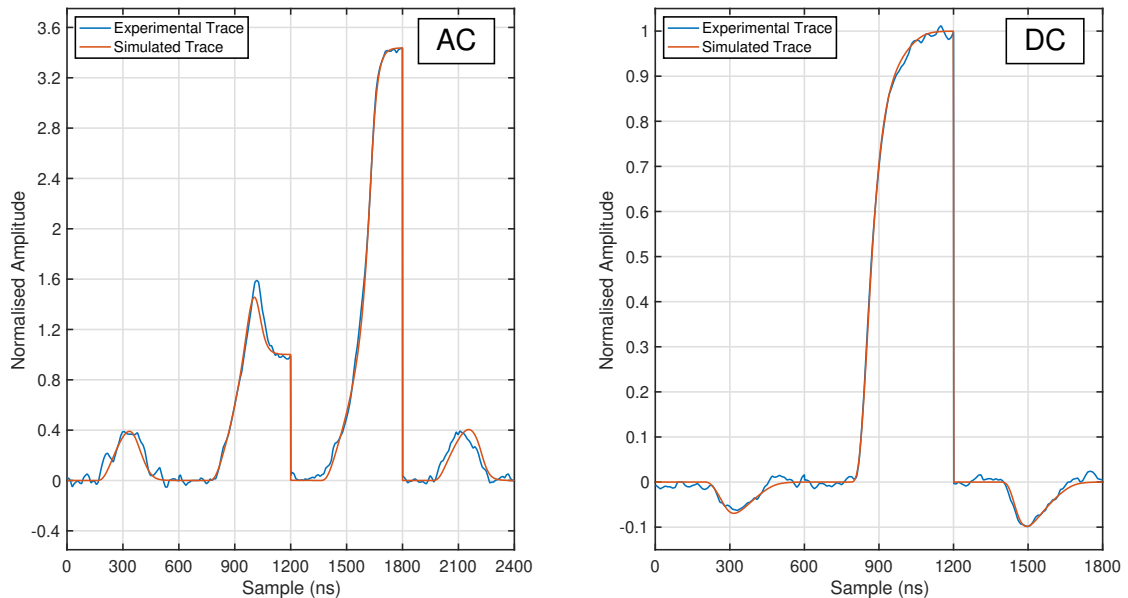
FIGURE 7.15: An example of the match found between the experimental and simulated supertrace for an adjacent F[2,1] event in which the charge collection signals are convoluted with image charges from the neighbouring interaction.

Fold 2,2

Events in which two strips on each face record charge collection are defined as F[2,2]. These events are not broken down into strip separation subcategories due to the large number of possible combinations. As the steps of the database algorithm are run twice for an F[2,2] event the computation time required is longer than that of an F[1,2] or F[2,1] event in which the fold 2 face positions are used as the initial guess for the fold 1 face. An example of an F[2,2] event is not provided as the output is similar to the fold 2 face of an F[1,2] & F[2,1] event but for both faces. It is treated separately due to the increased computation time. A more detailed computational assessment is presented in Section 8.3.

7.4   Event reconstruction

For the use of positions determined by database PSA in image reconstruction a check of both F[1,1] and F2 events was performed. This was to ensure that the algorithm could correctly select the first interaction in an F2 event as well as then assign all events to appropriate positions. The interaction selection in F2 was performed through the application of an event selection threshold. The results from this threshold and database PSA position assignment was then tested first by reconstruction of a γ-ray beam through the detector volume and then by the performance of single-detector image reconstruction.

7.4.1   Event Selection

In an F2 event, four positions are produced. These correspond to the interaction positions found by each set of signals for the two hit voxels. Final (x, y, z) positions are taken of each pair from the AC x position, the DC y positions and the AC and DC z-depth average. This produces two final (x, y, z) positions corresponding to the "low-energy" interaction and the "high-energy" interaction. To perform Compton imaging using F2 events within the HPGe the initial scatter event must be selected for use in conic back-projection. This is a Compton scatter interaction within the HPGe and is followed by either another Compton scatter or by photoelectric absorption. It possible to take a mean of these two interaction positions and weight it based upon energy deposition. This method, however, would yield incorrect interaction positions for every event and would so degrade image quality. Instead, in this work an energy threshold method has been employed to select the first scatter interaction in an event. This threshold was investigated for use with the GRI+ system and set at 450 keV [40] for imaging ^{137}Cs and other high energy isotopes. The total energy deposited in the HPGe across both interactions was compared against this threshold. If more than 450 keV was deposited then the higher energy of the two interactions was selected as the scatter event and the lower energy as the subsequent scatter or absorption. If less than 450 keV was recorded then this was reversed and the lower energy deposition selected as the initial scatter

interaction. This produced for each event a "wrong" position and a "correct" position to be used in image reconstruction. The "correct" position for imaging is the interaction selected as the Compton scatter as it forms the point from which the line is drawn for cone projection. The "wrong" event is therefore the secondary scatter or the photoelectric absorption following the initial interaction. This energy threshold based selection technique was tested in the following Sections.

7.4.2 Beam reconstruction

Reconstruction of a γ-ray beam path through the crystal checks both the distribution of F[1,1] events and the event selection threshold applied to F2 events. The γ-ray beam reconstructed was that of the collimated side scan beam used in the characterisation process. A single collimator location was selected and all full photopeak ^{137}Cs events recorded at this position investigated. The position selected was at a z-depth of 11 mm and central to strip DC06. F[1,1] and F2 events taken at this position were analysed with the grid-search algorithm presented in the previous section. The positions found for these events have been investigated separately for F[1,1] and F2. Intensity maps of the found interaction positions have been produced and are displayed in Figure 7.16. This figure shows the number of events found at each y-z mm position when the collimator is located at $z = 11$ mm. The intensity maps have been produced for F[1,1] events with no PSA applied (a), F[1,1] event following position determination by database PSA (b) and finally F2 event positions from database PSA when the "correct" event is selected (c) and when the "wrong" event is selected (d). The DC strips are parallel to the page and located at $z = 1$ mm. The AC strips, located at $z = 20$ mm, are normal to the page and numbered 1-12 from $y = 60$ mm to $y = 1$ mm while the collimated γ-beam is originating from below $y = 0$ mm.

When no PSA was applied the found positions are simply located centrally in z at $z = 10$ mm and centrally for each 5 mm wide AC strip through y. The application of database PSA to F[1,1] data in (b) results in a distribution of events located along the path of the γ-ray beam. The majority of events are placed at $z = 11$ mm. This corresponds to the collimator position. The distribution of events through y is most intense at $y = 4$ mm, the closest strip centre to the base of the detector. Very few events are placed in the final few mm of the detector at $y = 60$ mm. When F2 events are considered with database PSA analysis two positions are produced. Selecting based upon the energy threshold and taking the "correct" position (c) produces a distribution in y that is most intense at each AC strip centre. The z-depth intensity is highest at $z = 11$ mm but is more dispersed than the F[1,1]. If the "wrong" event selected for and the distribution of positions plotted (d) then the beam is not reconstructed through depth. Instead the events are distributed through all z-depths as well as through y.

To view the distribution better, a projection of events through y was produced and is displayed in Figure 7.17. The projection was produced for the F[1,1] distribution (b) and "correct" F2 distribution (c) and displays the number of events from all z-depths as a
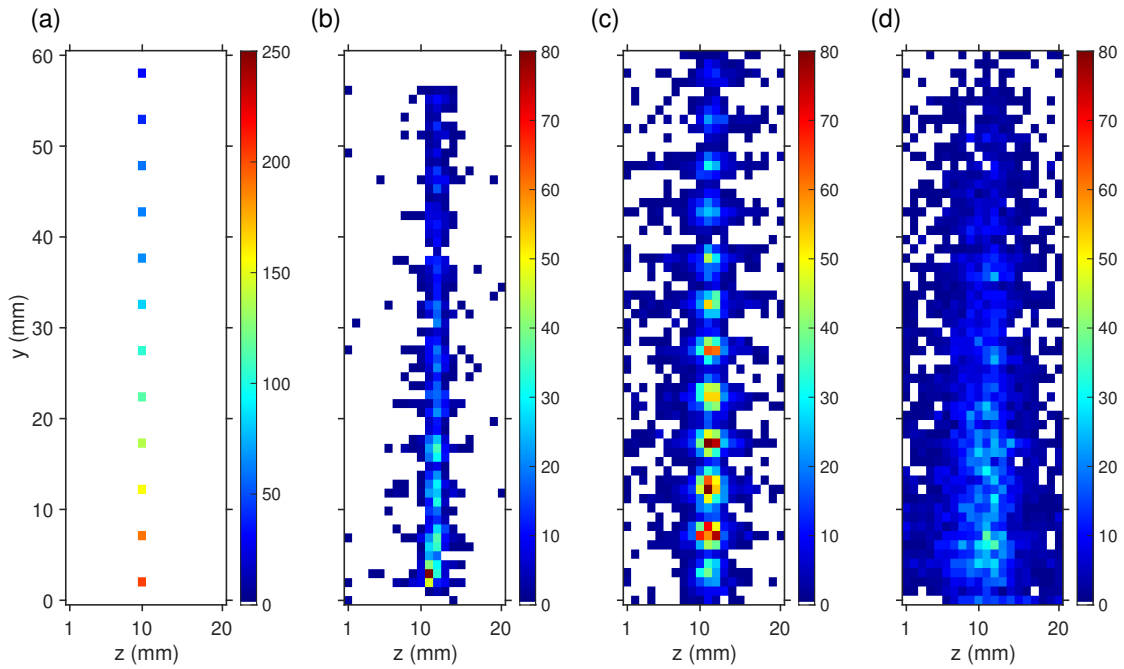
FIGURE 7.16: Distriubtion of ^{137}Cs full photopeak events through the detector in y-z from a $z = 12$ mm collimator position. Shown for F[1,1] positions produced with no PSA (a), F[1,1] after database PSA (b), fold 2 after database PSA with "correct" selected interactions (c) and "wrong" interactions (d).

function of y position. From this distribution the performance of the database algorithm for F[1,1] and F2 events can be assessed. It is assumed that an F[1,1] distribution would follow a simple γ-ray attenuation through the crystal with fewer events placed on or near the inter-strip gaps due to charge sharing affects resulting in F2 classification. An F2 distribution would be expected to have a larger number of events correspondingly placed on the inter-strip gaps and fewer events in the first few mm of the detector due to backscatter events leaving the system.
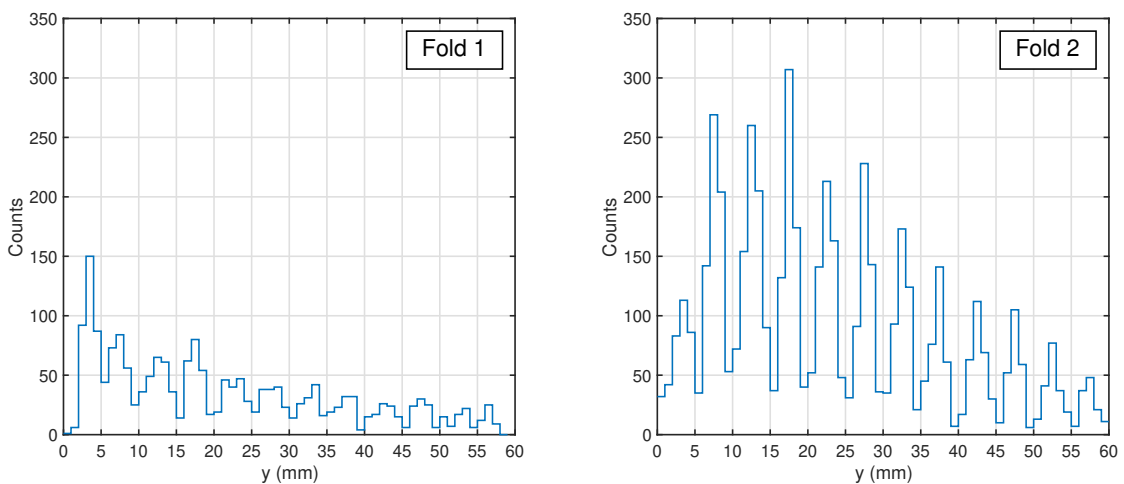
FIGURE 7.17: Projections of side scan position distributions from Figure 7.16 of F[1,1] positions following database PSA (left) and the "correct" F2 positions from database PSA (right).

The projection of F[1,1] events following database PSA in Figure 7.17 (left) follows the expected distribution through y. A larger number of events are observed close to the incident γ-ray beam at $y = 0$ mm compared to the number observed at the far end of the volume. Within all but one AC strip the events are clustered within the central 3 mm and the fewest at the edges. This is not the case for AC12, located at $y = 0$ to $y = 5$ mm. This is attributed to there only being one image charge for this strip for the algorithm to compare. The slight variation in distributions for each individual strip is attributed to the separate preamplifier convolution applied to each. When F2 events are considered (right) a similar distribution is observed to F[1,1]. Events are clustered in the central 3 mm of each strip apart from AC12, which is weighted towards the single neighbouring strip again. The distribution of events through y does not follow the γ-ray attenuation and fewer events are found in AC12 than the following strips. This is attributed to backscatter events that leave the system. If a backscatter event occurs in the first strip it is more likely that it will be lost from the crystal than if it backscatters further in the volume. It was expected that the F2 distribution would find a larger number of events at the strip gaps due to charge share events registering as multi-strip events. This is not observed to be the case and very few events are placed at the strip edges. This is not due to mistakenly selecting the "correct" event as the distribution of the "wrong" event through y does not show clustering at inter-strip gaps. This can be seen in Figure 7.16 (d). This clustering in the strip centre for F2 events is attributed to an algorithmic bias. This bias arises due to the difficulty in deconvolving charge collection signals from image charges. As mentioned in Section 7.3.2 these image charges are typically underestimated in magnitude. It is assumed that this contributes towards a bias of locating these events centrally in a strip in an F2 event in which the interactions are in adjacent strips. In Section 8.1.1 a breakdown of the event types is presented in detail. It is found that a large portion of 661.7 keV γ-ray F2 events occur in neighbouring strips. This results in this bias affecting a large portion of F2 events and causing a distribution weighted towards the strip centres.

This clustering towards the strip centre is not a desirable behaviour and represents mis-placement of the events. This will reduce the effectiveness of the algorithm when applied to F2 events and reduce the position resolution possible. The energy threshold applied to select the initial scatter event has been assessed to work well as the majority of events selected by the threshold as the initial interaction are successfully placed at a z-depth corresponding to the collimator position. Although the x-y position will not be obtained perfectly in F2 database analysis it can be stated that the z-depth determination appears to work well and will allow some improvement to position resolution still to be obtained from database PSA when applied to F2 events.

7.4.3 Single-detector imaging

Reconstruction of the γ-ray beam through the detector volume for F2 events demonstrated the ability both to select the scatter event using an energy threshold and to place

it in the correct location. This method did not show whether or not the position found for the second event was correct. To test the positions found for both the initial scatter event and the subsequent absorption single-detector, Compton imaging was performed. This was done by imaging a point source and reconstruction of its position through data taken only in the planar HPGe. By taking F2 data within the HPGe and deconvolving the z-depth interactions into two separate positions it is possible to back-project a cone using the image reconstruction technique described in Section 3.1.2. This is not possible with parametric PSA as the two interactions cannot be resolved into separate z-depths. Two points are required at different depths in order to be able to connect with a line from which to back-project the cone.
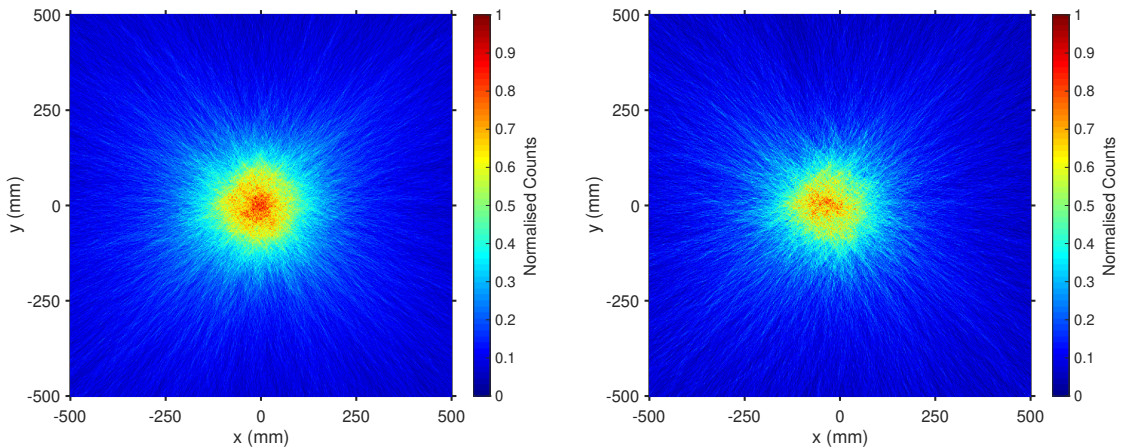
FIGURE 7.18: Number of reconstructed overlaps in x and y for a ^{137}Cs source located 17 cm from the HPGe crystal. Reconstruction performed for a centrally located source (left) and source offset at $x - 50$ mm (right) using 15,000 events for each.

Full photopeak F2 ^{137}Cs events were recorded in the HPGe for a point source placed in two positions. The source was placed 17 cm from the HPGe crystal; located first centrally and then offset at $x = -50$ mm. The offset source position was imaged in order to confirm that the events used in the image reconstruction were reconstructing the γ-ray source location correctly. For each run 15,000 F2, 661.7 keV, events were recorded and processed with the database algorithm. A requirement of 2 mm or more separation between the two found z-depth positions was imposed. This was to ensure that the events used were imageable. This reduced the number of events by ~35% of the events as they were formed of interactions that occurred within 2 mm of each other. The analytical imaging code was then used to reconstruct the image at the known stand-off distance of 17 cm using an image space of $1,500 \times 1,500$ mm^2, 20 points per degree, and a bin size of 1 mm. Intensity plots showing the number of conic overlaps at this stand-off distances are displayed in Figure 7.18 for the central source (left) and the $x = -50$ mm offset source (right). In each the number of counts has been normalised. Overlaps are found in a large portion of the image space. The highest concentration is found at $(0, 0)$ for the centrally located source (left) and offset in the negative x direction for the

$x = -50$ mm offset source (right). To view the location of the sources in x better and to quantify the resolution of these images slices have been taken at $y = 0$ mm.
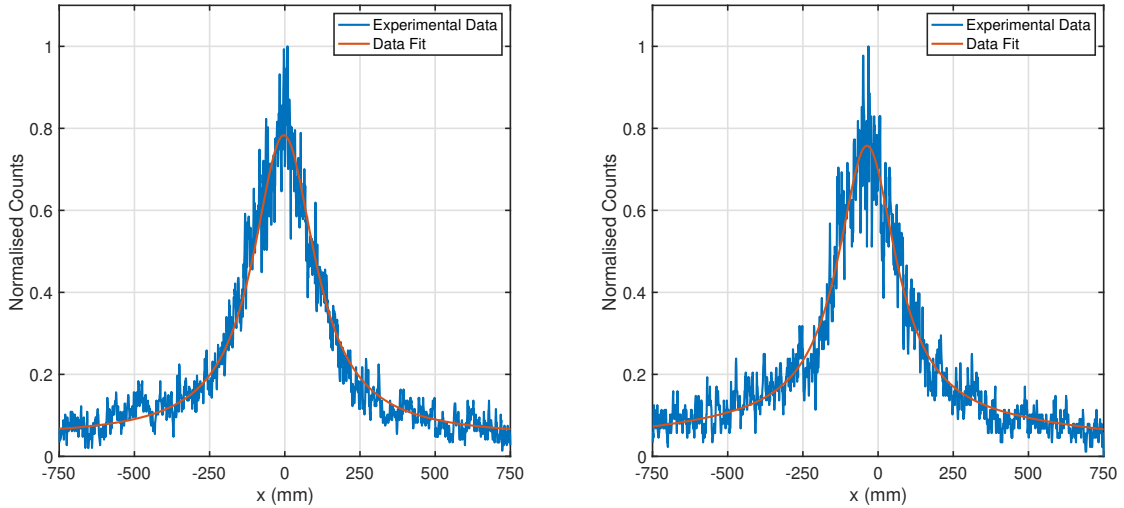
FIGURE 7.19: Number of reconstructed overlaps at $y = 0$ mm for a ^{137}Cs source located 17 cm from the HPGe crystal. Reconstruction performed for an $x = 0$ mm located source (left) and a $x = -50$ mm located source (right) when at least 2 mm separates the found z-depths.

These intensity slices are displayed in Figure 7.19 for the $(0, 0)$ mm source (left) and the $(-50, 0)$ mm source (right). Fits have been applied to the overlap intensity profiles produced from a Lorentzian placed atop a Gaussian background. The FWHM of the Lorentzian was taken as a quantification of the image resolution in x, the centroid of which represents the reconstructed γ-ray origin precision. The FWHM was found to be 253.1 ± 1.8 mm for the central source and 236.7 ± 4.8 mm for the offset source. The centroids were found to be at $x = -4.7$ mm and $x = -46$ mm for the central and offset sources respectively. These FWHM are large and represent a poor image quality considering the short stand-off distance of 17 cm. For comparison in the following section the FWHM when imaging ^{137}Cs at a stand-off of 10 cm with F[1,1] events and no PSA is found to be 22.4 ± 0.2 mm and 23.7 ± 0.1 mm in x and y respectively. The fit centroids of the single-detector images are found to be within 5 mm of the experimental source location for each reconstructed image. This represents a good ability to reconstruct the source location with single-detector Compton imaging, albeit with poor image resolution. It is inferred from this that the two interactions within the detector are resolved into two distinct z-depths and the initial event is correctly selected.

The poor image resolution was attributed to the small distance between the two resolved z-depths. In the typical, two planar-detector, Compton camera set-up at least 46 mm separates the two crystals. The larger separation between interaction points allows a more accurate calculation of the back-projected cone. This was confirmed by increasing the minimum distance between interaction points in single-detector imaging from a minimum of 2 mm to 5 mm. This reduced the number of imageable events to 20% of the original total. The image was then reconstructed for the centrally located
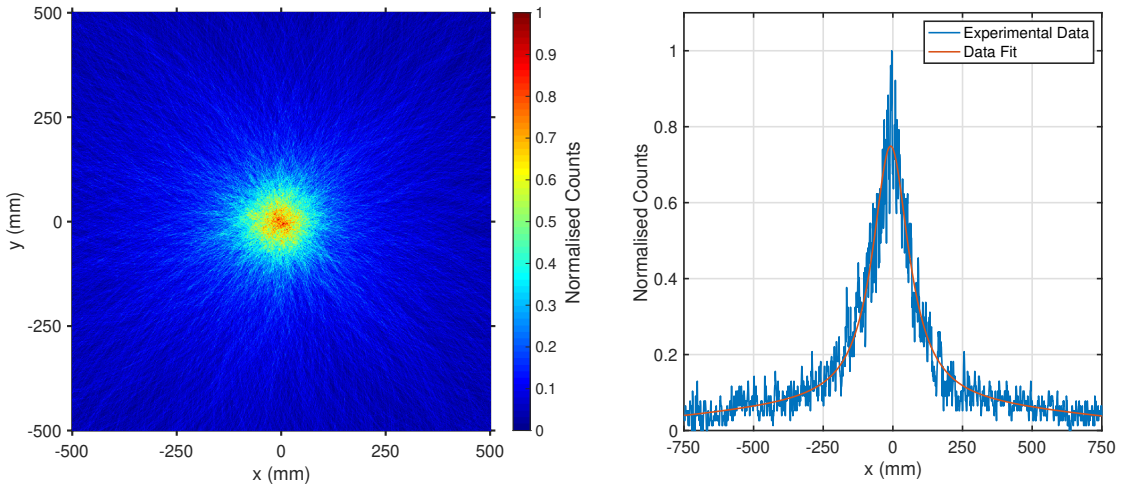
FIGURE 7.20: Number of reconstructed overlaps for a ^{137}Cs source centrally located 17 cm from the HPGe crystal when at least 5 mm separates the found z-depths. Overlaps shown in x-y (left) and as a function of x for a slice taken $y = 0$ mm (right).

source. The number of overlaps in x-y is shown in Figure 7.20 (left) along with the intensity profile taken from a $y = 0$ mm slice (right). The number of overlaps was again normalised. The FWHM of the Lorentzian fit was found to be 165.2 ± 3.3 mm and the centroid located at $x = -4.2$ mm. This was a significant reduction in the FWHM of over 90 mm compared to that produced with 2 mm minimum z-depth separation. The increased error in the fit is a consequence of the reduction in imaged events due to the cut-off.

The ability to reconstruct a γ-ray source location through single-detector imaging demonstrates the effectiveness of the database algorithm in deconvolving multiple z-depth interactions. This allows the use of F2 events in imaging with confidence that it is an improvement over simply placing the event at the mid-point of the detector z-depth, the most that could be previously achieved. This also demonstrated the ability of the simple energy threshold method to select the initial scatter event in an F2 interaction and so allows use of these events in F2 image reconstruction. This serves as sufficient verification for the database methods employed and allows quantification of the database PSA method and algorithm to be performed for both single interaction and multi-interaction events.

7.5   Summary of Results

The optimisation process of the ADL simulation has been presented through comparison of the simulated signals to average experimental signals at known positions from the side scan characterisation. This work included the generation of electric and weighting potentials using an optimised impurity gradient through the detector. This was found to differ to the manufacturer reported impurity values at the AC and DC contacts. In conjunction with this the mobility parameters have been changed to reflect better the cooler set-point temperature and a new set of simulated signals produced using mobility

parameters corresponding to 88 K. This was similar to the cooler set-point of 88.15 K. A preamplifier convolution was then applied individually to each strip in order to achieve the best match.

Validation of the pulse shapes across the detector face was then carried out. This was done through comparison of the pulse shapes across the surface to average signals produced at known positions from the ^{241}Am characterisation surface scan. It was confirmed that the image charges were of appropriate magnitudes across the width of a strip. The pulse response through the depth of the detector was confirmed to be appropriate through an RMSD comparison to the experimental ^{137}Cs side scan signals. The difference in z-position of the experimental and simulated signals was found to be 2 mm or less away from the collimator position for 96.9% of AC events and 95.5% of DC events. From these comparisons the simulation was judged to be validated and suitable for use in PSA.

A grid-search algorithm was developed to perform a comparison between the simulated database of signals and experimental signals in order to find the best matching position within the detector for each interaction. The algorithm script, developed within MATLAB, was written to take an input of signals from the HPGe representing an interaction. These represent the charge collection pulse observed on each set of contacts as well as the nearest neighbouring image charges. The algorithm processes the experimental input through alignment to t30 and interpolation to a 1 ns basis, the same as the simulated database of signals. Separate methods were developed to process the simplest data type, F[1,1], to the more complex F2 type in which multiple signals are convoluted with each other. A simple RMSD comparison was developed to compare all 500 possible positions for a F[1,1] while a more complex adaptive grid-search method, involving an initial guess, a coarse grid-search, and then a fine grid-search, was used to process multi-fold events.

An energy threshold developed for use with the Compton camera was employed to select the initial scatter in a multi-interaction event. The threshold was tested through the successful reconstruction of a collimated γ-ray beam through the detector volume. Single-detector image reconstruction was also performed and the source position in the image space successfully located through Compton image reconstruction using F2 interactions within the HPGe.

Chapter 8

Imaging Results

8.1 Imaging Resolution

Having validated both the match between experimental and simulated charge collection signals and the performance of the database algorithm for single and double-interaction events, the performance of database PSA was quantified. This was performed through the assessment of the image resolution at various source distances as well as the ability to resolve multiple point sources. The image resolution was quantified as the FWHM of the Lorentzian fit in x and y produced by the analytical reconstruction code from the conic overlap distributions. This FWHM quantifies the image resolution as a mm value in the two axes. The average of the FWHM in x and y was found as an angular resolution allowing direct comparison of this system to other position sensitive imaging systems.

8.1.1 Database Quantification

An initial quantification of database PSA was performed on a near-field located 0.25 MBq ^{137}Cs source, placed 10 cm from the Si(Li) cryostat centrally in x and y. The ^{137}Cs source was used for the quantification as the characteristic 661.7 keV photopeak is analogous to those energies present in a decommissioning environment. The image resolution was assessed separately for F[1,1] events, F[1,2] & F[2,1] events, and F[2,2] events in the HPGe. In each case only F[1,1] events in the Si(Li) were utilised and the coaxial detector was not used, resulting in a two-tier system. Data were collected for 75.8 hours as the coincidence trigger rate was small at only ~40 events per second. The distance between the two planar crystals was recorded as 53 mm and signals from all 48 channels were recorded when both tiers of the system triggered. Imageable events comprised those which recorded an F[1,1] event in the Si(Li) and an F[1,1], F[1,2], F[2,1], or F[2,2] event in the HPGe. These events were named after the type of interaction occurring in the HPGe and a breakdown of those which passed a 661.7 keV photopeak gate are displayed in Table 8.1. F2 refers to the combination of F[1,2], F[2,1] and F[2,2]

events. Coincidence energy sum spectra are displayed for the HPGe event types in Figure 8.1. F[1,2], F[2,1], and F[2,2] events have been combined into F2 for these spectra.

Breakdown of Imageable Event Types

Data Type (HPGe)	Number of Events	% of Imageable Events
F[1,1]	228,130	31.2
F[1,2] and F[2,1]	202,067	32.1
F[2,2]	267,997	36.7
F[1,1] and F2	730,938	100

TABLE 8.1: Breakdown of imageable event types recorded from a ^{137}Cs source located 10 cm from the system. All events are two-tier with an F[1,1] event occurring in the Si(Li) and either an F[1,1] or an F2 interaction in the HPGe.
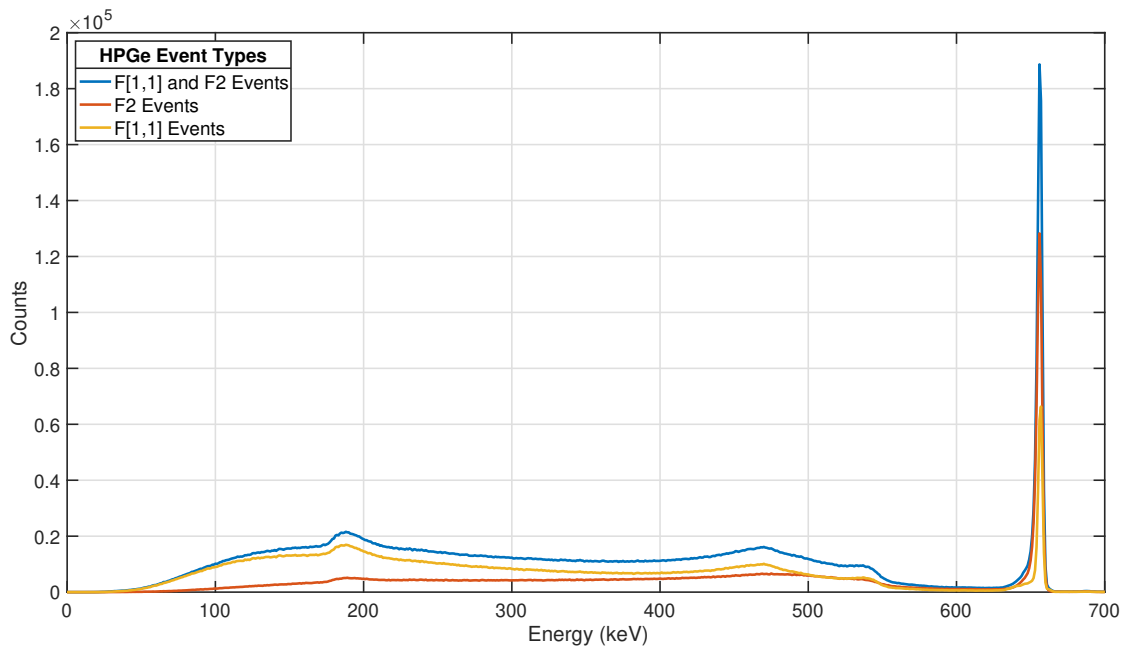
FIGURE 8.1: Coincidence energy sum spectra produced from imageable ^{137}Cs events. Events consist of an F[1,1] event in the Si(Li) and F[1,1] or F2 event in the HPGe.

A total of 730,938 full-photopeak events were recorded and resulted in reconstructed images with high statistics. This enabled reliable fits to be made to the data. Of those full-photopeak, events roughly one third fell into each category of HPGe interaction type. This resulted in 68.8% of events being fold 2 of some description, and the remaining 31.2% fold 1. The 228,130 imageable, F[1,1] HPGe full-photopeak events, represented 4.8% of the total events that fell into the F[1,1] spectrum, including the full ^{137}Cs Compton continuum. For F2 events the photopeak events were much higher at 17.9% of the total spectrum.

All images were reconstructed and fitted in a 600×600 mm^2 image space in 1 mm bins and the cones back-projected with 10 points per degree. The data were assessed with no PSA performed on the Si(Li) so that the contribution from PSA in the HPGe

to the image resolution could be observed. The database was utilised in the manner described in Section 7.3 and was applied to events passing a 656-664 keV gate set on the 661.7 keV photopeak. No effort was made to exclude multi-interaction events within a single voxel registering as fold 1 interactions. In future excluding these events would improve the image resolution produced from all event types.

Data Type (HPGe)	% of Events	x FWHM (mm)	y FWHM (mm)	Angular Res. (degrees)
No PSA Applied				
F[1,1]	31.2	22.4 ± 0.2	23.7 ± 0.1	13.2 ± 0.1
F[1,2] and F[2,1]	32.1	23.3 ± 0.1	24.4 ± 0.1	13.8 ± 0.1
F[2,2]	36.7	29.5 ± 0.2	27.5 ± 0.1	16.2 ± 0.1
F2 All types	68.8	26.5 ± 0.1	25.8 ± 0.1	14.9 ± 0.1
F[1,1] and F2	100	25.0 ± 0.1	25.0 ± 0.1	14.3 ± 0.1

TABLE 8.2: FWHM and angular resolution from the reconstructed image of a 10 cm stand-off ^{137}Cs source for various HPGe fold categories.

The 10 cm stand-off ^{137}Cs source was first imaged with no PSA applied to either detector. This was to quantify the base line image resolution of the system without PSA. The image resolutions measured are displayed in Table 8.2. The best angular resolution of $13.2 \pm 0.1°$ was measured when only F[1,1] events in the HPGe and Si(Li) were imaged. A small degradation in the angular resolution of $0.6 \pm 0.1°$ occurs when F[1,2] & F[2,1] are imaged and a further degradation of $2.4 \pm 0.1°$ occurs when F[2,2] are imaged. The angular resolution measured when imaging all F2 events together was about half-way between the resolutions found when imaging F[2,2] and F[1,2] & F[2,1] separately. This was due to the near equal contribution of each to the total number of events imaged. The imaging resolution for F[1,1] and F2 events combined was also calculated and found to be between the value of F[1,1] and F2 events. These followed the expected trend of increased total event fold resulting in a degradation of image resolution while also allowing the inclusion of more events. These values indicate that a good image resolution is achievable with the GRI+ system compared to competing image systems discussed in the Introduction and Chapter 3.

The deterioration of resolution achieved with F[2,2] events over F[1,1] is worse than that found from F[1,2] & F[2,1] when compared to F[1,1]. This is due to the larger maximum difference possible between the two events. In F[1,2] & F[2,1] events in neighbouring strips the interactions can be at maximum 10 mm apart. In an F[2,2] event the interactions occur in neighbouring pixels in which no strips are shared between the two interactions. As such, the maximum distance in a diagonally neighbouring pixel is ~14.14 mm as they can be of distance 10 mm in both x and y from each other. As such, an incorrect selection of the first event in a multi-pixel event would correspond to a larger mm difference from the true value and so a worsening in the resolution.

Database PSA Applied

Data Type (HPGe)	% of Events	x FWHM (mm)	y FWHM (mm)	Angular Res. (Degrees)
F[1,1]	31.2	17.6 ± 0.1	18.7 ± 0.1	10.4 ± 0.1
F[2,1] and F[1,2]	32.1	19.8 ± 0.1	20.9 ± 0.1	11.6 ± 0.1
F[2,2]	36.7	21.0 ± 0.1	22.0 ± 0.1	12.3 ± 0.1
F2 All types	68.8	20.4 ± 0.1	21.5 ± 0.1	11.9 ± 0.1
F[1,1] and F2 All types	100	19.3 ± 0.1	20.0 ± 0.1	11.3 ± 0.1

TABLE 8.3: FWHM and angular resolution from reconstructed images of a 10cm stand-off ^{137}Cs source for HPGe fold categories with database PSA applied.

The same events comprising the results in Table 8.2 were then reassessed with PSA. The signals from the HPGe were compared to the database and the grid-search algorithm used to find new mm positions representing the points of interactions. The analytical imaging code was again used to produce reconstructed images and the FWHM and angular resolution found. These are presented in Table 8.3. The same trend in angular resolution is observed when database PSA was applied as when images are constructed with no PSA. The best angular resolution of $10.4 \pm 0.1°$ was measured using F[1,1] events with degradation occurring every time the total fold used for the image was increased. An improvement is observed for every single fold type in the HPGe when database PSA is applied compared to the previously presented resolutions from non-PSA analysis. The worst angular resolution from database PSA of $12.3 \pm 0.1°$, obtained from F[2,2], was better than the best angular resolution achieved without PSA, corresponding to $13.2 \pm 0.1°$ using F[1,1] events. The overall improvement was $2.8 \pm 0.1°$ for F[1,1] events and $3.0 \pm 0.1°$ for F[1,1] and F2 together. This corresponds to an improvement of $21.2 \pm 0.3\%$ for F[1,1] and $21.0 \pm 0.3\%$ and F2 together compared to when no PSA is applied.

Database PSA F[2,1] and F[1,2] Types

Data Type (HPGe)	% of Events	x FWHM (mm)	y FWHM (mm)	Angular Res. (degrees)
Adjacent Interactions	27.6	19.6 ± 0.1	21.1 ± 0.1	11.6 ± 0.1
1 Strip Separation	2.9	22.2 ± 0.2	23.0 ± 0.1	12.9 ± 0.1
>1 Strip Separation	1.6	20.2 ± 0.3	18.7 ± 0.3	11.1 ± 0.2
Combined	32.1	19.8 ± 0.1	20.9 ± 0.1	11.6 ± 0.1

TABLE 8.4: FWHM and angular resolution from reconstructed images of a 10 cm stand-off ^{137}Cs source for HPGe F[1,2] & F[2,1] subsets after the application of database PSA.

The events comprising the F[1,2] & F[2,1] data type were investigated as part of the database performance assessment. They were broken down into three categories

based upon the separation of interactions on the fold 2 observing face. These were: adjacent-strip interactions, non-adjacent with 1 strip separation between interactions, and non-adjacent with greater than 1 strip separation. The number of events as a % of the total imageable events along with determined FWHM and angular resolutions are given in Table 8.4. From these three fold 2 categories the majority of events are seen to come from adjacent interactions while the fewest occur when the γ ray must travel at least 5 mm between interactions to a non-adjacent strip. In an F[1,2] & F[2,1] event ~86% of the fold 2 events were found to occur in adjacent strips. These events yielded an angular resolution of $11.6 \pm 0.1°$. The smallest percentage of events, occurring more than 1 strip apart, yielded the best angular resolution of the F[1,2] & F[2,1] subcategories at $11.1 \pm 0.2°$. Those events with 1 strip separation produced a similar angular resolution to that found from adjacent events. This distribution of events is specific to the 661.7 keV energy imaged. A higher energy γ-emitting source would produce a different distribution. Inclusion of three-tier events would also change the distribution due to the inclusion of forward scattered events that were otherwise lost.

The achievement of the best resolution from non-adjacent events with greater than 1 strip separation is explained through the lack of convolution of charge collection and image charge signals with each other. These interactions produce signals that are distinct from one another and so the database algorithm can find a good match for both. Non-adjacent interactions with 1 strip separation produced events in which the image charges from each charge collection signal were convoluted. These were observed to introduce larger RMSD values for the best found fits compared to non-adjacent events. This introduced a greater uncertainty when finding matches. As such, the database did not produce such a good match for these event types. These events are of similar angular resolution to those occurring in neighbouring strips in which the image and real signals are convoluted. F[2,2] event subcategories were not imaged separately in such a way due to the large number of possible permutations possible for an event registering two hit pixels. They would be expected to follow the same distribution with the majority occurring in diagonally neighbouring pixels, the closest possible pixel-pair in an F[2,2] scenario.

To determine the best resolution possible from the system for ^{137}Cs at 10 cm stand-off, the FWHM were calculated for the same results with the addition of parametric PSA applied to the Si(Li). The Si(Li) parametric PSA comprised x-y PSA through image charge asymmetry comparison, although scope remains in future work to improve the results further through the application of z-PSA in the Si(Li). These results are displayed in Table 8.5 with F[1,1], F[1,2] & F[2,1], and F[2,2] imaged both separately and together. An improvement in the angular resolution of between 1.3° and 1.9° is found for all data types compared to the previously found resolutions without parametric PSA applied to the Si(Li) in Table 8.3. Sub 10° resolution is measured for F[1,1] events as well as F[1,1] and F2 combined. The combination of parametric PSA applied to the Si(Li) and database applied to the HPGe yields a total improvement of $35.6 \pm 0.5\%$ for

Database PSA Applied and Si(Li) Parametric PSA

Data Type (HPGe)	% of Events	x FWHM (mm)	y FWHM (mm)	Angular Res. (Degrees)
F[1,1]	31.2	14.5 ± 0.1	15.5 ± 0.1	8.5 ± 0.1
F[2,1] and F[1,2]	32.1	17.3 ± 0.1	18.7 ± 0.1	10.3 ± 0.1
F[2,2]	36.7	18.3 ± 0.1	19.6 ± 0.1	10.8 ± 0.1
F2 All types	68.8	17.8 ± 0.1	19.2 ± 0.1	10.6 ± 0.1
F[1,1] and F2 All types	100	16.2 ± 0.1	17.5 ± 0.1	9.6 ± 0.1

TABLE 8.5: FWHM and angular resolution from reconstructed images of a 10 cm stand-off ^{137}Cs source for HPGe fold categories with database PSA applied. Parametric PSA is applied to the Si(Li).

F[1,1] HPGe events compared to when no PSA is applied. The improvement for F[1,1] and F2 combined is 32.9% over the non-PSA results. The results embody the successful development and application of database PSA to both single interaction events as well as multi-interaction, convoluted events. Consistent improvements in angular resolution was achieved for all studied event denominations.

8.2 Parametric and Database PSA Comparison

The benchmarking of database PSA was compared to those results achievable through parametric PSA for F[1,1] events. The results are compared in Table 8.6 for no applied PSA, parametric PSA applied to the HPGe and database PSA applied to the HPGe. Results are also shown for parametric and database methods with the addition of parametric PSA applied to the Si(Li). In each case the exact same events were analysed with no PSA, parametric PSA and database PSA. The improvement in angular image resolution when applying the two PSA methods to F[1,1] events in the HPGe compared to no PSA is:

Parametric PSA - $19.7 \pm 0.2\%$ improvement over no PSA

Database PSA - $21.2 \pm 0.3\%$ improvement over no PSA

These results are comparable, though a slightly larger improvement is achieved through database compared to parametric PSA. When parametric PSA is applied to Si(Li) events along with PSA in the HPGe the results are:

Parametric PSA - HPGe and Si(Li) - $34.1 \pm 0.5\%$ improvement over no PSA

Database PSA in HPGe and Parametric PSA in Si(Li) - $35.6 \pm 0.5\%$ improvement over no PSA

It is expected that the improvement achieved for both HPGe PSA methods with the addition of parametric PSA in the Si(Li) would be the same. This is seen to be the case with a further improvement of 14.4% is measured for both. Overall the improvement in image quality when applying database methods is small relative to that achieved with parametric methods. The difference between the image resolution measured from each method is only 0.2° and could be due to statistical errors.

F[1,1] HPGe PSA Comparisons

PSA Type	x FWHM (mm)	y FWHM (mm)	Angular Res. (Degrees)
No PSA	22.4 ± 0.1	23.7 ± 0.1	13.2 ± 0.1
HPGe Parametric PSA	17.9 ± 0.1	19.0 ± 0.1	10.6 ± 0.1
HPGe Database PSA	17.6 ± 0.1	18.7 ± 0.1	10.4 ± 0.1
HPGe Parametric PSA + Si(Li) PSA	14.8 ± 0.1	15.6 ± 0.1	8.7 ± 0.1
HPGe Database PSA + Si(Li) PSA	14.5 ± 0.1	15.5 ± 0.1	8.5 ± 0.1

TABLE 8.6: Comparison of no PSA, parametric PSA and database PSA applied to F[1,1] events in the HPGe with and without parametric PSA applied to the Si(Li).

As discussed at the beginning of this section, this represents the application of PSA to the 31.2% of imageable events which are F[1,1] interactions within the HPGe. The remaining 68.8% are multi-interaction, F2, events within the HPGe and so cannot be analysed with parametric PSA but can be processed with database PSA. A comparison can therefore be made as this represents the maximum imaging efficiency of the system as it has been presented in this work. The results when no PSA has been applied, when parametric PSA has been applied where eligible, and when database PSA has been applied to HPGe events and parametric to Si(Li) events are displayed in Table 8.7. An angular resolution of $14.3 \pm 0.1°$ is measured when imaging F[1,1] and F2 events together with no PSA methods applied. This is improved by $18.2 \pm 0.3\%$ to $11.7 \pm 0.1°$ when applying parametric PSA to eligible events. When database PSA is applied to all HPGe interactions and parametric PSA to Si(Li) interactions, the image resolution is improved by $35.6 \pm 0.5\%$ and is $9.6 \pm 0.1°$. When applying database PSA to the HPGe F[1,1] and F2 events and parametric PSA to the Si(Li), the final angular image resolution measured is degraded by $1.1 \pm 0.1°$ compared to that measured from just F[1,1] events. The number of coincident events imaged is increased from 228,130 to 730,938, an increase of more than three times. This represents a significant increase in imaging efficiency at the cost of a small decrease in angular resolution. If parametric methods only were used, the degradation in angular image resolution would be $3.0 \pm 0.1°$ for the same increase in imaging efficiency. It can be concluded that when imaging sources at 10 cm stand-off, the improvement in angular image resolution achieved through use of database PSA is significantly greater than that achieved with parametric PSA when maximising imaging efficiency.

F[1,1] and F2 HPGe PSA Comparisons

PSA Type	x FWHM (mm)	y FWHM (mm)	Angular Res. (Degrees)
No PSA	25.0 ± 0.1	25.0 ± 0.1	14.3 ± 0.1
HPGe Parametric PSA + Si(Li) PSA	20.5 ± 0.1	20.4 ± 0.1	11.7 ± 0.1
HPGe Database PSA + Si(Li) PSA	16.2 ± 0.1	17.5 ± 0.1	9.6 ± 0.1

TABLE 8.7: Comparison of no PSA, parametric PSA and database PSA applied to F[1,1] and F2 events in the HPGe with parametric PSA applied to the Si(Li).

It is possible that a greater improvement in image resolution can be still achieved through application of database PSA. In this work, multiple interactions occurring within a single pixel have not been classified as multi-interaction events. This has resulted in F[1,1] events that are made up of two interactions or more. It was decided during development of the grid-search algorithm not to treat these events separately due to the difficulty in selecting them. As it stands, they are fitted as a single charge collection signal by the algorithm. If these signals can be correctly identified as multi-interaction, perhaps through differentiation of the signal, then a fold 2 database PSA approach could be correctly applied to them. Parametric PSA would still be incapable of processing these events correctly, and instead would find mean depth-of-interaction positions based upon analysis of the total rise times. Application of database PSA in this scenario would further improve the image resolution. Due to the small voxel sizes in this work it is not thought that these single-pixel, multi-interaction events would be as numerous as in large-volume segmented detectors, such as those used in AGATA [22], but would still number enough to yield a measurable improvement in image resolution if correctly analysed.

8.2.1 Large Stand-Off

A large source stand-off of 1 m was imaged. This was to investigate whether the improvement of database PSA over parametric was independent of imaging distance. A 1 m stand-off was also more analogous to the nuclear decommissioning environments for which the Compton camera system was designed. A 16 MBq ^{137}Cs source was placed centrally to the system at 1 m stand-off and data were recorded for 3.1 hours with 138 coincidence triggers registered per second. The separation between the two planar crystals was 53 mm and the system was operated with all three tiers active. All 48 channels were recorded when both planar tiers of the system triggered. The breakdown of imageable full-photopeak HPGe event types is provided in Table 8.8. The difference in distribution of F[1,1] and F2 event types compared to that observed previously in Table 8.1 is due to operation of the system with all three-tiers active. It is more likely that F[1,1] events are recorded in both the planar detectors when the coaxial is operated due to the large probability of forward scattering at these energies. The FWHM obtained

from F[1,1] events in the HPGe without PSA applied was compared after the application of parametric PSA and database PSA in Table 8.9. The FWHM of F2 events and F[1,1] and F2 events combined are also given after database PSA was applied to the HPGe and parametric to the Si(Li). The images were reconstructed with 10 points per degree and an image space of 1,500 mm.

Breakdown of Imageable Event Types

Data Type (HPGe)	Number of Events	% of Imageable Events
F[1,1]	15,497	37.0
F[1,2] and F[2,1]	12,393	29.6
F[2,2]	13,996	33.4
F[1,1] and F2	41,886	100

TABLE 8.8: Breakdown of imageable event types recorded from a ^{137}Cs source located 1 m from the system. All events are two-tier or three-tier with an F[1,1] event occurring in the Si(Li), either an F[1,1] or an F2 event in the HPGe, and potentially an interaction in the tertiary coaxial detector.

The previously observed trend is again found with an increased event fold imaged resulting in a degraded angular resolution. For F[1,1] events an improvement of $33.3 \pm 0.5\%$ in angular resolution is measured for parametric PSA over no PSA while database PSA in the HPGe and parametric in the Si(Li) produces a $36.8 \pm 0.5\%$ improvement. This is a larger improvement relative to no PSA compared that measured at 10 cm stand-off. At 10 cm the best angular resolution measured is $8.5 \pm 0.1°$ as opposed to the $5.5 \pm 0.1°$ measured at 1 m. When F2 events were imaged parametric methods could not be applied to the HPGe, and database PSA resulted in an improvement of $37.6 \pm 0.5\%$ when compared to no PSA. When F[1,1] and F2 events are imaged an angular resolution of $9.8 \pm 0.1°$ is found when no PSA is applied. Application of parametric PSA to the HPGe and the Si(Li) detectors reduces this to $7.7 \pm 0.1°$, an improvement of $2.1 \pm 0.1°$. A larger improvement of $3.4 \pm 0.1°$ is measured when database PSA is applied to all events in the HPGe, resulting in an angular resolution of $6.4 \pm 0.1°$. In this case it can be seen that the improvements yielded from database PSA are larger than those from parametric PSA. This is a significant improvement from database PSA when imaging F[1,1] and F2 events. It can be concluded to perform well and to improve the image quality of the camera at 1 m stand-off. It is predicted that large stand-off distances would make the improvement even larger relative to that achieved with parametric PSA.

The performance of the system at 1 m stand-off was further tested through reconstruction of an offset source. The ^{137}Cs source was offset 30 cm in the positive x direction and image reconstruction performed at the known z-distance utilising database PSA on all F[1,1] and F2 events in addition to parametric PSA on Si(Li) events. Data were recorded for 3.83 hours with 130 coincidence triggers per second. A slice was taken of the reconstructed image at $y = 0$ mm and fits applied. The centroid of the Lorentzian fit was taken as the determined source location. This was also performed for the centrally

F[1,1] HPGe PSA Comparisons

+ Si(Li) Parametric PSA

HPGe PSA Type	x FWHM (mm)	y FWHM (mm)	Angular Res. (Degrees)
No PSA	156.7 ± 2.3	145.7 ± 2.0	8.7 ± 0.1
Parametric	101.9 ± 1.1	101.2 ± 1.0	5.8 ± 0.1
Database	94.6 ± 0.9	97.4 ± 1.0	5.5 ± 0.1

F2 All Types HPGe PSA Comparisons

+ Si(Li) Parametric PSA

HPGe PSA Type	x FWHM (mm)	y FWHM (mm)	Angular Res. (Degrees)
No PSA	189.1 ± 0.3	191.0 ± 2.5	10.9 ± 0.1
Database	112.6 ± 1.0	124.3 ± 1.0	6.8 ± 0.1

F[1,1] and F2 HPGe PSA Comparisons

+ Si(Li) Parametric PSA

HPGe PSA Type	x FWHM (mm)	y FWHM (mm)	Angular Res. (Degrees)
No PSA	175.1 ± 1.9	167.8 ± 1.8	9.8 ± 0.1
Parametric	138.8 ± 1.2	131.1 ± 1.1	7.7 ± 0.1
Database	110.8 ± 0.8	119.6 ± 0.8	6.4 ± 0.1

TABLE 8.9: FWHM and angular resolution from reconstructed images of a 100 cm stand-off ^{137}Cs source for HPGe fold categories with database PSA applied. Parametric PSA is applied to the Si(Li).

located source previously discussed in this section. From these fits the ability of the system to determine x-y position was assessed and it was also checked that the database PSA could correctly find the location from the chosen first event.

The slices of the reconstructed image taken at $y = 0$ mm are presented in Figure 8.2 for the centrally located source (left) and the 30 cm offset source (right). The experimental data are shown along with the combined Lorentzian and Gaussian fit and its individual components. The Gaussian background of the offset source is located centrally to the system's FoV. This is attributed to the efficiency of the camera being highest in the centre, so the largest background occurs there despite the source being offset. The centroids of the fit were found to be at $x = 0.3$ mm and $x = 301$ mm which matches well with the source placement. Differences between the known position and the found position can be attributed to errors in the point source placement and so the source location was correctly determined.
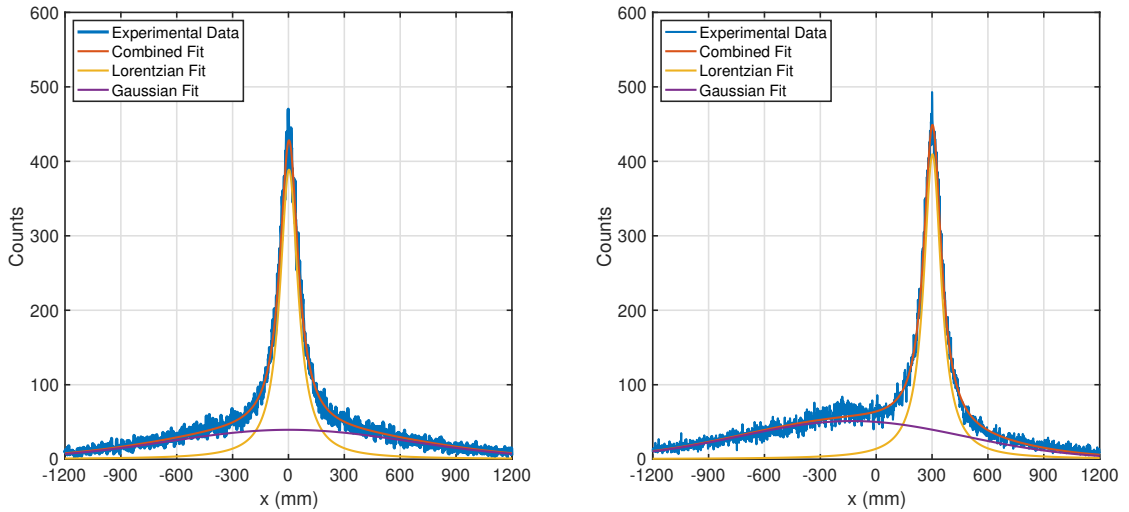
FIGURE 8.2: Slices from a reconstructed image of a 1 m stand-off source located centrally (left) and offset 30 cm in x (right). Image reconstructed using database PSA on F[1,1] and F2 events in the absorber in addition to parametric x-y PSA in the Si(Li).

8.2.2 Multi-source Imaging

The final check of the database algorithm and achievable results was performed with multiple γ-ray sources. This was to assess the abilities of the parametric and database PSA methods to resolve separate point sources at different stand-offs and separations. A total of 9 position combinations were imaged with two ^{137}Cs point sources. The sources were placed at $y = 0$ mm and separations of 2, 4 and 8 cm at stand-off distances of 10, 20, and 30 cm. The sources were offset equally either side from $x = 0$ mm. The sources selected were of similar activity and at each position the same number of coincident HPGe F[1,1] events (24,000) and HPGe F2 events (37,000) were collected. This required a variable data collection time for each run and ultimately the data set with the lowest statistics dictated the number of events chosen for comparison. Only two-tier events were considered. For each position the image was reconstructed with 10 points per degree and an image space of 400 mm. The separation between the two crystals for all 9 positions was 43 mm, 10 mm closer than previous runs demonstrated. A slice was taken of the reconstructed images at $y = 0$ mm and the experimental data are shown for each position along with the combined Gaussian background and the individual Lorentzian fits to the two sources.

The slices displaying the number of conic overlaps for F[1,1] events produced from database PSA determined positions is shown in Figure 8.3. Each column represents a different separation between the two sources while the rows each stand-off distance. A trend is observed in that larger separation between point sources results in clearer separation between peaks. This trend is also present for stand-off distance with nearer stand-offs resulting in clearer peaks. The most clearly resolvable peaks are at the smallest stand-off distances and largest separations while the largest stand-off and smallest separations is unresolvable. The 2 cm separation is also unresolvable at 20 cm but distinguishable at
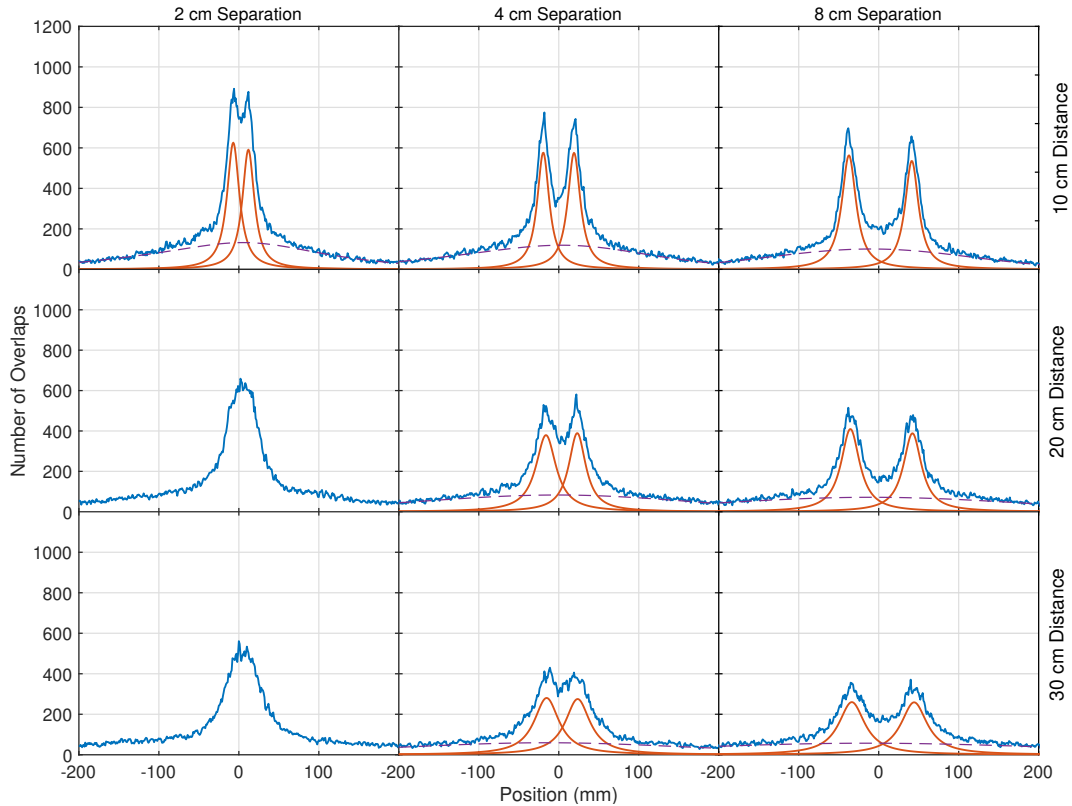
FIGURE 8.3: Image reconstruction slice taken at $y = 0$ mm for two ^{137}Cs sources at a combination of three separation and three stand-off distances. Events used were HPGe F[1,1] events, analysed with database PSA and Si(Li) parametric PSA.

2 cm stand-off. Resolving of the conic overlaps into two distinct peaks represents the system's ability to resolve individual γ-ray origins that are in close proximity. At 30 cm stand-off the two sources can be clearly resolved as two separate peaks when separated by 8 cm, corresponding to a separation of 7.6°. This clearly demonstrates better image resolution and resolvability than that provided by Polaris-H, discussed in Chapter 1.

When a low number of events are recorded it is desirable to include higher fold events. Including F2 events increases the number of overlaps in the image but degrades the resolution. Applying database PSA has been previously shown to recover some of the degraded angular resolution. To demonstrate this, F2 events were included and a comparison made between parametric and database PSA. The 9 intensity slices were reproduced with F[1,1] and F2 events combined, increasing the total number of events from 24,000 to 61,000. Parametric PSA was applied to the F[1,1] events and to the Si(Li). The slices are displayed in Figure 8.4. The resulting trends are the same as observed for F[1,1] events for increasing distance and stand-off. Broadening of all peaks occurs and 10 cm stand-off with 2 cm separation becomes unresolvable as two separate sources. This also occurs for 4 cm separation at 30 cm. This is due to the degradation in image resolution introduced through the inclusion of F2 events in the reconstruction.

The images were reproduced for a final time using F[1,1] and F2 events with parametric PSA applied to the Si(Li) and database PSA to all HPGe events. These slices
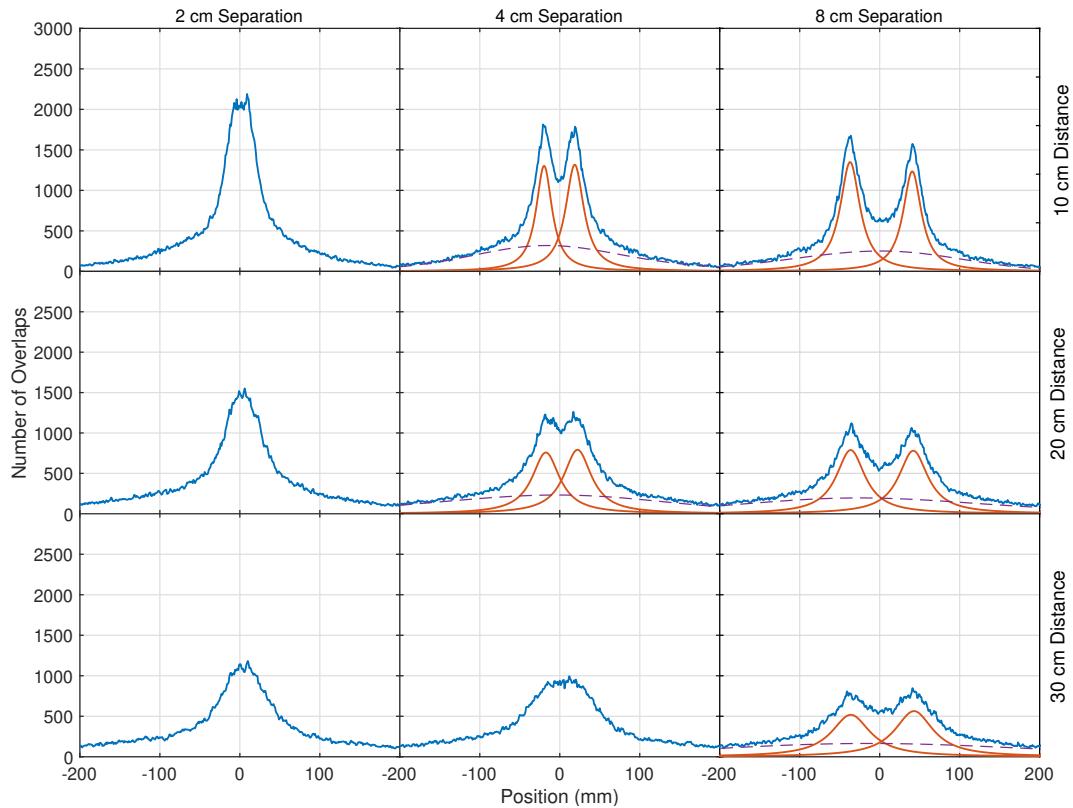
FIGURE 8.4: Image reconstruction slice taken at $y = 0$ mm for two ^{137}Cs sources at a combination of three separation and three stand-off distances. Events used were HPGe F[1,1] and F2 events with parametric PSA applied where eligible to both detectors.

are shown in Figure 8.5. Positions that were unresolvable as two separate sources with parametric PSA are now again resolvable with the application of database PSA. In all situations application of database PSA results in improvements in resolution and resolvability of the system relative to parametric PSA.

Multi-source Image Gating

When two sources are unresolvable it is possible to employ energy gating techniques if they are different isotopes. The camera is designed to utilise its excellent spectroscopic abilities to gain further information about the imaging environment but also to provide improved positional information. This was tested with the addition of database PSA in the HPGe and parametric PSA in the Si(Li).

A 0.25 MBq ^{137}Cs source and a 0.23 MBq ^{60}Co source were placed at 20 cm standoff and 2 cm separation, offset equally from the $x = 0$ mm axis. This set-up is the same as an unresolvable measurement in the previous section when performed with two ^{137}Cs sources. Data were collected for 17.6 hours with a coincident trigger rate of 66 events per second. F[1,1] and F2 events that passed energy gates placed on observed photopeaks in the recorded energy addback spectra were used. The energy spectrum formed from these events without the application of energy gates is displayed in Figure 8.6. These gates were 656-664 keV placed on the ^{137}Cs photopeak and 1167-1179 keV
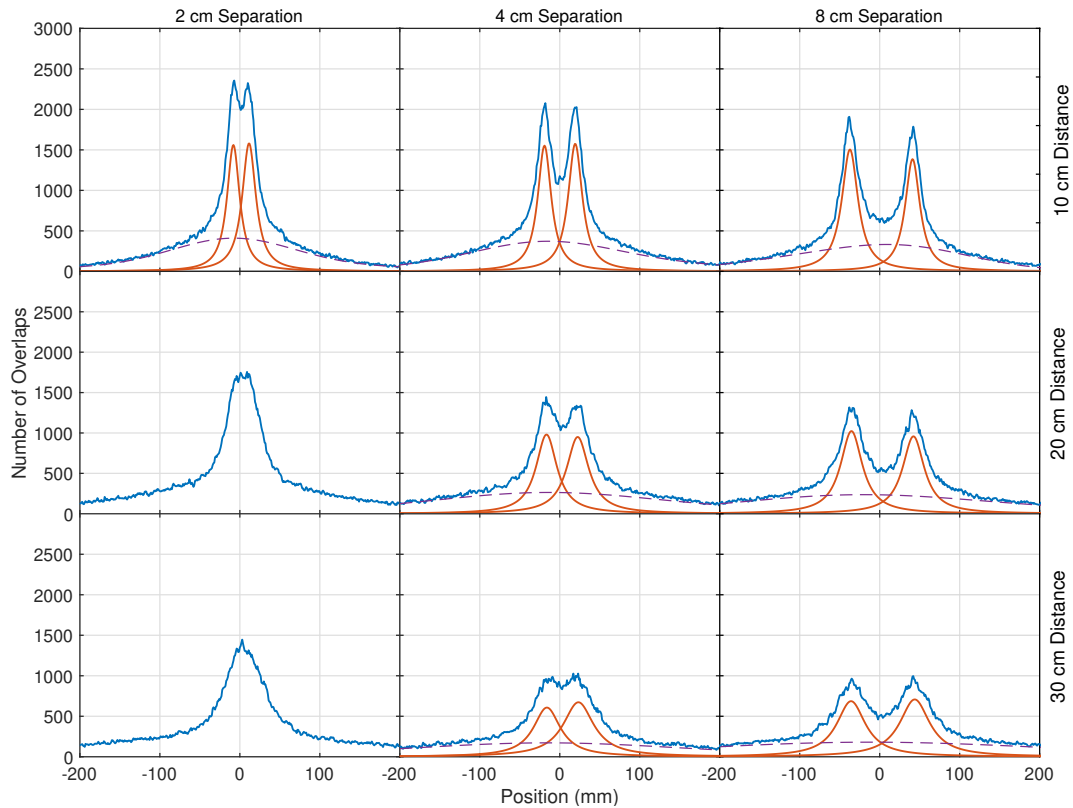
FIGURE 8.5: Image reconstruction slice taken at $y = 0$ mm for two ^{137}Cs sources at a combination of three separation and three stand-off distances. Events used were HPGe F[1,1] and F2 events with database PSA applied. Events in the Si(Li) were processed with parametric PSA.

and 1326-1338 keV placed on the two ^{60}Co photopeaks. The image was reconstructed at the known z-distance with 10 points per degree and an image space of 600 mm. These gates resulted in a total of 52,636 imageable events. Of these, 24,306 fell between the ^{137}Cs photopeak gates and 28,330 between the ^{60}Co energy gates.
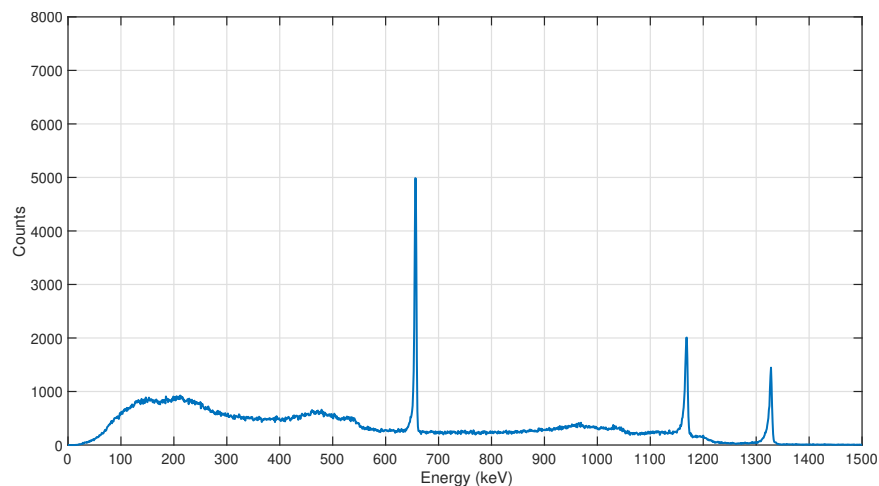
FIGURE 8.6: Energy spectrum obtained from a ^{137}Cs and a ^{60}Co point source. All events that registered an F[1,1] interaction in the Si(Li) and an F[1,1] or F2 interaction in the HPGe are included.
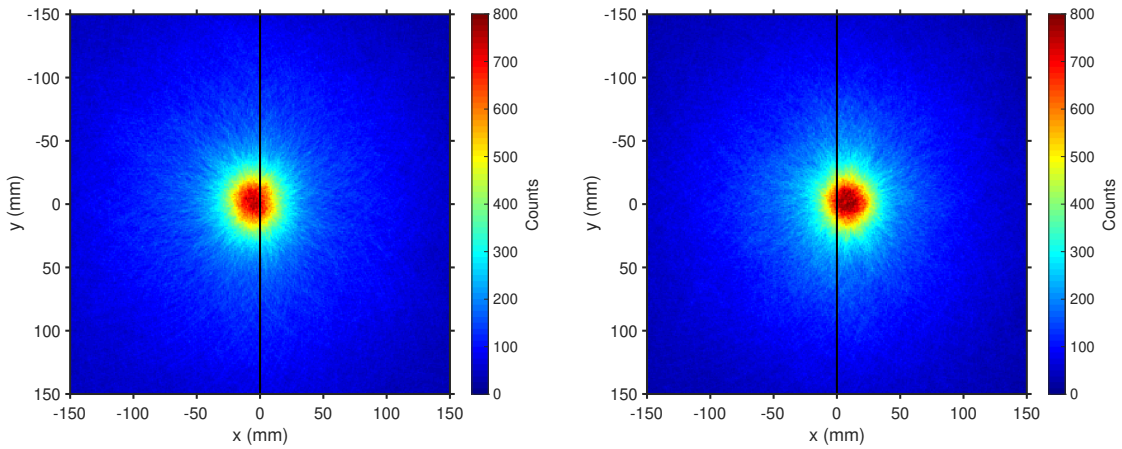
FIGURE 8.7: Reconstructed image of with ^{137}Cs photopeak gating (left) and ^{60}Co photopeak gating (right). The black line marks the centre point from which the sources are offset.

The overlap intensity maps produced from gating on each isotope individually are displayed in Figure 8.7. The reconstructed image produced when imaging the ^{137}Cs photopeak is displayed left while that produced from ^{60}Co photopeak events is displayed right. The black line is plotted along $x = 0$ mm to show the offset either side of the highest point of intensity. A slice was taken through $y = 0$ mm and the reconstructed overlap intensity profiles are displayed in Figure 8.8.

The Lorentzian fit obtained when all photopeaks were included in the reconstruction is shown left, while the Lorentzian fits produced when the ^{137}Cs and ^{60}Co photopeaks were gated on and fitted separately is shown right. When all photopeaks are included in the image reconstruction and a Lorentzian fit applied atop a Gaussian background only a single peak is distinguishable. The centroid of this fit was found to be 3 mm offset in the positive x direction and not equidistant between the two sources. When the photopeaks are gated on separately for each source and a fit applied to each they can be clearly distinguished as non-centred sources. The ^{137}Cs fit centroid was located at $x = -4.5$ mm while the ^{60}Co centroid was found to be at $x = 9.4$ mm. The sources were placed at $x = -10$ mm and $x = 10$ mm as accurately as possible. The large difference between the ^{137}Cs position and the reconstructed position is explained by the effect of the ^{60}Co Compton continuum, on which the 661.7 keV photopeak sits. Gating on the 661.7 keV energy therefor also includes γ rays from a different location and so skews the reconstructed centroid location. The ability to resolve a single peak into the constituent sources has been demonstrated though and using energy gating more precise positional information can be achieved.

8.3 Computational Cost

The improvement in image resolution measured through the application of database PSA has been displayed. The computational cost associated with these improvements must be assessed. Parametric PSA is performed "online" as data are recorded and
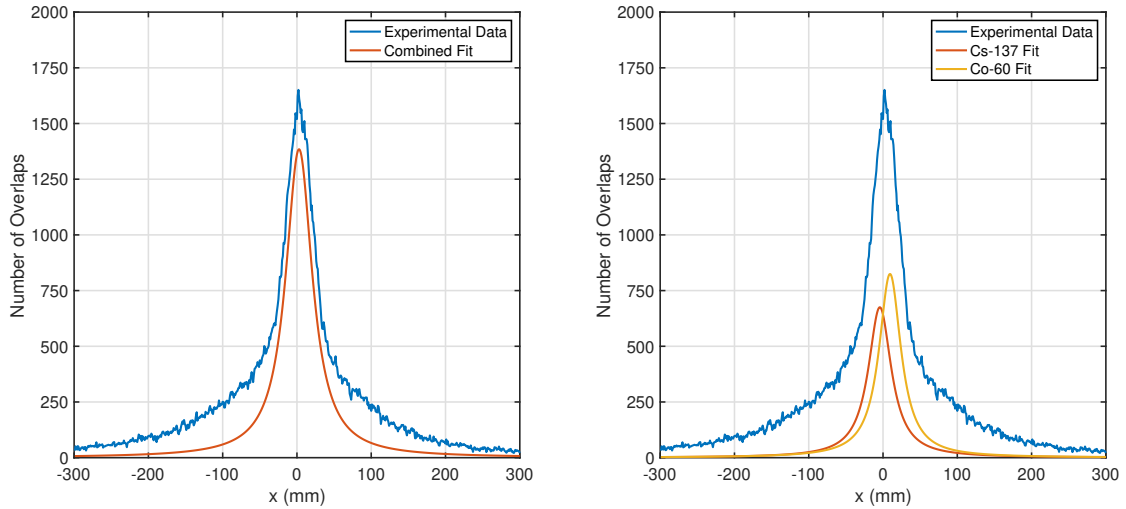
FIGURE 8.8: Slice taken at $y = 0$ mm from the reconstructed image of a ^{137}Cs and a ^{60}Co source with 2 cm separation. Experimental data and no energy gate Lorentzian fit are shown left while right shows Lorentzian fits produced for energy gates placed on individual photopeaks.

sorted. Conversely database PSA is performed "offline". The computational overhead of parametric PSA is low, and therefore has little to no impact on the data sorting rate. The improvement measured from database PSA must be weighed against the increased computational costs and time required to perform it. The database PSA algorithm is executed within MATLAB and performed on signals output when sorting data. There is no computational power or time required to output these signals for analysis and they are output in a normal data sorting process. The added time requirement comes from executing the grid-search algorithm. An assessment of the computational resources required to perform database PSA was made. The times taken for the grid-search algorithm to compare 1,000 events was recorded for the fold denominations and are displayed in Table 8.10. The times obtained were found when running on an Intel i7-7700K CPU at 4.2 GHz with 16 GB memory and a NVIDIA Quadro P5000 GPU. MATLAB was run as a script and not compiled.

| | Database Processing Time | | |
Data Type	% of Events at 661.7 keV	% of Events at 1332.5 keV	Time to Process 1,000 Events (s)
F[1,1]	39.4	34.4	95
F[1,2] and F[2,1]	28.9	29.4	490
F[2,2]	31.7	36.2	690

TABLE 8.10: Grid-search algorithm processing times for 1,000 events of various fold denominations.

The data type as a % of the total F[1,1] and F2 events is displayed along with the analysis time to give context to the time that would be required in experimental applications. The distributions of fold types in the HPGe is produced from two-tier and three-tier ^{137}Cs and ^{60}Co data with applied photopeak gates. The fastest analysis

performed is F[1,1] at 95 seconds per 1,000 events. F[1,2] & F[2,1] events taken an average of 490 seconds and F[2,2] even longer at 690 seconds. The drastic increase between F[1,1] and F2 is due to the necessary coarse and fine search required by the adaptive grid-search algorithm. The faster performance of F[1,2] & F[2,1] versus F[2,2] occurs as the initial guess from the fold 2 face is used to skip the initial algorithm steps for the fold 1 face. This is not possible for F[2,2] and each face is independently analysed. The number of F2 increases by 4.5% while F[1,1] drops 5.0% when comparing 661.7 keV against 1332.5 keV γ rays. This change in distribution results in longer computational times as the more intensive F2 methods are required. Following the time requirements for each method and the distribution present it would take approximately 111 hours to process 1,000,000 ^{137}Cs full photopeak events that are F[1,1] in the Si(Li) and F[1,1] or F2 in the HPGe. 1,000,000 ^{60}Co events from the 1332.5 keV γ would take 119 hours. The difference is small relative to the total computation time and so can be disregarded in deciding whether it is worth applying database PSA analysis based upon the γ-ray energy being imaged. This method can be said to be time-consuming and computationally expensive, even using a high-end PC to process the events. Methods should be investigated to improve the performance of database PSA. Several methods have been considered but not yet implemented and are discussed below.

- **Sampling** - The database of simulated signals was produced on a 1 ns sampling basis. This necessitates the interpolation of exported experimental pulses to match and so increased comparison times at all stages of the algorithm. A simple improvement to the method that would yield a reduction in analysis time would be to produce the database on a 2 ns or 5 ns basis. A comparison of these different sampling values with the output imaging resolution would give a quantification for the trade-off in resolution against the reduction in comparison time. Subsequent to the completion of this work the database was down-sampled to 2 ns and the time requirements for all event processing was halved. The impact on the image resolution was negligible and following work will utilise this down-sampled database. It is unlikely that a further reduction to a 5 ns basis would have a significant effect either but would reduce the time requirements by a further 2.5 times. Relative to the 1 ns database, the 5 ns should yield a fivefold speed improvement making the practicality of its application more feasible.

- **MATLAB** - The algorithm was developed and run as a MATLAB script. Compilation of the script with the MATLAB compiler may reduce run time. The added benefit would be the production of a stand-alone executable that would be easy to use. Alternatively transfer of the code to a different language may yield processing speed benefits.

- **Sensitivity Map** - Development of a sensitivity map for the HPGe detector volume could be used to reduce search time in areas of low sensitivity. The map would

quantify the relative sensitivity of all regions within the detector be used to determine which regions of the detector produce similar signals. This could be used to reduce search time in these regions by not comparing those points with little or no distinction in signal shapes. This is a method usually applied to large segment volume detectors, such as in the GRETINA project in which a quasi-cylindrical grid is used [80]. It is not thought that this would reduce the number of positions by much in a planar detector.

- **Parametric Information** - As parametric PSA is an online method of PSA the analysis of it is performed prior to the use of database PSA. Information obtained from the parametric method could be used to reduce the areas of the detector that the algorithm must compare. For example information regarding the rise time of a signal could be used to reduce the number of z-depth positions that are possible. A fast t30 present in the AC signal would require the pulse to occur close to those contacts and so only those events need be compared. This would likely only work for F[1,1] events as the convolution of multiple events would prevent its use.

- **GPU Acceleration** - Graphics Processing Unit (GPU) acceleration makes use of the parallel processing power of a GPU to perform tasks typically carried out by the CPU. The process of comparing signals in database comparison PSA is parallelisable and so scope exists to apply GPU acceleration methods.

Implementation of some or all of these techniques could drastically reduce the computational power and time required to perform database PSA. As the algorithm stands currently the time requirements are significant and are potentially prohibitive.

8.4 Summary of Results

The image resolution achievable through the application of database PSA was determined through analytical reconstruction of a ^{137}Cs source located at a known stand-off of 10 cm. Angular resolution, taken as an average of the FWHM in x and y of the Lorentzian fit from the reconstructed image, was used to quantify the performance. When only F[1,1] interactions in the HPGe and Si(Li) were considered and PSA methods not applied, an angular resolution of $13.2 \pm 0.1°$ was measured. This was improved by $19.7 \pm 0.2\%$ when the events were reassessed with parametric PSA applied to the HPGe, and by $21.2 \pm 0.3\%$ when the events were assessed with database PSA. Addition of parametric PSA to the F[1,1] events in the Si(Li) improved this by a further 14.4%. The best angular resolution of $8.5 \pm 0.1°$ was achieved when parametric PSA was applied to the Si(Li) and database PSA to F[1,1] events in the HPGe. Inclusion of F2 events in the HPGe more than tripled the number of imageable events but degraded the angular resolution to $14.3 \pm 0.1°$ if no PSA was applied. Applying parametric to eligible F[1,1] events resulted in an angular resolution of $11.7 \pm 0.1°$ while database PSA, which could be applied to all imaged HPGe events, produced an angular resolution of $9.6 \pm 0.1°$. The

results from database PSA were found overall to be a slight improvement when applied to F[1,1] events but a significant improvement when applied to F2 interactions in the HPGe, which could not previously be analysed with PSA. This achieves a large increase in imaging efficiency at a small cost to the image resolution.

A large stand-off distance of 1 m was also imaged as is it analogous to a decommissioning environment. Database PSA analysed events were found to improve the angular resolutions for all event combinations and so massively increased the number of imageable events. The improvement in angular resolution for F[1,1] and F2 imaged events was found to be $2.1 \pm 0.1°$ and $3.4 \pm 0.1°$ for HPGe applied parametric PSA and database PSA respectively, with parametric PSA applied to the Si(Li) also. A 1 m stand-off and 30 cm offset source was also imaged and the reconstruction found to reconstruct the source location correctly.

Multi-source imaging was performed at stand-off distances of 10, 20 and 30 cm with two ^{137}Cs sources separated by 2, 4 and 8 cm. This tested the system ability to resolve separate γ-sources located in close proximity. When imaging F[1,1] events within the HPGe and applying parametric PSA to the Si(Li) and database PSA to the HPGe interactions only the 2 cm separated sources were unresolvable at 20 and 30 cm stand-off. Inclusion of F2 events within the HPGe and the application of parametric PSA to those eligible events resulted in an overall degradation in image quality and the sources placed at 30 cm stand-off with 4 cm separation also became unresolvable along with the smallest stand-off 2 cm separated sources. This degradation is reversed when database PSA is applied to all F1 and F2 HPGe events instead and only the 2 cm separated sources at 20 cm and 30 cm stand-off are unresolvable again. Finally, a multi-source image was produced at the unresolvable position of 20 cm and 2 cm separation replacing one of the ^{137}Cs sources with ^{60}Co. Through the application of energy gates to the individual photopeaks they were recoverable as two separate sources.

The time and computational power required to execute the database algorithm was assessed. The time taken to run F[1,1] events was found to be 95 seconds per 1,000. This time is reasonable but as the resolutions are only slightly improved over that achievable with parametric analysis it cannot be recommended for use unless the optimal image resolution is desired. The largest improvement in resolution is that achieved for F2 events although these are the most computationally slow and intensive events at 490 and 690 seconds per 1,000 for F[1,2] & F[2,1] and F2 respectively. Methods of reducing the time requirement have been discussed and are recommended for future implementation.

Chapter 9

Conclusions and Discussion

The work performed in this study can be described as three work packages centred around improving the image resolution achievable from a three-tiered Compton camera system known as GRI+. These were: the novel characterisation through collimated scanning of a Mirion Technologies electrically-cooled planar HPGe detector that makes use of a-Ge based n^+ contacts; the simulation and validation therein of a signal database for the HPGe detector; and finally, the development and implementation of a signal database PSA adaptive grid-search algorithm to deliver improved position resolution and its direct comparison to parametric PSA methods. The results and work performed in each of these packages is described in the following sections after which recommendations for future work are made. The final achievement of the work can summarised as the improvement of position resolution within the second position-sensitive layer of a Compton camera. This enabled the subsequent improvement in the imaging resolution possible for single and multiple point sources in both near and far-field imaging. This improvement was achievable when imaging both single and multi-interaction events within the HPGe. The improvement found when analysing multi-interaction events represents the development of a successful signal comparison PSA algorithm for application in planar HPGe detectors. This overcomes the shortcomings in previously implemented parametric-based PSA methods within the Compton camera.

9.1   Detector Characterisation

Characterisation of the $60{\times}60{\times}20$ mm^3 planar HPGe semiconductor detector within the GRI+ system was performed. This process involved scanning the HPGe with a collimated γ-ray beam in two phases. First a "surface scan" was performed using low energy ^{241}Am to characterise the uniformity of response across the AC and DC contacts. Following this a "side scan" was carried out with a collimated ^{137}Cs source to characterise the signal response through z-depth of the detector.

   Electronic noise was quantified in the HPGe detector and the average peak-to-peak nose found to be 14.7 keV for the AC face and 14.5 keV for the DC face. Information obtained from the surface scans was used to quantify charge sharing at the detector

surface for γ rays of 59.5 keV. It was found to be 11.5% of events incident on the AC contacts and 10.3% of those incident on the DC. The quantity of charge sharing and nature of the energy split in these events was compared against a geometrically-similar HPGe planar detector that was previously characterised at the University of Liverpool. The charge loss and collection properties of the detector were also assessed. The charge collection properties were quantified through investigation of the charge collection times T30 and T90, or the times taken for 30% and 90% of the charge to be collected. These were found to be variable across the strips and inter-strip gaps as well as along the strips themselves, indicating variation of the electric field. Charge loss was found to not be an issue for the detector and low energy tailing was attributed to charge-share events in which energy was lost to the noise threshold. Some results were not fully understood as they contrasted with those observed in the SmartPET HPGe detector. These results were the preference for equal sharing of charge between neighbouring strips in a charge-share event and the faster rise times on the inter-strip gaps relative to the strips themselves observed in some sets of scan data. Recommendations to investigate these results further are presented in Section 9.4. The uniformity of the detector response across the surfaces was concluded to be adequate and the loss of uniformity likely due to unequal sharing of charge between strips. The side scan experimental data were used to produce average signals at each mm through the 20 mm z-depth of the detector. The signal response was compared to previous work done on planar HPGe detectors and found to respond in a similar fashion.

The characterisation of the signal rise times through depth was produced and used to aid in the production of accurate parametric z-PSA methods. A T30 linear rise time sensitivity of 6 ns per mm was found for the AC collection and 4 ns per mm for the DC collection through the bulk of the detector z-depth. T90 sensitivity was higher but non-linear through the bulk. A method of parametric z-PSA was optimised and implemented that made use of T30, T50 and T90. Values for each of these rise time parameterisations was produced for each pixel at each 1 mm position through z-depth. The method employed a χ^2-minimisation between parameterised experimental signal rise times from each detector face and these characterised values. Validation was performed through application of this method to the experimental side scan data and recording of the difference between collimator position and the found z-position. It was shown to perform well and 48.3% of the events analysed were placed at the same z-position as the collimator. In total, 95.5% of analysed events were placed ≤ 2 mm from the collimator z-position. Some of this was attributed to over-fitting of the data.

The highest position-change sensitivity was found when considering the total charge collection time, 1% to 99%, of averaged signals. In a typical experimental signal this is hard to utilise due to the presence of electronic noise. The sensitivity was found to be 16 ns per mm for the AC collection and 9 ns per mm for the DC collection. This helped motivate development of database signal comparison PSA that could make use of the full charge collection signal.

From the surface scan average charge collection and image charge signal responses were produced for each x-y collimator position. From the side scan the average charge collection signal for each strip through z-depth was produced. These signal responses were saved for use in validating simulated signals. The variable nature of individual strip rise time responses, attributed to preamplifiers, was also found and was again saved.

9.2   Simulated Database Generation and Validation

The simulation package ADL was used to solve numerically the electric and weighting potentials for the HPGe planar geometry. This was initially performed with values provided by the manufacturer regarding the impurity concentration. The inbuilt charge carrier mobilities were then used to generate a signal database, representing the response of the 24 strips through the full volume of the detector on a 1 mm basis, totalling 72,000 positions. The average signal data acquired in the characterisation process at constrained positions was used to validate the simulated signals at select points. This formed part of an optimisation process in which the impurity concentrations, charge carrier mobilities and individual preamplifier responses were varied until a satisfactory agreement was found between experimental signal averages and simulated equivalents. This notably resulted in impurity values close to those advised by the manufacturer except reversed in relative magnitudes at each face. The charge carrier mobilities found to produce the best match corresponded to a temperature of 88 K, very near to the cooler set-point temperature of 88.15 K. The temperature agreement means that future readings of electronically CP5 cooled detectors from the cooler itself can be relied upon to report temperatures close to that of the crystal itself. The variation in strip response due to the preamplifiers was accounted for and a bespoke preamplifier convolution applied to each of the 24 strips.

Validation of the simulated signal database was performed through comparison with the experimental signals obtained in the characterisation process. The response of the signal shape through z-depth of the detector was compared to the side scan data using the same method as the parametric comparison. The difference between the simulated signal position, found using an RMSD comparison, and the collimator position was calculated for all events. Of the events compared, 42.7% of AC signals and 41.8% of DC signals were placed at the same z-position as the collimator. For both the AC and the DC comparisons more than 95% were placed ≤ 2 mm from the collimator z-position. This validated the signal response through the depth of the detector. Image charges were compared to average signals formed from the surface scan data and were found to vary in amplitude appropriately across the width of the strips on both the AC and the DC faces. Differences between the experimental and simulated image charges were attributed to differential crosstalk and charge sharing.

9.3 Database Algorithm Testing and Results

The validated database of simulated signals was used to perform signal comparison PSA. For this a grid-search algorithm was developed that could, through RMSD comparisons, find matches for single interaction events within the HPGe and return a sub-voxel mm position. This was expanded upon to assess multi-interaction, complex events adaptively and provide mm positions for two interactions. This grid-search algorithm represented the implementation of a new form of PSA to the Compton camera system that could assess events that were previously immune to PSA techniques. The algorithm was used to reconstruct the profile of the collimated γ-ray beam obtained during the side scan for both single and double interactions. It was also used to demonstrate single-detector Compton imaging using data recorded in the HPGe only. Single-detector imaging was previously impossible within the system as two interactions could not be resolved into separate z-depths. Deconvolution of these multi-interaction events can only be performed with the adaptive grid-search algorithm developed in this work.

Improvements in image quality resulting from the application of the grid-search algorithm were quantified through analysis of the system's angular resolution. An analytical reconstruction code was used to obtain the image resolution in x and y, the average of which was converted into an angular value. The improvements found from database PSA were found to be comparable to those found after the application of parametric PSA when considering single-interaction events only. When imaging ^{137}Cs at 10 cm stand-off an angular resolution improvement of $2.8 \pm 0.1°$ was achieved after applying database PSA while the improvement from the application of parametric PSA was $2.6 \pm 0.1°$. When parametric PSA was included in the Si(Li) detector the improvement over no PSA is increased to $4.7 \pm 0.1°$ and $4.5 \pm 0.1°$ for database and parametric PSA applied to the HPGe respectively for single-interaction events. An improvement over no PSA of $4.3 \pm 0.1°$ was found when imaging and assessing F2 multi-interaction HPGe events with the database comparison method in addition to Si(Li) parametric PSA. These account for roughly 68% of the imageable events, which are those that register a F[1,1] interaction in the Si(Li) and either a F[1,1] or a F2 in the HPGe. Sub 10° angular resolution was achieved at 10 cm stand-off for F1 and F2 events combined after applying database PSA to the HPGe and parametric PSA to the Si(Li).

The improvement was shown to work at a larger stand-off distance of 1 m. After the application of database PSA to the HPGe and parametric PSA to the Si(Li), $6.4 \pm 0.1°$ angular resolution was achieved when imaging single and multi-interaction events. This was an improvement of $3.4 \pm 0.1°$ over no PSA. Parametric PSA applied to both planar detectors yielded an improvement of only $2.1 \pm 0.1°$. This is an observable improvement in image resolution achieved through the application of database PSA to the HPGe when imaging single and multi-interaction events. This is seen especially at large stand-off distances that are analogous to a nuclear decommissioning environment. This notably improves the image resolution that is obtained when including F2 events in the HPGe.

These events make up around 66% of imageable events and so their inclusion increases the imaging efficiency.

The database PSA algorithm was also proven to provide improvements when resolving multiple same-isotope sources in close proximity to each other. The ability to energy gate and resolve otherwise unresolvable different-isotope sources was demonstrated, as was the reconstruction of offset sources. In all scenarios it can be stated that database PSA was successfully applied, with the only drawback being computational cost of its application.

9.4 Future Work

This work has improved the position resolution possible within the HPGe planar detector beyond that possible from the physical voxel size. This was done through a process of characterisation and simulation in order to generate a simulated database of validated signals. There remain some aspects of the work performed that would benefit from further analysis and improvement or were not fully investigated due to time constraints and the scope of this study. Discussed below in the subsections under which the work initially fell are presented ideas on the routes these investigations might take. These cover the three main areas investigated in this thesis.

9.4.1 Detector Characterisation

Some of the results obtained during the charge collection assessment were interesting and could be investigated further. The most notable results that require further work to understand are the preference of equal sharing of charge on the inter-strip gaps contrary to previously observed HPGe detectors as well as the faster rise times observed on the inter-strip gaps in some of the scan data. As it is proposed that these are a result of the electric field in these regions further investigation may require simulation in conjunction with experimental data.

To investigate the proportion of charge shared between neighbouring strips in a charge-share event the electric field simulation can be used. When simulating signals within ADL the time-dependent charge carrier path can be simultaneously read out. This can be used to produce charge carrier tracks for all positions within the detector. If the electric field simulation was reproduced on a much finer grid it can be used to investigate the charge carrier paths at positions close to the contacts and at interaction positions from one strip across to another. Charge carriers within ADL are treated as a single point and not as a charge carrier cloud as is the case. To model this, a GEANT4 simulation [81] of the detector crystal and collimated γ-source could be used. The charge carrier cloud size following a γ-ray interaction could be produced in GEANT4. Tracking of the charge carrier paths for all positions within the charge carrier cloud would reveal the percentage of charge shared in an event. It would be ideal also to model the effects of thermal diffusion and Coulomb interactions between carriers as they then make their way

to the far side contacts. This would reveal whether the charge is typically preferentially shared due to the splitting of field lines or whether other effects are at play. This could be compared to experimental scan data taken with a finer collimator and a small step size. A 0.5 mm internal diameter collimator in conjunction with 100 μm step size with the Velmex system would yield a very fine scan. Even without the comparison to simulation of charge sharing this finer scan would yield a more detailed and complete picture of charge share as a function of position. Information could be inferred of the magnitude of lateral field splitting between the strips from this alone. This finer scan and simulated signal database could also be used to investigate the faster rise times observed on the inter-strip gaps in some of the scan data.

The charge-share events identified during the scan process could also be corrected for. This process results in single-interaction events being incorrectly identified as charge-share events and so are processed incorrectly with PSA. If they can be identified as charge share events they there are constrained tightly to the inter-strip gap and so could be included in fold 1 imaging. This possibility of identifying charge share events has been discussed [62] through analysis of the leading edge of charge share pulses. It is recommended that the current scan data are investigated and an attempt made at correcting for it. It is proposed that this would be easier with a collimated γ-ray beam of a higher energy, as the produced signals would then be more prominent relative to the noise. Average signals formed from a high-statistics and fine-step collimated scan could be used to investigate this in detail.

In future effort should be made to utilise a large percentage of the full rise time when applying parametric PSA. Utilisation of the information contained in t01 to t99 of a pulse would allow a more effective form of z-PSA to be developed and applied. The signal parts included in this way would allow access to information that is otherwise lost and would allow recovery of a linear response through much of the detector as well as high sensitivity at the detector edge. This would improve the effectiveness of online PSA that does not require further analysis. This would require low-noise HPGe detectors, the likes of which are currently in development [82].

9.4.2 Simulated Database Generation and Validation

In this work the simulated database was validated to a standard that allowed its use, with confidence, in database signal comparison PSA. It is recommended that the validation and optimisation of the simulated database is revisited in order to improve the closeness of the match. Reinvestigating the preamplifier convolution and correcting for the variance in response between different coupled strips would improve the quality of the matches found. This is important as several strips showed a better optimised preamplifier convolution than others. This could be studied further alongside further testing of the impurity concentrations used.

The validation of the database was performed with singles data in which the location of each interaction was not constrained in all axes within the detector volume. This

introduces uncertainties to the interaction locations. In this work, these uncertainties were reduced through averaging of many positions. The validation could be improved upon through use of coincidence scan data in which each interaction is constrained in all three degrees of freedom. These data could be taken with the Liverpool coincidence scan system in which a collimated γ-ray beam is used in conjunction with collimated BGO detectors to constrain interactions in (x, y, z). It is recommended that coincidence scan data be taken at a selection of points within the detector volume. These should include several depth positions representing points close to the AC contacts, the detector centre, and the DC contacts. At each of these depths the transient image charge response should be compared by recording several points in x-y. This would ideally be for strip contacts at both the detector centre and close to the guard ring edge, such that the non-uniformity of the electric field can be confirmed.

Finally, the same methodology developed in this study could be expanded to the Si(Li). The lack of any z-PSA in the Si(Li) results in the optimum image resolution not being achieved. In this work the electric and weighting potentials were produced for the Si(Li) geometry and material but not used. The Si(Li) was also surface scanned along with the HPGe but the data were not investigated as the Si(Li) had been previously characterised and the response understood. These data, along with data from the previous characterisation process, could be used to validate a signal database simulated on top of the already produced Si(Li) fields. This could would improve the image resolution of GRI+ even further.

9.4.3 Database Signal PSA

Several methods of improving the grid-search algorithm's speed and accuracy could be implemented. It is first recommended that the methods discussed in Chapter 7 are investigated and implemented if feasible. These methods would reduce the computational cost associated with running the algorithm and reduce the time required to run it. If the time required to run the grid-search algorithm was reduced then methods to increase the accuracy could be implemented without increasing the time requirements past an acceptable value.

To improve the accuracy, the supertraces compared, typically comprising a charge collection signal and neighbouring image charges, could be lengthened to include image charges in non-neighbouring strips. This would increase the number of image charges considered when performing an RMSD comparison between real and simulated and so increase the information considered by the grid-search algorithm. It is also thought that the algorithm be modified to align all experimental and database signals with each other through an RMSD comparison. This is currently only done for some signals in the F2 method. If it was expanded and applied to all signals then the computational cost would be increased for each event compared to the current method of aligning most signals to t30 initially. This alignment would produce more accurate matches between experimental and simulated signals as it reduces the alignment error present in

assuming t30 will match the entire signal length. This would be increasingly important if the down-sampled database is implemented as a reduction in the sampling basis would increase the alignment error.

9.4.4 Scene Data Fusion

Scene data fusion is the combination of contextual information, obtained through imaging devices, with γ-ray images produced by the Compton camera. As discussed in Chapter 4 this is a proven and widely used concept and is the area in which the GRI+ system is most lacking in terms of competing with similar systems. Proof of concepts have been produced with the Liverpool Compton camera system [45] and it is regrettable that improvement upon this work could not be included in this thesis. Alternatives have been investigated in the same time-frame as the work done in this thesis, most notably in the thesis work of A. Caffrey [40] using a LIDAR system. An Xbox Kinect has also been briefly tested as a cheap, easy to use alternative, and image fusion produced by J. Platt and A. Caffrey [47]. This device is not yet fully integrated with the system and work to produce scene data fused with γ-images is being performed. It is recommended that future work focuses on developing the practical aspect of the GRI+ system and investigate proven techniques to integrate external scene information with that produced by the Compton camera.

Bibliography

[1] Nuclear Decomissioning Authority, Business Plan, 1 April 2018 to 31 March 2021.

[2] [Online]. Available: https://www.gov.uk/government/organisations/ nuclear-decommissioning-authority/about

[3] *Sellafield Magazine: Issue 2*, 2015.

[4] International Atomic Energy Agency (IAEA) and others, Fundamental safety principles. Safety fundamentals, 2007.

[5] G. Britain and N. D. Authority, *UK strategy for the management of solid low level radioactive waste from the nuclear industry.* NDA, 2010.

[6] M. R. W. Safely, "A framework for implementing geological disposal," *DEFRA June*, 2008.

[7] A. AC02459866, *Radiological characterization of shut down nuclear reactors for decommissioning purposes.* Internat. Atomic Energy Agency, 1998.

[8] "Products and services: Radscan® 900," Cavendish Nuclear, Tech. Rep., 2019.

[9] R. Todd, J. Nightingale, and D. Everett, "A proposed γ camera," *Nature*, vol. 251, no. 5471, pp. 132–134, 1974.

[10] J. Dreyer, M. Burks, and E. Hull, "Next generation germanium systems for safeguards applications," Lawrence Livermore National Lab.(LLNL), Livermore, CA (United States), Tech. Rep., 2014.

[11] C. G. Wahl, W. R. Kaye, W. Wang, F. Zhang, J. M. Jaworski, A. King, Y. A. Boucher, and Z. He, "The polaris-h imaging spectrometer," *Nuclear Instruments and Methods in Physics Research Section A: Accelerators, Spectrometers, Detectors and Associated Equipment*, vol. 784, pp. 377–381, 2015.

[12] C. E. Ordonez, A. Bolozdynya, and W. Chang, "Doppler broadening of energy spectra in compton cameras," in *1997 IEEE Nuclear Science Symposium Conference Record*, vol. 2. IEEE, 1997, pp. 1361–1365.

[13] C. G. Wahl, W. Kaye, W. Wang, F. Zhang, J. Jaworski, Y. A. Boucher, A. King, and Z. He, "Polaris-h measurements and performance," in *2014 IEEE Nuclear Science Symposium and Medical Imaging Conference (NSS/MIC)*. IEEE, 2014, pp. 1–4.

[14] H. Boston, J. Gillam, A. Boston, R. Cooper, J. Cresswell, A. Grint, A. Mather, P. Nolan, D. Scraggs, G. Turk *et al.*, "Orthogonal strip hpge planar smartpet detectors in compton configuration," *Nuclear Instruments and Methods in Physics Research Section A: Accelerators, Spectrometers, Detectors and Associated Equipment*, vol. 580, no. 2, pp. 929–933, 2007.

[15] T. Woodroof, "Quantitative compton imaging of caesium-137 in porous media," Ph.D. dissertation, University of Liverpool, 2019.

[16] K. Vetter, A. Kuhn, M. Deleplanque, I. Lee, F. Stephens, G. Schmid, D. Beckedahl, J. Blair, R. Clark, M. Cromaz *et al.*, "Three-dimensional position sensitivity in two-dimensionally segmented hp-ge detectors," *Nuclear Instruments and Methods in Physics Research Section A: Accelerators, Spectrometers, Detectors and Associated Equipment*, vol. 452, no. 1-2, pp. 223–238, 2000.

[17] M. R. Dimmock, "Characterisation of agata symmetric prototype detectors," Ph.D. dissertation, University of Liverpool, 2008.

[18] H. Boston, A. Boston, R. Cooper, J. Cresswell, A. Grint, A. Mather, P. Nolan, D. Scraggs, G. Turk, C. Hall *et al.*, "Characterisation of the smartpet planar germanium detectors," *Nuclear Instruments and Methods in Physics Research Section A: Accelerators, Spectrometers, Detectors and Associated Equipment*, vol. 579, no. 1, pp. 104–107, 2007.

[19] L. Harkness, D. Judson, A. Boston, H. Boston, J. Cresswell, P. Nolan, A. Sweeney, J. Beau, M. Lampert, B. Pirard *et al.*, "Characterisation of a si (li) orthogonal-strip detector," *Nuclear Instruments and Methods in Physics Research Section A: Accelerators, Spectrometers, Detectors and Associated Equipment*, vol. 726, pp. 52–59, 2013.

[20] M. Deleplanque, I. Lee, K. Vetter, G. Schmid, F. Stephens, R. Clark, R. Diamond, P. Fallon, and A. Macchiavelli, "Greta: utilizing new concepts in γ-ray detection," *Nuclear Instruments and Methods in Physics Research Section A: Accelerators, Spectrometers, Detectors and Associated Equipment*, vol. 430, no. 2-3, pp. 292–310, 1999.

[21] B. Bruyneel, B. Birkenbach, and P. Reiter, "Pulse shape analysis and position determination in segmented hpge detectors: The agata detector library," *The European Physical Journal A*, vol. 52, no. 3, p. 70, 2016.

[22] D. Bazzacco, B. Cederwall, J. Cresswell, G. Duchêne, J. Eberth, W. Gast, J. Gerl, W. Korten, I. Lazarus, R. Lieder *et al.*, "Agata, technical proposal for an advanced gamma tracking array for the european gamma spectroscopy community," 1991.

[23] R. D. Evans and R. Evans, "The atomic nucleus," 1955.

[24] G. F. Knoll, *Radiation detection and measurement.* John Wiley & Sons, 2010.

[25] N. Mori, "Electronic band structures of silicon–germanium (sige) alloys," in *Silicon–Germanium (SiGe) Nanostructures.* Elsevier, 2011, pp. 26–42.

[26] C. Canali, G. Majni, R. Minder, and G. Ottaviani, "Electron and hole drift velocity measurements in silicon and their empirical relation to electric field and temperature," *IEEE Transactions on Electron Devices*, vol. 22, no. 11, pp. 1045–1047, 1975.

[27] L. Mihailescu, W. Gast, R. Lieder, H. Brands, and H. Jäger, "The influence of anisotropic electron drift velocity on the signal shapes of closed-end hpge detectors," *Nuclear Instruments and Methods in Physics Research Section A: Accelerators, Spectrometers, Detectors and Associated Equipment*, vol. 447, no. 3, pp. 350–360, 2000.

[28] G. Ottaviani, C. Canali, and A. A. Quaranta, "Charge carrier transport properties of semiconductor materials suitable for nuclear radiation detectors," *IEEE Transactions on Nuclear Science*, vol. 22, no. 1, pp. 192–204, 1975.

[29] B. Bruyneel, P. Reiter, and G. Pascovici, "Characterization of large volume hpge detectors. part ii: Experimental results," *Nuclear Instruments and Methods in Physics Research Section A: Accelerators, Spectrometers, Detectors and Associated Equipment*, vol. 569, no. 3, pp. 774–789, 2006.

[30] L. Reggiani, C. Canali, F. Nava, and G. Ottaviani, "Hole drift velocity in germanium," *Physical Review B*, vol. 16, no. 6, p. 2781, 1977.

[31] W. Shockley, "Currents to conductors induced by a moving point charge," *Journal of applied physics*, vol. 9, no. 10, pp. 635–636, 1938.

[32] D. Mackin, J. Polf, S. Peterson, and S. Beddar, "The effects of doppler broadening and detector resolution on the performance of three-stage compton cameras," *Medical physics*, vol. 40, no. 1, p. 012402, 2013.

[33] D. Copeland and E. Benjamin, "Pinhole camera for gamma-ray sources." *Nucleonics*, vol. 5, no. 2, p. 44, 1949.

[34] H. O. Anger, "Scintillation camera with multichannel collimators," 1964.

[35] H. H. Barrett, "Fresnel zone plate imaging in nuclear medicine," *J. Nucl. Med*, vol. 13, no. 6, pp. 382–385, 1972.

[36] R. Dicke, "Scatter-hole cameras for x-rays and gamma rays," *The astrophysical journal*, vol. 153, p. L101, 1968.

[37] S. R. Meikle, R. R. Fulton, S. Eberl, M. Dahlbom, K.-P. Wong, and M. J. Fulham, "An investigation of coded aperture imaging for small animal spect," *IEEE Transactions on Nuclear Science*, vol. 48, no. 3, pp. 816–821, 2001.

[38] M. Woodring, D. Souza, S. Tipnis, P. Waer, M. Squillante, G. Entine, and K. Ziock, "Advanced radiation imaging of low-intensity gamma-ray sources," *Nuclear Instruments and Methods in Physics Research Section A: Accelerators, Spectrometers, Detectors and Associated Equipment*, vol. 422, no. 1-3, pp. 709–712, 1999.

[39] B. Phlips, W. Johnson, R. Kroeger, J. Kurfess, G. Phillips, E. Wulf, and P. Luke, "Development of germanium strip detectors for environmental remediation," in *2000 IEEE Nuclear Science Symposium. Conference Record (Cat. No. 00CH37149)*, vol. 1.   IEEE, 2000, pp. 4–72.

[40] A. Caffrey, "The development and evaluation of a compton camera for imaging spent fuel rod assemblies," Ph.D. dissertation, University of Liverpool, 2019.

[41] A. P. Dempster, N. M. Laird, and D. B. Rubin, "Maximum likelihood from incomplete data via the em algorithm," *Journal of the Royal Statistical Society: Series B (Methodological)*, vol. 39, no. 1, pp. 1–22, 1977.

[42] V. Y. Panin, F. Kehren, C. Michel, and M. Casey, "Fully 3-d pet reconstruction with system matrix derived from point source measurements," *IEEE transactions on medical imaging*, vol. 25, no. 7, pp. 907–921, 2006.

[43] N.-V. G. Imager. createc. [Online]. Available: https://www.createc.co.uk/innovation/products-technologies/n-visagegamma-imager/

[44] K. Vetter, "Multi-sensor radiation detection, imaging, and fusion," *Nuclear Instruments and Methods in Physics Research Section A: Accelerators, Spectrometers, Detectors and Associated Equipment*, vol. 805, pp. 127–134, 2016.

[45] J. Dormand, "The proof of concept of a fused radiometric and optical stereoscopic imaging system," Ph.D. dissertation, University of Liverpool, 2014.

[46] [Online].   Available: http://www.faro.com/en-us/products/3dsurveying/faro-focus3d/overview

[47] A. Caffrey, Personal Communication, 2019.

[48] R. Barnowski, A. Haefner, L. Mihailescu, and K. Vetter, "Scene data fusion: Real-time standoff volumetric gamma-ray imaging," *Nuclear Instruments and Methods in Physics Research Section A: Accelerators, Spectrometers, Detectors and Associated Equipment*, vol. 800, pp. 65–69, 2015.

[49] R. Cooper, A. Boston, H. Boston, J. Cresswell, A. Grint, A. Mather, P. Nolan, D. Scraggs, G. Turk, C. Hall *et al.*, "Smartpet: Applying hpge and pulse shape analysis to small-animal pet," *Nuclear Instruments and Methods in Physics Research*

Section A: Accelerators, Spectrometers, Detectors and Associated Equipment, vol. 579, no. 1, pp. 313–317, 2007.

[50] F. Crespi, F. Camera, B. Million, M. Sassi, O. Wieland, and A. Bracco, "A novel technique for the characterization of a hpge detector response based on pulse shape comparison," *Nuclear Instruments and Methods in Physics Research Section A: Accelerators, Spectrometers, Detectors and Associated Equipment*, vol. 593, no. 3, pp. 440–447, 2008.

[51] M. Nakhostin, *Signal processing for radiation detectors.* John Wiley & Sons, 2017.

[52] L. Harkness, D. Judson, H. Kennedy, A. Sweeney, A. Boston, H. Boston, J. Cresswell, P. Nolan, J. Sampson, I. Burrows *et al.*, "Semiconductor detectors for compton imaging in nuclear medicine," *Journal of Instrumentation*, vol. 7, no. 01, p. C01004, 2012.

[53] G. H. B. Turk, "The characterisation of the first smartpet hpge planar detector," Ph.D. dissertation, University of Liverpool, 2006.

[54] R. J. Cooper, "Performance of the smartpet positron emission tomography system for small animal imaging," Ph.D. dissertation, University of Liverpool, 2007.

[55] J. Stein, F. Scheuer, W. Gast, and A. Georgiev, "X-ray detectors with digitized preamplifiers," *Nuclear Instruments and Methods in Physics Research Section B: Beam Interactions with Materials and Atoms*, vol. 113, no. 1-4, pp. 141–145, 1996.

[56] A. Georgiev, W. Gast, and R. Lieder, "An analog-to-digital conversion based on a moving window deconvolution," *IEEE transactions on nuclear science*, vol. 41, no. 4, pp. 1116–1124, 1994.

[57] J. Cresswell and J. Sampson, "Mtsort language."

[58] R. Cooper, A. Boston, H. Boston, J. Cresswell, A. Grint, L. Harkness, P. Nolan, D. Oxley, D. Scraggs, I. Lazarus *et al.*, "Charge collection performance of a segmented planar high-purity germanium detector," *Nuclear Instruments and Methods in Physics Research Section A: Accelerators, Spectrometers, Detectors and Associated Equipment*, vol. 595, no. 2, pp. 401–409, 2008.

[59] M. Cromaz, "The gretina spectrometer," in *Journal of Physics: Conference Series*, vol. 606, no. 1. IOP Publishing, 2015, p. 012016.

[60] M. Berger, J. Hubbell, S. Seltzer, J. Chang, J. Coursey, R. Sukumar, D. Zucker, and K. Olsen, "Nist standard reference database 8 (xgam)," *XCOM: Photon Cross Sections Database*, 2008.

[61] W. Coburn, S. Amrose, S. E. Boggs, R. P. Lin, M. S. Amman, M. T. Burks, E. L. Hull, P. N. Luke, and N. W. Madden, "3d positioning germanium detectors for

gamma-ray astronomy," in *X-Ray and Gamma-Ray Detectors and Applications IV*, vol. 4784.   International Society for Optics and Photonics, 2003, pp. 54–64.

[62] L. Mihailescu, K. Vetter, M. Burks, D. Chivers, M. Cunningham, D. Gunter, and K. Nelson, "Methods for increasing the efficiency of compton imagers," Lawrence Livermore National Lab.(LLNL), Livermore, CA (United States), Tech. Rep., 2005.

[63] J. L. Dobson, "The characterisation and position resolution of a planar germanium strip detector," Ph.D. dissertation, University of Liverpool, 2005.

[64] W. Coburn, S. Boggs, S. Amrose, R. Lin, M. Burks, M. Amman, P. Luke, N. Madden, and E. Hull, "Results of charge sharing tests in a ge-strip detector," in *2001 IEEE Nuclear Science Symposium Conference Record (Cat. No. 01CH37310)*, vol. 1. IEEE, 2001, pp. 226–229.

[65] M. Descovich, "Improving the position resolution of highly segmented hpge detectors using pulse shape analysis methods," 2002.

[66] I. Mateu, P. Medina, J. Roques, and E. Jourdain, "Simulation of the charge collection and signal response of a hpge double sided strip detector using mgs," *Nuclear Instruments and Methods in Physics Research Section A: Accelerators, Spectrometers, Detectors and Associated Equipment*, vol. 735, pp. 574–583, 2014.

[67] M. Schlarb, R. Gernhäuser, S. Klupp, and R. Krücken, "Pulse shape analysis for γ-ray tracking (part i): Pulse shape simulation with jass," *The European Physical Journal A*, vol. 47, no. 10, p. 132, 2011.

[68] J. P. Wright, "A study of the effects of position resolution and energy resolution on compton imaging using a single planar strip detector," Ph.D. dissertation, University of Liverpool, 2016.

[69] M. C. Seiler and F. A. Seiler, "Numerical recipes in c: the art of scientific computing," *Risk Analysis*, vol. 9, no. 3, pp. 415–416, 1989.

[70] K. Vetter, A. Kuhn, I. Lee, R. Clark, M. Cromaz, M. Deleplanque, R. Diamond, P. Fallon, G. Lane, A. Macchiavelli *et al.*, "Performance of the greta prototype detectors," *Nuclear Instruments and Methods in Physics Research Section A: Accelerators, Spectrometers, Detectors and Associated Equipment*, vol. 452, no. 1-2, pp. 105–114, 2000.

[71] R. Kroeger, N. Gehrels, W. Johnson, J. Kurfess, B. Phlips, and J. Tueller, "Charge spreading and position sensitivity in a segmented planar germanium detector," *Nuclear Instruments and Methods in Physics Research Section A: Accelerators, Spectrometers, Detectors and Associated Equipment*, vol. 422, no. 1-3, pp. 206–210, 1999.

[72] Canberra UK, Private Communication, 2015.

[73] M. Schlarb, "Simulation and real-time analysis of pulse shapes from segmented hpge-detectors," Ph.D. dissertation, Technische Universität München, 2009.

[74] R. Lawrance, "The temperature dependence of drift mobility in germanium," *Physical Review*, vol. 89, no. 6, p. 1295, 1953.

[75] M. Prince, "Drift mobilities in semiconductors. i. germanium," *Physical Review*, vol. 92, no. 3, p. 681, 1953.

[76] B. Birkenbach, B. Bruyneel, G. Pascovici, J. Eberth, H. Hess, D. Lersch, P. Reiter, and A. Wiens, "Determination of space charge distributions in highly segmented large volume hpge detectors from capacitance–voltage measurements," *Nuclear Instruments and Methods in Physics Research Section A: Accelerators, Spectrometers, Detectors and Associated Equipment*, vol. 640, no. 1, pp. 176–184, 2011.

[77] M. R. Dimmock, A. J. Boston, J. R. Cresswell, I. Lazarus, P. Medina, P. Nolan, C. Parisel, C. Santos, J. Simpson, and C. Unsworth, "Validation of pulse shape simulations for an agata prototype detector," *IEEE Transactions on Nuclear Science*, vol. 56, no. 4, pp. 2415–2425, 2009.

[78] B. Bruyneel, P. Reiter, A. Wiens, J. Eberth, H. Hess, G. Pascovici, N. Warr, S. Aydin, D. Bazzacco, F. Recchia *et al.*, "Crosstalk corrections for improved energy resolution with highly segmented hpge-detectors," *Nuclear Instruments and Methods in Physics Research Section A: Accelerators, Spectrometers, Detectors and Associated Equipment*, vol. 608, no. 1, pp. 99–106, 2009.

[79] R. Venturelli and D. Bazzacco, "Adaptive grid search as pulse shape analysis algorithm for γ-tracking and results," *LNL Annual Report*, vol. 2005, 2004.

[80] I. Doxas, C. Nieter, D. Radford, K. Lagergren, and J. R. Cary, "An approximate method for linear signal decomposition in γ-ray tracking detectors," *Nuclear Instruments and Methods in Physics Research Section A: Accelerators, Spectrometers, Detectors and Associated Equipment*, vol. 580, no. 3, pp. 1331–1337, 2007.

[81] S. Agostinelli, J. Allison, K. a. Amako, J. Apostolakis, H. Araujo, P. Arce, M. Asai, D. Axen, S. Banerjee, G. . Barrand *et al.*, "Geant4—a simulation toolkit," *Nuclear instruments and methods in physics research section A: Accelerators, Spectrometers, Detectors and Associated Equipment*, vol. 506, no. 3, pp. 250–303, 2003.

[82] P. Barton, M. Amman, R. Martin, and K. Vetter, "Ultra-low noise mechanically cooled germanium detector," *Nuclear Instruments and Methods in Physics Research Section A: Accelerators, Spectrometers, Detectors and Associated Equipment*, vol. 812, pp. 17–23, 2016.